Investigation of the effect of process parameters on the formation of recast layer in wire-EDM of Inconel 718

A Thesis
Presented to
The Academic Faculty

by

Thomas R. Newton

In Partial Fulfillment
of the Requirements for the Degree
Master of Science

George W. Woodruff School of Mechanical Engineering
Georgia Institute of Technology

May 2008

Investigation of the effect of process parameters on the formation of recast layer in wire-EDM of Inconel 718

Approved by:

Dr. Shreyes N. Melkote
(ME, Georgia Tech), Committee Chair

Dr. Steven Danyluk
(ME, Georgia Tech)

Dr. Steven Liang
(ME, Georgia Tech)

Date Approved: February 11, 2008

Dedicated to my grandfathers, Dr. J.Q. Williams and Russell Newton Sr., for imparting me with a desire to learn about science and engineering

ACKNOWLEDGEMENTS

I would like to thank the following people for helping me along the way:

- My parents, grandparents, sister Elizabeth, girlfriend Sunni, and the rest of my family for always supporting and encouraging me.
- All of my friends in the Machine Shop, and especially John Graham and Donald Long for patiently teaching me about machining and lending me their wisdom and experience.
- Steven Sheffield for introducing me to the PMRC, helping me with the equipment, and always have a good story to tell.
- All of the members of the PMRC, in particular my office mates, Matt Breland, Chris Golden, Mukund Kumar, Ramesh Singh and Sathyan Subbiah for helping me along, and always lightening the mood with their discussions.
- The many people of the High Temperature Materials Laboratory at the Oak Ridge National Laboratory, including Dr. Tom Watkins for hosting me and performing the x-ray diffraction experiments, Rosa Trejo and Laura Reister for their great assistance with nano-indenter, and Larry Walker for conducting the electron probe microanalysis.
- Dr. Melkote, for advising and guiding me, always having time to meet and remaining enthusiastic though it all.

TABLE OF CONTENTS

LIST OF TABLES

LIST OF FIGURES

SUMMARY

Inconel 718 is a high nickel content superalloy possessing high strength at elevated temperatures and resistance to oxidation and corrosion. The non-traditional manufacturing process of wire-electrical discharge machining (EDM) possesses many advantages over traditional machining during the manufacture of Inconel 718 parts. However, certain detrimental effects are also present. The top layer of the machined surface is melted and resolidified to form what is known as the recast layer. This layer demonstrates microstructural differences from the bulk workpiece, resulting in altered material properties.

An experimental investigation was conducted to determine the main machining parameters which contribute to recast layer formation in wire-EDM of Inconel 718. It was found that average recast layer thickness increased with energy per spark, peak discharge current, current pulse duration, and open-voltage time and decreased with sparking frequency and table feed rate. Over the range of parameters tested, the recast layer was observed to be between 5 and 10 μm in average thickness, although highly variable in nature.

Surface roughness of the cut parts showed an increase with energy per spark. Electron Probe Microanalysis (EPMA) revealed the recast layer to be alloyed with elements from the wire electrode. X-ray diffraction testing showed the residual tensile stresses evident near the cut surface to decrease with energy per spark. Additionally, nano-indentation hardness testing indicated that the recast layer is reduced in hardness and elastic modulus compared to the bulk material. Vibratory tumbling was found to be a moderately effective post-processing tool for recast layer removal when using pre-formed ceramic abrasive media or fine grained aluminum oxide.

CHAPTER I

INTRODUCTION

1.1 Background

Wire-electrical discharge machining (EDM) is a non-traditional machining process in which a pulsed voltage difference between a wire electrode and a conductive workpiece initiates sparks which erode workpiece material. Removing material in such a way is often advantageous when the workpiece material would be difficult to machine with traditional machine tools due to high strength, hardness, toughness, etc. This process has been used in commercial machine tools for nearly half a century. It is well known that the EDM process has a detrimental impact on the surface integrity of machined surfaces. Each spark melts a small portion of the workpiece. A portion of this molten material is ejected and flushed away. The remaining material re-solidifies to form a surface layer known as the recast layer. This layer can contain an altered microstructure, tensile stresses, microcracks, impurities, and other undesirable features which can lead to premature part failure when put to service. Consequently, wire-EDM cut parts must often be post-processed to remove the negatively affected material. Furthermore, the surface integrity effects are dependent upon both the wire-EDM process parameters and the chemical composition of the workpiece.

Much work has been devoted to the study of surface integrity in wire-EDM of common steel alloys, particularly tool and die steels. However, little research has been reported on the effects of wire-EDM on high nickel content superalloys. Specifically, no significant literature has been found by the author relating to surface integrity of Inconel 718 in wire-EDM. Inconel 718 is comprised of 52% nickel, 20% chrome and 18% iron and possesses high strength at elevated temperatures, while resisting oxidation and corrosion. It is currently used in gas turbines, cryogenic tanks, and as fasteners or springs for aerospace applications. Before safely usable parts of Inconel 718 can be manufactured by wire-EDM, the resulting recast layer must be characterized, and its formation understood.

1.2 Problem Statement

As stated above, critical Inconel 718 parts cut with wire-EDM must be post-processed to remove the affected surface layers, primarily the recast layer. The formation and characteristics of the recast layer must be studied. Furthermore, while recast layer formation can be altered by process parameters, it cannot be completely eliminated. Thus, there is still a need for some post-processing in certain applications. This thesis will attempt to address the following:

- What wire-EDM process parameters have an effect on the formation of recast layer in Inconel 718?
- What are the characteristics of this recast layer?
- How can post-processing techniques be used to remove this recast layer?

1.3 Research Goals

The research described in this thesis will attempt to solve the problems detailed in the previous section. To meet these ends, the following goals have been set:

1. To design and conduct a series of experiments which will reveal the impact of various wire-EDM process parameters on the thickness of the recast layer formed in Inconel 718.
2. To characterize this recast layer in terms of hardness and residual stresses though nano-indentation hardness testing and x-ray diffraction, respectively.

3. To investigate removal of the recast layer through various post-processing techniques, and experimentally study one low-cost method.

1.4 Thesis Outline

Chapter II will first discuss the development of electrical discharge machining, followed by a summary of reported knowledge pertaining to the effects of various process parameters. Additionally, currently practiced post processing techniques will be covered, along with a detailed description of Inconel 718. The experimental work conducted here, including the methods, measurements and results obtained will be given in Chapter III. Chapter IV will discuss the findings of the two main characterizations undertaken. Chapter V will cover post-processing for recast layer removal, while Chapter VI will summarize the key findings of this thesis.

CHAPTER II

LITERATURE REVIEW

2.1 Introduction to EDM

Electrical Discharge Machining (EDM) is a non-traditional manufacturing process in which electric sparks are used to remove workpiece material. There are two main types of EDM: ram or die-sinking EDM, and traveling-wire, wire-cut, or simply wire-EDM. In either kind, the underlying principle is the same. A power supply initiates a voltage potential between the electrode and the electrically conductive and grounded workpiece. This scenario is analogous to the two plates of a parallel plate capacitor. As the tool approaches the workpiece, the electric field strength grows in the gap until the dielectric medium separating the tool and the workpiece breaks down. At this point, electrical discharge is initiated and the voltage drops as the current rises. The dielectric ionizes and a plasma channel is created, compressing the surrounding dielectric. The plasma may reach a temperature of as high as 40,000 K and a pressure of 3 kbar. As both electrons and ions bombard the workpiece surface, the workpiece is heated such that a portion of the surface is melted. However, the plasma pressure prevents vaporization. At the conclusion of the discharge, the plasma channel collapses and a vapor bubble occurs causing the superheated molten material on the surface of the workpiece to explode into the dielectric. The ejected material is flushed away, while a portion of the molten material resolidifies onto the workpiece surface forming a crater [10]. This resolidified material is known as the remelted, or recast layer.

In die-sinking EDM, the electrode is a specific shape and machines the negative of this shape into the workpiece. Typically the tool is the anode and the workpiece is the cathode with discharges occurring over tens to hundreds of microseconds. The dielectric medium is often a hydrocarbon such as kerosene. In wire-EDM, the tool is a wire which can cut an extruded geometry similar to a conventional band saw. Generally, the wire is the cathode, and the duration of each discharge is usually less than 10 μs, and often less than 1 μs. De-ionized water is the usual dielectric. Figure 2.1 displays a typical discharge in wire-EDM.

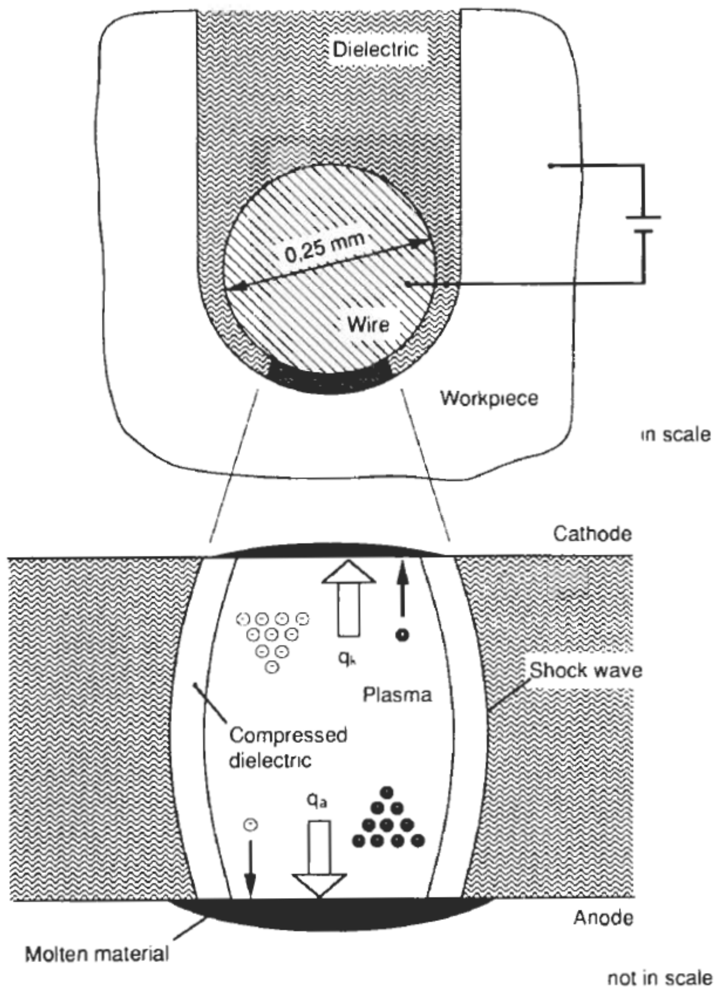

Figure 2.1: Diagram showing the material removal mechanism in wire-EDM due to a single discharge [2]

In wire-EDM, the wire travels perpendicular to the direction of cut from a supply spool, though the cutting zone, and is then collected for scrap, as displayed in Figure 2.2. The speed at which the wire feeds is generally much greater then the table feed rate. Some machines will allow the upper and lower wire guides to be moved independently, creating a tapered cut. However, the wire guides are fixed in the machine used in this research. One of the advantages to wire-EDM is the narrow kerf created. The kerf width is equal to the diameter of the wire electrode, plus twice the gap in which the electrical discharges take place. Usually, there are nozzles directing dielectric into the cutting zone to flush out the chips.

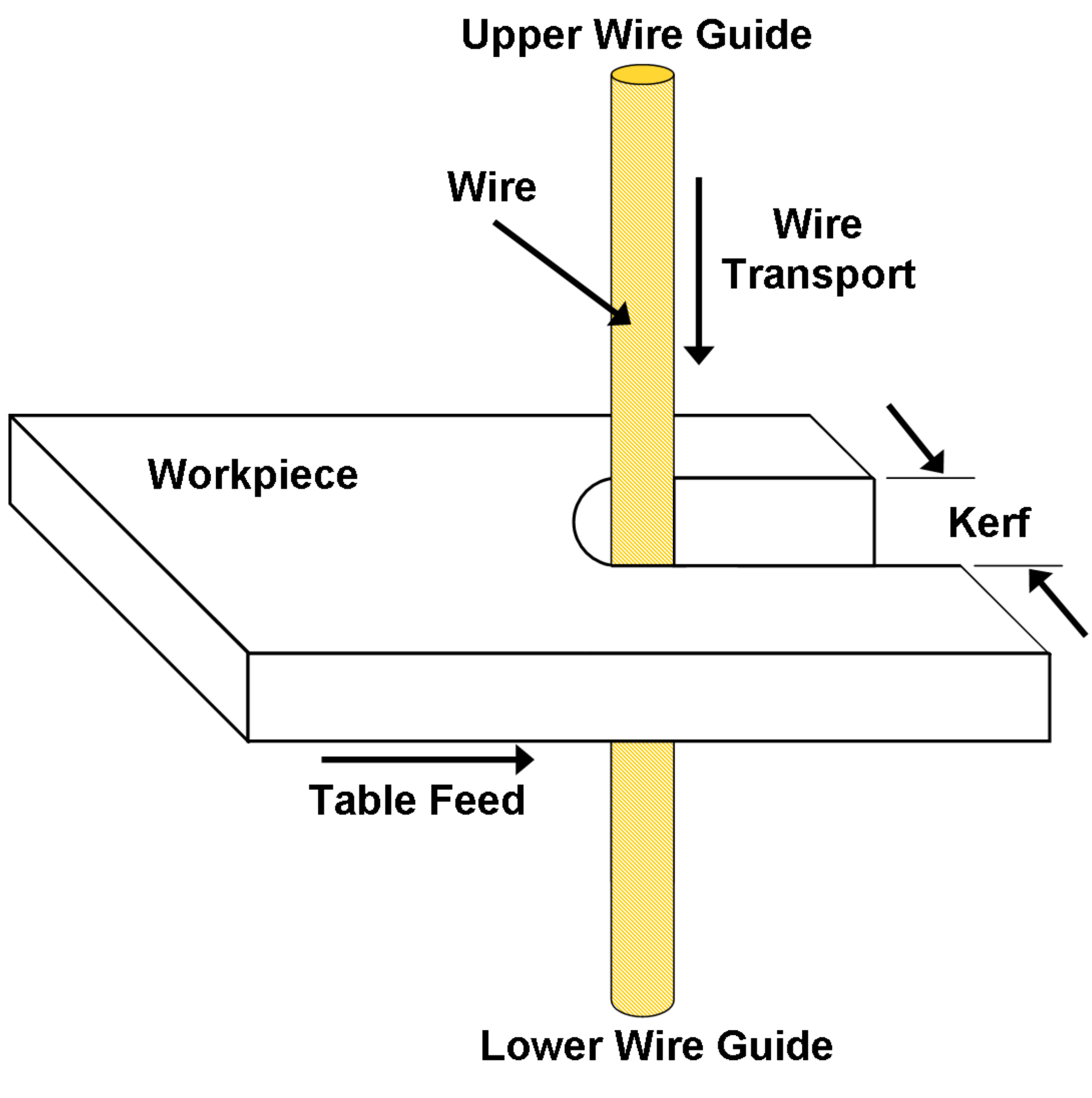

Figure 2.2: Diagram showing orientation of the wire electrode in wire-EDM

It is important to note that the sparking process is extremely stochastic. Observe the situation seen in Figure 2.3. The discharge will occur at the point where the electric field is the strongest. This will primarily be located between peaks of the wire and workpiece surface profile because the gap distance is the shortest. However, the wire will vibrate and bend due to the electrostatic forces and explosive forces from previous discharges [11]. The wire is also subject to forces from the jets of dieletric. It is held in tension, and transported through the machine. The sparking gap may also contain swarf generated from previous cuts. Consequently, the sparking locations are extremely difficult to predict. At the point where a discharge occurs material will be ejected leaving behind a crater. As the table continues to feed toward wire the next spark will now occur at a new location.

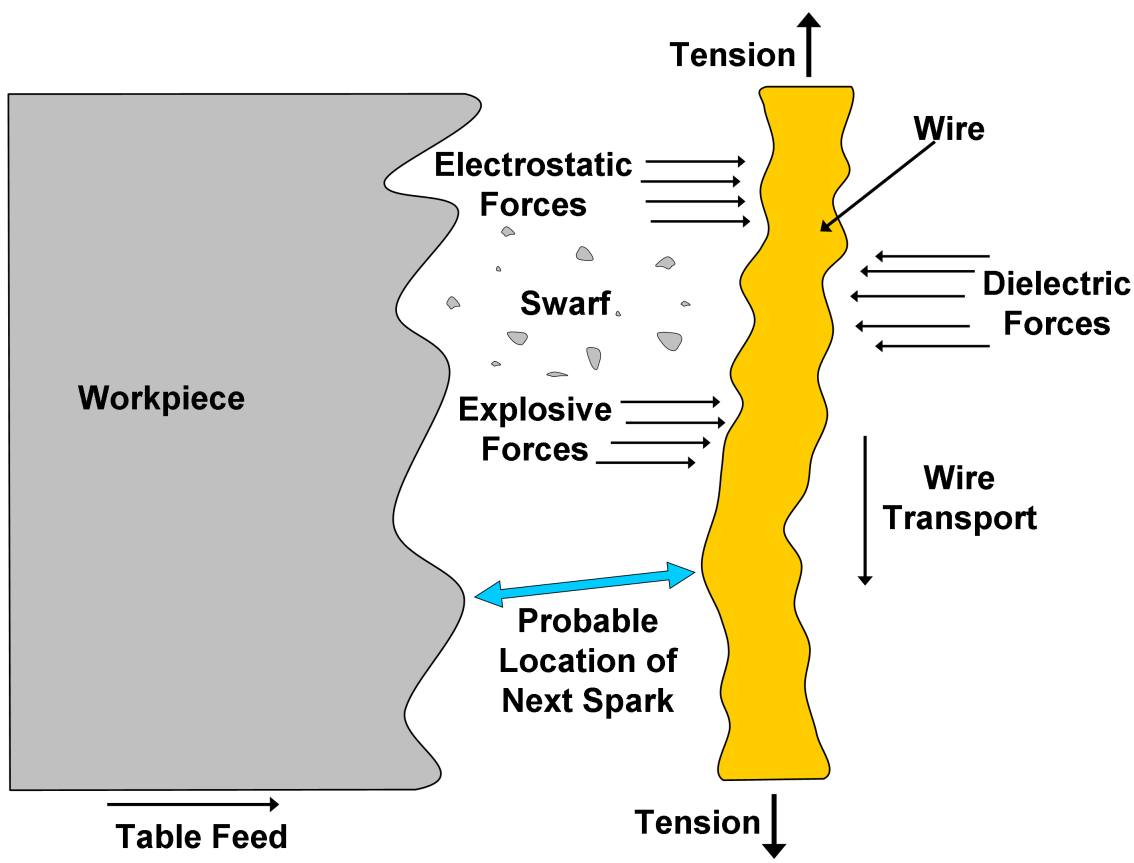

Figure 2.3: Diagram showing the many factors which affect the spark location in wire-EDM

Critical to analysis of electrical discharge machining is the signal from the EDM pulse generator, shown below in Figure 2.4. While there are multiple systems for controlling the EDM process, a general, idealized signal should be common. To clarify the nomenclature, the words given in this diagram will be used throughout this work. The open-voltage is usually a fixed value, and is also referred to as the open-circuit voltage. The open-voltage period is also known as the ignition delay time, or the build-up period. What is referred to here as the current pulse duration is sometimes called the pulse on-time, or on-time. The sum of the open-voltage period and the voltage off-time is sometimes known as the pulse off-time, or off-time. Some researchers may also refer to the sum of the open voltage time and the current pulse duration as the pulse on-time. This confusion may derive in part from the different current pulse durations in wire-EDM and die-sinking EDM.

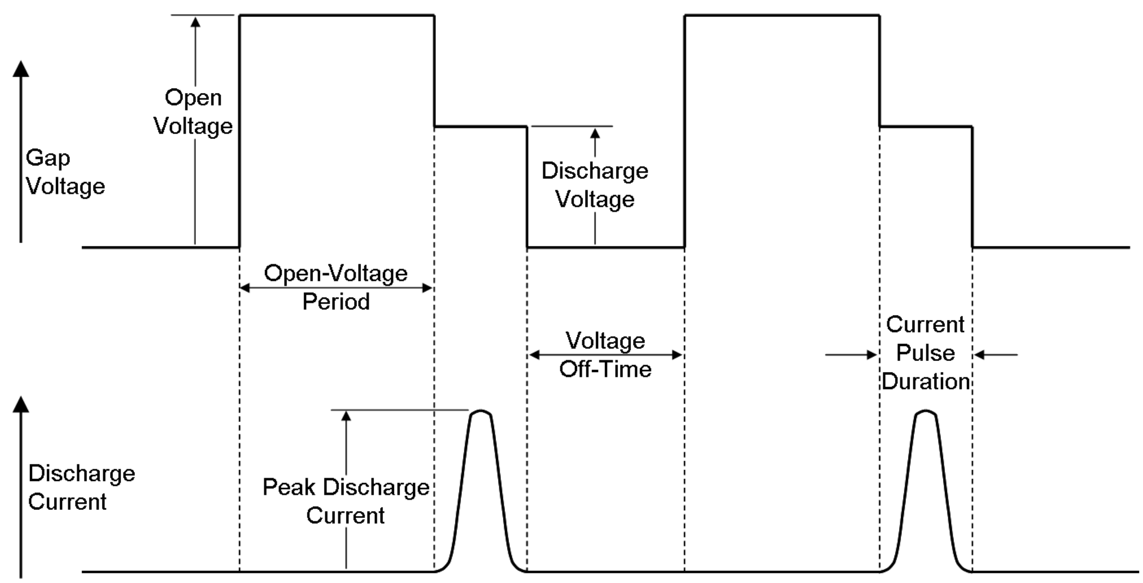

Figure 2.4: Diagram of nomenclature describing the current and voltage signals in EDM

2.2 Development of EDM

The first reported experiment in which electrical discharges were used to melt and erode a metal workpiece was performed by Joseph Priestley in 1766. Using a battery and a brass knob as an electrode, he found that the diameter of the crater created depended both on the workpiece material, and the degree to which the battery was charged [12].

The Soviets Boris and Natalie Lazarenko are credited with development of the first machine tool to use electrical discharges as a method of material removal. Their work was first reported in the U.S. in 1947 [13]. A later publication describes a converted drill press which was essentially the first die-sinking EDM, displayed in Figure 2.5. Also discussed was a machine for grinding tools in a process similar to electrical discharge grinding [3].

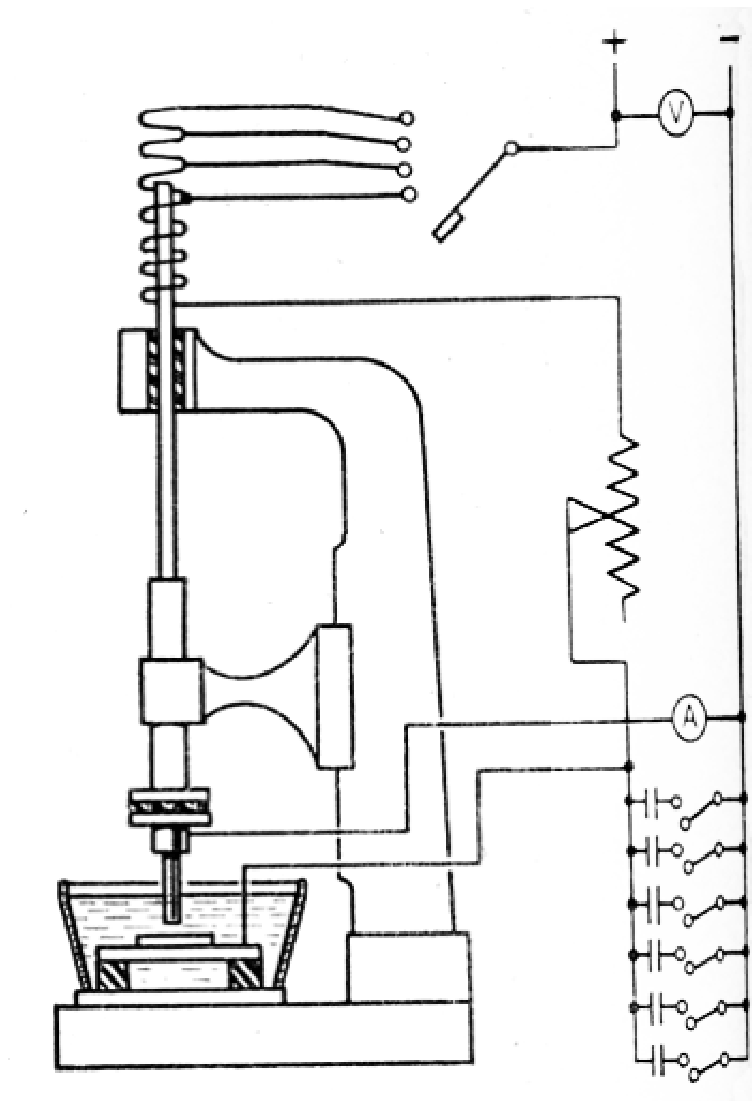

Figure 2.5: Drawing of the first die-sinking EDM [3]

The first EDM with a traveling wire electrode, shown in Figure 2.6, was patented in 1961 [4], although wire-EDM in its modern form did not become commonplace until the advent of computer numerical control (CNC).

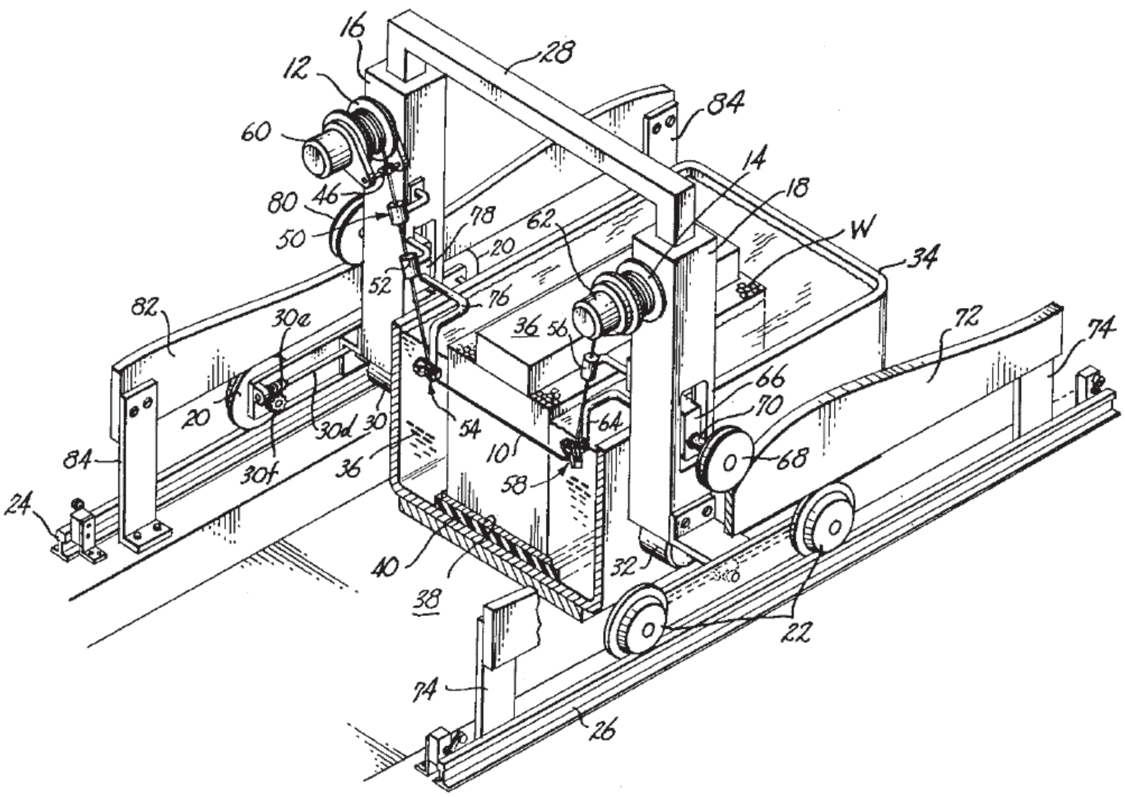

Figure 2.6: Patent drawing of the first wire-EDM [4]

2.3 Effects of Process Parameters

This section will describe the known effects of various wire-EDM parameters on the machined workpiece as it has been long established that electrical discharges impact the surface integrity of the workpiece [14, 15]. Although a great deal more research has focused on die-sinking EDM, this survey will cover mainly wire-EDM. It is felt that the dielectric media, discharge parameters and electrode materials are too different to directly compare findings between the two types of EDM. Accordingly, die-sinking EDM related findings will only be substituted when no relevant wire-EDM work can be found. Also, as mentioned, nomenclature tends to vary from one research to the next, so every effort has been made to assure “apples to apples” comparisons.

2.3.1 Current Pulse Duration

It has been well established that increasing the current pulse duration increases the surface roughness of the machined surface [16, 17, 18, 19, 20, 21, 22, 23]. Recast layer depth has also been shown to increase with current pulse duration [16, 24, 21]. Surface crack density also tends to increase with increased current pulse durations [21].

2.3.2 Voltage Off-Time

Reducing the voltage off-time has been shown to minimize the formation of an oxide layer in Ti-6Al-4V [25].

2.3.3 Peak Discharge Current

Surface roughness is known to increase with the peak discharge current [19, 26, 27].

2.3.4 Energy per Spark

It has been found that gap width increases with the energy per spark [16], as well as surface roughness and recast layer [16, 21]. Surfaces machined with both short and long current pulse durations had almost identical surface roughnesses as long as the energies per spark were equal to one another. However, a comparison of the morphologies revealed great differences between the two cases. Over the ranges examined, short current pulse durations created craters by vaporization, while long current pulse durations generated craters through melting [28].

2.3.5 Dielectric Properties

Although wire-EDM can be conducted in a dry gas atmosphere [29], it is typically conducted in the presence of a liquid dielectric. The dielectric flushing pressure has been shown to have an insignificant or minor effect on the surface roughness [16, 20, 21].

The same results were concluded when the dielectric flow rate was instead measured [19]. Flushing pressure was found to have no effect on the recast layer thickness in D2 tool steel [16]. The microhardness distribution below the surface remains constant in tool steels with increased dielectric flushing pressure, while the surface hardness slightly increases. Further, the microstructure was shown to remain constant with increased pressure [21]. Maintaining proper flushing conditions is necessary to prevent wire rupture as the convective heat transfer coefficient is the most important parameter governing the maximum wire temperature [30].

Although the electrical conductivity of the dielectric does not have an impact on surface roughness, it can impact the discharging process. As the conductivity is increased, current leakage due to electrolysis appears during the open-voltage period. Electrolysis will lead to oxidation of the entire workpiece surface [22] and may also lead to a decrease in the hardness of a wire-EDM cut surface [31]. Some researchers have developed a non-electrolysis power supply to prevent this corrosion and alteration of properties [32].

2.3.6 Wire Properties

Originally, copper wire was used in wire-EDM because of its high electrical conductivity. However, plain copper wire is difficult to vaporize. Consequently, zinc, with its lower melting point, was added to the wire. During cutting, the zinc vaporizes and helps to flush debris from the gap. One of the most common types of wire used in non-tapered wire-EDM cutting is hard brass wire. Composed of 63% copper and 37% zinc, hard brass wire typically has a 2% elongation [33]. When using smaller diameter wires, as in micro-wire EDM, tungsten wire is sometimes utilized [34, 35, 36]. It is well established that wire materials can become deposited on the machined surface [37, 27, 38, 39, 40]. This phenomenon has shown some dependence on machine polarity [38].

Wire speed does not seem to influence surface roughness [21], though increasing wire tension can serve to minimize surface roughness [22]. It has been proposed that the average wire temperature distribution along the wire axis is only 100°C, thus the local elevated temperatures must be the important factor [41]. Wire rupture, caused by high temperature and power density, can be limited by controlling the sparking frequency [42]. The melting temperature and work function of the wire and its coating affect the maximum cutting speed [43]. It has also been put forth that since the electric field increases with radius of curvature, wire with more sharp edges might increase the cutting efficiency [44].

Many researchers have studied micro-wire-EDM [45, 46, 34, 35, 47, 48]. Although experimentation has been done over a range of wire diameters, little work appears to have examined wire electrode size effects. It is known that the material removal rate decreases for thinner wires as a result of the lower allowable discharge current [49]. Additionally, the power supply, or pulse generator, must be more sensitive and provide a finer degree of control than is necessary in conventional wire-EDM [45, 46, 48]. Due to the small nature of the parts and electrode (wire), handling can become difficult [50]. The limited back tension allowed by the narrow diameter wire causes part tolerances and accuracy to be more greatly affected by both the cutting forces [36], and the flow of the dielectric [47].

2.3.7 Table Feed Rate

In micro-wire-EDM, it has been found that a high table feed rate will contribute to a diminished gap, and consequently an increased short ratio [45]. Some researchers have found that the table feed rate has no effect on the surface roughness [51]. Others contend that there is an effect on surface roughness [20]. In trim cutting, a low table feed rate can effectively remove surface peaks and can also have a significant effect on the removal thickness of previously imparted recast layer [16].

2.3.8 Miscellaneous

Surface roughness and crack density increase with the open voltage [21].

2.4 Inconel 718

2.4.1 Background Information

Inconel 718 is an age hardening nickel base superalloy. It retains its strength across both high and low temperatures and has good corrosion resistance. It is used in aircraft turbine engines, as high temperature fasteners, as well as in cryogenic tanks [52]. Inconel 718 is readily weldable and machinable and was originally manufactured by the International Nickel Company [53]. The exact chemical composition of this alloy is shown below in Table 2.1. This alloy is also known as IN-718, Inco-718, alloy 718 and United Numbering System (UNS) N07718 [52]. It has been suggested that in recent times Inconel 718 has comprised more than 60% of total superalloy consumption [54].

Table 2.1: Chemical composition of Inconel 718 [1]

Element	Range (%)
Ni	51.5
Fe	20.24
Cr	18.16
Nb	5.02
Mo	2.91
Ti	1.05
Al	0.62
Co	0.15
Si	0.08
Mn	0.07
Cu	0.06
C	0.05
P	0.008
Ta	0.003
B	0.003

At room temperature, annealed Inconel 718 has a density of 8.19 g/cm^3, thermal conductivity of 11.2 W/m-K, electrical resistivity of 127 microhm-cm, and an elastic modulus of 200 GPa [55]. It has a yield strength of 434 MPa, a tensile strength of 855 MPa and a hardness of 95 HRB [1].

Inconel 718 has an austenitic face-centered cubic (FCC) structure. It is strengthened primarilly by the γ'' precipitate. This phase consists of body-centered tetragonal (BCT) Ni_3Nb. Alloying with chrome promotes resistance to environmental degradation [52]. Inconel 718 is often used in the solution and aged condition. In practice, a wide variety of heat treatments are used to impart various desired combinations of yield strength, tensile strength, toughness, grain size, fatigue properties, and corrosion resistance [56].

2.4.2 Wire-EDM of Inconel 718

Few publications relating to the wire-EDM of Inconel 718 have been found by the author. It has been shown that increasing the current pulse duration as well as the open voltage period tends to increase the surface roughness [23]. In solution treated and aged Inconel 718, it was shown that the wire-EDM cut surface increased in hardness above the parent material on the Rockwell C scale [51]. In a thin membrane of solution treated and aged Inconel 718, it was shown that the Vickers microhardness of the wire-EDM cut surface was raised above the bulk, and decreased as the distance from the cut surface increased. However, great variation in the microhardness was observed, and attributed to the variety of phases present. The cut surface also demonstrated an increase in copper content after machining [37].

2.5 Post-Processing

It has been shown above that EDM can impart many undesirable characteristics on a machined surface. These may include large surface roughness, surface cracks, residual stresses, changes in hardness, surface contamination, surface oxidation as well as other metallurgical changes. Consequently, it is often necessary to post-process wire-EDM cut parts to alleviate these problems. A variety of post-processing methods are available and a survey of these is given below.

2.5.1 Abrasive Flow Machining

One popular abrasive finishing technique is known as abrasive flow machining (AFM). Here, abrasive media is extruded through a machine to deburr, polish and radius part surfaces and edges. Extrusion pressure, flow volume and speed can be controlled to allow stock removal controllable to 30 μm. Tooling can direct media to desired areas, including internal passageways. High viscosity media can uniformly abrade walls of passages, while lower viscosity media can radius edges, and reach small internal regions. AFM is a reliable method to remove EDM recast layer, yielding up to a 90% improvement in surface finish [57]. This allows for the elimination of finishing or trim cuts in wire-EDM [58]. To avoid the cost of commercial abrasive media, a mixture of vinyl-silicon polymer and abrasive particles can be substituted while still satisfactorily removing wire-EDM caused recast layer [59].

2.5.2 Abrasive Micro-Blasting

A similar process to shot peening is abrasive micro-blasting, although the media is abrasive silicon carbide (SiC). Experiments conducted with wire-EDM cut tungsten carbide-cobalt (WC-Co) composite revealed that the EDM induced recast layer and heat affected zone (HAZ) could be quickly eroded with 4 to 20 μm SiC abrasives. Compressive stresses can also be imparted [60].

2.5.3 Electrochemical Processes

Much work has been devoted to the realm of electrochemical processes. In electrochemical processing, the workpiece is immersed in an electrolyte bath and a current is passed between a cathodic electrode and the anodic workpiece. The current, electrode gap distance, electrolyte flow rate, electrolyte temperature, and type of electrolyte all impact the workpiece surface dissolution rate [61]. The current can be constant or pulsed, and the polarity can be reversed [62]. Electrochemical machining has been used to remove EDM imparted recast layer and improve surface finish [63, 64]. Alternatively, electrochemical processes can be combined with die-sinking EDM [61, 65] and wire-EDM [66] to form a single process.

Due to their high resistance to corrosion, nickel-base superalloys will form a thin oxide coating on their surface during ECM. Consequently high voltage or current is necessary to break this film. Pulse reverse current electrochemical machining (PRECM) has displayed improved machining of Inconel 718 over direct or pulse current electrochemical machining [62].

One issue with electrochemical processing is due to environmental concerns. Although the electrolytes can be physiologically safe, heavy metals can accumulate in the electrolyte. It is believed that toxic chromate, nitrate and ammonia may be adsorbed to metal hydroxides in the electro-chemical slurry, causing the necessity for detoxification of the hydroxide slurries to impact the economic efficiency of this process [67].

2.5.4 Loose Abrasive Mass Finishing

Loose abrasive mass finishing is also known as tumbling. It has been shown to improve part surface finish, as well as induce compressive residual stress [68, 5]. Additionally, scale, dirt and oil can be removed with minimal part handling [5].

Tumbling can be divided into three main types: rotary, vibratory and centrifugal. Rotary tumbling is the oldest form of form of finishing, and is characterized by the "climb and slide" motion. In this process, parts roll around in a mass of media inside a drum rotating about a single axis. The speed of rotation, and size and configuration of drum can be altered. In vibratory tumbling, an eccentric weight on a drive shaft causes vibration of a tub or bowl. This vessel contains the media and parts, and is mounted on springs. The amplitude of vibration and frequency of vibration can be altered. Centrifugal equipment uses a spinning disk located at the bottom of the vessel to cause a rotation of the parts and media. Although the action is similar to rotary tumbling, the work is accomplished six to twenty times faster. The speed and orientation of the rotating disk can be altered, as well as the size of the process chamber [69].

The media can be composed of steel, ceramic, plastic, or wood. Abrasive media is generally aluminum oxide, either natural or synthetic, fused silicon carbide, or a preformed ceramic or resin bonded media containing aluminum oxide, silica or silicon carbide. The media is available in a variety of shapes, as shown in Figure 2.7. It is important to select the proper media to part ratio. Typical ratios range from 1:1 to 10:1. A higher ratio delivers a greater finish quality, but requires a greater amount of media. Another critical factor is the compound solution. The compound should serve to clean, lubricate and inhibit corrosion or oxidation[5].

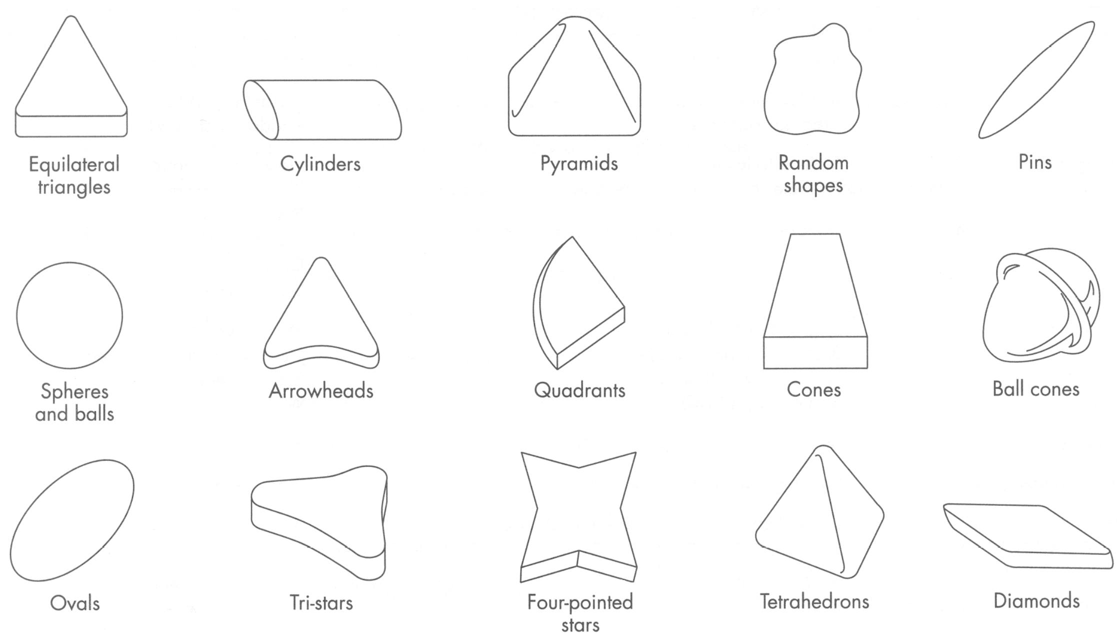

Figure 2.7: Media shapes which are available for tumbling [5]

2.5.5 Shot Peening

Shot peening is a process in which media, usually steel or glass, are impacted upon the surface of a part many times. This cold working process does not remove material but does plastically deform a shallow surface layer and induce compressive residual stresses on the surface. Shot peening can increase the fatigue life of a part, as well as increase its hardness and prevent stress corrosion. It effects only the surface of a part, and is limited in how well it can reach internal radii [70]. The elevated temperature fatigue life of nickel base super alloys has been shown to increase with shot peening [71]. The surface roughness, hardness, and fatigue life of wire-EDM cut thin Inconel 718 membranes was also improved by shot peening [37].

2.5.6 Other Processes

Other more limited post-processing techniques have been investigated. These include magnetic abrasive finishing (MAF) in which EDM induced recast layer and micro-cracks are removed from a shaft using a slurry of SiC abrasive and steel grit in a magnetic field. A method for expanding this technique to other part geometries has been proposed, but not yet demonstrated [72]. A method of combined ball-burnishing and EDM operation has been demonstrated and shown to improve the surface roughness and eliminate surface cracks and pores [73]. Neither of these methods are suitable for general purpose use.

2.6 Summary

Electrical discharge machining is a process which has existed in principle for 250 years, but which was not developed in practice until the 1940s. It has since become one of the most established non-traditional machining processes. This research focuses on wire-EDM, in which the electrode is a traveling wire.

Numerous process variables exist, although drawing broad conclusions can at times be difficult due to machine and material specificities. Regardless, it is clear that increasing the energy per spark, due to increasing the peak current or the current pulse duration, serves to increase both the surface roughness and recast layer thickness. Metallurgical changes, and resulting characteristics such as grain size and hardness are specific to material classes. Dielectric and wire variables seem to have secondary effects, although they must be set to an appropriate value to prevent wire rupture. Although a range of wire diameters are available, no report of the wire diameter size effect has been found. The effects of table feed rate seem somewhat in dispute, likely due to difficulties previously mentioned.

Inonel 718 is perhaps the most commonly used superalloy. It has high nickel and chrome content, and undoubtedly exhibits different metallurgical properties than the tool and die steels most commonly researched in EDM. Ramakrishnan and Karunamoorthy [23] examined surface roughness of wire-EDM of Inconel 718, but no other aspects of surface integrity, and did not report what heat treatment the workpieces had undergone. Jeelani and Collins [51] found the Rockwell C hardness of a wire-EDM cut surface of age hardened Inconel 718 to be higher than the original workpiece, but did not report the wire-EDM parameters. Lastly, Fordham et. al. [37] studied wire-EDM of a 0.33 mm thick membrane of aged and solution treated Inconel 718. They found the Vickers microhardness to decrease with distance from the edge, but could not measure the hardness of the actual recast layer. Again, wire-EDM parameters were not reported. There is clear need for further investigations into the recast layer and surface integrity in wire-EDM of Inconel 718.

It is established that the surface integrity of wire-EDM cut parts has a detrimental effect on their service life. Consequently, a variety of post-processing steps can be taken to rectify this fault. These may include abrasive flow machining, abrasive micro-blasting, electrochemical machining or polishing, loose abrasive mass finishing, and shot peening. Each has a different combination of performance, cost and time.

While post-processing techniques for wire-EDM cut parts have been reported, they are either expensive, inaccurate, or pose environmental hazards. There is a need for a simple and low cost post-processing solution for wire-EDM cut parts.

CHAPTER III

RECAST LAYER THICKNESS EXPERIMENTS

3.1 Goal & Approach

This chapter details the steps taken to find the impact of process parameters in wire-EDM of Inconel 718 on the resulting recast layer. Before the experiments could be undertaken, it was necessary to fully understand the process variables. The stochastic nature of wire-EDM required that the pulse generator signal be recorded and analyzed. Once this was achieved, preliminary experiments were conducted to find the available parameters and the range over which they could be varied. An experiment was designed and conducted to test the effect of each variable. The measured output, recast layer thickness, was analyzed. Through these experiments, the major contributing factors could be identified.

3.2 Brother HS-3100

All of the wire-EDM cuts reported here were made on a Brother HS-3100 Wire-EDM machine, as shown in Figure 3.1. This machine is capable of CNC motion in two-axes and with the appropriate wire guides can accept wire from a diameter of 100 μm to 300 μm. The machine has a reservoir of water, which acts both as a dielectric and as a flushing medium for the swarf. The machine controls the conductivity of the water by de-ionizing it with a resin tank. A chiller maintains the water at a constant temperature. This particular model is an operator-oriented machine tool. While it has a range of parameters which can be varied, given in Table 3.1, it was often not clear what each parameter controlled. Hence, it was necessary to develop a method to measure the pulse generator signal directly, as explained in the next section. Also, the machine contained several "auto-controls" which attempted to maximize the cutting rate while preventing wire ruptures. These features were disabled for the extent of this research.

Figure 3.1: Brother HS-3100 Wire-EDM

3.3 Measurements

3.3.1 Data Acquisition

A schematic of the system for capturing the voltage and current waveforms of the electrical discharges is shown below in Figure 3.2. The current carrying wires connecting the pulse generator to the brushes were passed through a Pearson Electronics model 110 current monitor. This sensor operates on the principle of induction and was chosen because of its peak measurable current of 5000 A, maximum RMS current of 65 A and its usable rise time of 13 ns. It also had a safety advantage in that it

Table 3.1: Range of machine settings for the Brother HS-3100

Machine Parameter	Setting	Range
Table feed rate	-	0.061 to 304.8 mm/min
Spark cycle	-	6 to 999 μs
Spark Energy	2 to 18	0.073±0.03 to 2.00±0.16 μs, 119±12 to 601±60A
Wire Speed	1 to 25	48 to 261 mm/sec
Wire Tension	0 to 25	200 to 2500 gf
Target Gap Voltage	-	30 to 70 V
Water Conductivity	0 to 6	8 to 65 μS/cm
Wire Diameter	-	100 to 300 μm
Stabilizer	1 to 3	-
Dielectric Flow Rate	-	0 to 8 ℓ/min

remained electrically isolated from the machine circuitry. The voltage probe was a Stack Electronics CP-209 and was attached to the brush. The bandwidth necessary to accurately monitor the signal was too great for any available PC-based data acquisition system. Therefore, a Tektronix model TDS420A oscilloscope was employed to record the signal. From there it was transfered to a PC for analysis. A detailed description of the experimental setup is given in Appendix A.

3.3.2 Data Analysis

Once the current and voltage data were obtained, it was necessary to analyze them to determine the various aspects of a signal. A simple program was written in Matlab to complete this task. The code for this program can be found in Appendix A. A sample set of analyzed waveforms is given below in Figures 3.3 and 3.4.

A close-up of an electrical discharge, shown in Figure 3.5, reveals that at the end of the discharge the current reverses direction and the voltage becomes negative. This can be attributed to the inevitable inductance present in the discharge circuit [15]. It is also seen that the voltage signal indicates some presence of ringing, which can again be attributed to the inherent inductance and capacitance of the circuit [74].

From this data, the following metrics could be calculated: average peak discharge

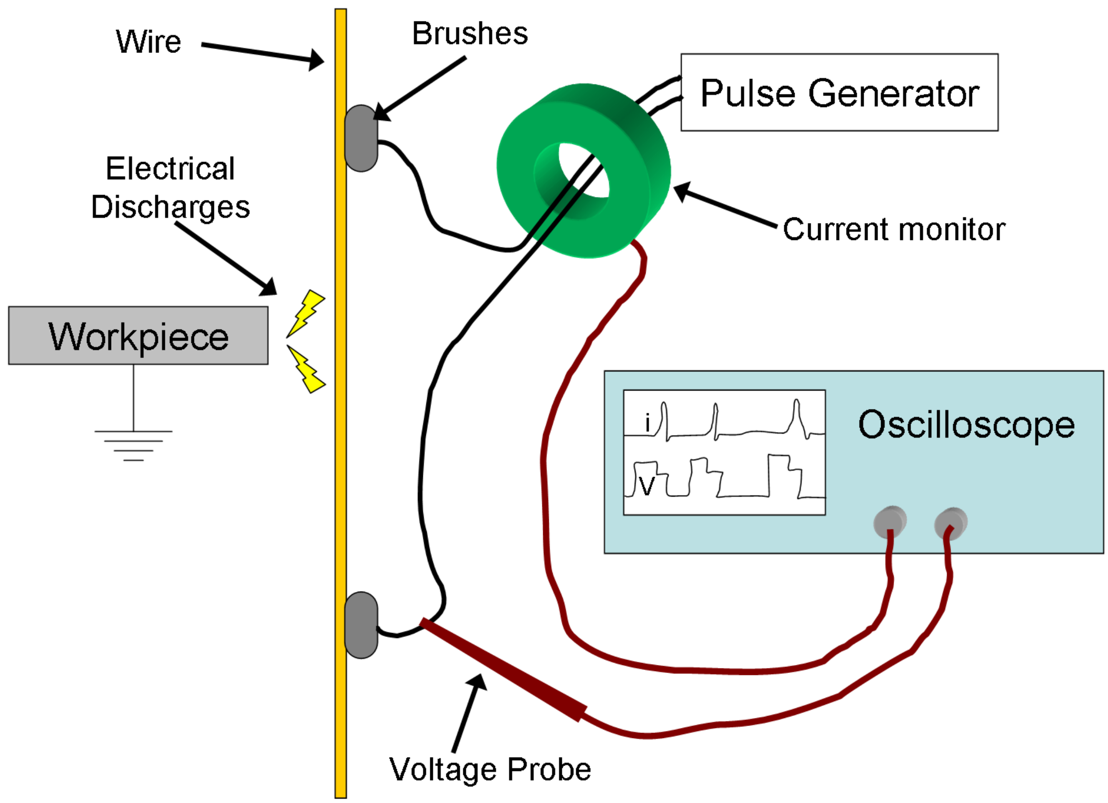

Figure 3.2: Schematic of voltage and current measurements on Brother HS-3100 Wire-EDM

current, average current pulse duration, average sparking frequency, average open-voltage time, average voltage off-time, average energy per spark, and average power. The report generated for the sample conditions shown in Figures 3.3 and 3.4 is shown in Table 3.2. The definitions of these measures are given in Figure 2.4. Bear in mind that the term spark energy refers to a machine setting, while energy per spark refers to the actual quantity of energy contained within each spark.

Due to a limitation in the oscilloscope, a maximum of 3 ms worth of data could recorded. Thus, for any given set of parameters, numerous data sets were collected and averaged to obtain a single set of values. From this type of analysis, it was confirmed that the wire-EDM process is stochastic in nature. From visual inspection of Figures 3.3 and 3.4, it can be seen that while each spark had a similar duration and peak

Table 3.2: Sample report of analysis for current and voltage waveforms

Pulse Number	Time [μs]	Duration [μs]	Peak Current [A]	Open-Voltage Time [μs]	Off-Time [μs]	Open Voltage [V]	Off-Time Voltage [V]	Discharge Voltage [V]	Energy per Spark [mJ]
1	17.80	1.10	122	16.7	0.4	75.98	76.80	18.00	3.60
2	114.70	1.10	126	80.2	15.7	76.39	-4.41	31.67	5.14
3	143.60	1.10	130	13.1	14.7	74.73	14.35	-5.00	3.04
4	189.10	1.10	138	38.0	6.40	76.19	-9.85	10.33	4.40
5	300.1	1.10	126	103.4	6.4	76.32	-5.85	2.67	2.80
6	448.6	1.10	130	140.9	6.5	76.01	20.24	32.33	5.27
7	585.2	1.10	122	118.6	16.9	76.15	-2.99	17.33	3.01
8	778.3	1.10	130	183.8	8.2	75.91	-3.57	34.33	5.05
9	840.5	1.10	126	54.0	7.2	75.67	-10.74	17.67	4.34
10	943.8	1.20	130	93.2	8.9	76.03	-3.6	-5.85	2.78
11	969.1	1.10	130	17.8	6.3	74.95	21.38	7.67	3.06
12	994.8	1.20	134	16.2	8.4	75.02	-6.78	7.38	3.67

Average peak discharge current is 125 Amps

Average discharge current pulse duration is 1.09 microseconds

Average sparking frequency is 15.33 kHz

Average open-voltage time is 52.53 microseconds

Average voltage off-time is 10.99 microseconds

Average open-voltage is 65.95 volts

Average off-time voltage is 0.65 volts

Average discharge voltage is 13.81 volts

Average energy per sparkis 3.71 millijoules

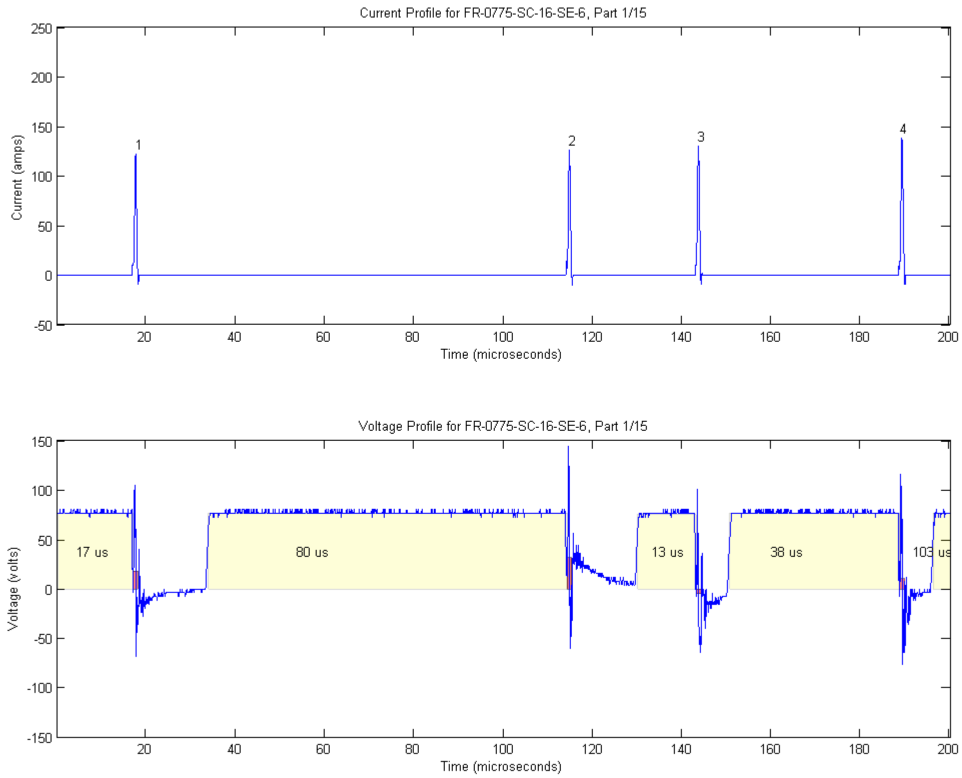

Figure 3.3: Sample current [A] and voltage [V] waveforms

current, imparting a similar quantity of energy, the period of time between sparks, largely dictated by the open-voltage time, varied greatly. This further demonstrates the need to monitor the actual pulse signal in place of simply relying on the machine settings.

3.3.3 Correlation with Machine Settings

Using the type of analysis shown in the preceding section, the EDM signals due to a variety of combinations of machine settings were studied to observe the effects of each setting. For these tests, four machine settings expected to have the greatest impact on the signal parameters were chosen: spark energy, spark cycle, wire diameter and table feed rate. Although choosing appropriate machine settings can be difficult [75], once a working set of parameters was identified, the maximum ranges over which

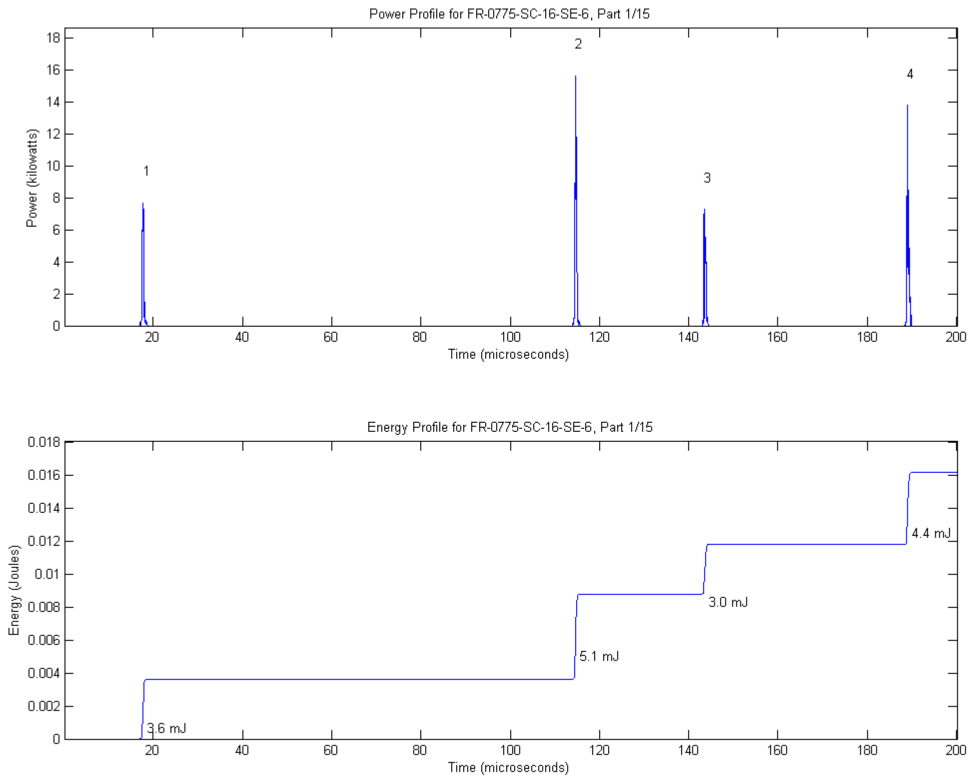

Figure 3.4: Sample power [kW] and energy [J] waveforms

they could be varied were determined. The qualitative effects of the varied factors are given in Table 3.3.

It is apparent that the effects of the machine settings on the signal parameters are confounded with one another. What can be concluded from this experiment is that the spark energy machine setting tends to increase numerous factors which lead to an increased energy per spark. The spark cycle setting is well correlated with the voltage off-time. While not directly related to the discharge signal, increases in table feed rate lead to increases in the sparking frequency. Lastly, it is found that a larger diameter wire results in greater sparking frequency, peak discharge current, and power.

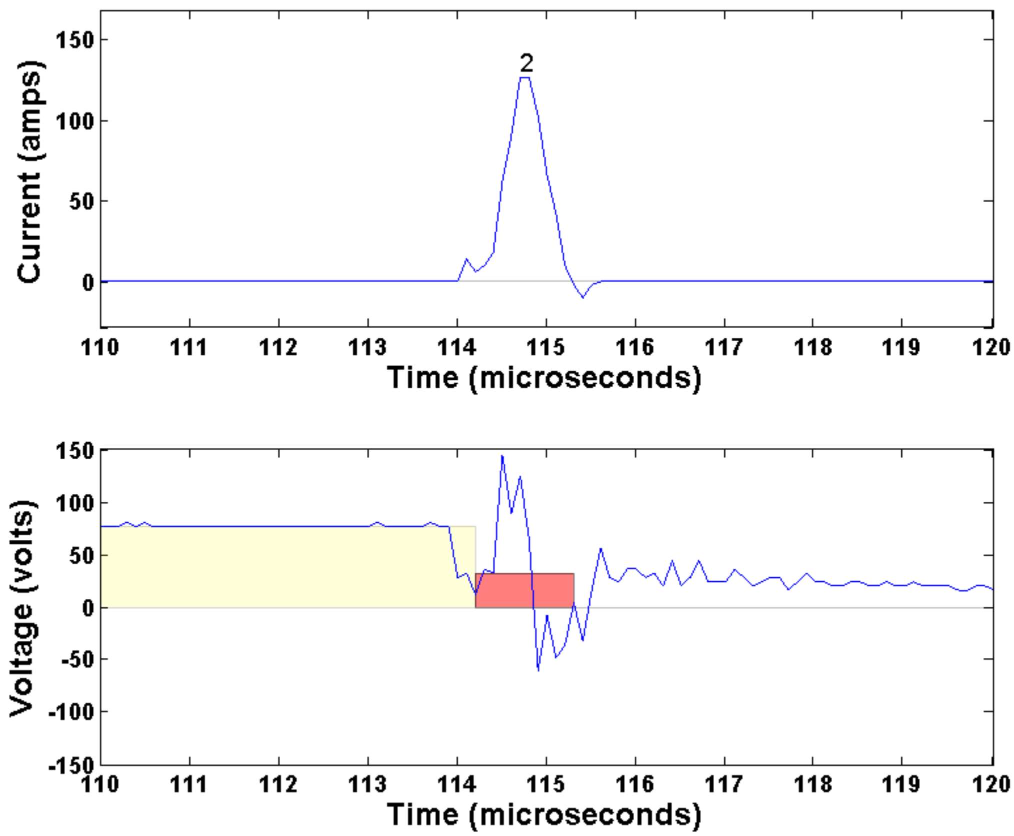

Figure 3.5: Sample close-up of current [A] and voltage [V] for a discharge

3.4 *Design of Experiments*

3.4.1 Process Parameters

From the literature survey conducted in Chapter II, it is clear that several factors can contribute to recast layer formation. However, many of the factors reported in the literature are machine specific, or cannot be directly controlled on the Brother HS-3100. Therefore, the selected machine settings were chosen to alter the parameters reported in literature which in turn are believed to have the largest impact on recast layer formation. Wire-EDM differs from die-sinking EDM in that if the settings are not chosen properly, the wire electrode will fail. This can occur either from a table feed rate which is too high and allows the wire to come in contact with the workpiece,

Table 3.3: Machine setting to signal parameter correlations for the Brother HS-3100

Machine Setting	Signal Parameter
Spark Energy ↑	Peak Discharge Current ↑
	Current Pulse Duration ↑
	Sparking Frequency ↓
	Open-Voltage Time ↑
	Voltage Off-Time ↓
	Energy per Spark ↑
	Power ↑
Spark Cycle ↑	Voltage Off-Time ↑
Table Feed Rate ↑	Sparking Frequency ↑
	Open Voltage Time ↓
Wire Diameter ↑	Sparking Frequency ↑
	Power ↑
	Peak Discharge Current ↑

or from sparking parameters under which the wire electrode is eroded to the point that it fails under the normal tension at which it is held.

The material examined in these experiments was a sheet of annealed 3.962 mm thick Inconel 718. The chemical composition of this alloy can be found in Table 2.1. Tests were conducted to find the widest range of feasible machine settings when cutting this particular alloy. Based on these results, a factorial design of experiments was chosen, and can be seen below in Table 3.4. Note that the wire diameter and spark energy settings are not balanced. This was done to maximize the effect of spark energy. The 100 μm diameter wire was unable to sustain a spark energy setting greater than 8, while the 250 μm wire was able to cut up to a setting of 18. This element of the design must be considered in the later analysis. Both size wire diameters were made of hard brass with an electrical resistivity of 9 $\mu\Omega$-cm. Additionally, the wire transport speed was altered from 261 mm/sec with the smaller diameter wire to 48 mm/sec with the larger diameter wire. This was done to minimize excessive consumption of the larger diameter wire. At the speeds indicated, the mass flow rate of the two wire diameters was held to within 14%, the best achievable on the Brother HS-3100. All other parameters were held constant across all tests. Wire tension was kept at 300gf, water conductivity was maintained at 37 μS/cm, and the dielectric flow rate in the upper and lower nozzles was held at 2 ℓ/min. The machine-specific stabilizer function, which attempts to avoid wire breakage by limiting the number of sparks that can occur in a given time, was set to a value of 1. This serves to limit the impact of the Stabilizer as much as possible. From observation of the pulse signal, it was obvious when the Stabilizer was engaged and consequently these machine settings were later avoided.

Table 3.4: Experimental Design

Wire Diameter [μm]	Table Feed Rate [mm/min]	Spark Cycle [μs]	Spark Energy [setting]
100	1.969	16	4
100	1.969	16	6
100	1.969	16	8
100	1.969	28	4
100	1.969	28	6
100	1.969	28	8
100	2.223	16	4
100	2.223	16	6
100	2.223	16	8
100	2.223	28	4
100	2.223	28	6
100	2.223	28	8
250	1.969	16	6
250	1.969	16	12
250	1.969	16	18
250	1.969	28	6
250	1.969	28	12
250	1.969	28	18
250	2.223	16	6
250	2.223	16	12
250	2.223	16	18
250	2.223	28	6
250	2.223	28	12
250	2.223	28	18

3.4.2 Experimental Procedure

At each of the conditions listed in Table 3.4, a 6.3 mm by 12.7 mm specimen was cut out of the Inconel 718 sheet. The nomimal chemical composition of this alloy is detailed in Table 2.1. Observation of the recast layer necessitated that each specimen be metallographically prepared. The first step was to thoroughly clean the specimen in acetone, then in sodium hydroxide. Using the Buehler Edgemet kit, each specimen underwent an electroless nickel plating process to protect specimen edges. This nickel layer was nominally 25 μm in thickness. Specimens were next mounted in EpoMet G, a thermosetting epoxy resin to aid in further preparation. A drawing detailing the orientation of the specimens is shown in Figure 3.6.

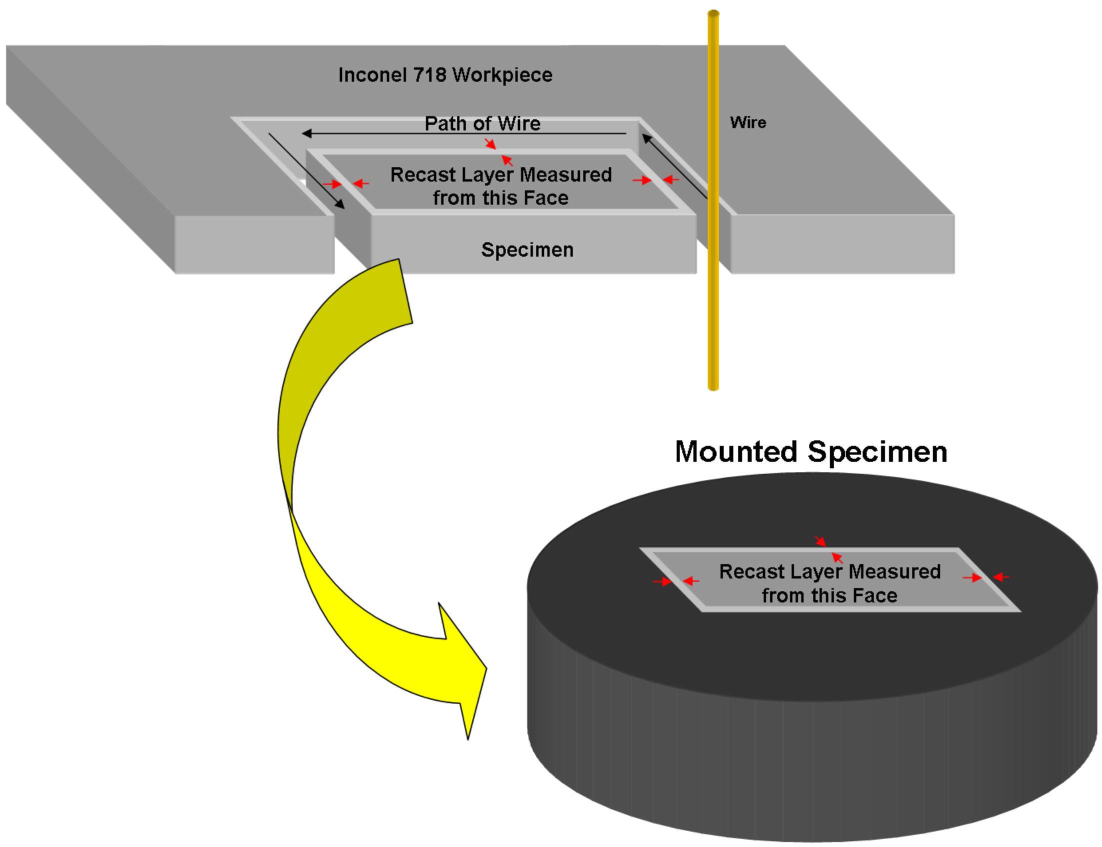

Figure 3.6: Drawing demonstrating the orientation of a specimen as it is mounted in epoxy

Once mounted, the specimens were ground and polished on a Buehler Ecomet 6

Variable Speed Grinder-Polisher with an Automet 2 Power Head according to the procedure outlined in Table 3.5. This procedure is based upon advice given by an expert at Buehler [76]. Carbimet is a silicon carbide sandpaper and MasterPrep is a 0.05 μm agglomerate-free seeded-gel alumina suspension.

Table 3.5: Grinding and polishing procedure

Step	Abrasive	Time [min]	Speed [RPM]	Load [N]	Notes
1	180 grit 8” Carbimet paper	4:00	250 comp.	36	Repeat until plane
2	240 grit 8” Carbimet paper	5:00	250 comp.	31	
3	320 grit 8” Carbimet paper	5:00	250 comp.	27	
4	400 grit 8” Carbimet paper	5:00	250 comp.	22	
5	600 grit 8” Carbimet paper	5:00	250 comp.	22	
6	3 m Diamond Suspension with 8” Texmet 1500 Pad	3:00	150 comp.	18	Longer time if necessary
7	MasterPrep Solution with Microcloth	3:00	150 contra.	18	Longer time if necessary

At this point, the specimens could be observed under an optical microscope, as seen in Figure 3.7. While some recast material is visible, it is necessary to etch the specimen to fully observe the recast layer. In practice, Inconel 718 is frequently electrolytically etched to reveal its microstructure. For simplicity, this option was avoided in favor of a simpler method. Several resources were used to find possible etching procedures [76, 77, 78, 79]. Approximately twenty different combinations of etchants, concentrations and times were attempted to determine the best procedure. Etching the specimens in a mixture composed of 25 ml HCl, 5 ml HNO_3 and 5 ml glycerol for 3 minutes was found to provide the best results. The specimen from Figure 3.7 has been etched and is shown again in Figure 3.8, although the micrograph is of a different region.

For the purpose of these experiments, the recast layer has been assumed to be the region between the nickel plating and the dark horizontal lines which appear with etching. These dark lines are not thought to be micro-cracks, primarily because they are not revealed until after etching. Cracks would form in order to relieve tensile residual stresses imparted during the machining process. From the analysis of these stresses in Chapter IV, any cracks would be expected to appear at the outer edge of the recast material and run normal to the surface. The darkened regions of the micrograph were most likely preferentially etched due to their chemical composition, which has been altered during the machining process. Although only the upper portion of this region appears darkened, the lower portion has been included in the recast layer thickness measurements as it is bounded by the dark lines which have also been chemically altered from the original workpiece. Notice how the thickness of the recast layer varies across the specimen.

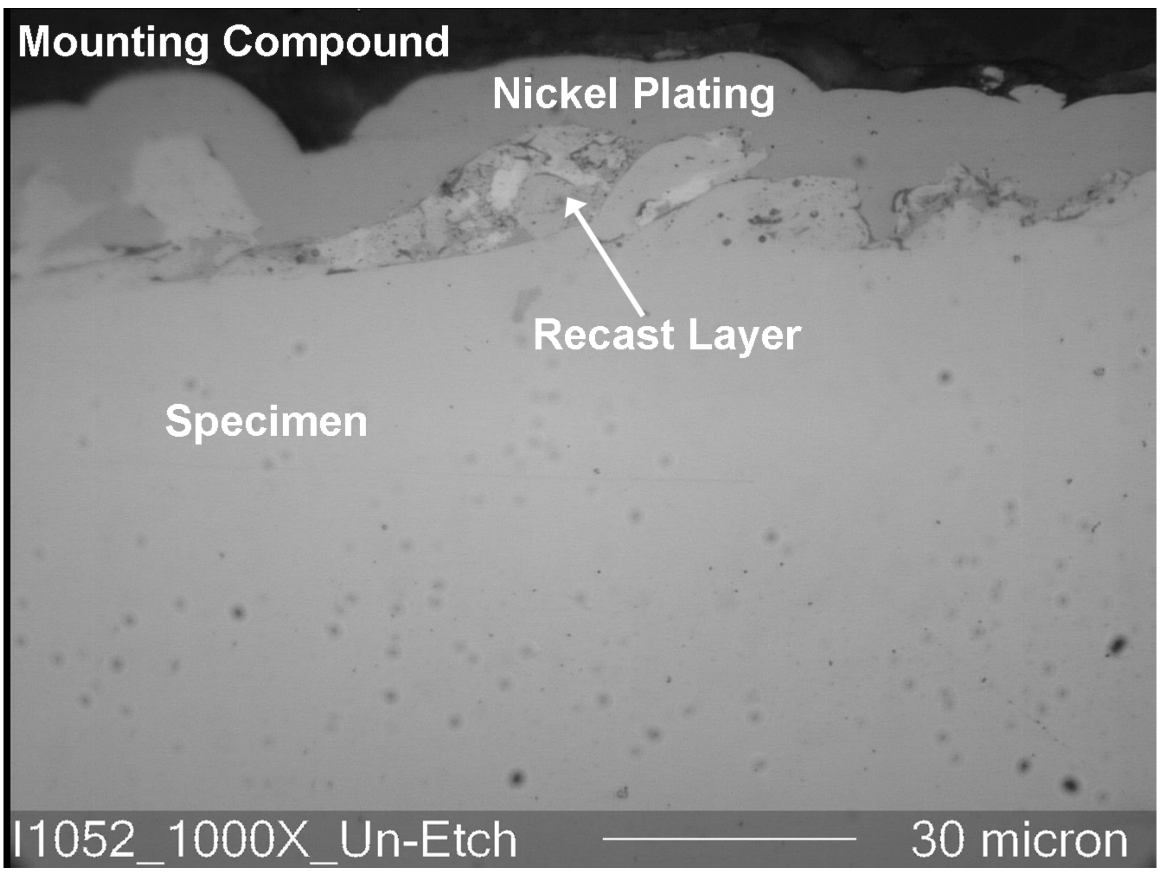

Figure 3.7: Micrograph of polished, but un-etched specimen cut under the following machine settings: wire diameter of 250 μm, table feed rate of 2.223 mm/min, spark cycle setting of 28 μs, spark energy setting of 18

The selected output for these experiments is the recast layer thickness. Due to

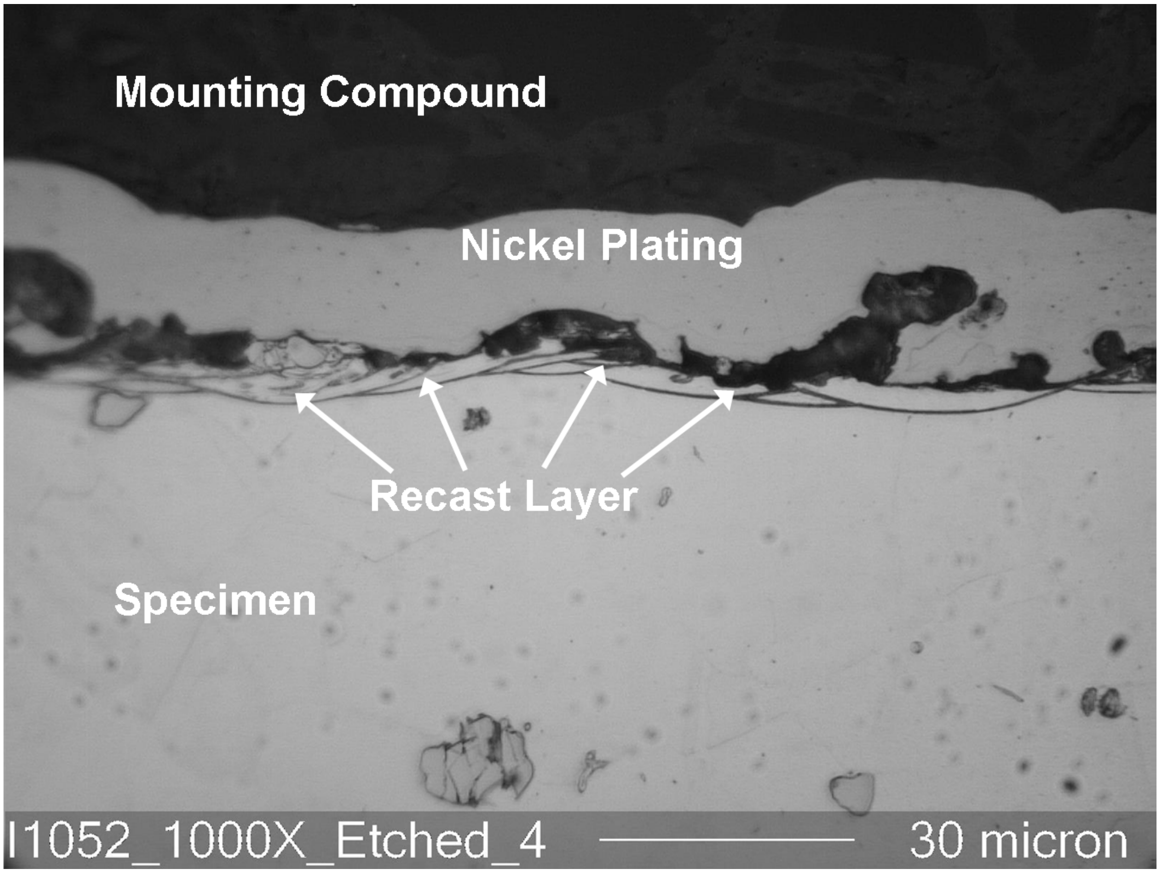

Figure 3.8: Micrograph of polished and etched specimen cut under the following machine settings: wire diameter of 250 μm, table feed rate of 2.223 mm/min, spark cycle setting of 28 μs, spark energy setting of 18

the variable nature of the recast layers observed, an average must be taken. The best results were obtained when an average recast layer thickness was calculated by measuring the area of the recast material and dividing by the length of the measurement, as shown in Figure 3.9. The recast area was always measured in three different location on the specimen. However, in cases where the variance between measurements was deemed sufficiently large, measurements at additional locations were taken. Area measurements were made by importing the micrographs into AutoCAD 2007 and tracing a polyline around the perimeter of the recast region.

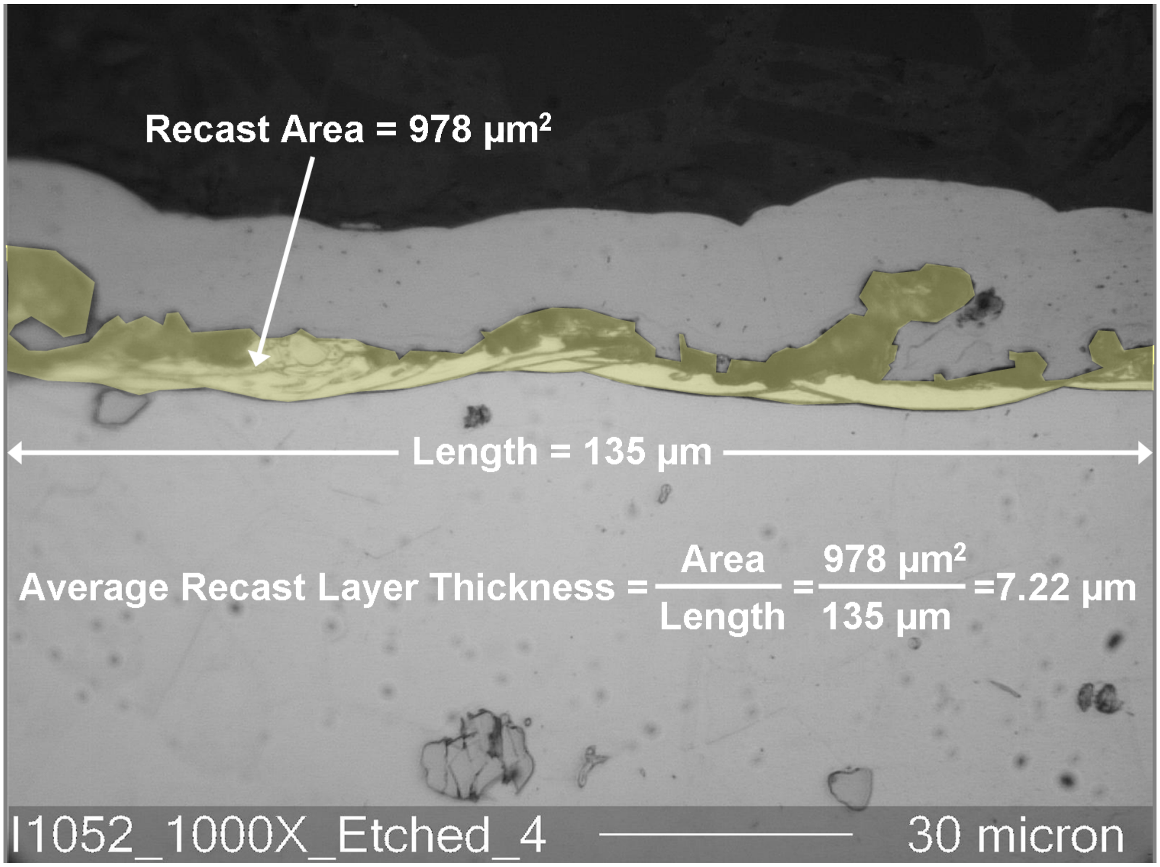

Figure 3.9: Example of how average recast layer thickness measurements were made

3.5 Results

3.5.1 Results

The average recast layer thickness measurements for each test condition, as well as the analyzed EDM signal parameters can be seen in Table 3.6. The measurements comprising each average recast layer thickness measurement are found in Appendix B. Notice the large variance in both the EDM signal parameters and in the measured average recast layer thicknesses. While average recast layer thickness measurements were taken from several locations of each specimen, no replicates of the actual cutting experiments were conducted.

Table 3.6: Average recast layer thickness measurements and EDM signal Parameters

Wire Dia. [μm]	Table Feed Rate [mm/min]	Spark Cycle [μs]	Spark Energy [setting]	Peak Current [A]	Current Pulse Duration [μs]	Freq. [kHz]	Open-Voltage Time [μs]	Voltage Off-Time [μs]	Energy per Spark [mJ]	Power [W]	Avg. Recast Layer Thickness [μm]	Std. Dev. of Avg. RLT [μm]
100	1.969	16	4	93.7	0.87	12.1	71.5	10.9	2.59	31.3	8.07	1.74
100	1.969	16	6	116.7	1.04	10.1	89.7	10.6	3.92	39.7	5.10	0.34
100	1.969	16	8	132.3	1.19	8.8	93.1	10.2	7.25	64.3	6.57	0.25
100	1.969	28	4	91.3	0.92	12.8	59.8	17.8	2.47	31.3	7.17	0.85
100	1.969	28	6	115.3	1.02	11.2	69.9	16.5	3.66	40.9	5.46	0.65
100	1.969	28	8	134.0	1.20	8.9	94.3	14.2	7.73	68.2	7.63	0.69
100	2.223	16	4	88.0	0.90	16.0	50.7	10.2	2.39	38.0	5.88	0.48
100	2.223	16	6	113.3	1.03	11.7	73.9	10.9	3.59	42.1	6.40	0.39
100	2.223	16	8	127.3	1.14	9.3	96.5	8.8	6.99	65.7	6.86	0.57
100	2.223	28	4	89.3	0.89	15.6	43.6	17.8	2.40	37.3	6.24	0.45
100	2.223	28	6	112.0	1.01	11.3	65.7	18.3	3.51	39.7	6.15	0.44
100	2.223	28	8	137.7	1.19	8.8	95.8	11.8	5.41	47.3	7.50	0.96
250	1.969	16	6	124.0	1.06	16.3	48.6	11.3	3.62	59.3	8.09	0.82
250	1.969	16	12	220.3	1.63	5.7	170.0	9.1	10.35	58.2	8.39	2.47
250	1.969	16	18	317.0	1.89	3.2	325.0	8.6	21.52	68.0	7.80	1.01
250	1.969	28	6	127.3	1.08	14.6	48.8	17.9	3.76	54.8	6.82	1.02
250	1.969	28	12	226.3	1.66	5.2	171.7	13.9	10.49	55.4	8.51	0.22
250	1.969	28	18	313.3	1.90	2.6	358.4	11.0	23.03	58.9	7.84	1.63
250	2.223	16	6	123.7	1.03	20.7	35.1	11.0	3.65	75.6	5.71	0.45
250	2.223	16	12	228.0	1.68	4.5	206.5	8.4	11.97	52.2	8.00	1.07
250	2.223	16	18	309.7	1.88	4.1	232.3	9.3	20.17	82.6	6.67	0.97
250	2.223	28	6	121.7	1.03	20.7	27.8	19.1	3.42	70.8	5.94	0.79
250	2.223	28	12	221.7	1.63	7.1	127.9	14.5	9.99	71.1	7.21	1.07
250	2.223	28	18	265.3	1.69	4.1	208.1	11.8	19.45	79.0	7.89	1.34

Table 3.7: Analysis of Variance (ANOVA) for cases where spark energy is set to 6 to determine the effect of wire diameter on recast layer thickness

Source	Degrees of Freedom	Sequental Sum of Squares	Adjusted Sum of Squares	Adjusted Mean of Squares	F-statistic	p-value
Wire Dia.	1	1.488	1.488	1.488	1.39	0.303
Feed Rate	1	0.202	0.202	0.202	0.19	0.686
Spark Cycle	1	0.108	0.108	0.108	0.1	0.766
Error	4	4.266	4.266	1.067		
Total	7	6.064				

3.5.2 Analysis

Due to the unbalanced design, analysis of the experiments is complicated by the correlation between wire diameter and spark energy settings. Consequently, the first analysis will be to determine the influence of wire diameter on average recast layer thickness in Inconel 718. Performing an Analysis of Variance (ANOVA) on only the cases where spark energy was set to a level of 6 will allow for such a determination to be made. The results of the ANOVA are seen in Table 3.7. The p-value for the effect of wire diameter on recast layer thickness is 0.303, indicating an insignificant effect. For the following analyses, it will be assumed that, over the range of values measured, the effect of wire diameter is negligible.

Performing an ANOVA on the complete dataset, found in Table 3.8, confirms the assumption that wire diameter effect on recast layer thickness is negligible. With an α=0.05 significance level, the spark energy setting is a significant parameter, and with a α=0.10 level, table feed rate is also significant. The main effects are shown in Figure 3.10.

By applying the machine setting to signal parameter trends given in Table 3.3, the effect of the underlying EDM signal parameters can be found. As table feed rate increases, average recast layer thickness decreases. This suggests that recast layer thickness increases with decreasing sparking frequency and increasing open-voltage time. A higher spark energy setting leads to thicker recast layer. This indicates that

Table 3.8: Analysis of Variance (ANOVA) to determine effect of machine settings on recast layer thickness

Source	Degrees of Freedom	Sequental Sum of Squares	Adjusted Sum of Squares	Adjusted Mean of Squares	F-statistic	p-value
Wire Dia.	1	4.034	1.488	1.488	2.88	0.109
Feed Rate	1	2.042	2.042	2.042	3.96	0.064
Spark Cycle	1	0.028	0.028	0.028	0.05	0.819
Spark Energy	4	8.075	8.075	2.019	3.91	0.021
Error	16	8.253	8.253	0.516		
Total	23	22.432				

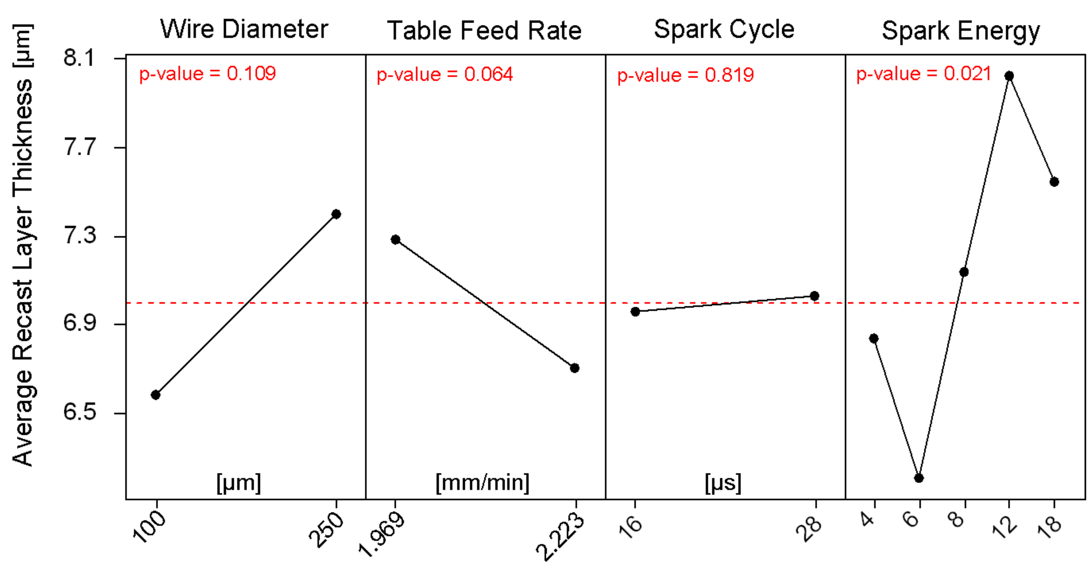

Figure 3.10: Main effects of machine settings on average recast layer thickness [μm]

Table 3.9: Pearson correlation between EDM signal parameters and average recast layer thickness

	Peak Current	Pulse Duration	Freq.	Open-Voltage Time	Voltage Off-Time	Energy per Spark	Power
Correlation Coefficient	0.508	0.555	-0.560	0.516	-0.303	0.475	0.190
p-value	0.011	0.005	0.004	0.010	0.150	0.019	0.374

recast layer thickness increases with an increasing peak discharge current, current pulse duration, open-voltage time, energy per spark and power and with decreasing sparking frequency and voltage off-time.

An ANOVA cannot be performed directly on the actual EDM signal parameters, but similar results are obtained by utilizing the Pearson product moment correlation, which measures the degree of linear relationship between two variables. Table 3.9 shows the correlation coefficients and p-values for each correlation. The correlation coefficient ranges from -1 to +1. A positive correlation coefficient indicates that the variables increase together, while a negative coefficient indicates that one increases as the other decreases. A correlation coefficient of 0 indicates no relationship between the variables. A p-value less than α=0.05 indicates significance. This analysis suggests that average recast layer thickness increases with increasing average peak pulse current, current pulse duration, open-voltage time and energy per spark and with decreasing frequency. This largely agrees with with what was found from the EDM signal parameters correlated with the machine settings found to be significant by the ANOVA. The correlated ANOVA analysis indicated that power and voltage-off time were significant factors, while the Pearson correlation did not. This suggests that although power and voltage-off time are tied to changes in the spark energy setting, it is the other factors, peak discharge current, current pulse duration, frequency, open-voltage time and energy per spark which have more dominant effects over this range.

The literature survey conducted in Chapter II found that it has been reported by several researchers that, for other alloys, recast layer thickness tends to increase with increased current pulse duration and increased energy per spark. The findings from the experiments conducted here match those results, and augment them with the fact that recast layer is also affected by peak pulse current, open-voltage time, and decreasing frequency.

Plots of average recast layer thickness versus the aforementioned parameters are given in Figures 3.11 - 3.15. In each plot, the wide dispersion in recast layer thickness versus the varied parameter is clear. Nonetheless, over a wide enough range, the statistically significant trends become evident. Note that the figures distinguish the data points collected with each of the two wire diameters from each other. The linear trend line is based on the complete data set, as the wire diameter was shown to have an insignificant effect on recast layer thickness.

The increase in recast layer thickness with decreasing frequency can be explained by the correlation between frequency and energy per spark. As the energy per spark increases, the frequency correspondingly decreases, see Figure 3.16. It is likely the increase in energy per spark that drives the increased recast layer thickness rather than the decrease in frequency. With greater energy release in each spark, the quantity of workpiece material which is melted is greater, resulting in a larger quantity of molten material which resolidifies to form the recast layer. Since the voltage on the Brother HS-3100 is fixed, the same argument could be made for increases in the current leading to greater recast layer thicknesses. As sparking frequency decreases, with constant table feed rate and voltage-off time, open-voltage time will correspondingly increase. Thus, the open-voltage time is correlated with increased recast layer thickness because sparking frequency decreases with increasing energy per spark. Recast layer thickness decreases with increasing table feed rate because as the table feed rate increases, the sparking frequency increases, and energy per spark decreases. The peak discharge

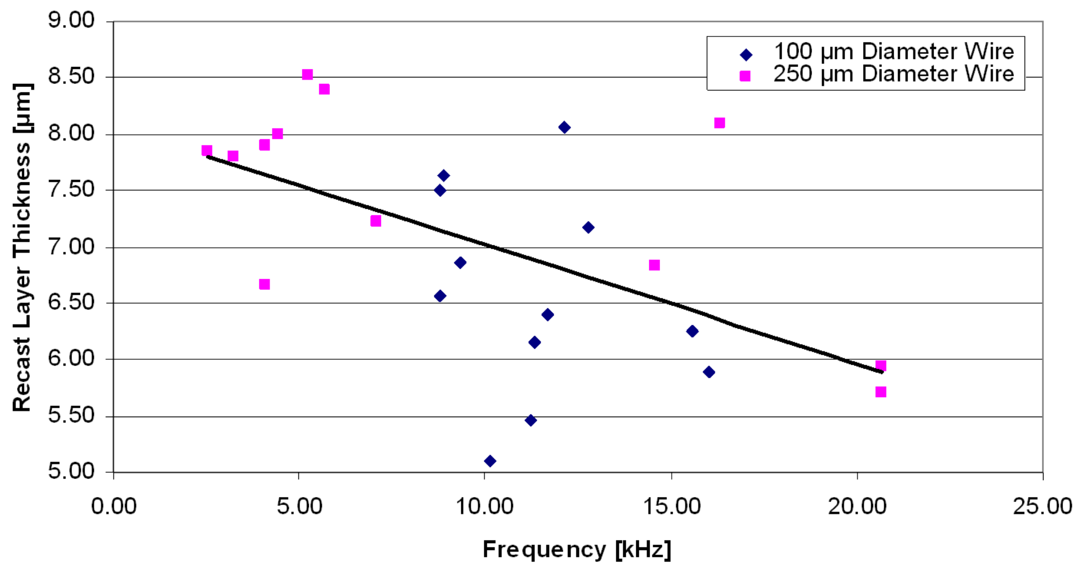

Figure 3.11: Average recast layer thickness [μm] plotted against average sparking frequency [kHz]

current and current pulse duration, and equivalently the energy per spark, are the fundamental parameters which increase recast layer thickness in wire-EDM. This is in agreement with what has been found for other workpiece materials [16, 24, 21].

3.6 Summary

In order to find the influence of various wire-EDM parameters on the recast layer thickness, a set of experiments were undertaken. These experiments were conducted on a Brother HS-3100 Wire-EDM. Due to machine limitations, the exact signal parameters could not be varied directly. Instead, it was necessary to alter machine settings and correlate them with more general parameters. A 36-run experimental design was conducted. Each specimen was nickel plated, mounted, polished and etched to reveal the recast layer. Numerous measurements were taken from each specimen to calculate an average recast layer thickness for each condition. It was found that the diameter of the wire electrode did not demonstrate an effect on recast layer thickness. However, recast layer thickness decreased with increasing table feed rate. Additionally, recast

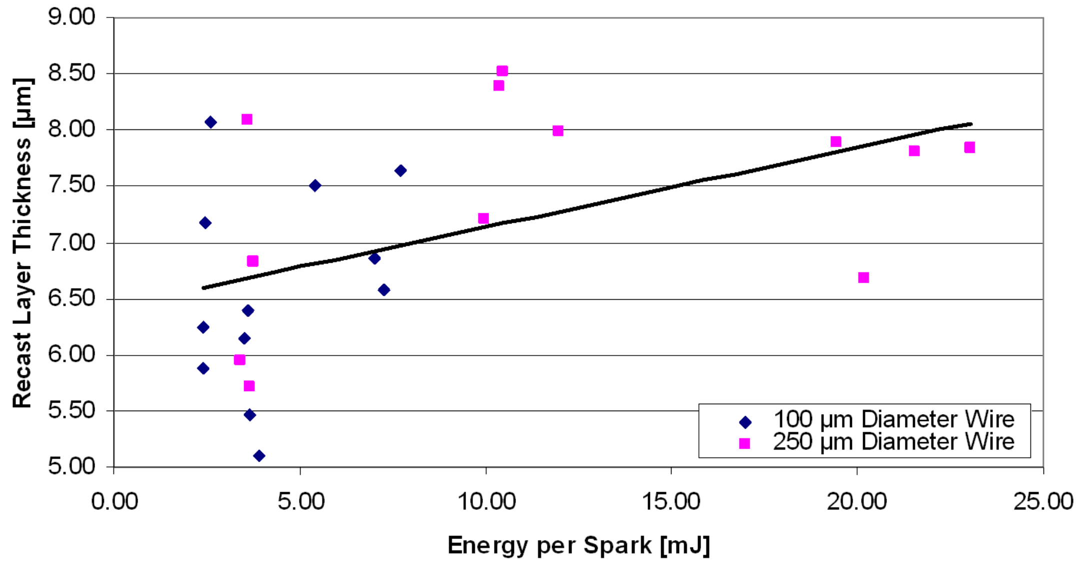

Figure 3.12: Average recast layer thickness [μm] plotted against average energy per spark [mJ]

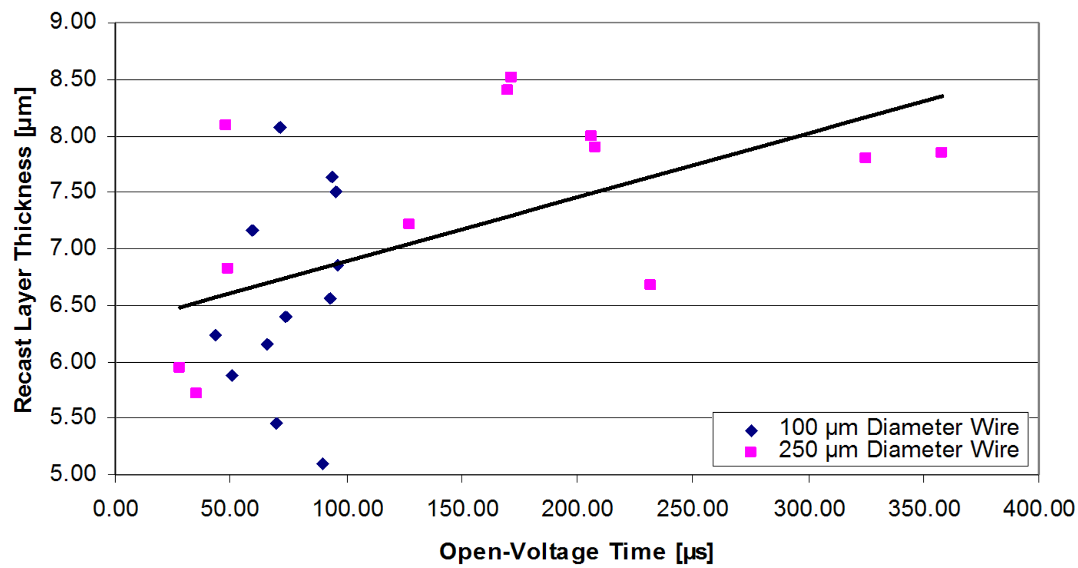

Figure 3.13: Average recast layer thickness [μm] plotted against average open-voltage time [μs]

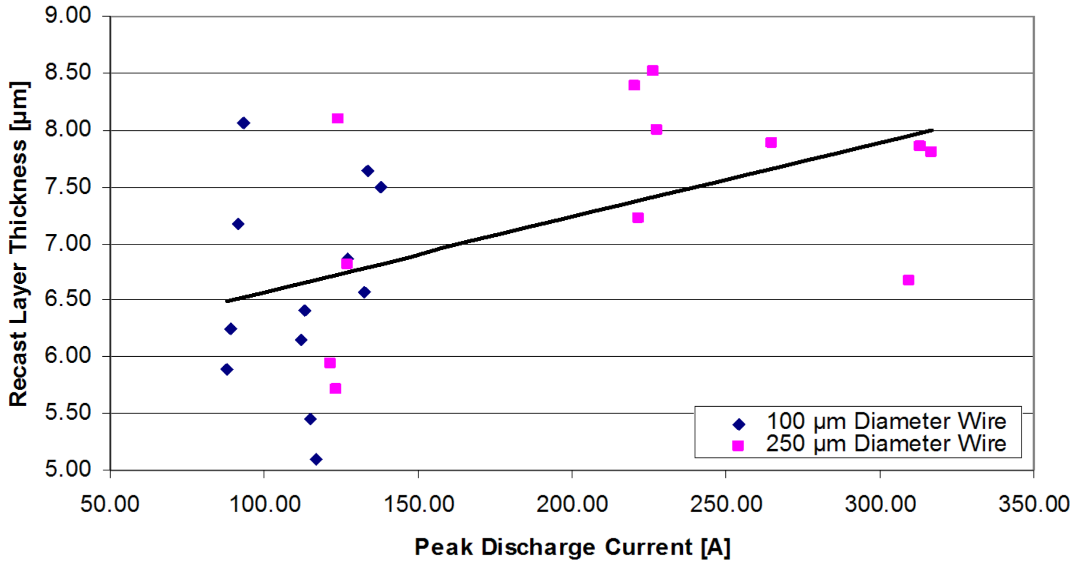

Figure 3.14: Average recast layer thickness [μm] plotted against average peak discharge current [A]

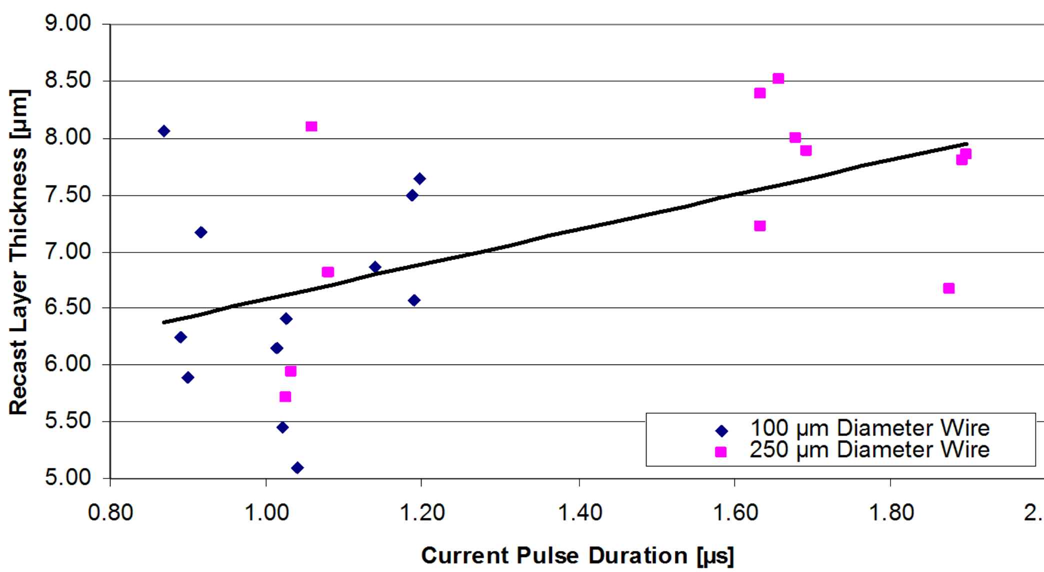

Figure 3.15: Average recast layer thickness [μm] plotted against average current pulse duration [μs]

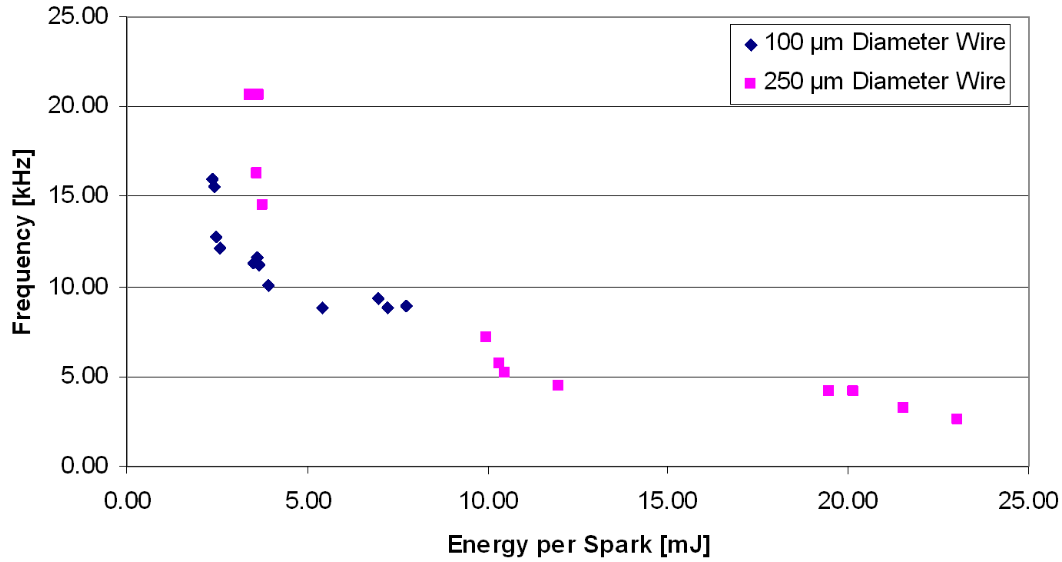

Figure 3.16: Sparking frequency [kHz] plotted against energy per spark [mJ]

layer thickness increased with an increasing energy per spark, peak discharge current, current pulse duration, and open-voltage time and decreasing sparking frequency. Further, it was determined that the underlying cause for increases in average recast layer thickness were increases in peak discharge current, current pulse duration and energy per spark.

CHAPTER IV

RECAST LAYER CHARACTERIZATION

4.1 Goal & Approach

In this chapter, the recast layer formed due to wire-EDM of Inconel 718 will be characterized through several methods. Wherever possible, the effects of the wire-EDM process parameters on the following characterizations will be examined: scanning electron microscopy to observe surface morphology, white light interferometry to measure surface roughness, electron probe microanalysis to find chemical composition, x-ray diffraction to detect and measure residual stresses and nano-indentation hardness testing to determine hardness and elastic modulus. From what is learned, a better understanding of the properties of the recast layer can be gained. This will serve as a guide in understanding the effects of wire-EDM on a surface, as well as in the post-processing steps discussed in the following chapter.

4.2 Scanning Electron Microscopy

Several scanning electron microscope (SEM) images were taken of a specimen to characterize surface morphology. Figures 4.1 - 4.4 are taken from a Hitachi S3400N SEM with an accelerating voltage of 15.0kV and a working distance of 17.9 mm. The specimen was machined with the following machine settings: wire diameter of 100 μm, table feed rate of 1.969 mm/min, spark energy setting of 8 and a spark cycle setting of 28 μs. Notice the overlapping craters of the spark eroded surface. In these figures, the wire electrode was oriented vertically, and the table fed from left to right. These micrographs demonstrate a surface similar to what has been previously reported for wire-EDM [16, 17, 26, 39, 27, 38]. However, since only one sample was able to be analyzed with SEM, no observation on the influence of the experimental variables on crater size or morphology can be made.

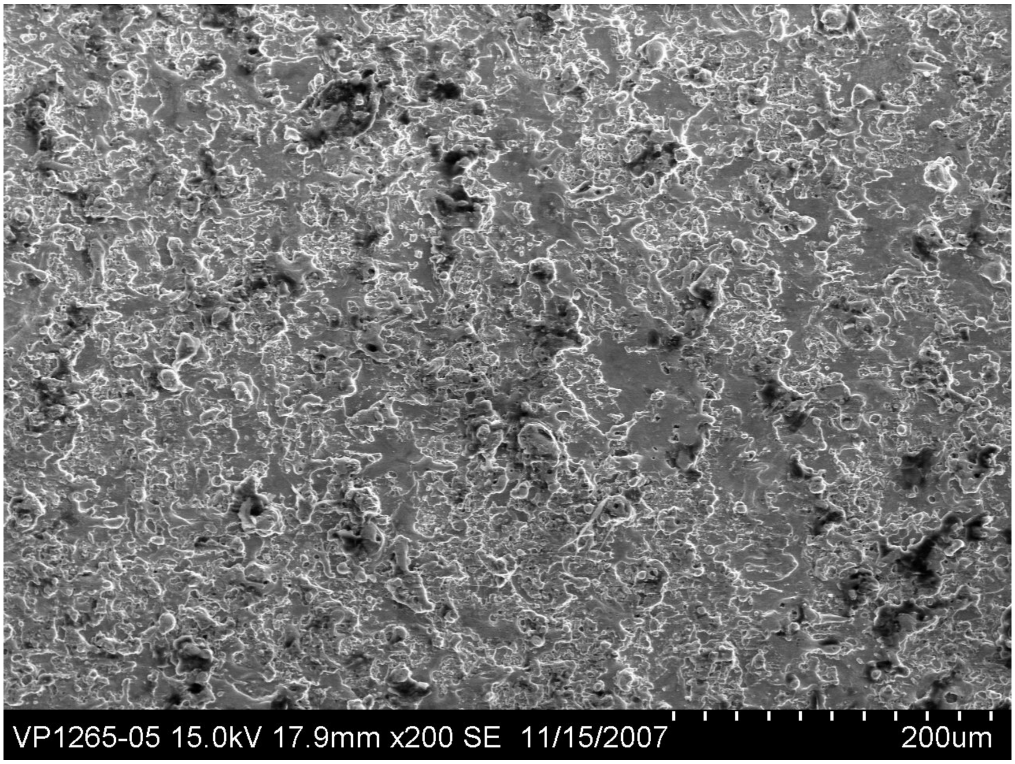

Figure 4.1: SEM image of wire-EDM cut surface at 200X

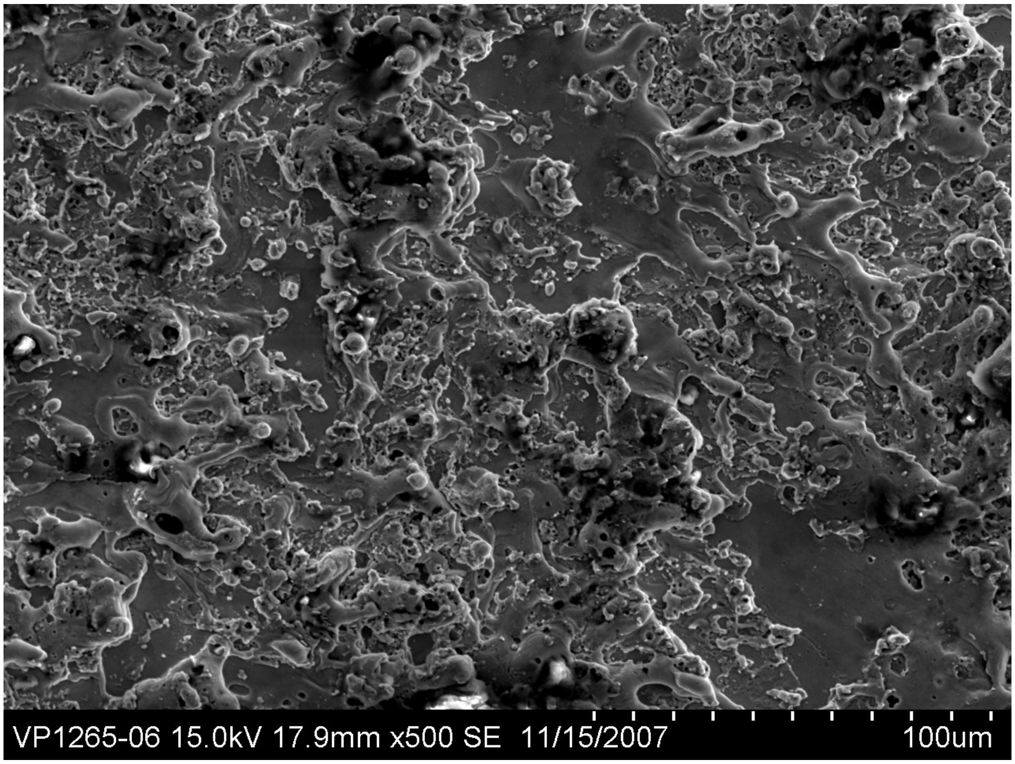

Figure 4.2: SEM image of wire-EDM cut surface at 500X

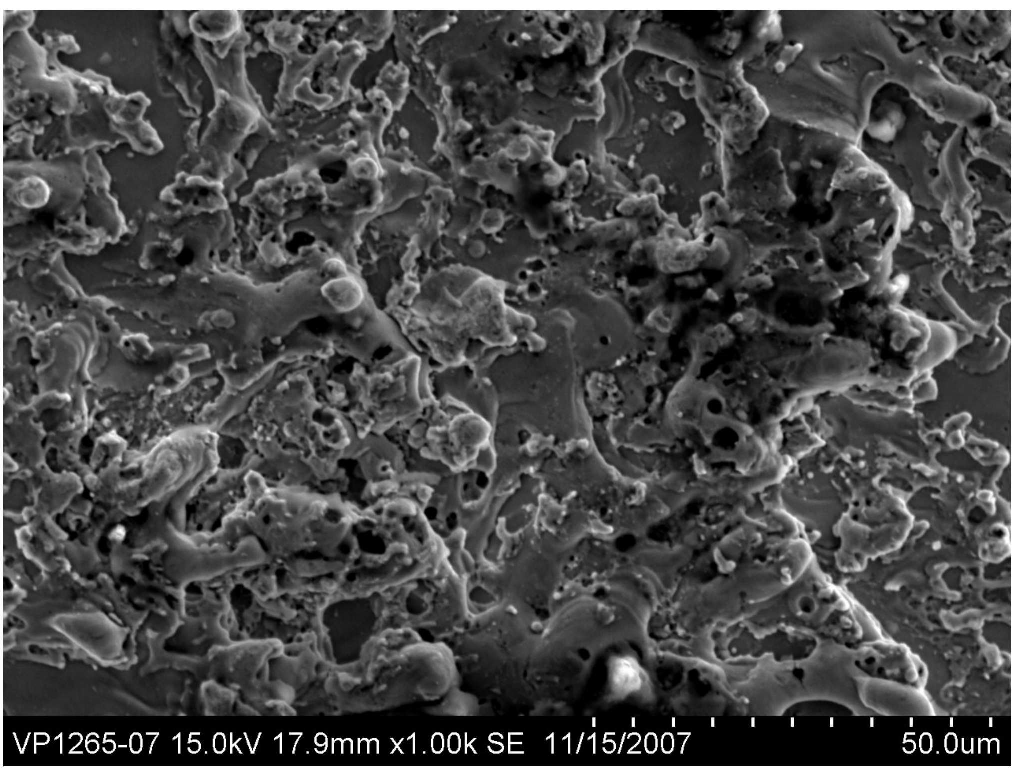

Figure 4.3: SEM image of wire-EDM cut surface at 1000X

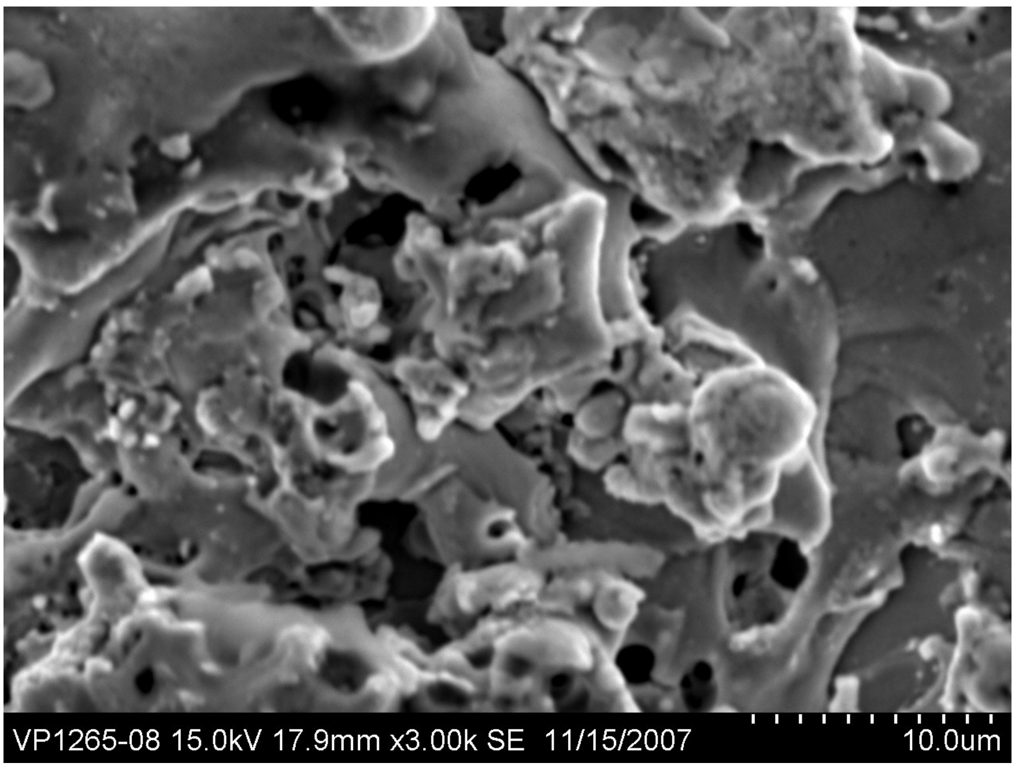

Figure 4.4: SEM image of wire-EDM cut surface at 3000X

4.3 Surface Roughness Measurements

As discussed in Chapter II, surface roughness has been correlated to certain machine settings, most notably the peak pulse current. To analyze surface roughness, four samples, machined with two wire diameters, and two energies per spark were selected. These particular specimens were chosen to isolate the effects of wire diameter and energy per spark. Although the high and low levels of energy per spark are not equal across wire diameters, the effect can still be viewed within a wire diameter. Table 4.1 shows the machine settings, selected discharge signal parameters and resulting recast layer thicknesses for the selected samples. The complete data for these machine settings can be found in Table 3.6.

Table 4.1: Average recast layer thickness measurements and selected EDM signal parameters for surface roughness measurement samples

Sample	Wire Dia. [μm]	Table Feed Rate [mm/min]	Spark Cycle [μs]	Spark Energy	Peak Current [A]	Current Pulse Dur. [μs]	Freq. [kHz]	Energy /Spark [mJ]	Recast Layer Thickness [μm]
1	100	2.223	16	4	88.0	0.90	16.0	2.39	5.88
2	100	1.969	28	8	134.0	1.20	8.9	7.73	7.63
3	250	2.223	28	6	121.7	1.03	20.7	3.42	5.94
4	250	1.969	28	18	313.3	1.90	2.6	23.03	7.84

All of the surface roughness measurements were made on a Zygo NewView 200 white-light interferometer. Figure 4.5 shows a sample measurement. The instrument software, MetroPro 7.2.2, calculates the RMS surface roughness over the area of measurement. The readings were not filtered in any way other than to remove the least-squares plane. An average was taken of three measurements, each from a different location on a specimen. The complete surface roughness data can be found in Appendix C. The average RMS surface roughness values are plotted by sample in Figure 4.6. The error bars denote a single standard deviation in the data above and below each mean value. Plotting surface roughness against energy per spark, Figure 4.7, it can clearly be seen that surface roughness increases with energy per spark.

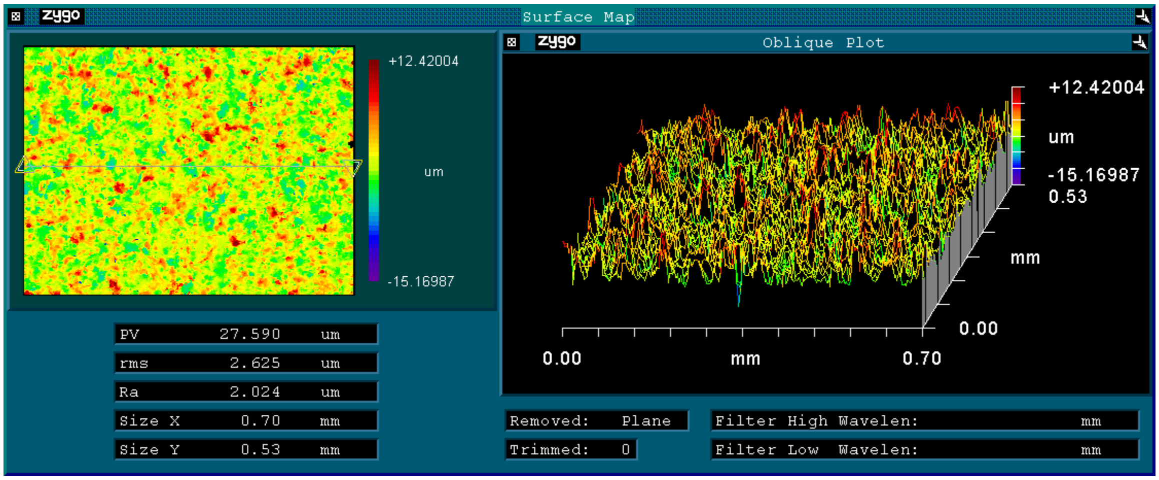

Figure 4.5: Sample image from Zygo NewView 200

This matches what others have reported [16, 21]. Turning now to surface roughness as a function of wire diameter, shown in Figure 4.8, it can be seen that a similar trend exists between energy per spark and RMS surface roughness within either wire diameter. The data indicates that surface roughness is slightly larger with a larger diameter wire electrode. If significant, this effect is not due to differences in sparking frequency, as the average frequencies for the two wires are approximately equal. However, with the larger wire diameter the relative wire transport speed was lower and the gap width was larger, raising the possibility that one of these factors could contribute to this phenomenon.

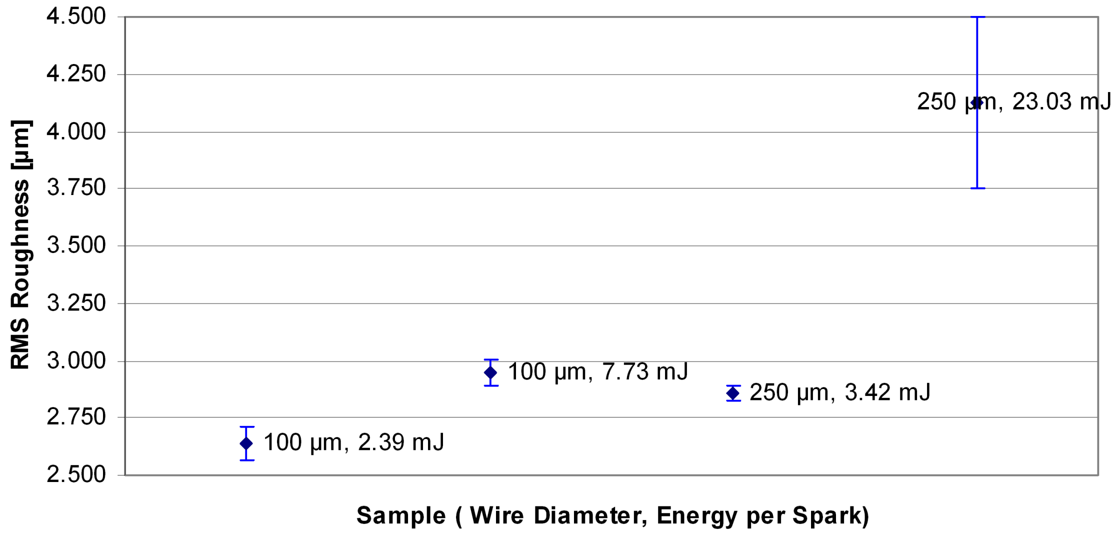

Figure 4.6: RMS surface roughness [μm], sorted by sample

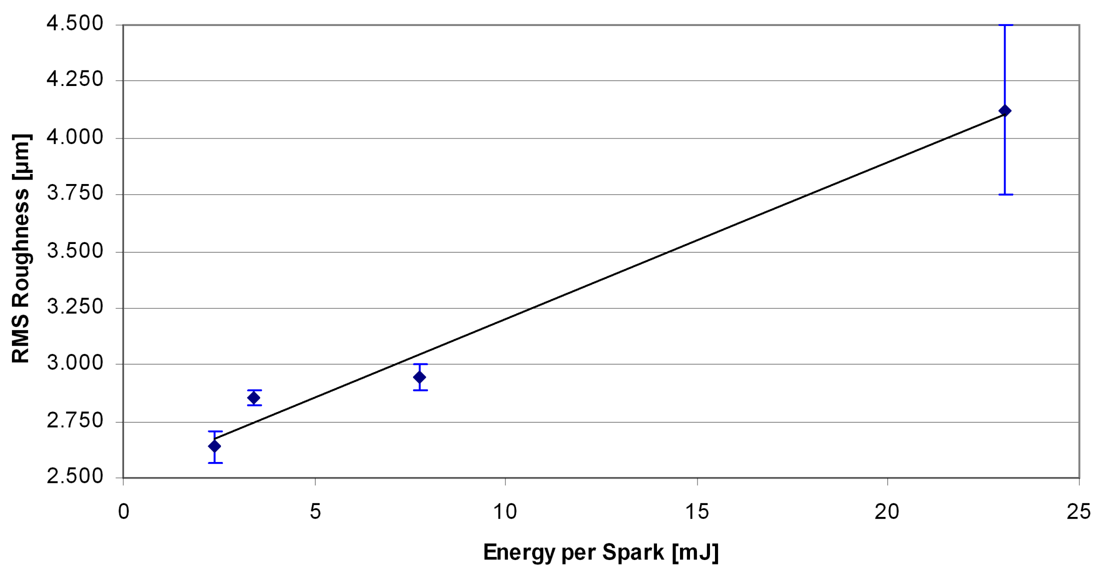

Figure 4.7: RMS surface roughness [μm], sorted by energy per spark [mJ]

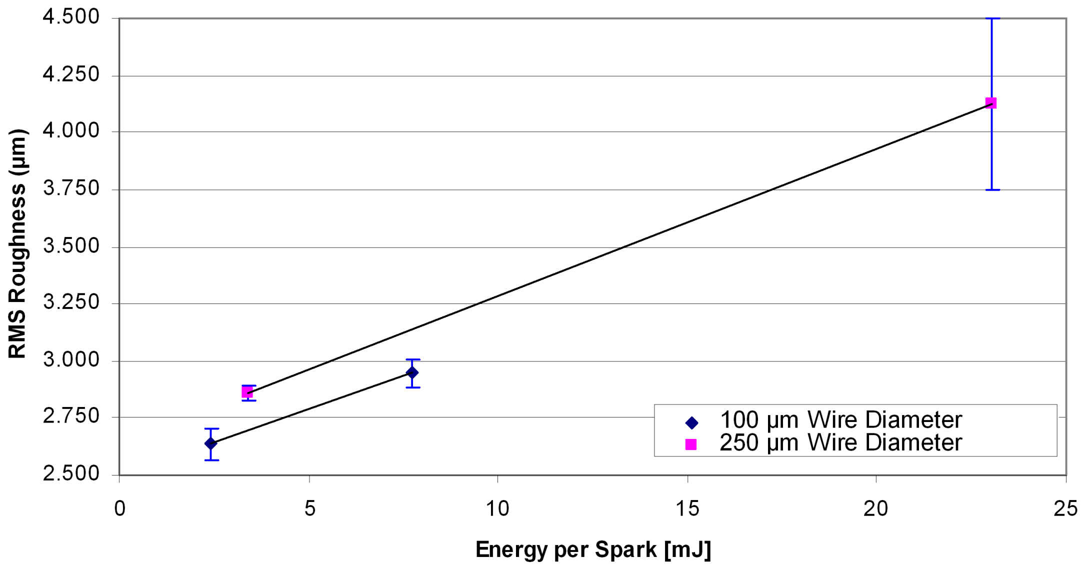

Figure 4.8: RMS surface roughness [μm], sorted by wire diameter [μm] and energy per spark [mJ]

4.4 Electron Probe Microanalysis

4.4.1 Introduction

An Electron Probe Microanalyzer (EPMA) is an instrument similar to an SEM, but with an added x-ray detector which combines structural and compositional analysis of a small, local region in a single operation. When the specimen to be analyzed is bombarded with electrons, characteristic x-rays are emitted. These x-rays can be measured using two methods, energy dispersive spectrometry (EDS) or wavelength dispersive spectrometry (WDS). Most modern SEMs are capable of EDS. By making use of the photoelectric effect, an energy-dispersive x-ray spectrometer is able to count the electric pulses generated each time an x-ray strikes the detector. Each x-ray count is associated with energy units, and a histogram can be generated across the entire spectrum of energies to determine the elemental composition. WDS separates x-rays of different energies by using the wave nature of photons. X-rays are diffracted off of a crystal with a known interplanar spacing and by using Bragg's law, the wavelength of the x-ray can be determined [6].

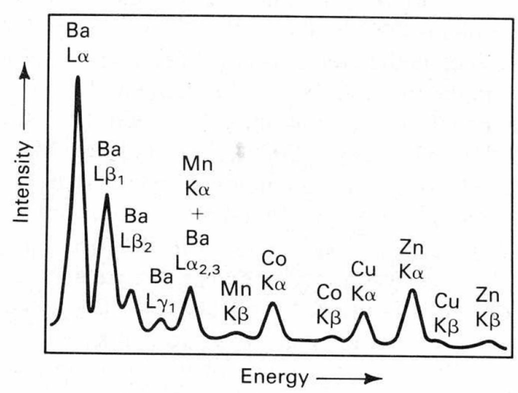

(a) EDS

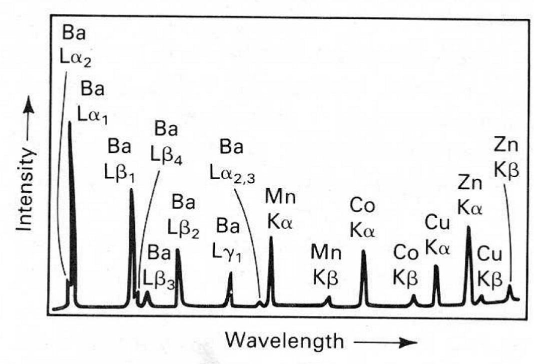

(b) WDS

Figure 4.9: Example comparison of spectra for EDS and WDS [6]

Figure 4.9 shows a comparison between the EDS and WDS spectra of a multicomponent glass. Notice the vastly superior resolution of WDS over EDS. However, this resolution comes at a price. EDS can generate an observation of the entire spectrum nearly simultaneously, while WDS requires several time consuming crystal changes in order to observe the entire spectrum. EPMA has difficulty observing elements with atomic numbers less than fifteen due to the low energy of the x-rays. This means that notable elements such as oxygen and carbon are not typically viewable. A benefit of EPMA is elemental mapping. Elemental composition can be generated in tandem with SEM imaging, allowing the composition of a specimen to be matched with its morphology[6].

4.4.2 Experimental Procedure

The specimen to be analyzed was cut under the same conditions as the sample from the SEM analysis and Sample 2 from the surface roughness analysis: wire diameter of 100 μm, table feed rate of 1.969 mm/min, spark energy setting of 8 and a spark cycle setting of 28 μs. However, in this case, a 12° taper section was taken to make the recast layer appear thicker. This sample was mounted and prepared in the manner described in Table 3.5. To improve the microprobe image, the sample was coated with a 5 nm thick layer of carbon in a process similar to chemical vapor deposition (CVD). The instrument used in these measurements was a Jeol JXA-8200 SuperProbe Electron Probe Microanalyzer (EPMA). It is an SEM and is capable of wavelength and electron dispersive spectrometry (WDS/EDS). To form an elemental map of the surface, two scans were required. The first scan looked at aluminum, copper, silicon and niobium with WDS and titanium, iron, chrome and nickel with EDS. The second scan was for phosphorus, zinc and molybdenum with WDS. Titanium, iron, chrome and zinc exhibit characteristic energies which are sufficiently distinguishable to appear well resolved with EDS meaning little would be gained from an additional scan of WDS.

4.4.3 Results

A composition view of the analyzed area is shown in Figure 4.10. This composition view was generated through electron backscattering. White indicates higher atomic number elements, while black indicates lower atomic number elements. The relative intensity elemental maps of each element within the scan area are shown in the Figures 4.11 - 4.16. In these images, white indicates a high intensity and black indicates a low intensity. The reader is cautioned that the color scales from element to element are different. It is not possible to compare elemental intensity from one element to the next.

From observing the relative intensity of nickel in the area, Figure 4.14(a), it is evident that the nickel plated layer contains a higher nickel content than the workpiece, as would be expected. Figure 4.14(b) shows that a much higher content of phosphorus is found in the nickel plating than the workpiece. This is also expected, as electroless nickel contains between 1 - 12% phosphorous [80], and Inconel 718 contains only 0.008% phosphorus. Figures 4.12(a) and 4.16 clearly indicate the presence of copper and zinc in the recast layer. Since Inconel 718 contains only 0.06% copper and no zinc, it is fair to say that these elements migrated into the workpiece from the wire electrode during cutting, as has been previously reported [27, 38, 39, 40]. It does not appear as though either element has diffused into the workpiece beyond the recast layer. It also appears that the some evidence of chrome depletion in the recast layer is present as the chrome intensity drops by 15% in the recast material. Additionally, nickel and iron drop by 8% and 7% respectivly when comparing the bulk workpiece to the recast layer.

One unexpected finding from this analysis is the presence of an inhomogeneity in the workpiece material. Chrome, iron, molybdenum and niobium all display a clear vertical banding of relative intensities in the workpiece material. These bands do not appear to align with the grain boundaries, which are relatively equiaxed. Although faint in the original pictures, the raw data indicates that relative intensities vary as much as 3% between bands. These differences can be brought out by adjusting the colorscale of the image, as shown in Figure 4.17 for iron and moldbdenum. The source of this phenomenon is unknown, and it is unclear what role this may play in recast layer formation. At the least, it would likely contribute to the large variance observed in recast layer thickness.

A secondary electron image (SEI) of the analyzed area is displayed in Figure 4.18. An SEI conveys topographical data about the specimen. It is seen that the nickel plating is slightly recessed below the workpiece. This area was likely preferentially polished during the specimen preparation. Two SEM images of the analyzed area are shown in Figures 4.19 and 4.20. These images were taken at progressively lower magnifications. It can be seen that the varying nature of the recast layer continues across the sample. The grains are also apparent here.

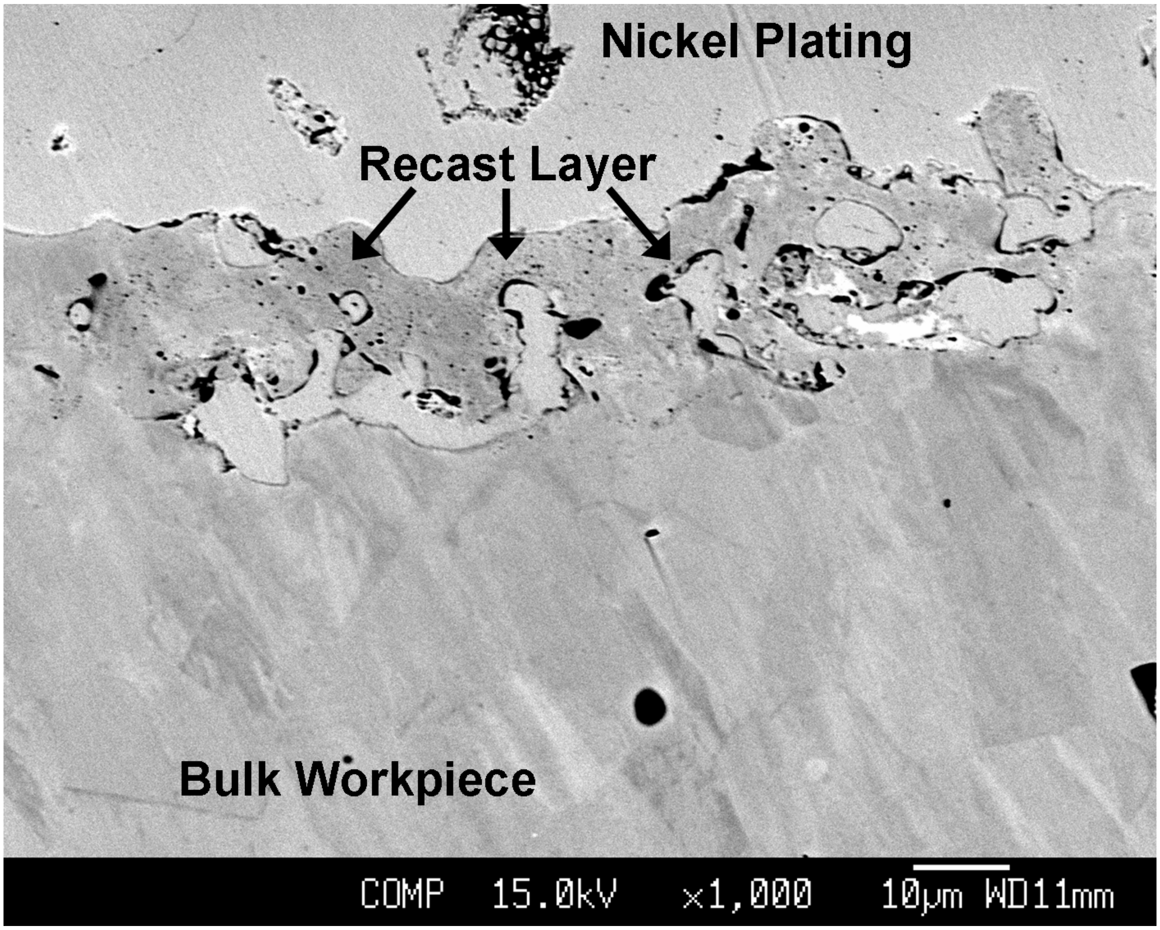

Figure 4.10: Composition view of the taper section to be analyzed (1000X)

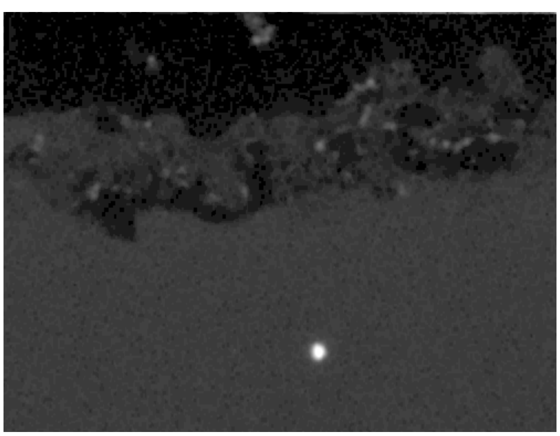

(a) Aluminum (WDS)

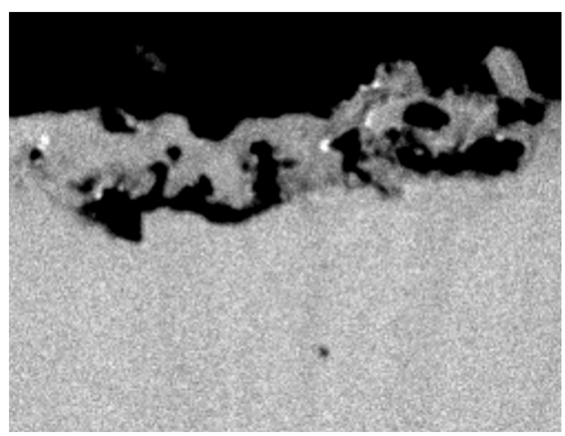

(b) Chrome (EDS)

Figure 4.11: Relative intensities of aluminum (WDS) and chrome (EDS) within the scan area

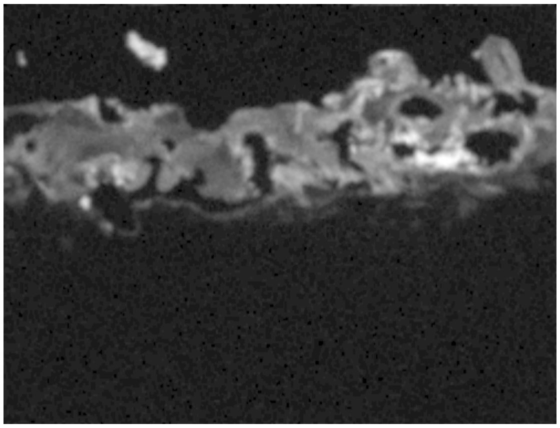

(a) Copper (WDS)

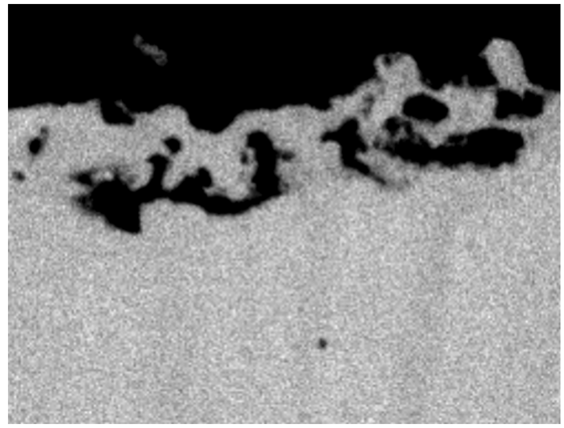

(b) Iron (EDS)

Figure 4.12: Relative intensities of copper (WDS) and iron (EDS) within the scan area

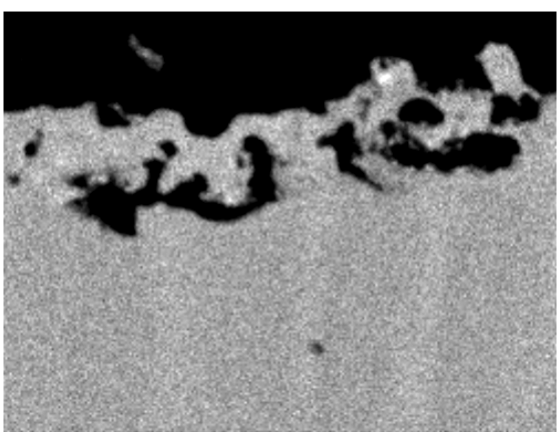

(a) Molybdenum (WDS)

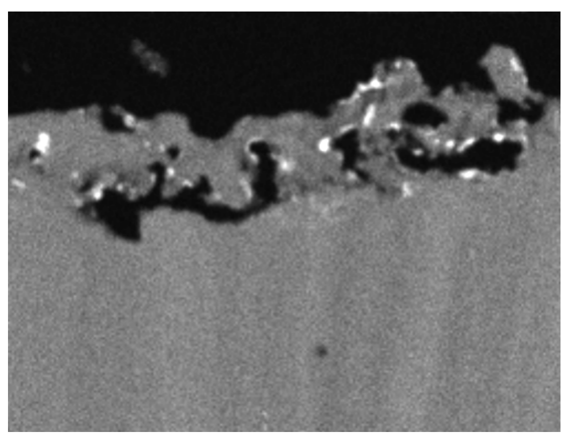

(b) Niobium (WDS)

Figure 4.13: Relative intensities of molybdenum (WDS) and niobium (WDS) within the scan area

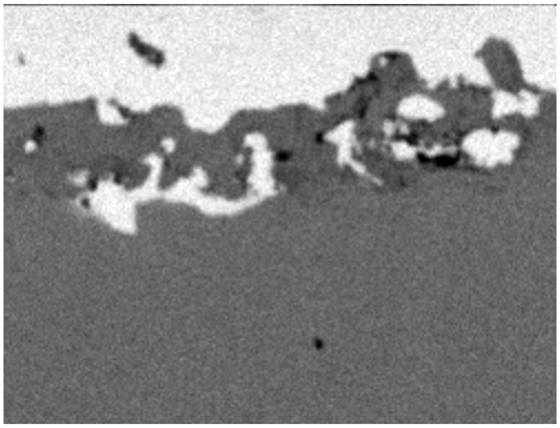

(a) Nickel (EDS)

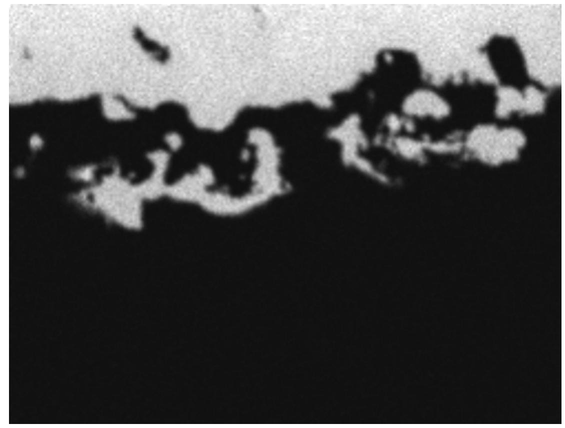

(b) Phosphorous (WDS)

Figure 4.14: Relative intensities of nickel (EDS) and phosphorous (WDS) within the scan area

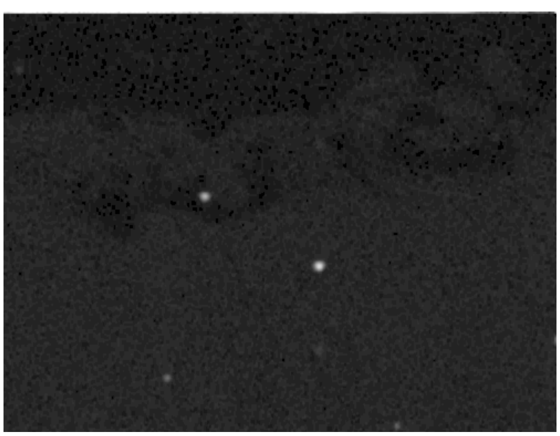

(a) Silicon (WDS)

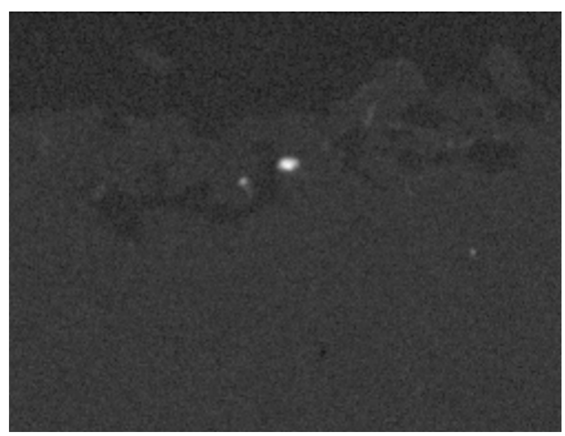

(b) Titanium (EDS)

Figure 4.15: Relative intensities of silicon (WDS) and titanium (EDS) within the scan area

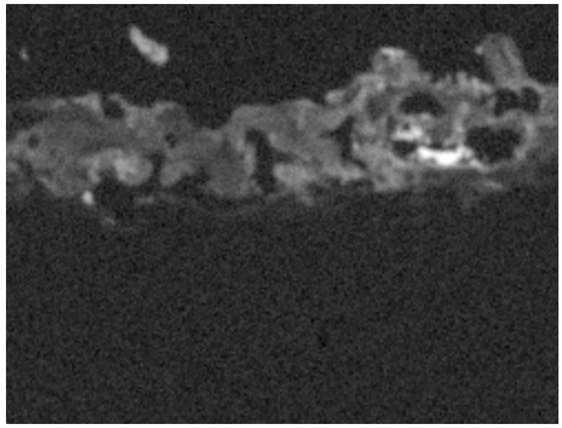

Figure 4.16: Relative intensity of zinc (WDS) within the scan area

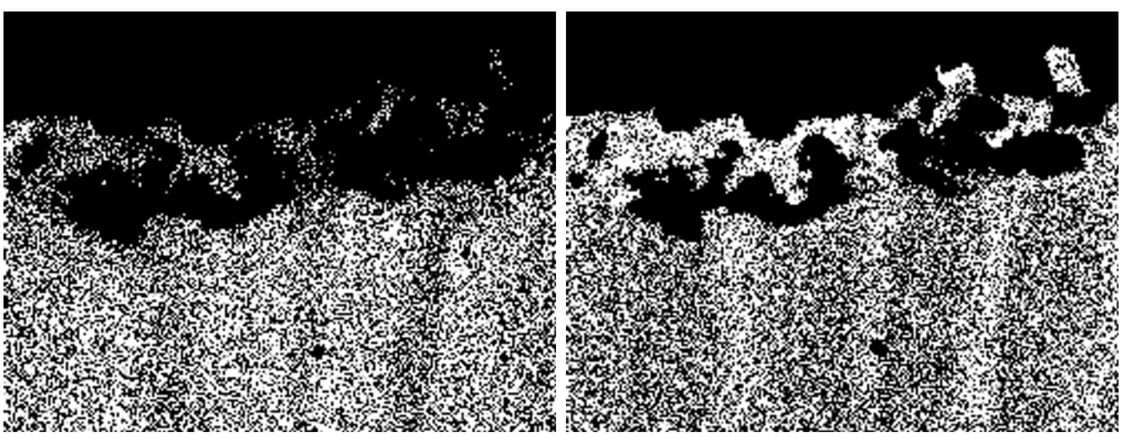

(a) Iron (adjusted, EDS)

(b) Molybdinum (adjusted, WDS)

Figure 4.17: Adjusted intensities of iron (EDS) and molybdenum (WDS) to highlight vertical banding inhomogenuity

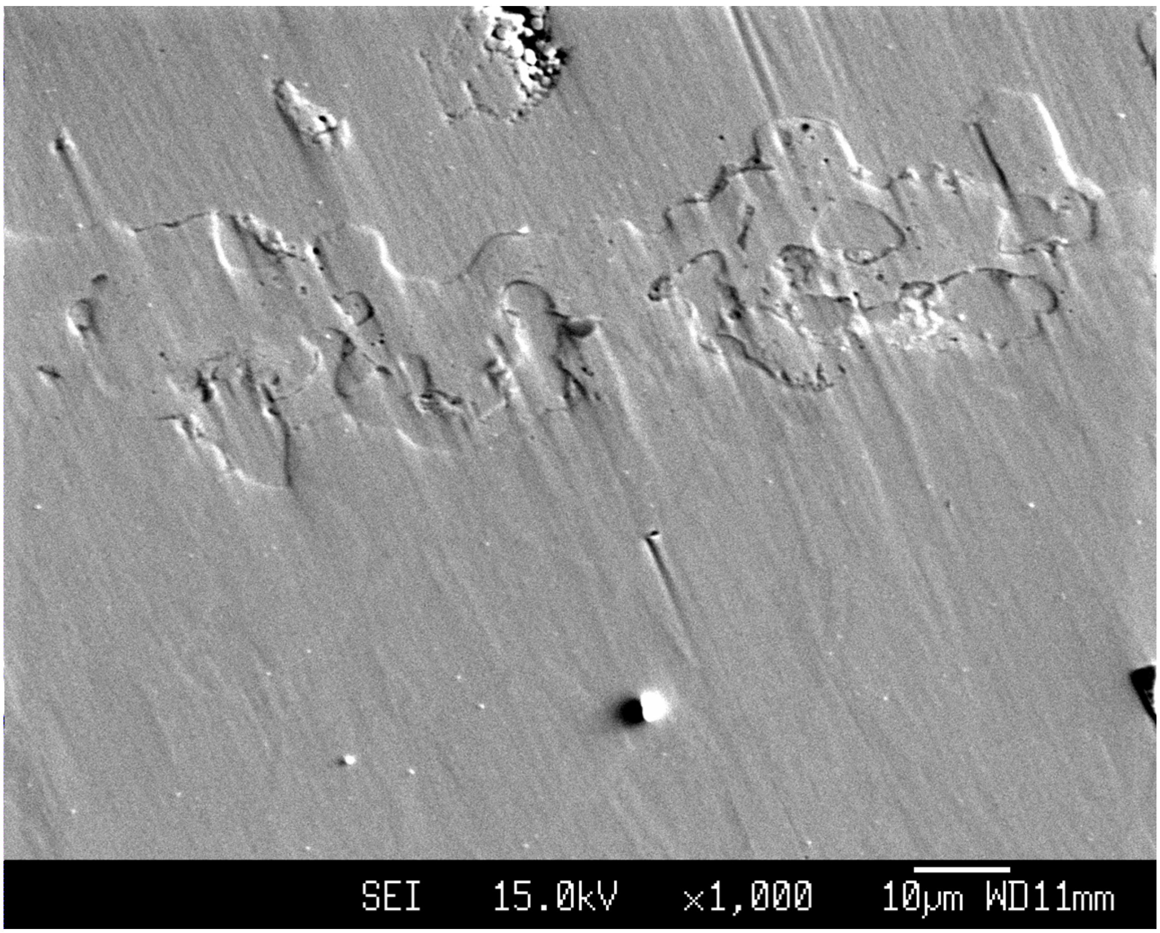

Figure 4.18: 1000X SEI image of scan area

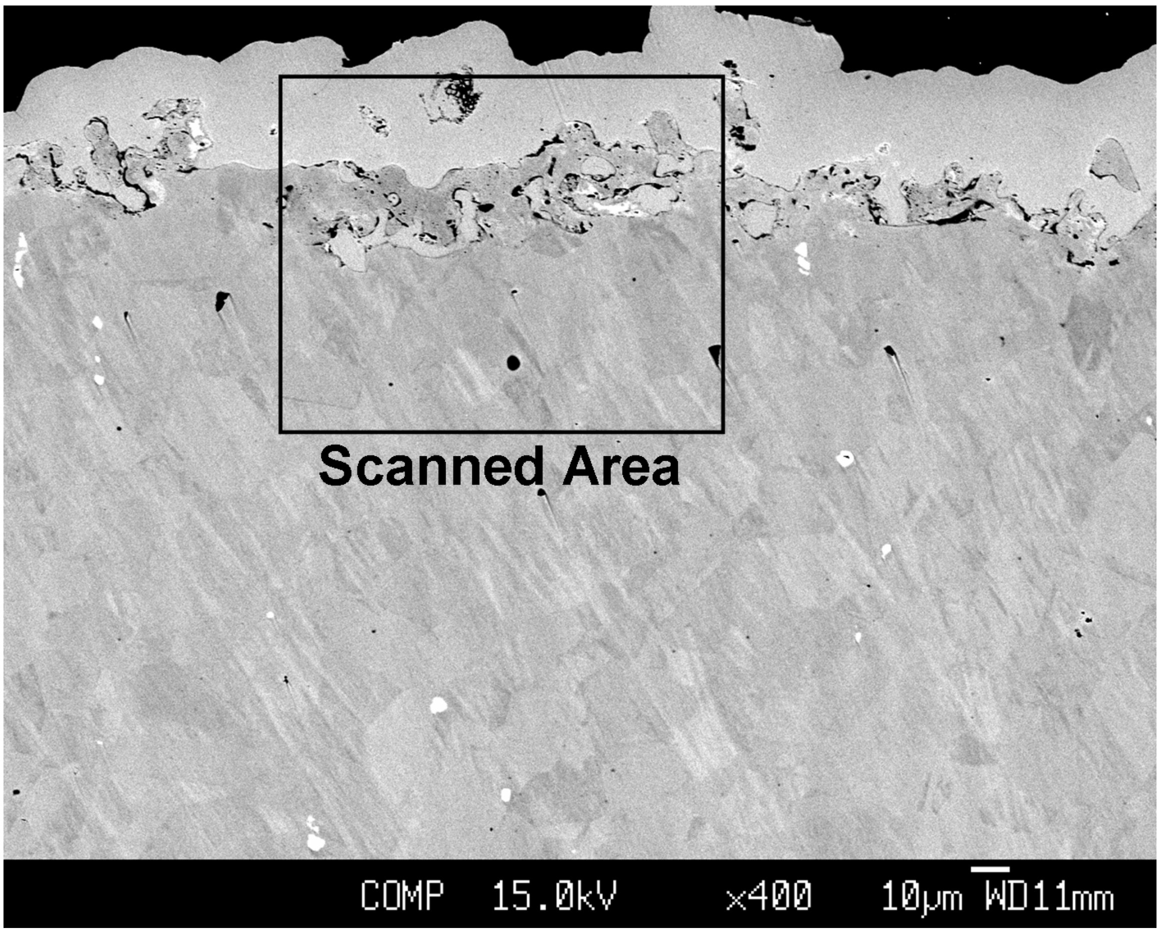

Figure 4.19: 400X SEM image of scan area

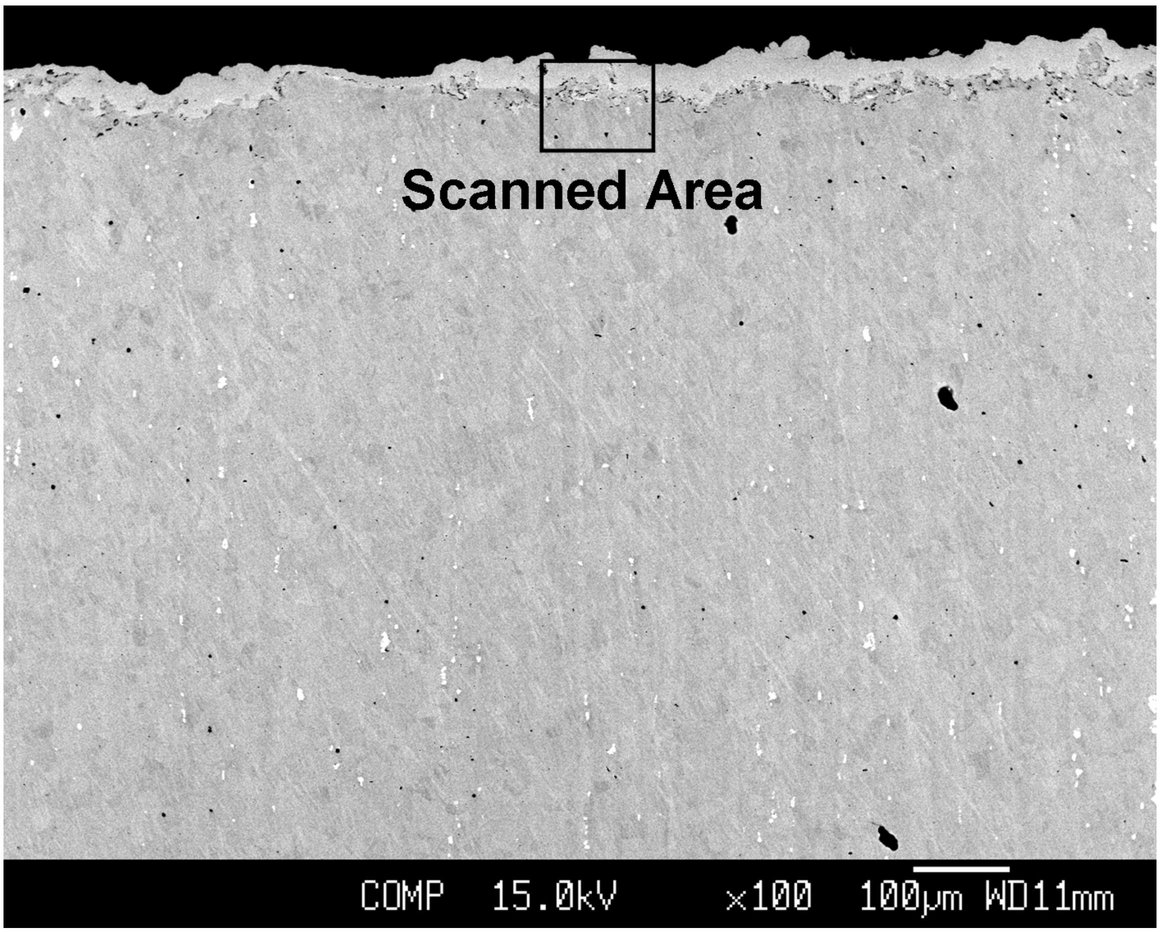

Figure 4.20: 100X SEM image of scan area

4.5 X-Ray Diffraction

4.5.1 Overview

In this section, residual stress imparted by the wire-EDM process will be measured using the method of x-ray diffraction. Residual stresses can originate in nearly every type of material processing, including machining, rolling, welding, heat treatments, and phase transformations, etc. Residual stresses will affect the strength of a part under an applied cyclic load, and can significantly affect fatigue life [7]. The rapid heating and cooling rates, as well as the possible resulting phase changes, present in wire-EDM will undoubtedly lead to the presence of residual stresses.

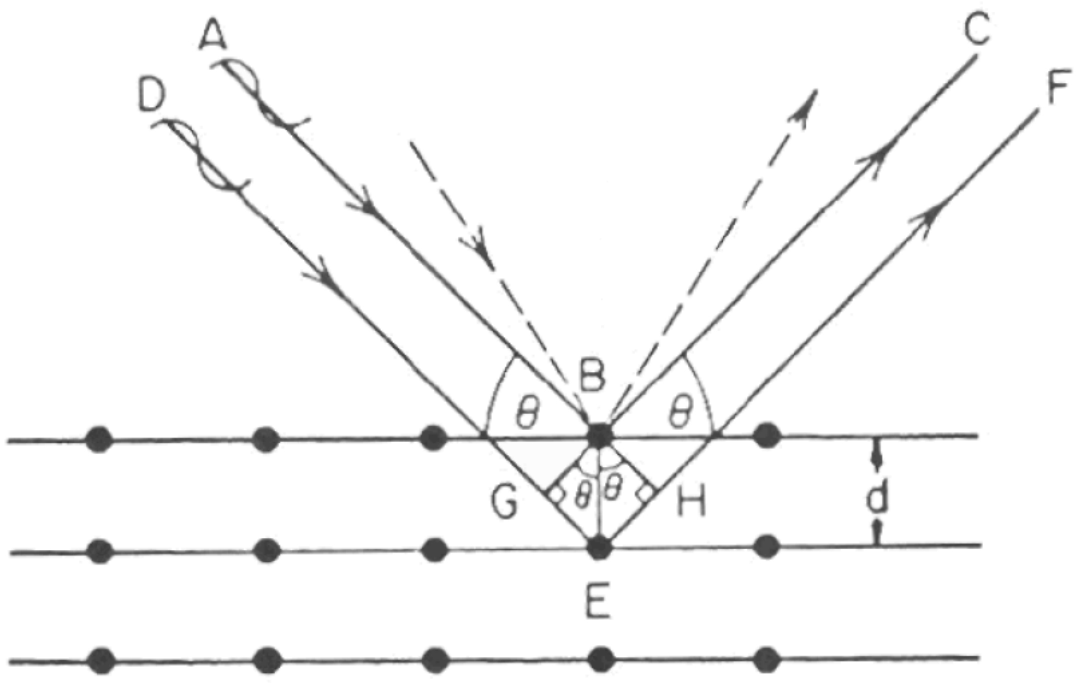

Figure 4.21: Diffraction of x-rays from crystal atomic planes [7]

X-ray diffraction is a non-destructive testing technique for measuring residual stresses. The fundamental principle on which x-ray diffraction operates is based on the fact that the atoms in a specimen are arranged in crystallographic planes. Observe Figure 4.21. Consider two parallel x-rays, ABC and DEF, impinging several crystallographic planes of atoms. Prior to striking the surface, the waves are in-phase with one another. The reflected waves have now traveled different distances and may now be out of phase. Thus, either constructive or destructive interference between the reflected rays may result. If the distance GEH is an integral multiple (n) of the wavelength, λ, then the wave will be in constructive interference. This relationship can be described mathematically through Bragg's Law, Equation 4.1,

$$n\lambda = 2d\sin\theta \tag{4.1}$$

where d is the interplanar, or lattice spacing and θ is the angle of incidence. Thus, for an x-ray beam of known Bragg angle and wavelength, the interplanar spacing can be calculated. If the interplanar spacing of an unstressed material is known, x-ray diffraction can be used to measure the interplanar spacing of the same material once it has been stressed. Any difference in the two distances will dictate the strain present in the material, which in turn can be used to find the residual stress.

A diagram of the actual orientation of the x-ray source, x-ray detector and the specimen is shown in Figure 4.22. The θ angle determines from which crystallographic plane the measurements are made. Varying Φ allows measurements to be made along different directions in the sample. In a polycrystalline material, ψ and χ can be altered to expose different grains while still measuring from the same set of planes, as shown in Figure 4.23. ψ is measured from the normal of the specimen face to the bisector of the angle between the incident x-ray and the reflected x-ray.

4.5.2 Experimental Procedure

X-ray diffraction residual stress measurements were made on four 3.962 mm $\times$ 30 mm $\times$ 30 mm specimens of Inconel 718 cut under the conditions given in Table 4.1. All experiments were conducted on a MAC Science X-Ray Diffractometer with an 18 kW rotating anode generator, Scintag PTS goniometer and parallel beam optics

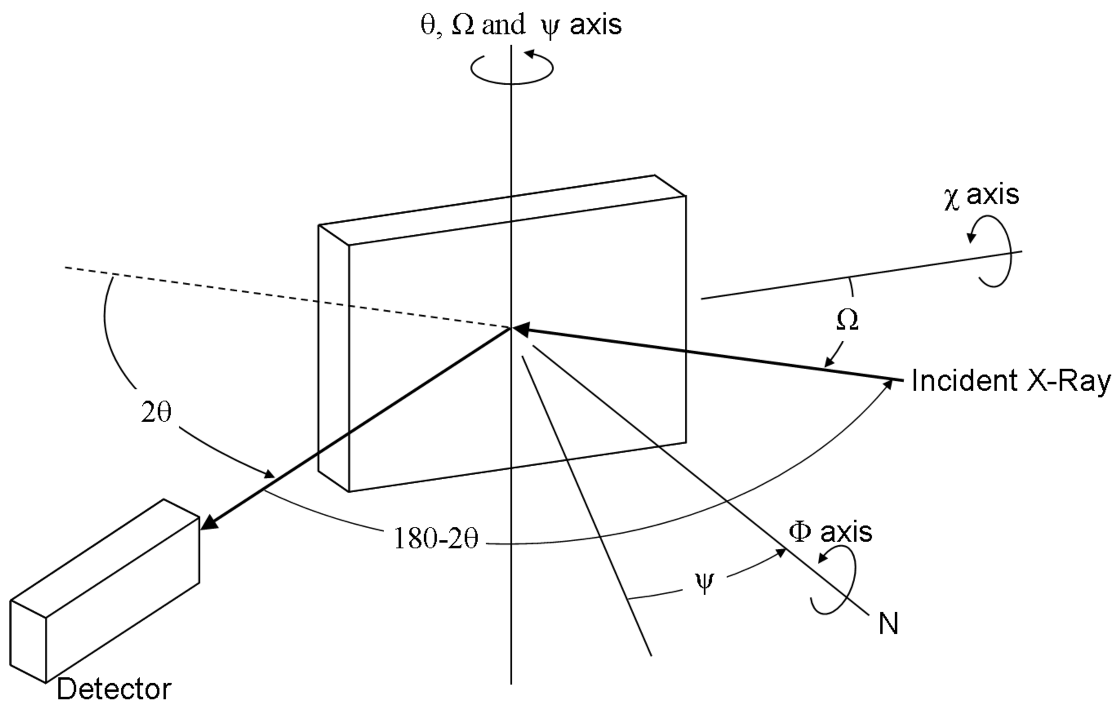

Figure 4.22: Orientation of x-ray source, x-ray detector and the specimen to be measured by x-ray diffraction

to eliminate sample surface displacement errors. The "ψ-goniometer geometry" was employed, and in all experiments χ was fixed at 0°. The specimen was not oscillated and copper radiation of wavelength 1.54059 Å was used. The current was 200 mA and the voltage was 40 kV in all experiments.

The first step was to conduct a θ-2θ scan for phase identification. The non-wire-EDM cut face of the Sample 1 was observed at 2θ varying between 10° and 154.9° at 0.02° per step, and 1° per minute. The results, shown in Figure 4.24, revealed several peaks. Two peaks at the highest 2θ values were selected for further analysis to maximize strain measurement sensitivity. These peaks were identified and corresponded to the (331) and (420) planes (in Miller indices) which correspond to 2θ angles of 137.7° and 146.2°, respectively.

The next step was to determine the unstressed lattice spacing of the two planes. This was accomplished by scanning the surface of the un-machined face of Sample 1,

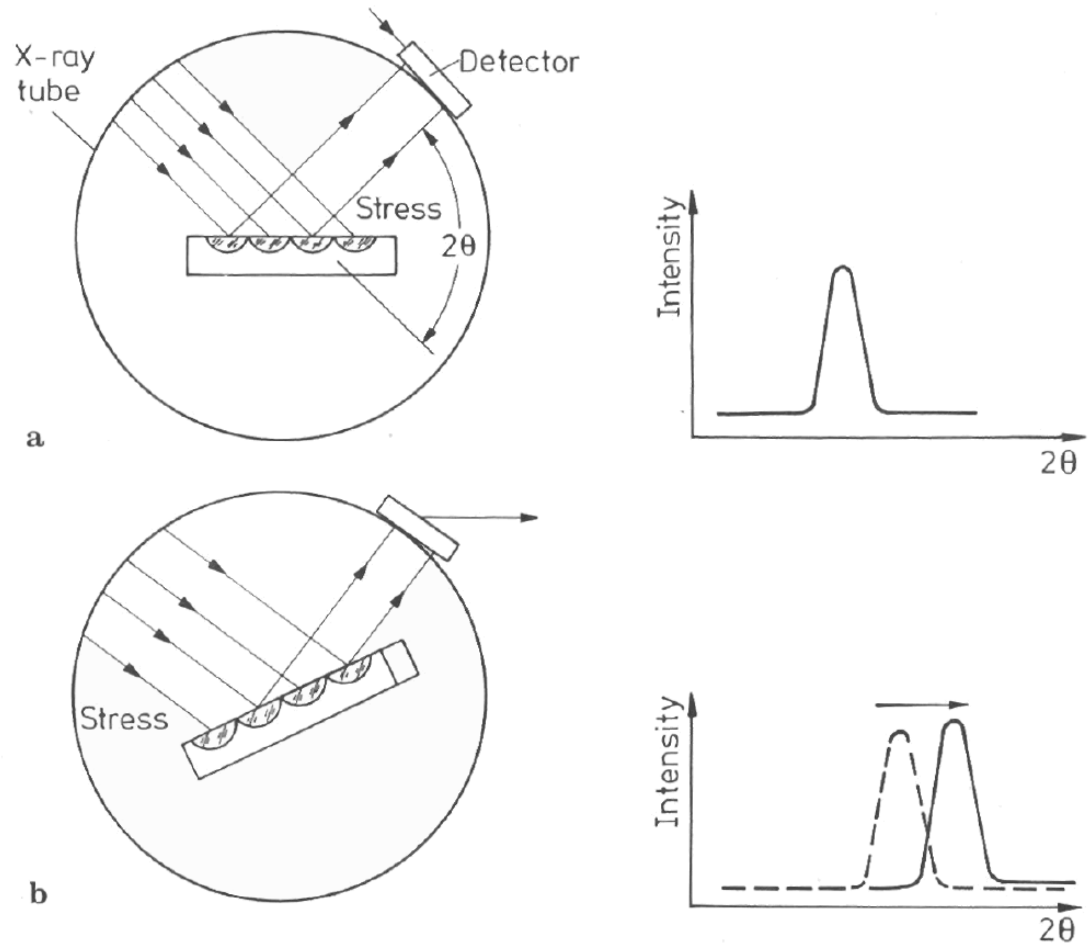

Figure 4.23: Varying ψ exposes a different subset of grains to x-ray diffraction [7]

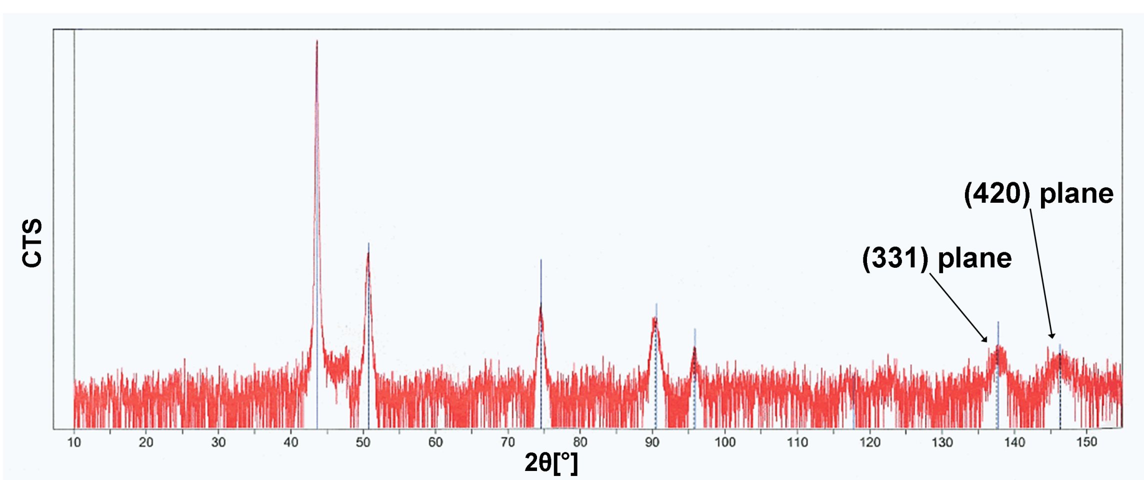

Figure 4.24: θ-2θ scan for Inconel 718, 138° and 146° peaks were further examined

Table 4.2: Scan Table for (331) plane, repeated with 2θ varying from 134° to 142° at 0.02° per step

ϕ [°]	Nominal 2θ [°]	θ [°]	ψ [°]	Ω [°]
0.0	137.5	68.8	-55.0	13.8
0.0	137.5	68.8	-45.2	23.6
0.0	137.5	68.8	-35.4	33.4
0.0	137.5	68.8	-24.2	44.6
0.0	137.5	68.8	0.0	68.8
0.0	137.5	68.8	24.2	93.0
0.0	137.5	68.8	35.4	104.2
0.0	137.5	68.8	45.2	114.0
0.0	137.5	68.8	55.0	123.8
90.0	137.5	68.8	-55.0	13.8
90.0	137.5	68.8	-45.2	23.6
90.0	137.5	68.8	-35.4	33.4
90.0	137.5	68.8	-24.2	44.6
90.0	137.5	68.8	0.0	68.8
90.0	137.5	68.8	24.2	93.0
90.0	137.5	68.8	35.4	104.2
90.0	137.5	68.8	45.2	114.0
90.0	137.5	68.8	55.0	123.8

assumed to be representative of the virgin, non-wire-EDM cut surface. These, and all subsequent scans were conducted according to the scan tables given in Tables 4.2 and 4.3. For the (331) plane, scans were conducted at 2θ values ranging from 134° to 142° in 0.02° per step increments. In the (420) plane, scans were conducted at 2θ values ranging from 144° to 150° in 0.02° per step increments. The scan rate was always 14 seconds per step or slower. A measurement of both planes required around 20 hours. Since the machine was running overnight, the scan rate was adjusted to maximize time usage. The data from each scan can be found in Appendix D.

Once the unstressed lattice spacing was found, the residual stresses on the wire-EDM cut surface could be determined. Scans of the (331) and (420) planes were made on the wire-EDM cut surface of each of the four samples according to the aforementioned scan tables. The depth of penetration of the x-rays was between 4 and 11 μm, meaning the x-ray diffraction measurements were averaged over this

Table 4.3: Scan Table for (420) plane, repeated with 2θ varying from 142° to 151° at 0.02° per step

ϕ [°]	Nominal 2θ [°]	θ [°]	ψ [°]	Ω [°]
0.0	146.4	73.2	-55.0	18.2
0.0	146.4	73.2	-45.2	28.0
0.0	146.4	73.2	-35.4	37.8
0.0	146.4	73.2	-24.2	49.0
0.0	146.4	73.2	0.0	73.2
0.0	146.4	73.2	24.2	97.4
0.0	146.4	73.2	35.4	108.6
0.0	146.4	73.2	45.2	118.4
0.0	146.4	73.2	55.0	128.2
90.0	146.4	73.2	-55.0	18.2
90.0	146.4	73.2	-45.2	28.0
90.0	146.4	73.2	-35.4	37.8
90.0	146.4	73.2	-24.2	49.0
90.0	146.4	73.2	0.0	73.2
90.0	146.4	73.2	24.2	97.4
90.0	146.4	73.2	35.4	108.6
90.0	146.4	73.2	45.2	118.4
90.0	146.4	73.2	55.0	128.2

region. Three replicates of the measurements were made on Sample 2 in order to estimate the standard deviation in the measurements based on plane and Φ. It was assumed that each sample demonstrated the same variance.

Lastly, Sample 4 was selected for further study to quantify the residual stress as a function of depth into the wire-EDM cut surface since it contained the thickest recast layer and would represent the worst case. To accomplish this, material removal was necessary. The sample was lightly ground with wet P4000 grit silicon carbide sand paper on one of the wire-EDM cut surfaces. Residual stress measurements were made after 9 μm were removed, and again after a total of 26 μm were removed. Although mechanical removal of material will necessarily alter the stress state, the significance of this effect can be estimated with subsequent analysis.

4.5.3 Results

The method of determining the unstressed lattice spacing, d_0, is given by Hauk et al. [81]. Assuming a biaxial stress state, d_0 can be determined by Equation 4.2,

$$\sin^2\psi^* = \frac{\nu/E}{(1+\nu)/E}\left(1+\frac{m_1}{m_2}\right) \tag{4.2}$$

where where m_1 and m_2 are the slopes of the d vs. $\sin^2\psi$ plot at Φ=0° and Φ=90°, respectively. These plots are shown for the (331) plane in Figures 4.25 and 4.26. The $\sin^2\psi^*$ term can be used to determine the ψ value for which the strain is zero. In turn, d_0 can be found from the d vs. $\sin^2\psi$ at Φ=0° line. Unstressed lattice spacings of 0.8255 Å and 0.8048 Å for the (331) and (420) planes, respectively, were determined.

Next, the Xpert Stress software version 1.1a from PANalytical was used to calculate residual stresses from the x-ray diffraction data. The uni-axial $\sin^2\psi$ method was used. The stress tensor was given by Equation 4.3 [7],

$$\frac{d_{\Phi\Psi}-d_0}{d_0} = \frac{1+\nu}{E}\sigma_{11}\sin^2\psi - \frac{\nu}{E}\sigma_{11} \tag{4.3}$$

and was evaluated separately for both Φ=0° and Φ=90° from the slopes of the $\sin^2\psi$ plots. Consequently, the relationship shown in Equation 4.4,

$$\sigma_{11} = \frac{m_\Phi E}{d_0\,(1+\nu)} \tag{4.4}$$

where m_Φ is the slope of the d vs. $\sin^2\psi$ plot can be derived. For these calculations a modulus of elasticity of 205 GPa and a Poisson's ratio of 0.3 were assumed.

The residual stresses for each specimen, plane and ϕ angle are given in Table 4.4. At ϕ=0°, the stress was in the direction of table feed, and at ϕ=90° the stress was parallel to the axis of the wire electrode, as explained in Figure 4.27. The results of each scan table can be seen in Appendix D. Notice that every stress measurement is

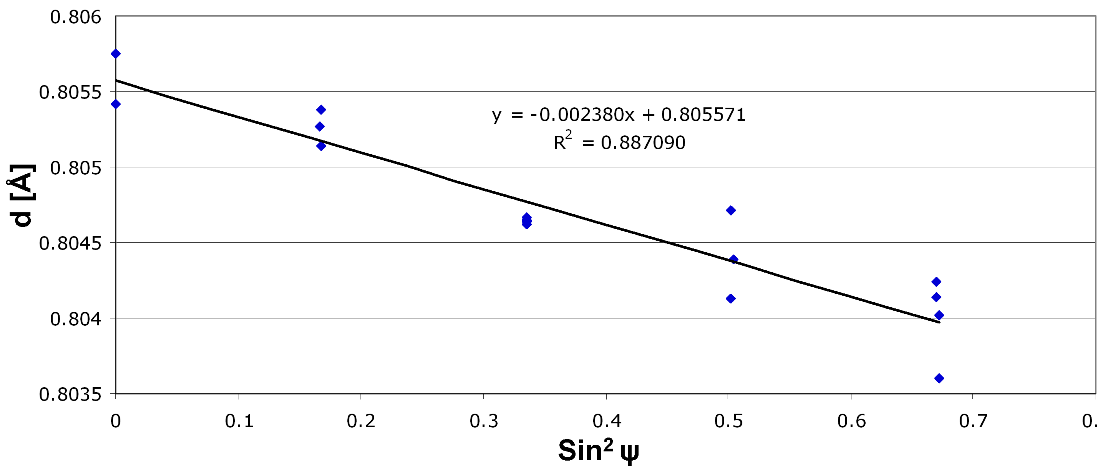

Figure 4.25: d [Å] vs. $\sin^2\psi$ at Φ=0° for determination of the unstressed lattice spacing of the (331) plane

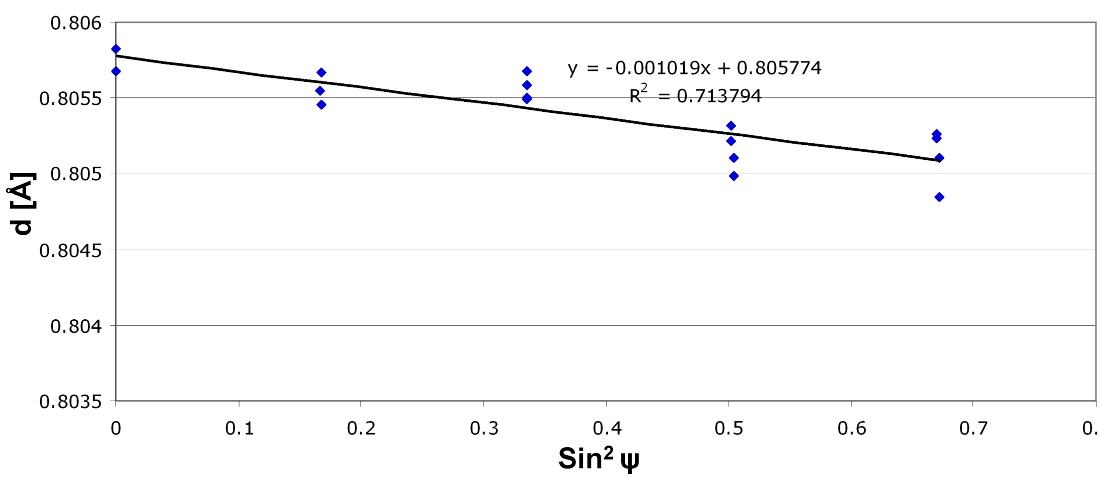

Figure 4.26: d [Å] vs. $\sin^2\psi$ at Φ=90° for determination of the unstressed lattice spacing of the (331) plane

Table 4.4: Residual stress [MPa] measurements of wire-EDM cut surfaces

Sample	Plane	ϕ [°]	Stress [MPa]
Sample 1	(331)	0	453
	(331)	90	302
	(420)	0	478
	(420)	90	407
Sample 2	(331)	0	272
	(331)	90	209
	(420)	0	483
	(420)	90	277
Sample 2 (repeated)	(331)	0	249
	(331)	90	192
	(420)	0	428
	(420)	90	269
Sample 2 (repeated)	(331)	0	202
	(331)	90	220
	(420)	0	345
	(420)	90	250
Sample 3	(331)	0	236
	(331)	90	268
	(420)	0	475
	(420)	90	392
Sample 4	(331)	0	195
	(331)	90	227
	(420)	0	168
	(420)	90	281

positive, indicating that the surface of the wire-EDM cut face is in tension. This is in accordance with what others have reported [82, 83].

To estimate the error in the residual stress measurements, the standard deviation of the 3 replicates conducted for Sample 2 was found. These are listed in Table 4.5. Note that the variance of the stress in the ϕ=0° direction is much greater than in the ϕ=90° direction. This is due to the orientation and shape of the samples. At ϕ=0°, the direction of table feed, x-rays are able to reflect off of large portions of the width of the sample, but with fewer x-rays given the 0.5×10 mm (w×h) beam. However, at ϕ=90°, the direction of the wire electrode axis, a smaller amount of material was examined with more x-rays.

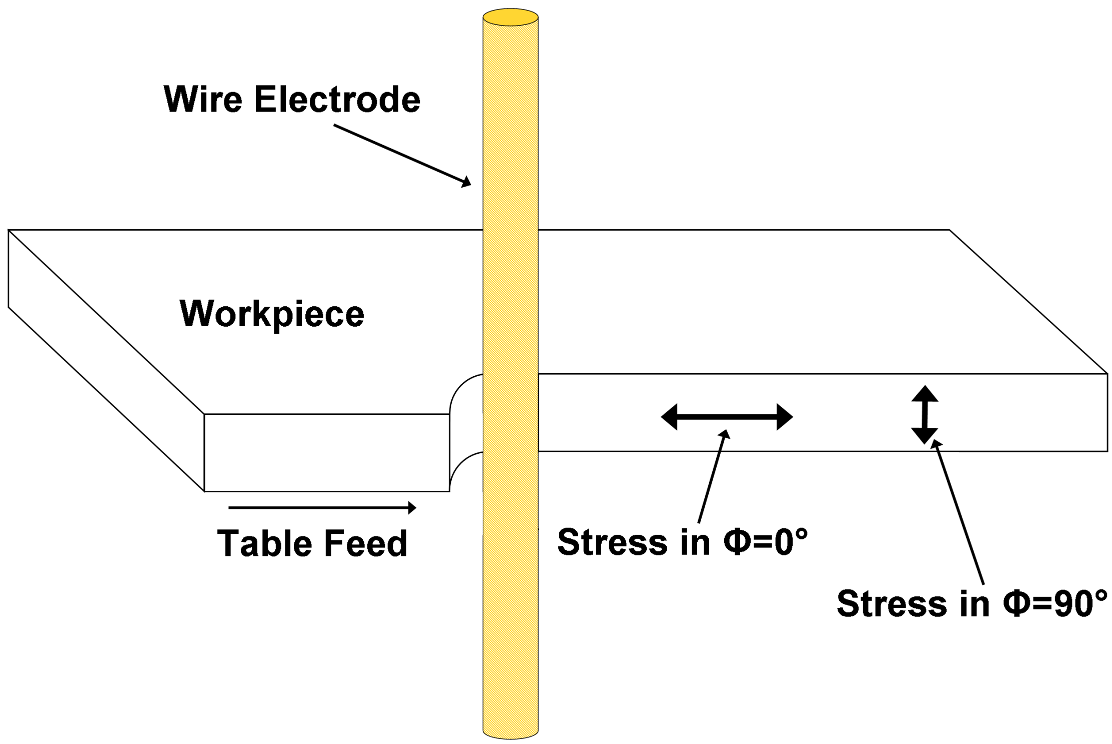

Figure 4.27: Orientation of stress measurements at ϕ=0° and ϕ=90°

Table 4.5: Standard deviation [MPa] of residual stress measurements from Sample 2

Std. Dev. Of Stress [Mpa]		
Plane	ϕ=0°	ϕ=90°
(331)	±36	±14
(420)	±69	±14
Average	±53	±14

For the following analysis, the stresses from the (331) and (420) planes were averaged to represent the values for the entire specimen. The residual stresses in the directions of table feed (ϕ=0°) and wire electrode axis (ϕ=90°) are plotted versus energy per spark in Figure 4.28. Assuming the influence of wire diameter is negligible overall, it appears that as energy per spark increases, the magnitude of the residual stresses decrease. This can be explained by considering that these residual stresses are largely generated due to thermal gradients during cooling of the recast layer. As the recast layer resolidifies and its temperature drops downs to that of the bulk workpiece, its contraction is opposed by the bulk workpiece. This results in the wire-EDM cut surface exhibiting tensile residual stresses and the bulk workpiece exhibiting compressive residual stresses. Since the temperatures present during machining would be relatively similar, regardless of energy per spark, the same thermal gradients would be present. Consequently, the same forces due to the thermal contraction of the recast layer would also be present. When a larger energy per spark is used, the recast layer is thicker, and this force would be distributed over a larger region, thus lowering the magnitude of the tensile residual stress.

It is also seen from Figure 4.28 that the stresses oriented in the direction of table feed are generally higher than in the direction of the wire-electrode axis. One possible explanation for this phenomenon can be understood by considering the following simplified analysis. Consider the situation shown in Figure 4.29. The dotted lines indicate the element of melted and resolidifying workpiece material at any instantaneous moment during machining. This idealized element takes the form of an extruded semi-circle. The heat contained within this element will dissipate in all directions. It will conduct to the workpiece, and it will convect to the dielectric. It is possible that the relative magnitudes of the heat flow rates through these two modes differ significantly. Consider that this element is much taller than it is wide. Further, as energy per spark increases, the proportions of the heated element will change, as

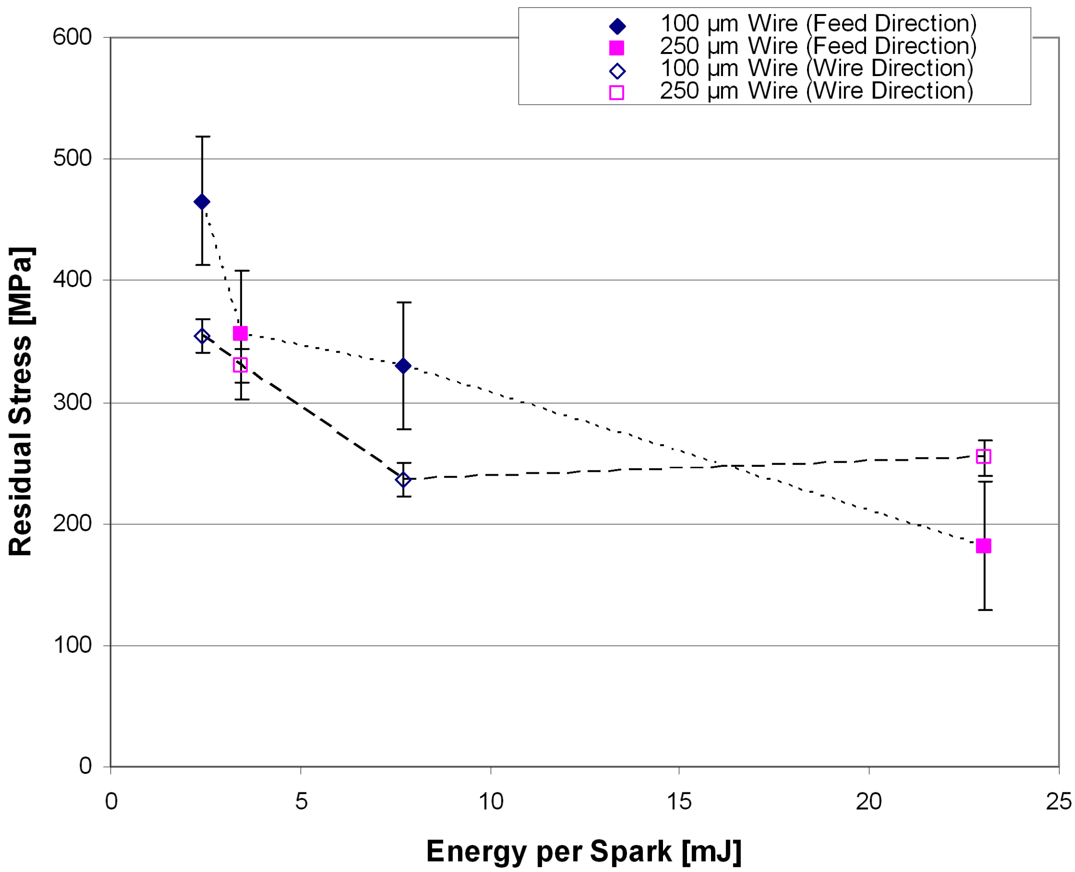

Figure 4.28: Residual stress [MPa] versus energy per spark [mJ]in the directions of table feed and wire electrode axis

seen in Figure 4.30. Additionally, the shape of the workpiece could also have an effect as it is much wider than it is tall. The combination of these factors may contribute to the differences in residual stress observed in Figure 4.28.

The residual stresses versus wire diameter are displayed in Figure 4.31. At the smaller wire diameter (and lower energy per spark) the stresses are greater in the table feed direction than in the wire-electrode axis direction. However, at the larger wire diameter (and higher energy per spark) the stresses in the two directions are not significantly different from one another. This effect is likely caused by the differences in energy per spark, as discussed previously, rather than effects from the diameter of the wire electrode.

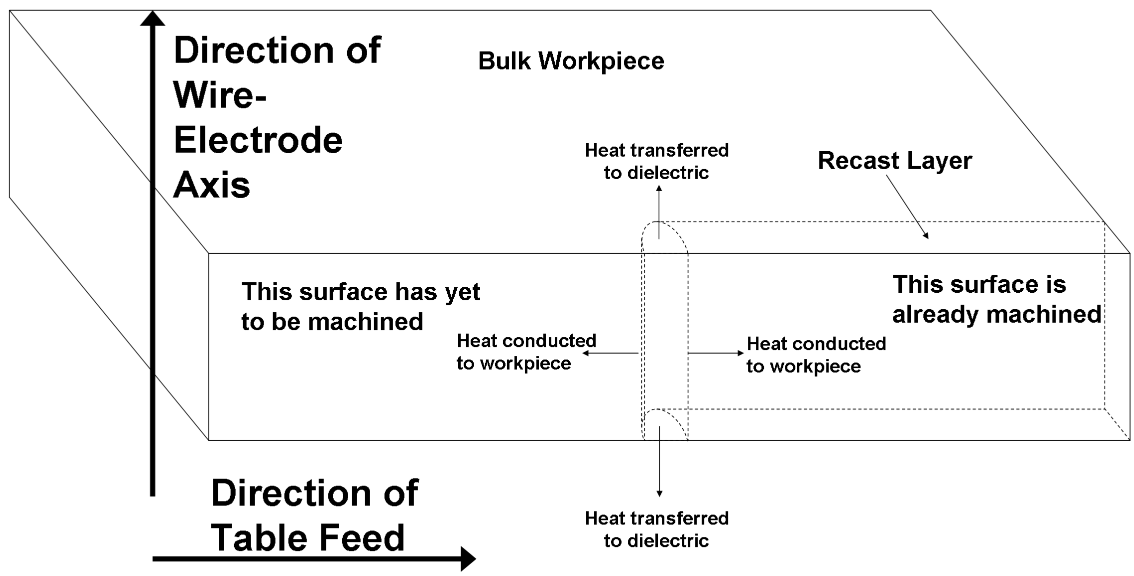

Figure 4.29: Diagram showing simplified analysis of heat flow from resolidified zone during wire-EDM with a small energy per spark

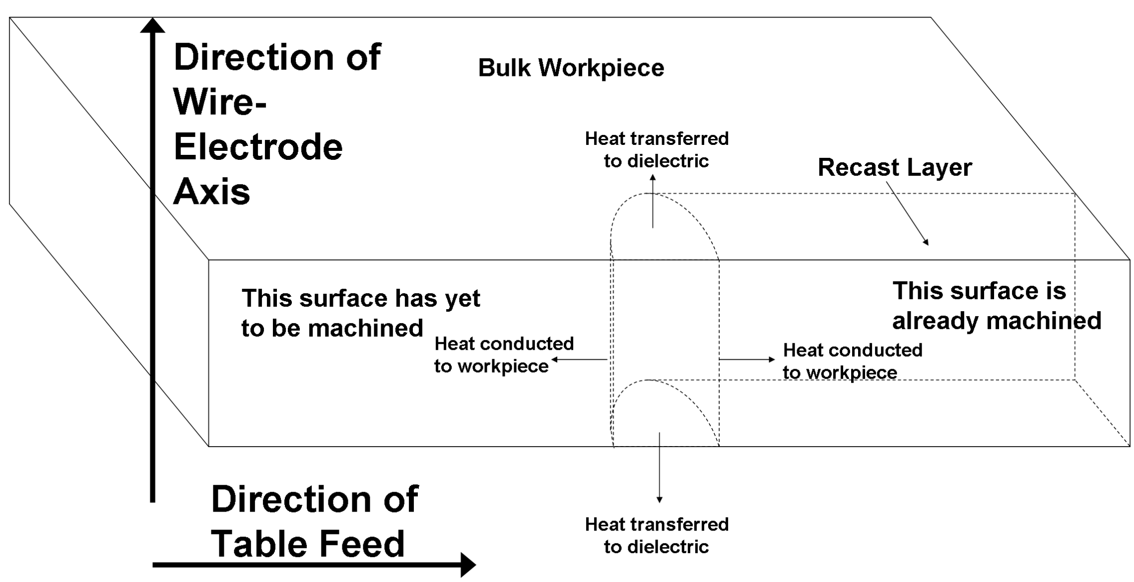

Figure 4.30: Diagram showing simplified analysis of heat flow from resolidified zone during wire-EDM with a large energy per spark

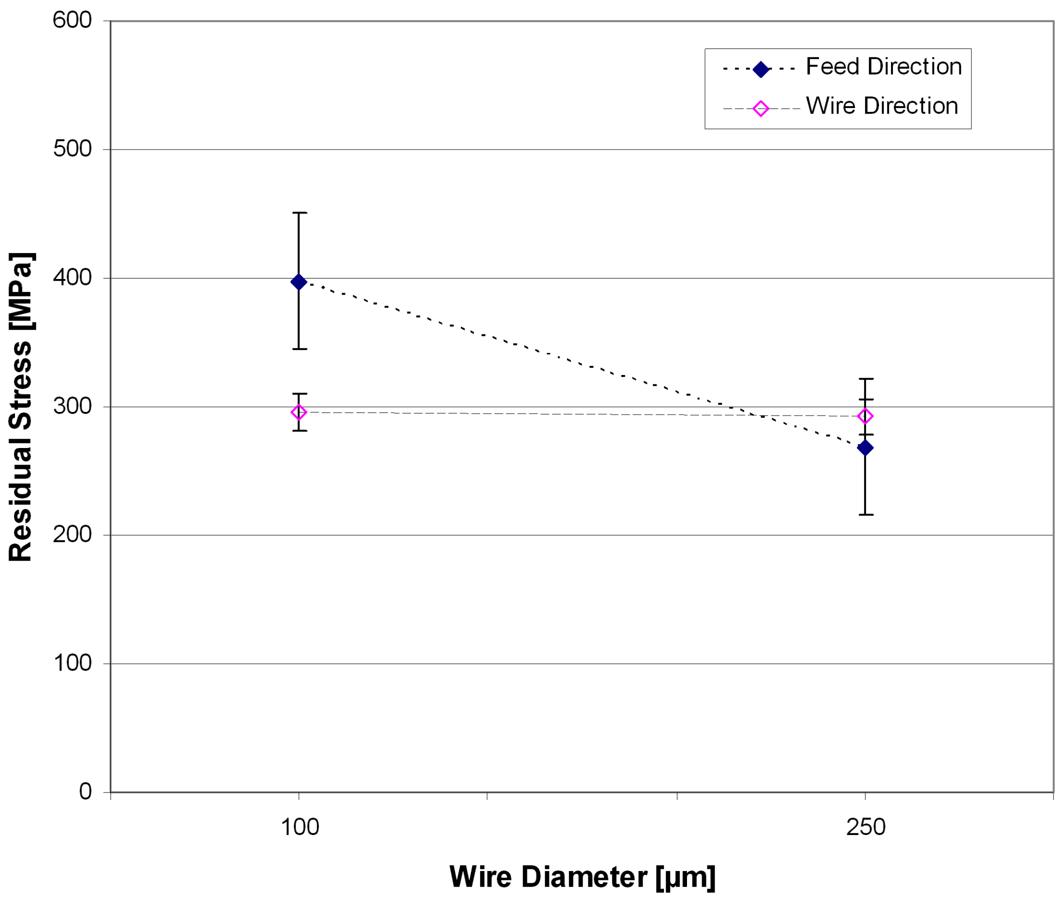

Figure 4.31: Residual stress [MPa] versus wire diameter [μm] in the directions of table feed and wire electrode axis

From the measurements made after material was removed from the surface of Sample 4, the changes in residual stress as a function of depth into the workpiece were analyzed. By applying the same techniques described earlier, the residual stress at the three stages of material removal are given in Table 4.6. With 26 μm of material removed from the wire-EDM cut surface, the residual stresses have switched from tensile to compressive. However, the material removal process itself may induce compressive stresses, thus clouding the data. To check this effect the peak widths from the various planes appearing in the θ-2θ scans were compared. Peak broadening indicates that significant polishing damage has been introduced, typically resulting in compressive stresses [84]. For each of the stages of material removal, the full width at half maximums (FWHM) were compared. These data are given in Appendix D, and plotted in Figure 4.32. Comparison of the FWHM for each 2θ peak shows a majority are within 15% of the value prior to material removal. This was not the case for the (331) plane (2θ value of 137°, peak 6), however, the residual stress was close to that of the (420) plane. Consequently, it was assumed that the hand polishing material removal process did not introduce significant compressive residual stresses.

The residual stress as a function of depth into the wire-EDM cut surface is shown in Figure 4.33. Again, the stresses of (331) and (420) planes have been averaged. The stress shows a clear trend of tensile residual stress transitioning to compressive residual stress in the vicinity of between 15 and 20 μm into the workpiece. In the original surface scan, the residual stress in direction of the wire-electrode axis appeared greater than in the table feed direction. However, after material has been removed, no significant difference in residual stress in the two directions can be observed.

Table 4.6: Residual stress [MPa] measurements of Sample 4 as a function of depth [μm] into the wire-EDM machined surface

Material Removed [μm]	Plane	ϕ [°]	Stress [MPa]
0	331	0	195
	331	90	227
	420	0	168
	420	90	281
9	331	0	155
	331	90	152
	420	0	216
	420	90	198
26	331	0	-173
	331	90	-258
	420	0	-197
	420	90	-205
26 (repeated)	331	0	-138
	331	90	-240
	420	0	-209
	420	90	-190

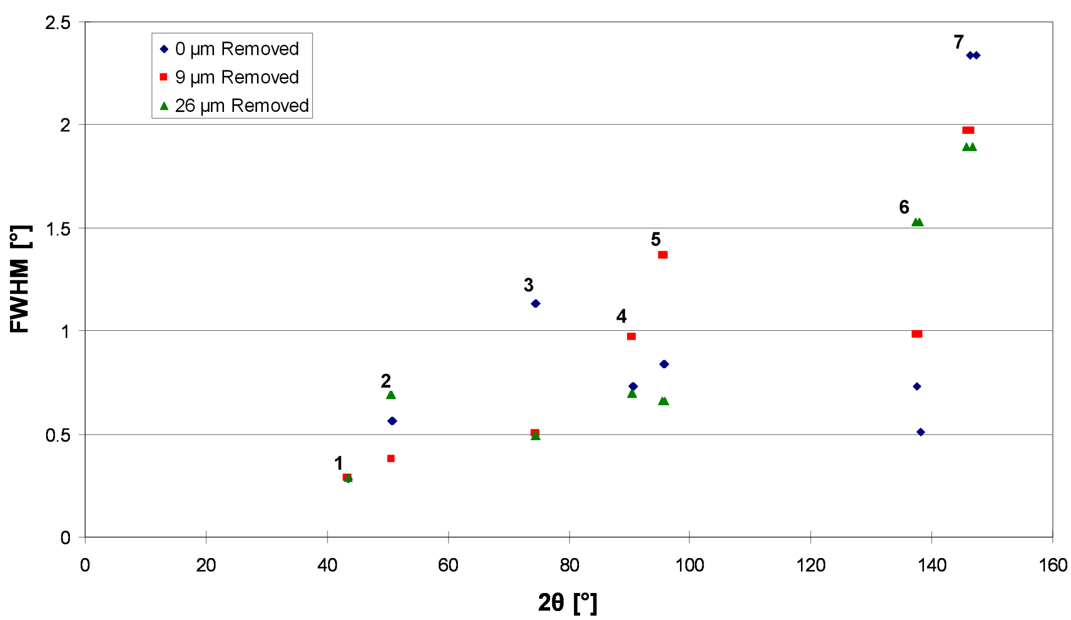

Figure 4.32: FWHM [°] of peaks plotted by 2θ [°] and material removal

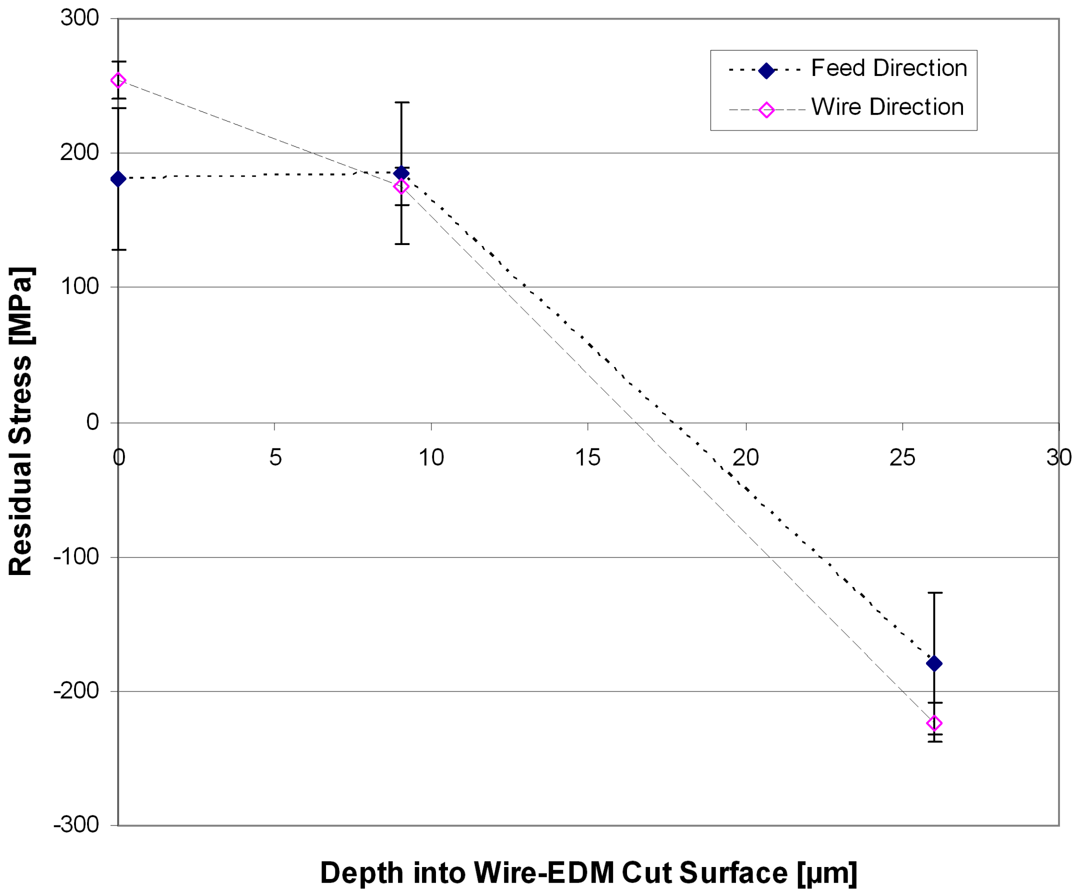

Figure 4.33: Residual stress [MPa] as a function of depth [μm] into the wire-EDM cut surface, taken from Sample 4

4.6 Nano-Indentation Hardness Testing

4.6.1 Overview

The final material characterization undertaken was nano-indentation hardness testing. In hardness testing, an indenter of known geometry is applied with a known load to a test specimen for a known amount of time. From the amount of displacement, both the hardness and elastic modulus can be calculated. The hardness scale is dictated by the shape of the indenter and the applied load, so comparisons from one hardness scale to another are not exact. Nano-indentation hardness testing is often used to measure the properties of films as thin as a few nanometers [85]. The recast layer observed in wire-EDM of Inconel 718 is on average five to ten microns in thickness, and thus nano-indentation testing is necessary to quantify the changes in its hardness.

A typical load-displacement curve for an indentation test is shown in Figure 4.34. The unloading curve differs from the loading curve due to plastic deformation of the specimen. The slope of the unloading curve, S, is the stiffness. Two calculations frequently made from a load-displacement curve are the reduced modulus and the hardness. The reduced modulus is described by Equation 4.5,

$$E_r = \frac{1}{2} S \sqrt{\frac{\pi}{A}} \tag{4.5}$$

where A is the calibrated area function of the tip relating the projected contact area to the contact depth. The reduced modulus includes contributions from both the specimen and the indenter. These contributions are related by Equation 4.6,

$$\frac{1}{E_r} = \left(\frac{1-\nu^2}{E}\right)_{specimen} + \left(\frac{1-\nu^2}{E}\right)_{indenter} \tag{4.6}$$

where E and ν are the elastic modulus and Poisson's ratio of the specimen and the indenter respectively. The hardness is defined by Equation 4.7,

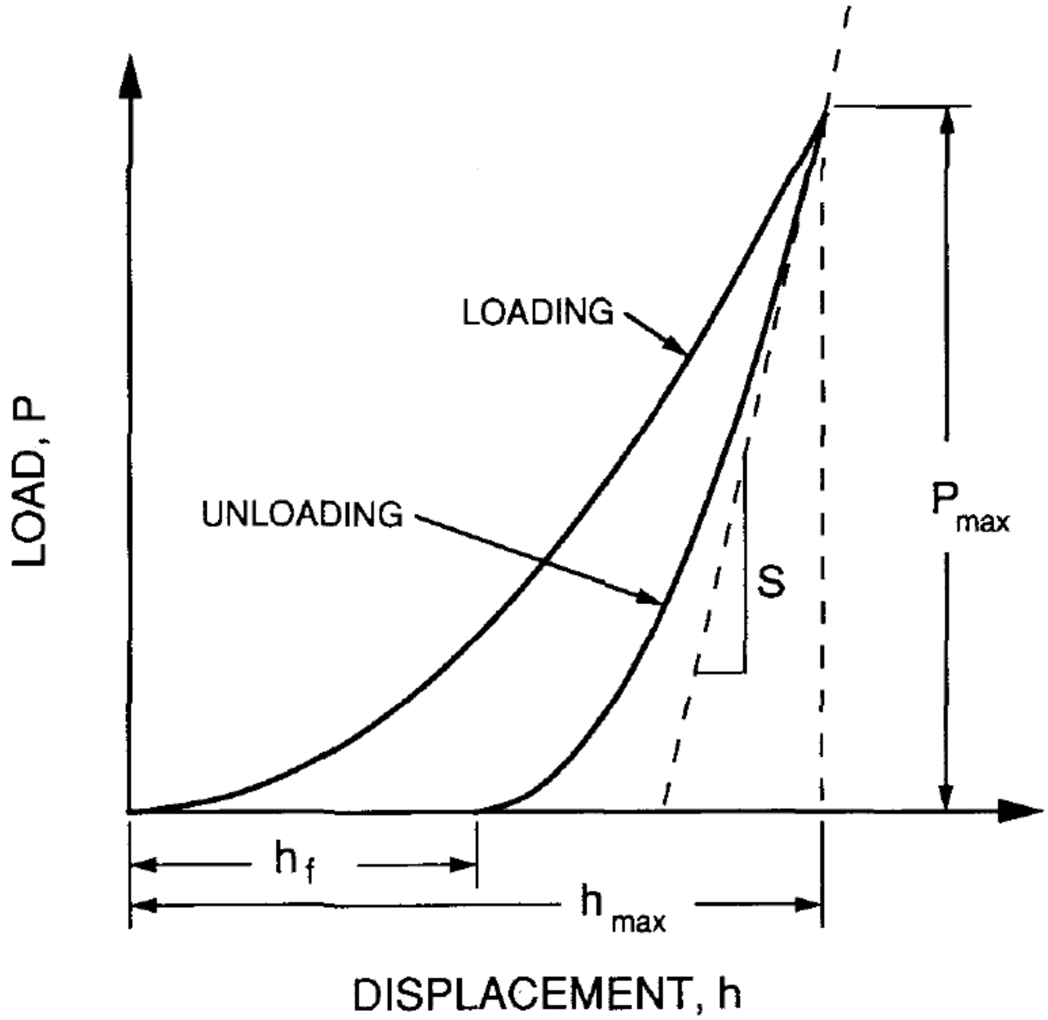

Figure 4.34: Typical load-displacement curve generated in an indentation test [8]

$$H = \frac{P_{max}}{A} \tag{4.7}$$

where P_{max} is the maximum indentation force and A is the area function for the projected contact area at P_{max} [86].

4.6.2 Experimental Procedure

Four specimens of Inconel 718 to be examined were cut at the same conditions as were studied in the surface roughness measurements and under x-ray diffraction.

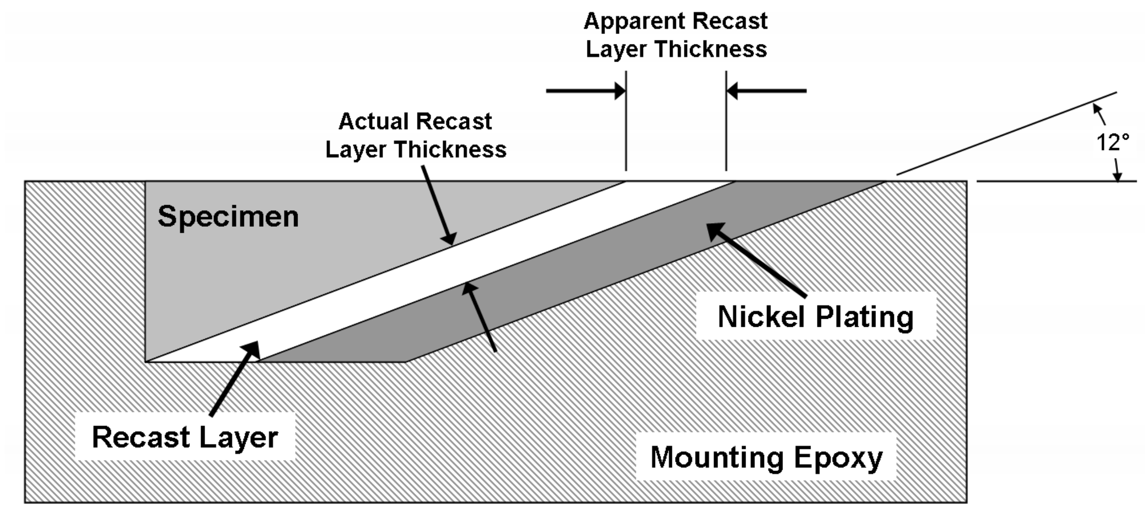

Figure 4.35: Cross-section of mounted 12° taper sections for nano-indentation measurements

Their cutting conditions are shown in Table 4.1. A 12° taper section was cut, just as in the EPMA. A cross-section of the mounted sample is shown in Figure 4.35. The recast layer will appear cosecant 12°, or 4.81 times thicker. The samples were nickel plated, mounted in epoxy and prepared in the manner described in Table 3.5. Care was taken, as a flat, smooth, scratch free surface is essential in obtaining good results in nano-indentation.

All of the experiments described here were conducted on a Hysitron TriboIndenter, displayed in Figure 4.36(a) with a 10mN load cell. The indents were made with a Berkovich tip, shown in Figure 4.36(b), with an included angle of 142.3° and a radius of curvature of between 100 and 200 nm. Every test was conducted with the load function given in Figure 4.37. The load was linearly applied for 10 seconds up to 2,500 μN, held for 5 seconds, and linearly unloaded over 10 seconds.

If the indent landed on a scratch, inclusion, grain boundary or other uneven surface, the load displacement curve did not appear normal. Examples of a good indent and a bad indent are shown in Figure 4.38. Bad indents were identified from an unusual load displacement curve, or from an image of the indented surface. The

(a) TriboIndenter (b) Berkovich tip

Figure 4.36: Hysitron TriboIndenter nano-indentor[9] and Berkovich indenter[9]

TriboIndenter is capable of an imaging technique known as scanning probe microscopy (SPM) in which the intender tip is scanned across the specimen surface in a raster pattern. The height of the tip is controlled by a force feedback loop. SPM is able to generate images of both the topography and gradient of an indented region on a specimen surface, as shown in Figure 4.39. The bad indent, located near the center of the image, is clearly evident.

4.6.3 Results

Although each sample was cut from the same original piece of material, the bulk properties of each sample were measured. Fifteen indents were made into the bulk,

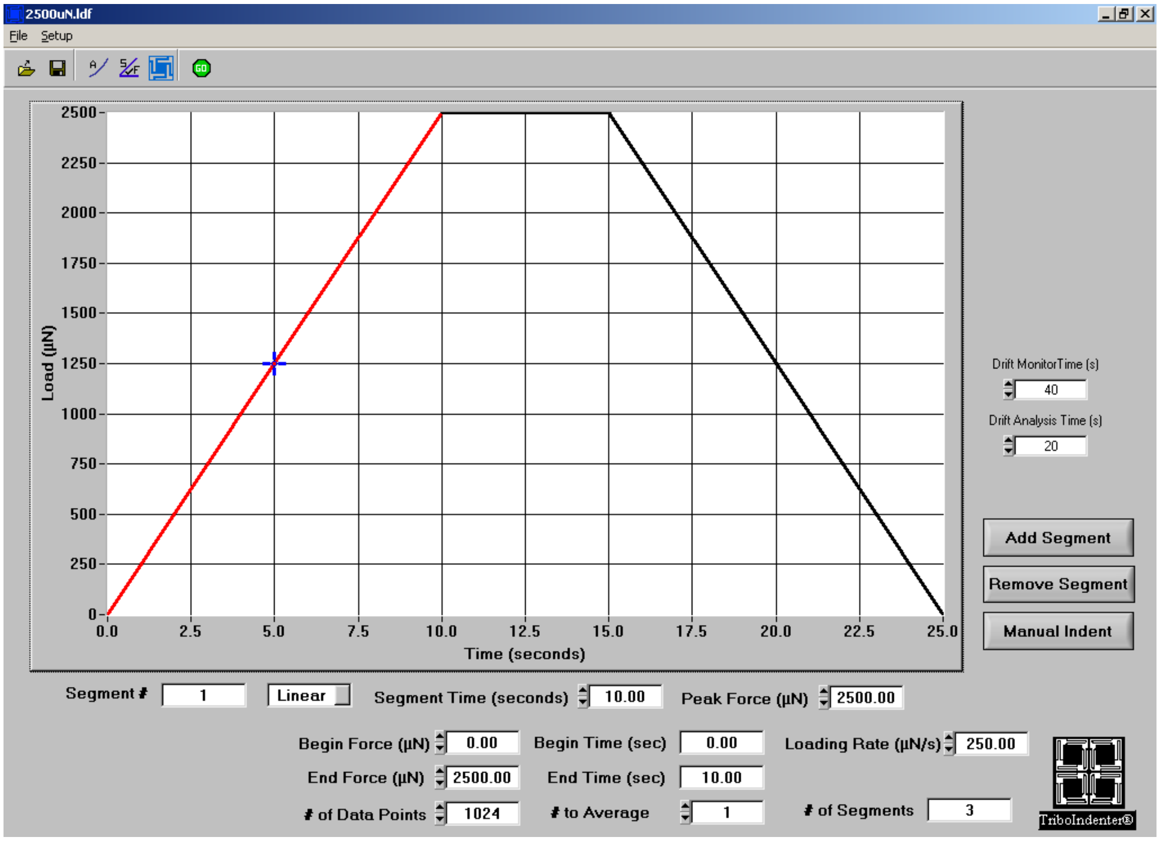

Figure 4.37: Load function for nano-indentation hardness tests

and the results are shown in Figures 4.40 and 4.41. As expected, there are no significant differences between samples. The average bulk reduced modulus is 195 GPA, which is near the quoted material value of 200 GPa for Inconel 718. The average bulk hardness was 6.62 GPa, although this value cannot be directly compared with the quoted bulk macro-hardness value of 95 HR_B. The data for each indent is available in Appendix E.

To examine the impact of the wire-EDM process on the samples, elastic modulus and hardness profile as a function of depth into the surface were generated, and can be seen in Figures 4.42 and 4.43, respectively. Note that the depth, or distance from edge values on the x-axis of each plot are in terms of the tapered section. The edge is defined as the interface between the recast material and the nickel plated layer. Data from indents nearer than 5 μm to the edge would include contributions from the nickel

Figure 4.38: Load-displacement curves demonstrating a good and a bad indent

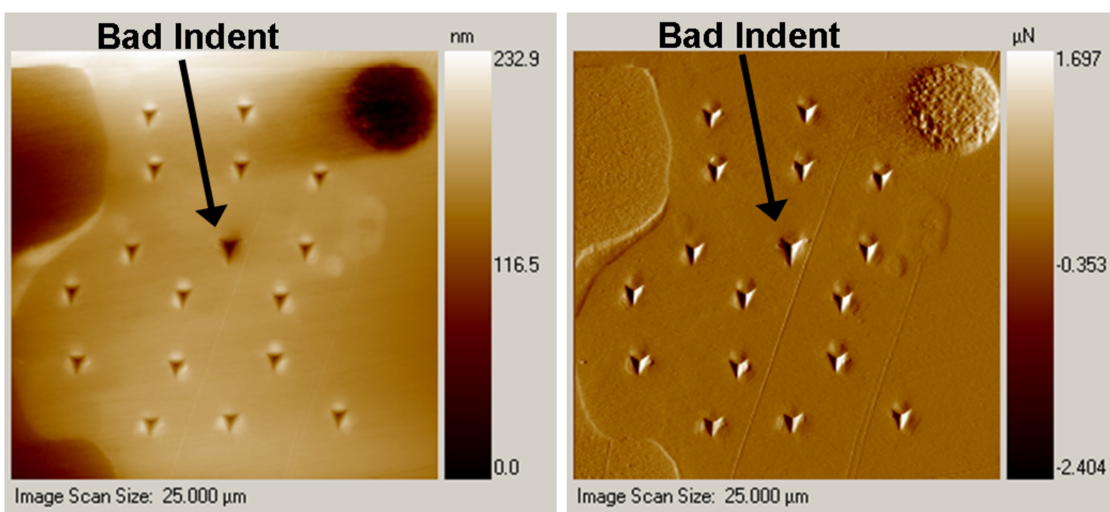

(a) Topography

(b) Gradient

Figure 4.39: Sample images from Sample 4 of specimen topography and gradient made using SPM, notice the difference between the good indents and the bad indent

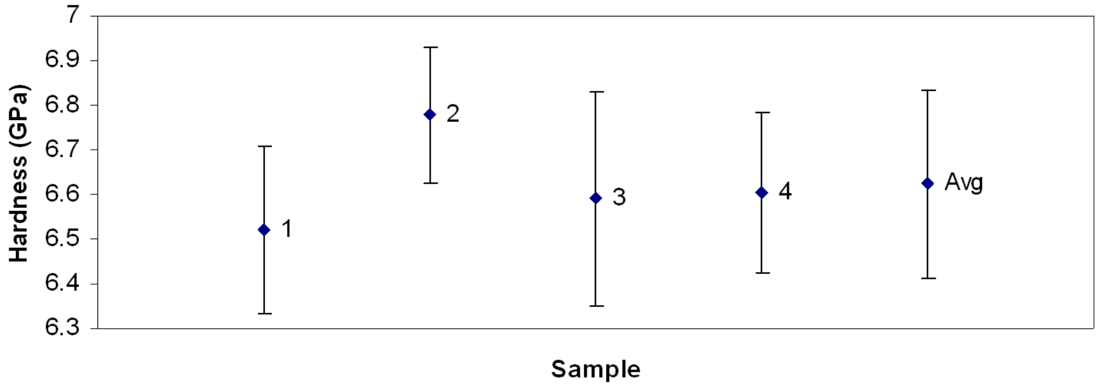

Figure 4.40: Sample to sample bulk hardness [GPa] nano-indentation tests

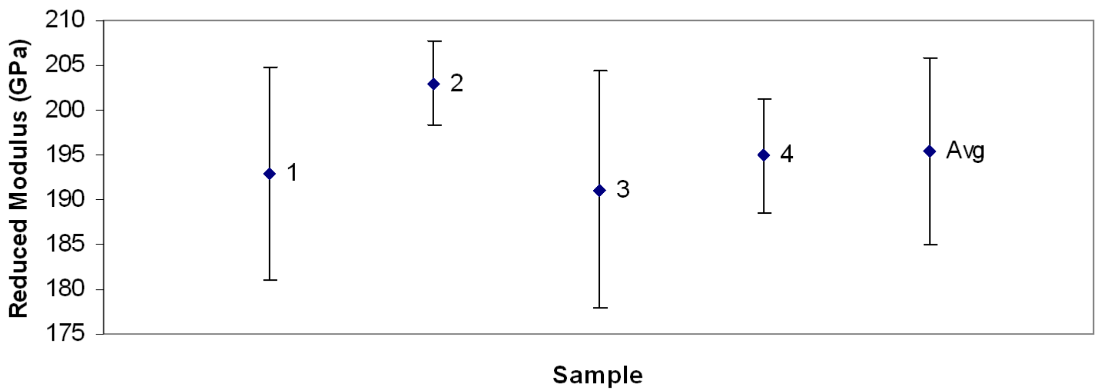

Figure 4.41: Sample to sample bulk reduced modulus [GPa] nano-indentation tests

and the mounting epoxy and consequently were not included in the analysis. Some degree of dispersion in the data is evident since nano-indentation hardness testing is very sensitive to any surface flaws, and further, the true nano-properties can vary from grain to grain. Consequently, a large number of indents were necessary. Between 140 and 200 indents were made on each sample, not counting any bad data points which were removed.

From Figure 4.42 it can be seen that every indent indicates a lower reduced modulus than that of the bulk. The average bulk reduced modulus, and average recast layer thicknesses are shown on the plot. It appears that Samples 3 and 4 demonstrate

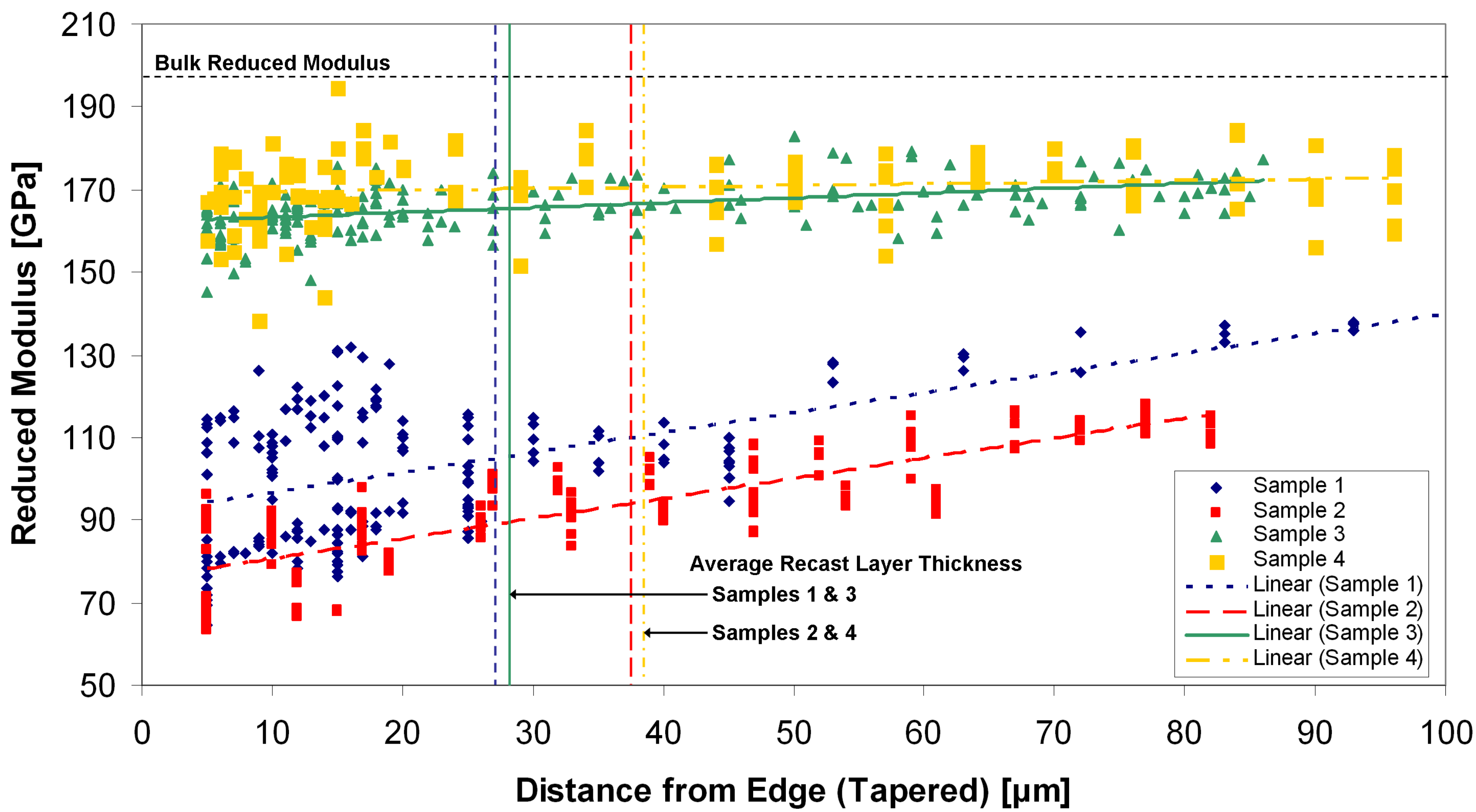

Figure 4.42: The reduced modulus [GPa] depth profile in all samples

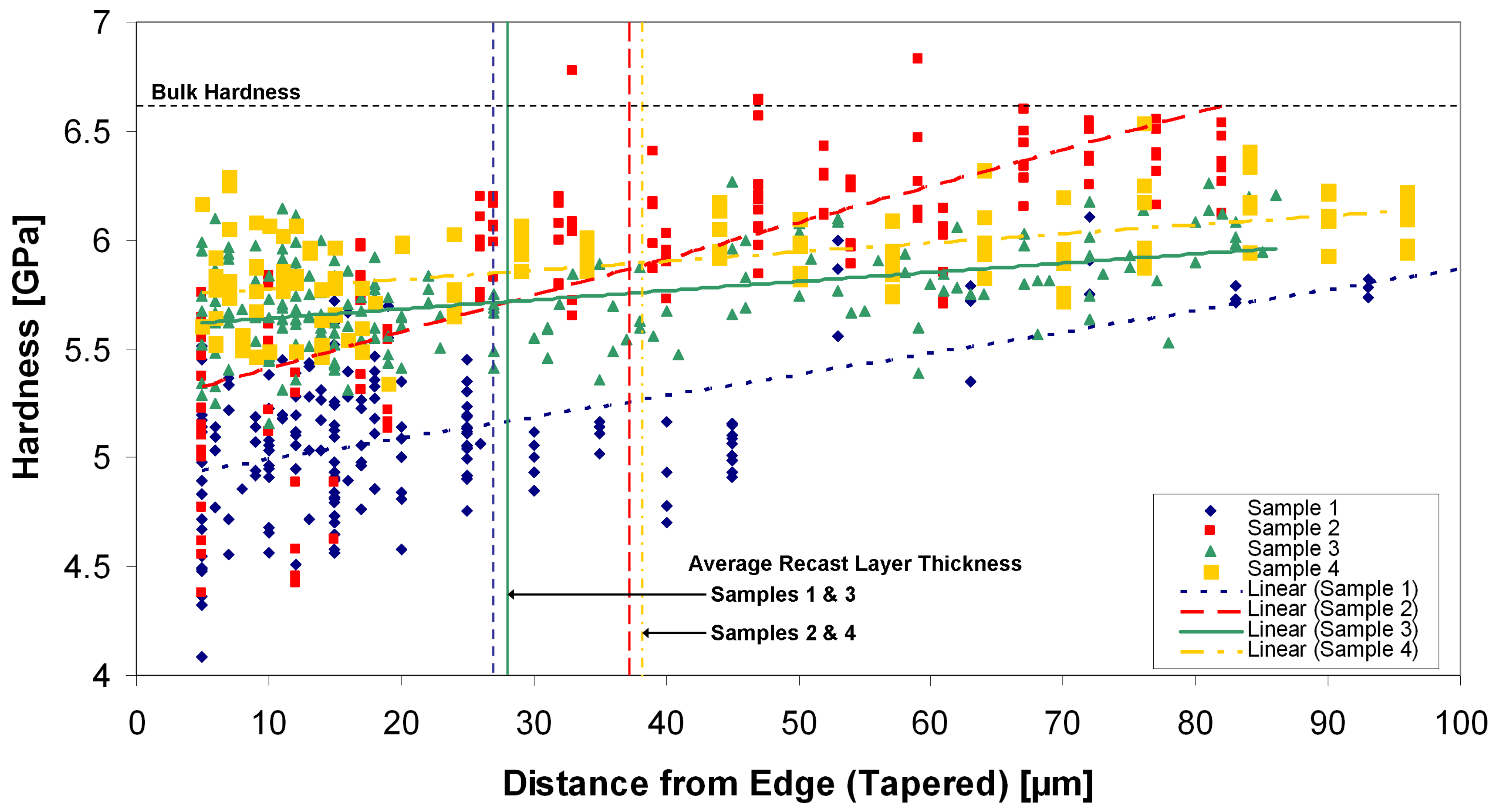

Figure 4.43: The hardness depth [GPa] profile in all samples

a distinctly higher reduced modulus than Samples 1 and 2. The linear trend line for each sample is plotted, and each exhibits an increasing trend as the distance from the edge of the sample increases. This indicates that the recast and sub-layers are reduced in elastic modulus by wire-EDM. The hardness, shown in Figure 4.43 displays a similar trend. Again, the bulk hardness and average recast layer thicknesses are indicated. The hardness of each sample possesses an increasing linear trend with distance from the edge; however, the large difference between Samples 1 and 2 and Samples 3 and 4 is not as apparent in this case. This analysis suggests that the wire-EDM process tends to soften the machined surface below the hardness of the bulk material.

To more thoroughly examine the properties of the recast layer itself, the data was analyzed by only considering the indents made within the average recast layer thickness of each material. A box plot of the reduced modulus within the recast layer of each sample and the bulk workpiece is shown in Figure 4.44. This type of graph conveys a description of the distribution of the data by displaying the range as a line, and a box from the first to the third quartile. The horizontal line through the box represents the second quartile, or median and a star represents an outlier. This figure clearly conveys that the recast layer in Samples 1 and 2 has a lower reduced modulus than Sample 3 and 4, and that all four recast layers have a lower modulus than the bulk. Samples 1 and 2 were cut on the wire-EDM with a 100 μm diameter wire, while Samples 3 and 4 were produced with a 250 μm diameter wire. The wire diameter factor has not been identified as having a significant effect on recast layer thickness or residual stress, although it does have a slight effect on surface roughness. It is unknown why it has such a pronounced effect on the reduced modulus.

A box plot of the hardness in the recast layer of each sample and the bulk workpiece is displayed in Figure 4.45. While the recast layer hardness values are more clustered together, all four are less than in the bulk workpiece material. It has been

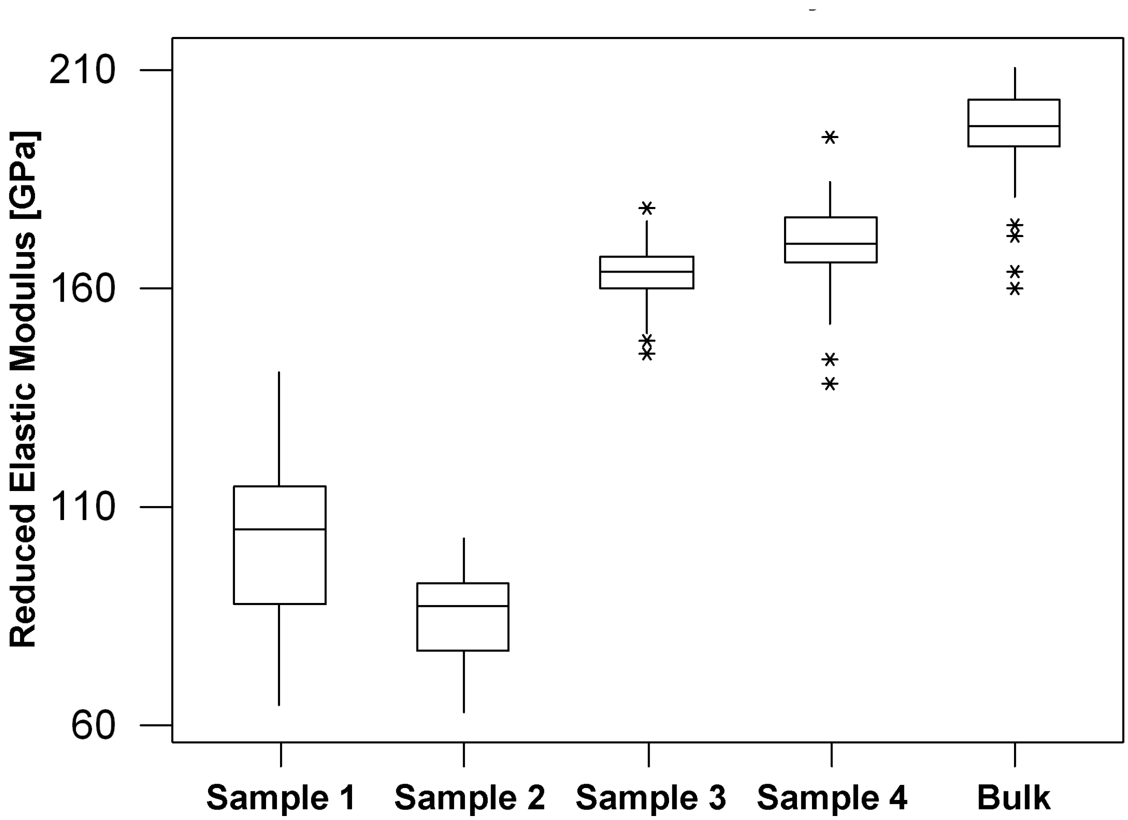

Figure 4.44: The reduced modulus [GPa] in the recast layer versus the bulk material

reported that a dielectric exhibiting high conductivity can lead to electrolysis which may soften the wire-EDM cut surface [31]. However, to preclude this possibility, the conductivity of the dielectric was maintained at a reasonable level throughout the experimentation performed in this thesis. The drop in hardness could be due in part the metallurgical changes in the recast layer uncovered in EPMA. The depletion of chrome, nickel and molybdenum and the addition of copper and zinc would conceivably lower the hardness of the recast layer. Additionally, it is well established that tensile residual stresses can lower the measured hardness of a material [87]. To examine this possibility, hardness in the recast layer has been plotted against surface residual stress in the table feed direction in Figure 4.46. Note that as the tensile residual stress increases in magnitude, the hardness value decreases. This effect has

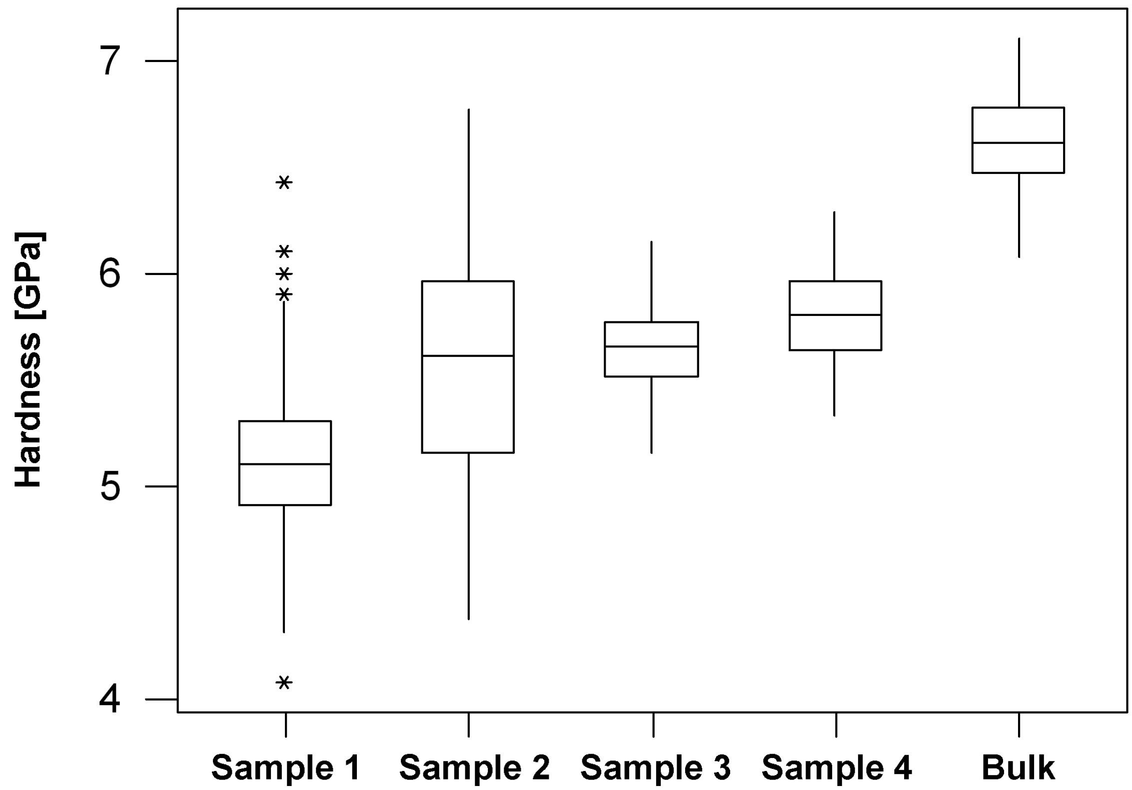

Figure 4.45: The hardness [GPa] in the recast layer versus the bulk material

also been documented when using a Berkovich tip in nano-indentation hardness testing. By decreasing the slope of the initial loading curve, tensile residual stresses tend to increase the total indentation depth. Consider a small element of material directly below the indenter tip. The presence of tensile residual stresses will increase the maximum shear stress in this element. A greater shear stress will therefore lead to a greater amount of plastic deformation and a larger indentation depth. For a constant load, a deeper indent results in a lower hardness measurement [88].

It can be concluded that, for the range of process parameters examined here, the recast layer formed during wire-EDM of annealed Inconel 718 is lower in both elastic modulus and hardness than the bulk material. However, these findings are in contrast to what has been reported for wire-EDM of solution treated and aged Inconel 718 [51, 37]. A direct comparison from the current findings to these two reported cases

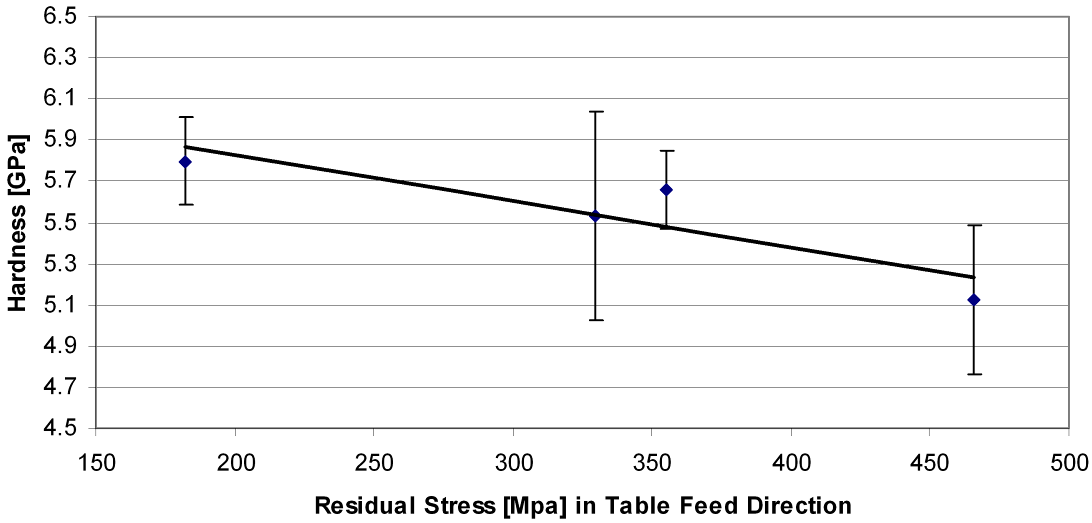

Figure 4.46: The hardness [GPa] in the recast layer versus residual stress [MPa] in the table feed direction

may be a dubious one since machining parameters were not reported in the earlier studies and different microstructures are undoubtably present after heat treatment. More experimentation must be conducted for this discrepancy to be further explained.

4.7 Summary

In this chapter the recast layer formed during wire-EDM of Inconel 718 was studied using several different methods. SEM photographs revealed that the wire-EDM cut surface was covered in pits and craters. A white-light interferometer was utilized to study the surface roughness. It was found that the RMS surface roughness increases mainly with increases in energy per spark, and to a much lesser extent with a larger wire diameter. Electron probe microanalysis revealed that copper and zinc from the wire electrode had migrated and alloyed with the recast layer. Additionally, some degree of chrome depletion was present. X-ray diffraction measurements showed the in-plane surface residual stresses to be tensile, and to decrease with increasing energy per spark. The difference in stress magnitude in the table feed direction and the wire-electrode axis direction was discussed. The tensile stresses were found to transition to compressive residual stresses at a depth between 15 and 20 μm into the cut surface. Lastly, nano-indentation hardness testing showed that the recast layer exhibited a lower modulus of elasticity as well as a lower hardness when compared with the bulk material.

CHAPTER V

RECAST LAYER REMOVAL

5.1 Goal & Approach

This chapter seeks to further investigate post-processing techniques for removal of wire-EDM induced recast layer in Inconel 718. The goal is not to completely develop a new method, but to apply existing methods to the particular situation examined in this thesis. Further, since it is assumed that recast layer removal is possible by utilizing numerous well known methods, a simple, low cost solution will be sought. In doing so, brief experimentation will be carried out, and from evaluation of the results recommendations will be made.

5.2 Selection of Post-Processing Technique

Numerous post-processing techniques were examined in Chapter II. In order to select one for further exploration, some aspects of each will be considered. Abrasive flow machining (AFM) is a capable and flexible process which is often used for recast layer removal. However, it requires large capital investment and a moderate amount of part handling. Abrasive micro-blasting is quick process; but, the effect on part dimensional accuracy is questionable. Internal features that cannot reached by the stream of abrasives may only experience a limited benefit from this method. Part handling would also be an issue. Electrochemical processes offer a possible solution. However, the various chemicals required for this process may present a problem for a shop not equipped for chemical handling, storage and disposal. Combined electrochemical EDM processes are still limited to the academic realm. Although environmental concerns are present with any of the methods discussed, they are particularly salient to electrochemical processing. Loose abrasive media finishing is a well established, traditional finishing technique. Several types are practiced. While material removal rates are lower than what can be achieved with other processes, parts can be mass finished. Capital investment can range from small to large, depending on the scale. The range of internal feature surfaces which can be finished is dependent on the abrasive size and shape. Shot peening can improve the surface integrity of EDM cut surface. However, it is only a cold working process, and thus recast material is not removed.

Table 5.1: Summary of post-processing techniques

Process	Proven for Recast Layer Removal	Positive Aspects	Negative Aspects
Abrasive flow machining	Yes	Established, Controllable, Internal finishing	Expensive, Part handling
Abrasive micro-blasting	Yes	Quick, Inexpensive,	Uncontrolled, Part handling, Geometry limitations
Electrochemical processes	Yes	Proven	Chemicals, Environmental
Loose abrasive media	No	Well established, Mass finishing	Slow
Shot Peening	No	Established	No material removal

Table 5.1 summarizes the aspects of each type of post-processing. Each method required some amount of consumables. It was decided that loose abrasive media finish would be selected for further exploration for the following reasons: it is a common well-known process; it is a material removal process although it has not been reported in literature as a recast layer removal tool; small machines are inexpensive; it is a mass finishing process. Of the three loose media finishing processes, vibratory finishing was selected because it finishes faster than than barrel tumbling, and the equipment costs an order of magnitude less than centrifugal finishing equipment [5].

5.3 Vibratory Tumbling

After hand deburring, vibratory tumbling is the most popular mass finishing technique. There are two types of vibratory tumbling: tub and bowl. In tub-type vibratory finishing, the parts and media are placed in a open tub mounted on springs. In bowl-type, the parts and media are placed in a toroidal bowl, also mounted on springs. In either type, an eccentric weight on a motor shaft causes the vibrations [5]. In practice the selection of which type of vibratory tumbler to use should be based on part geometry. Smaller parts are more efficiently processed in a bowl-type tumbler while large, bulky or long parts dictate a tub-type vibratory tumbler [89]. Most smaller, less expensive vibratory tumblers are of the bowl-type. Consequently, the bowl-type was selected for these experiments. The motion of parts and media inside a bowl-type vibratory tumbler is shown in Figure 5.1. It can be seen that the parts and media are continually moving about the bowl, ensuring an even finish.

5.4 Experimental Procedure

5.4.1 Experimental Set-Up

To test the use of vibratory tumbling as a finishing process for removal of wire-EDM recast layer, a small bowl-type vibratory tumbler was purchased. The particular model selected was the Ultra-Vibe 18 "Thumbler's Tumbler" from True-Square Metal Products. It has a polyelthelene bowl with a 5.7 liter capacity. Two small experiments were designed to evaluate recast layer removal for parts cut with either the 100 μm or the 250 μm diameter wire.

5.4.2 250 μm Wire Samples

The first test with the vibratory tumbler was to observe the finishing of a part cut with the 250 μm diameter wire. Ten 25.4 mm by 25.4 mm samples were cut from the same 3.962 mm thick sheet of Inconel 718 used in Chapter III. Each was cut

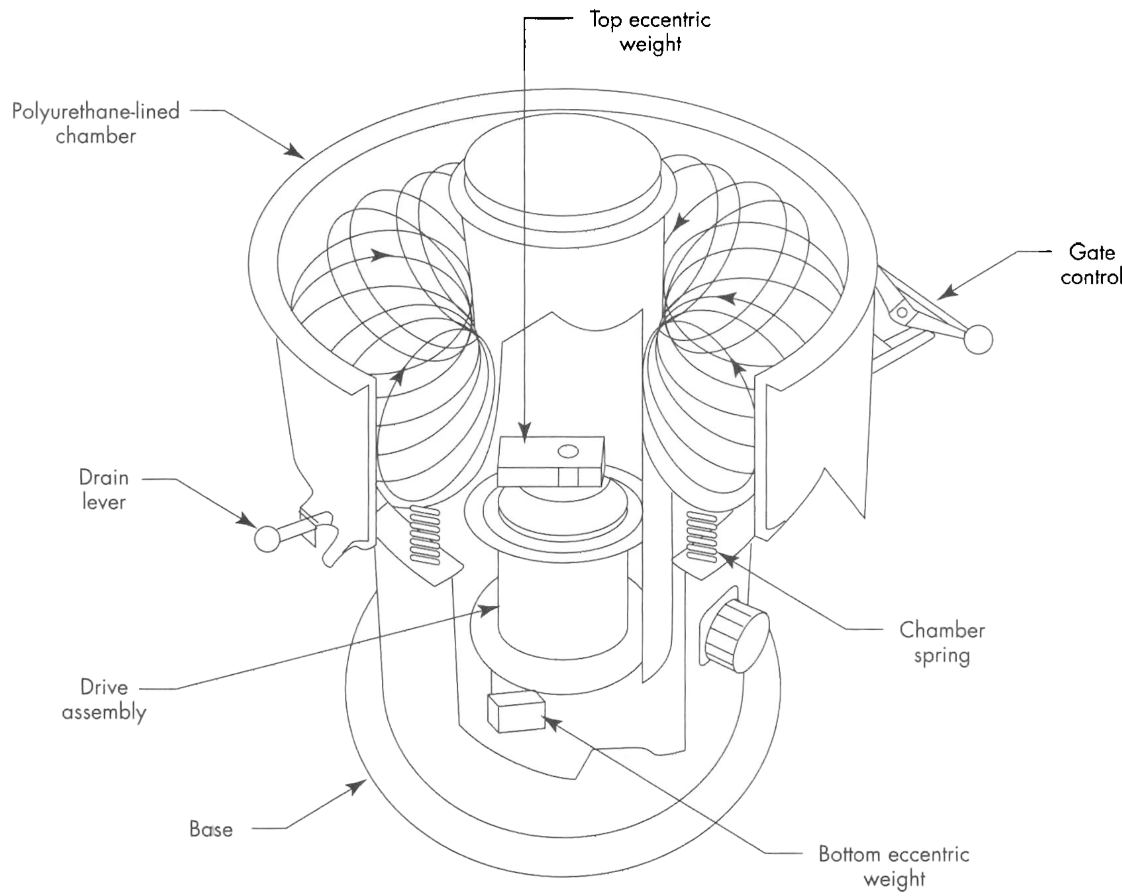

Figure 5.1: Motion of parts and media in bowl-type vibratory tumbler [5]

with the machine setting found to impart the greatest average recast layer thickness (table feed rate: 1.969 mm/min, spark cycle: 28 μs, spark energy: 12). These settings were found to result in a average recast layer 8.51 μm in thickness. More detailed information regarding these settings can be found in Table 3.6.

The abrasive media chosen for these tests were preformed ceramic media containing aluminum oxide. Coarse 22° ended cylinders, Figure 5.3 and 5.4, were chosen because they are both relatively small and are commonly used in industry. In addition, 90 ml of liquid cleaner and rust inhibitor were diluted in 3.8 liters of tap water for use with the media.

The specimens were placed in the vibratory tumbler, along with approximately 1.6 liters (4.5 kgs) of abrasive media and 260 ml of diluted cleaner. The length and width

Figure 5.2: Ultra-Vibe 18 bowl-type vibratory tumbler

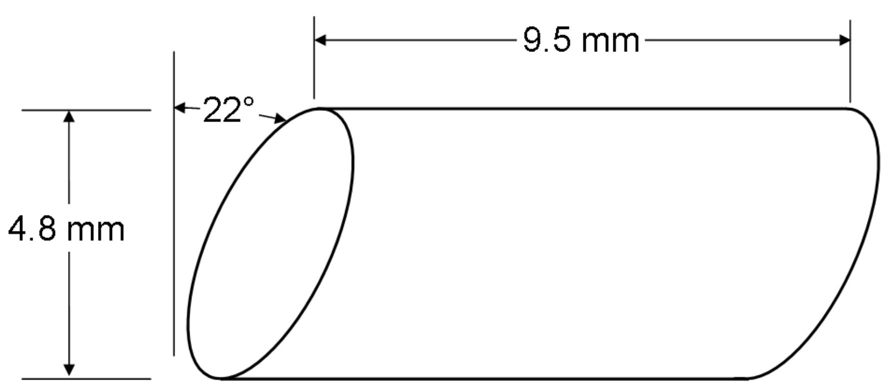

Figure 5.3: Coarse 22° ended cylinder preformed abrasive vibratory tumbling media

Figure 5.4: Photograph of coarse 22° ended cylinder preformed ceramic abrasive vibratory tumbling media

of the specimens were initially checked with a micrometer, and periodically afterward. The average material removal is shown in Figure 5.5 and the raw data collected is given in Appendix F. It can be seen that the cutting rate drops immediately off in a dramatic fashion. In total, 26 μm were removed from the width. Thus, 13 μm were removed from each side, which is greater than the recast layer thickness of 8.51 μm. However, these values are average values and to see the actual extent to which the recast layer was removed the specimen must be observed through metallography. Note that at the conclusion of the experiment, all of the abrasive media were replaced to check that the media had not worn. Several of the samples were tumbled for an additional hour with the new media, but no measurable material was removed. This indicates that the severe decrease in rate of dimensional change in the specimens was not due to the media having dulled or glazed. Since the wire-EDM surface is rough and cratered, it is suspected that the part dimensions changed rapidly as the surface peaks were removed, leaving a flatter surface behind. The overal material removal rate may not have decreased as rapidly as Figure 5.5 would indicate.

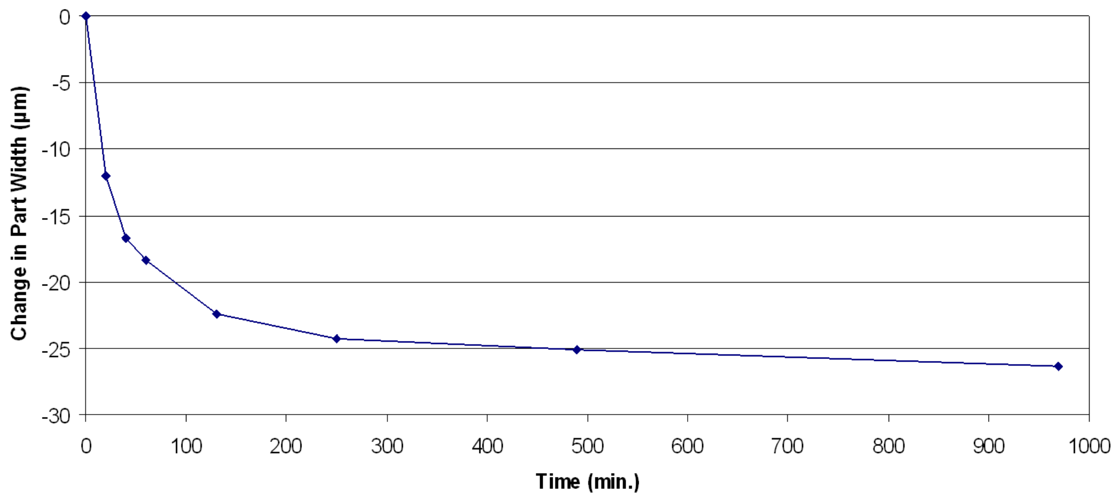

Figure 5.5: Average change in specimen size [μm] for parts cut with 250 μm diameter wire

A specimen was cut from one of the tumbled samples, and was prepared metallographically as described in Chapter III. An example micrograph of this specimen is shown in Figure 5.6. Recast material is still evident between the sample and the nickel plated layer. Notice how smooth and even the surface is compared to an untumbled sample cut generated under the same wire-EDM parameters, as shown in Figure 5.7. Surface roughness measurements of the manner described in Section 4.3 were conducted on the wire-EDM cut and vibratory tumbled surface of the original sample. These were found to exhibit an RMS surface roughness of 1.34 μm. This represents an improvement from the untumbled samples, which yielded an RMS surface roughness of 3.42 μm. The data from these measurements are given in Appendix C. The average recast layer thickness of the tumbled sample is 4.46 μm with a standard deviation of 0.68 μm. Thus the for the given cutting conditions, nearly half of the recast layer material was removed and the surface roughness was clearly improved. Although this experiment was only partially successful, refinement of the vibratory tumbling parameters may enable the complete removal of the wire-EDM imparted recast material. All of the recast layer thickness measurements in this chapter can be found in Appendix B.

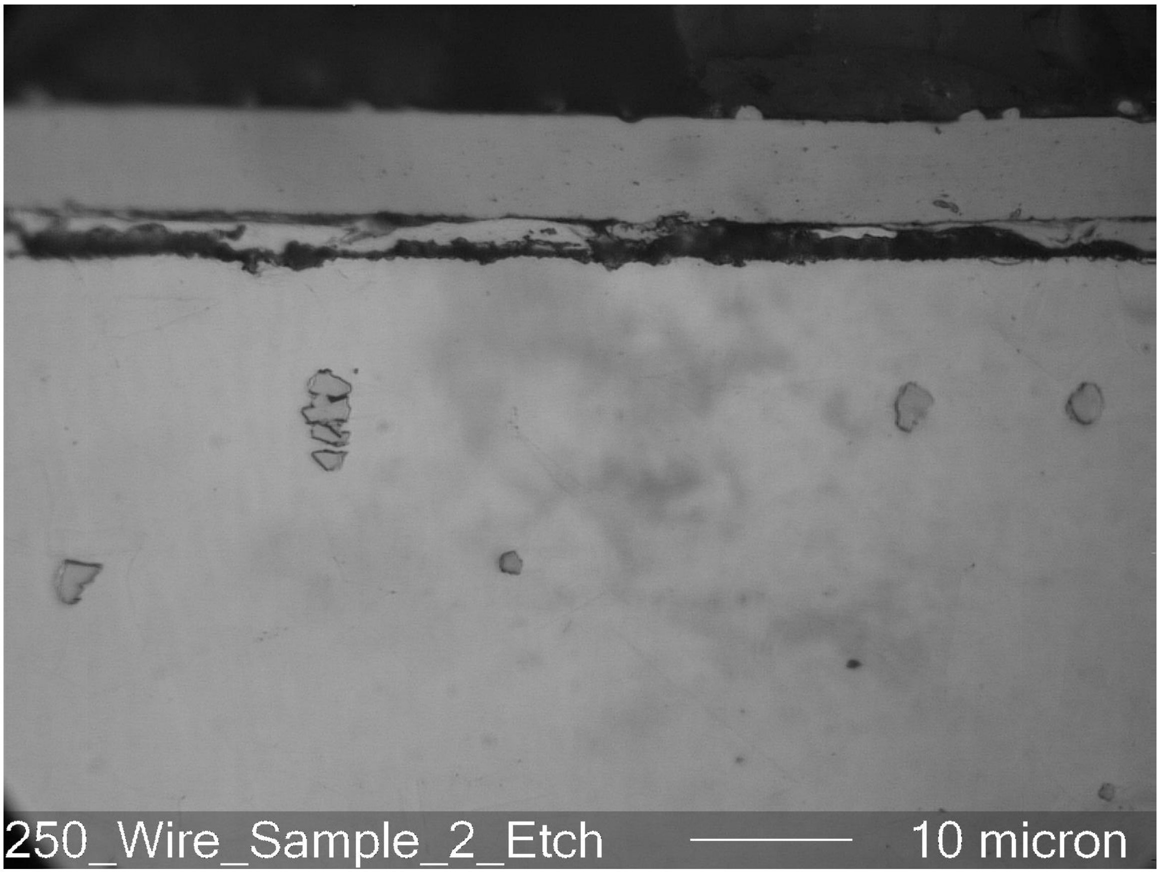

Figure 5.6: 1000X micrograph of etched specimen from vibratory tumbled sample cut with 250 μm diameter wire (average recast layer thickness: 8.51 μm)

5.4.3 100 μm Wire Samples

Next, the feasibility of post-processing parts with small features was examined. The 100 μm diameter wire was used to cut the half-gears shown in Figure 5.8 on the wire-EDM. The cuts were again made at the conditions yielding the largest average recast layer thickness (table feed rate: 1.969 mm/min, spark cycle: 16 μs, spark energy: 4).

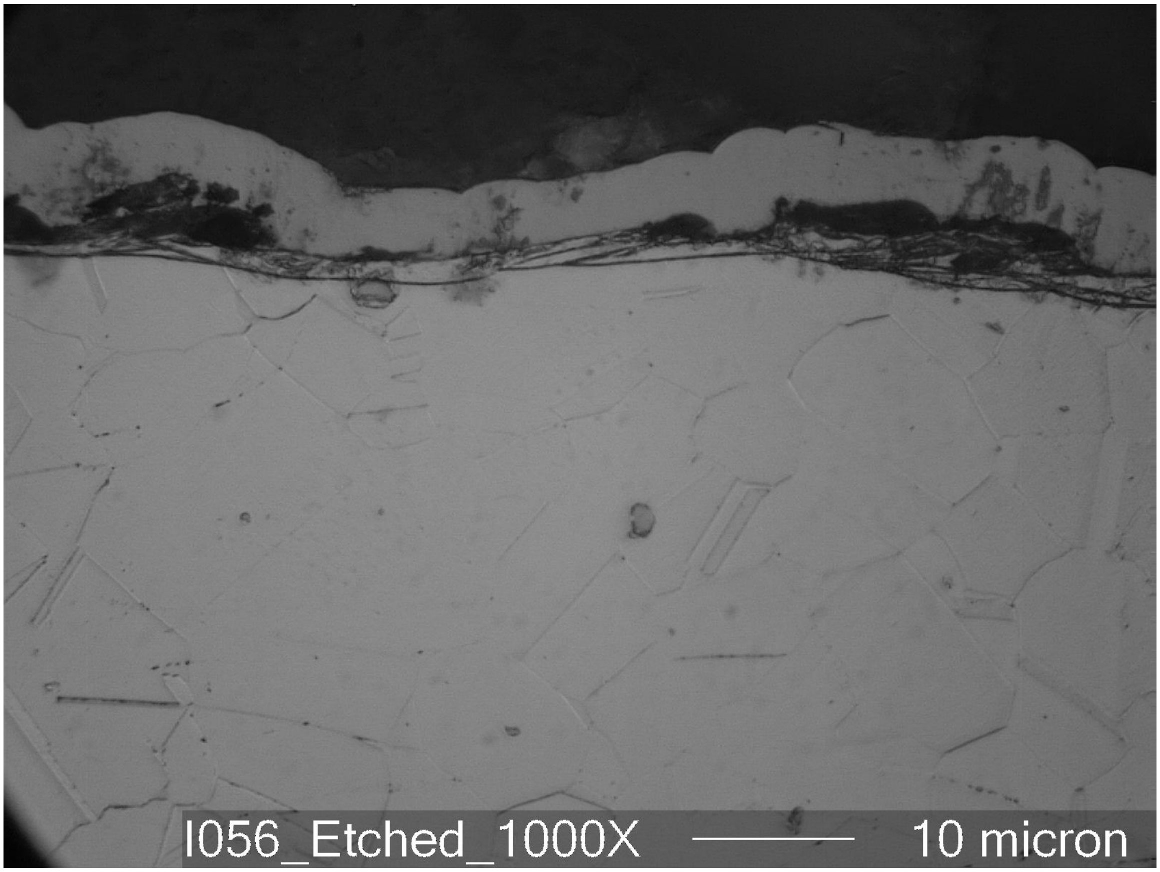

Figure 5.7: 1000X micrograph of etched specimen cut with 250 μm diameter wire before vibratory tumbling (average recast layer thickness: 4.46 μm)

The chosen part geometry will allow the effectiveness of this finishing technique on both flat surfaces and small features to be studied. The roots of the gear teeth have a radius of 75 μm, and thus the media used in the previous experiment will not be adequate. To reach the entirety of the feature, a smaller abrasive was necessary. 1200 grit 99.5% pure white aluminum oxide (AL_2O_3) was chosen. It is the smallest grain sized aluminum oxide generally available, with an average diameter of 3 μm. This abrasive is typically used for making lapping compounds.

A test was first conducted with 2.2 ℓ of abrasives and 1 ℓ of diluted liquid cleaner. It was hoped by the author that a slurry would form, however, the abrasive grains separated from the liquid to form a thick, sticky sludge. The parts and media were held together by surface tension and did not move about in the bowl at all. Consequently,

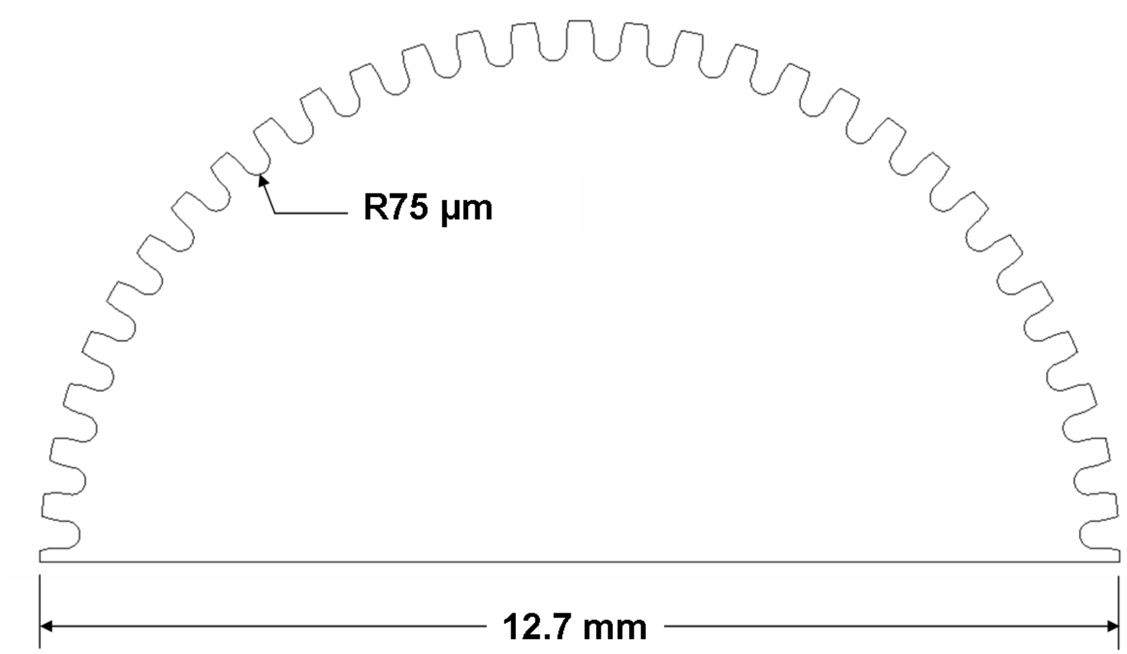

Figure 5.8: Profile of half-gear cut with 100 μm diameter wire

the experiment was aborted after four hours and repeated without any liquid cleaner. Tumbling without the liquid cleaner was acceptable since Inconel 718 is resistant to rust and oxidation. For other alloys this may not be the case and consequently some form of rust inhibition would be necessary.

Throughout the experiments, the thickness of the half-gears was periodically checked with a micrometer. The specimen tumbled in the media and liquid cleaner mixture did not display any material removal. After nearly 6 days of tumbling, only 3 microns of material had been removed from the half-gear which was "dry" tumbled. Nonetheless, the samples were metallographically prepared to quantify recast layer removal. The half-gear which was finished in the aluminum oxide and liquid cleaner demonstrated an average recast layer thickness of 7.4 μm and a standard deviation of 2.94 μm. This represents an insignificant difference from the unfinished recast layer thickness of 8.07 μm.

A sample micrograph of the flat side of the dry finished half-gear is shown in Figure 5.9, while the root of a gear tooth is shown in Figure 5.10. Notice that the

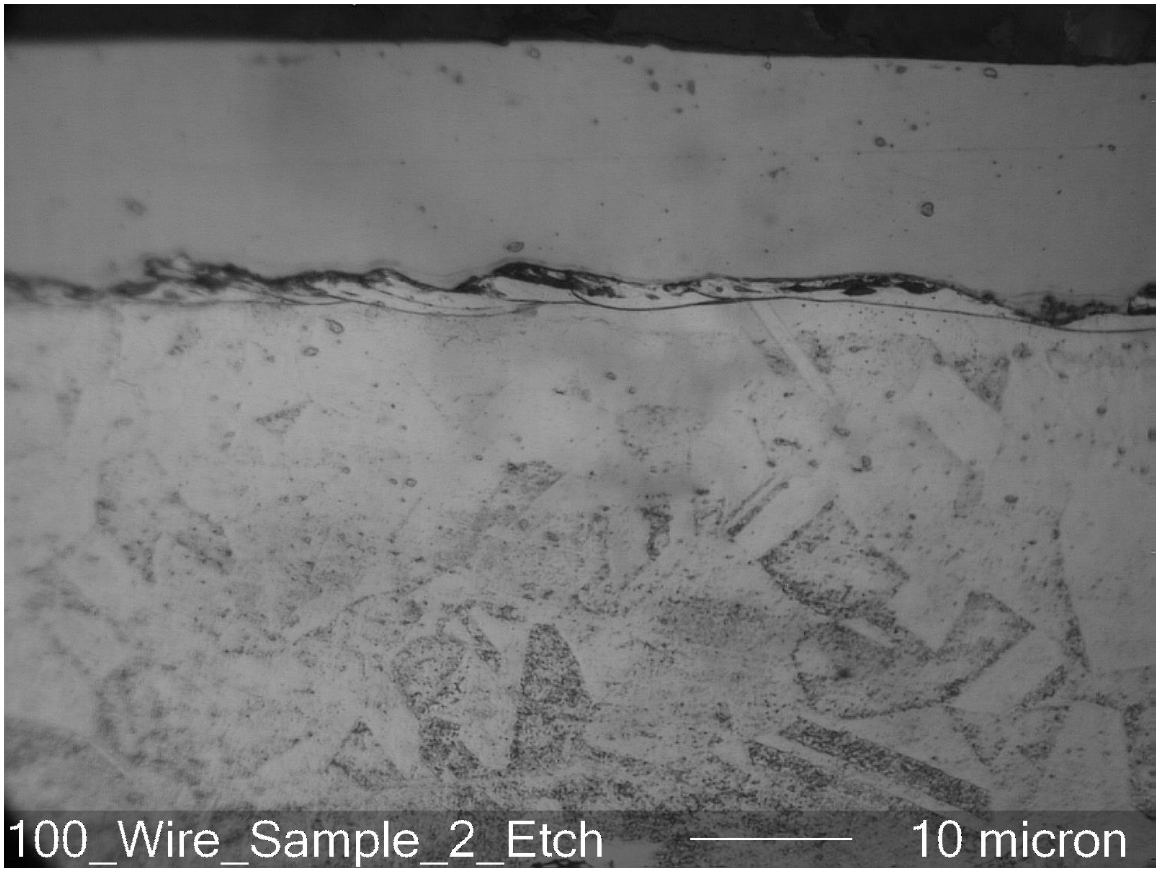

Figure 5.9: Micrograph of the flat edge of the dry vibratory tumbled half-gear (average recast layer thickness: 4.22 μm)

surface of the recast material is not as smooth as the parts finished with the much larger preformed ceramic abrasives. However, it can still be seen that some material was removed. In fact, the average recast layer of the flat side was measured to be 4.22 μm with a standard deviation of 0.81 μm. This does represent a significant removal of recast layer. The average recast layer thickness at the roots of the gear teeth was measured to be 4.39 μm with a standard deviation of 0.83 μm. Again, this is a significant decrease in the amount of recast material. These tests were not completely successful, but it was demonstrated that vibratory tumbling can be used to finish wire-EDM parts by removing recast layer material. The vibratory tumbler utilized in these experiments did not allow for adjustments to the frequency of vibrations, but higher frequency vibrations would be required to impart enough kinetic energy to the

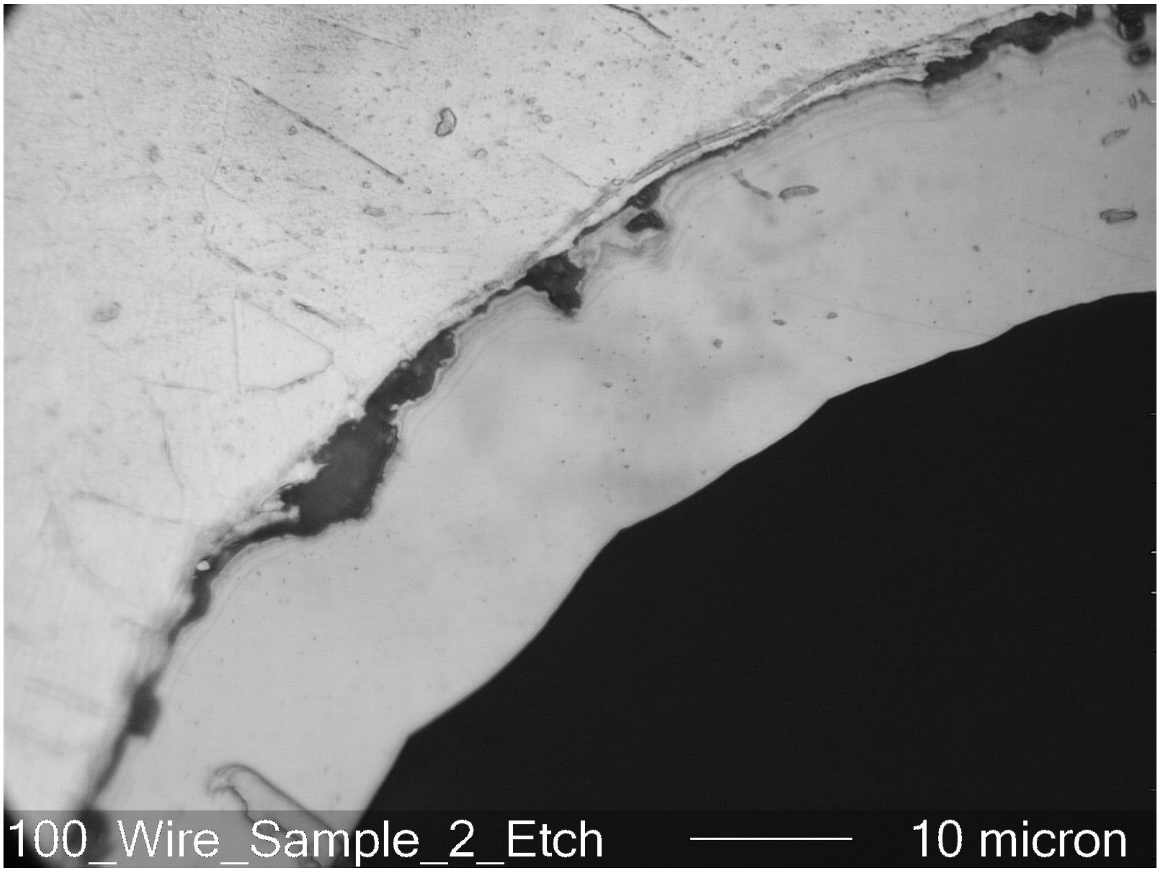

Figure 5.10: Micrograph of the root of a gear tooth of the dry vibratory tumbled half-gear (average recast layer thickness: 4.39 μm)

aluminum oxide grains to make material removal more feasible.

5.5 Summary

It this chapter, a simple and low cost technique for post-processing small wire-EDM cut Inconel 718 parts was demonstrated. A survey of existing post-processing techniques was taken. After examining the merits of each method, loose abrasive finishing was selected for examination. Within this category, vibratory tumbling was deemed the most likely method to deliver the stated goals. A small machine was purchased, and sample parts of Inconel 718 for finishing were wire-EDM cut with two different wire-electrode diameters.

The parts cut with the larger diameter wire electrode were tumbled with preformed ceramic abrasives. Although the recast layer was not entirely removed, it was reduced in thickness by nearly 50%, and the surface roughness was markedly improved. A half-gear was cut with the smaller diamter wire to examine vibratory tumbling for parts with small features. Loose 1200 grit aluminum oxide was the selected abrasive media. Again, it was found that some recast layer material was removed, however, surface roughness did not appear to have been improved.

These experiments represent a preliminary look into a post-processing technique for finishing of wire-EDM cut parts on improve surface integrity. The results showed promise, but more testing is necessary to make this finishing method feasible. With trial-and-error refinement of the process parameters, complete removal of the recast material using this simple, low cost method seems possible.

CHAPTER VI

CONCLUSIONS

6.1 Overview

In this thesis, recast layer formation during wire-EDM of the nickel base superalloy Inconel 718 was examined. It is well known that wire-EDM cut parts can demonstrate poor surface integrity, due in large part to the presence of the recast layer. This project detailed experiments conducted to study the effects of various process parameters on recast layer formation, different surface and mechanical characterizations of the recast layer and preliminary investigation of post-processing techniques for recast layer removal.

6.2 Experimental Findings

6.2.1 Recast Layer Thickness

A set of experiments was undertaken to find the effects of various wire-EDM process parameters on recast layer formation. A system for measuring the discharge current and voltage signals was implemented in an attempt to avoid machine specific findings. Four machine settings were examined: wire diameter, table feed rate, spark cycle and spark energy. Test specimens were first nickel plated, then mounted, polished and etched to reveal the recast layer. Average recast layer thickness measurements were made using images from an optical microscope. The following results were obtained:

- Average recast layer thickness was generally between 5 and 10 μm
- Average recast layer thickness tended to increase with increasing spark energy setting

- Increases of the spark energy setting increased energy per spark, peak discharge current, current pulse duration and open-voltage time

- Average recast layer thickness tended to decrease with increasing table feed rate

- Increases of the table feed rate increased sparking frequency

- The energy per spark appeared to be the driving factor in determining average recast layer thickness

- The wire diameter and spark cycle (voltage-off time) settings did not display a significant effect on average recast layer thickness

6.2.2 Characterizations

In order to fully understand the properties and effects of the recast layer, numerous characterizations were undertaken. These included SEM photographs, surface roughness measurements, EPMA, x-ray diffraction and nano-indentation hardness testing. The wire-EDM induced recast layer of annealed Inconel 718 demonstrated the following characteristics:

- An undulating, pitted and cratered surface morphology

- A surface roughness which increases mainly with energy per spark, and slightly with wire diameter

- The presence of copper and zinc which has migrated from the wire electrode

- Chrome depletion near the recast layer

- Tensile in-plane surface residual stresses which decrease with increasing energy per spark

- A transition from tensile to compressive residual stresses at a depth of between 15 and 20 μm from the wire-EDM cut surface

- A decreased hardness and elastic modulus compared with the bulk material, in contrast to what has been reported in literature for solution treated and aged Inconel 718

6.2.3 Post-Processing

The post-processing technique of vibratory tumbling was examined due to the combination of its performance, ease of use and cost. Brief experiments were conducted on different Inconel 718 specimens cut with two wire diameters. Although the experiments were not completely successful, the following results were found:

- Preformed ceramic abrasive media were able to remove some recast material from flat surfaces

- Fine grain aluminum oxide media were able to remove some recast material from small internal features

- With refinement of the process-parameters, vibratory tumbling has the potential to offer a simple and low cost finishing method for improving the surface integrity of wire-EDM cut parts

6.3 Future Work

The author recommends the following areas of future work relating to recast layer formation in wire-EDM of Inconel 718:

- More exhaustive experimentation should be conducted to yield greater in-processes recast layer minimization

- Experimentation should be conducted for Inconel 718 under various heat treatments, since, as the hardness characterizations demonstrated, heat treatment can have a significant effect on the characteristics of the wire-EDM induced recast layer

- More in depth characterizations of the residual stress and hardness should be made as a function of depth into the workpiece
- Vibratory tumbling process parameters should be optimized
- Experiments should be conducted with additional post-processing techniques

APPENDIX A

EXPERIMENTAL SET-UP

A.1 Method of Data Acquisition

This section describes the method used in this thesis for measuring the discharge current and voltage on a Brother HS-3100 wire-EDM.

A.1.1 Voltage Measurement

The method of voltage measurement is fairly straightforward. A Stack Electronics CP-209 voltage probe was connected to a socket head cap screw on the upper head, as shown in Figure A.1. This location is at the same voltage potential as the wire electrode. The ground lead was attached to a different socket head cap screw which was directly connected to the work table, also shown in Figure A.1.

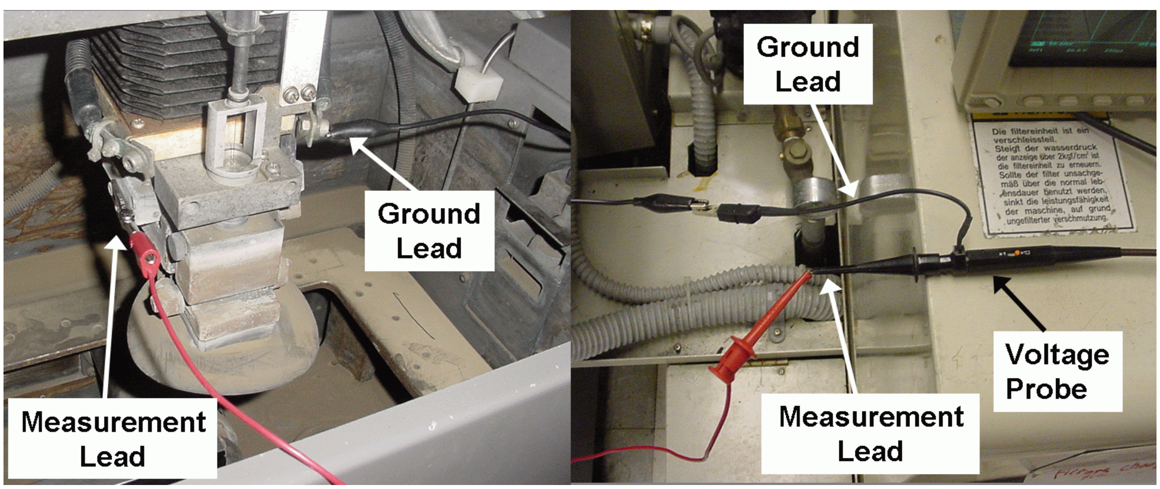

Figure A.1: Photograph indicating connection of voltage probe

A.1.2 Current Measurement

The technique utilized to measure the discharge current was considerably more involved. The current sensor chosen was a model 110 current monitor from Pearson Electronics, shown in Figure A.2. It has a usable rise time of 13 ns and is rated for a maximum peak current of 5000 Amps. This sensor measures the net current passed through it and outputs a proportional voltage signal.

(a) Top view (b) Front view

Figure A.2: Model 110 Pearson Current Monitor

The method given here requires access to the electrical cabinet in the back of the wire-EDM, seen in Figure A.3(a). Before opening the electrical cabinet, the hard power switch should be turned off as shown in Figure A.3(b). Figure A.4 displays the pulse generator of the wire-EDM. The arrows in the picture point out the twelve leads which go from the pulse generator to the brushes which charge the wire electrode. These wires have white labels reading 33HXX, where XX corresponds to the terminal location where it should be connected. The twelve wires with yellow labels reading 32HXX go to ground.

In order to pass the twelve white 33HXX leads through the current sensor, it was necessary to disconnect each of the white wires from the terminal, insert an additional length of wire from the end of the original white wire, pass it through the current

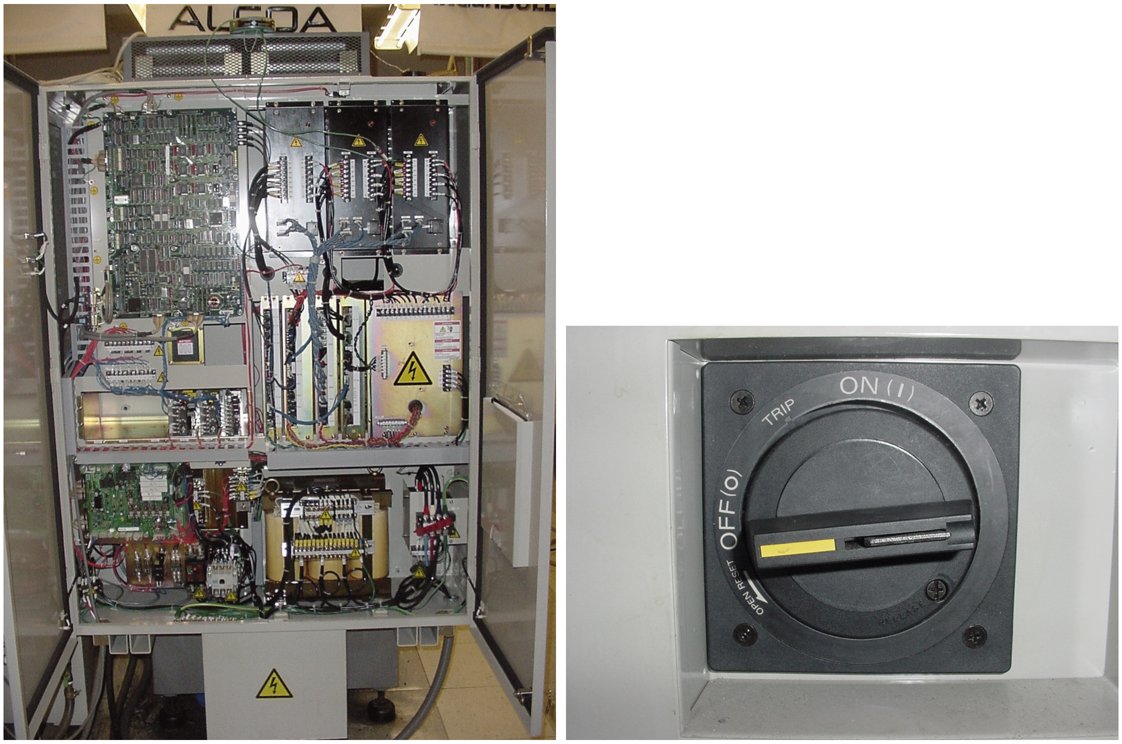

(a) Electrical cabinet (b) Hard power switch

Figure A.3: The hard power switch must be turned off before opening the electrical cabinet

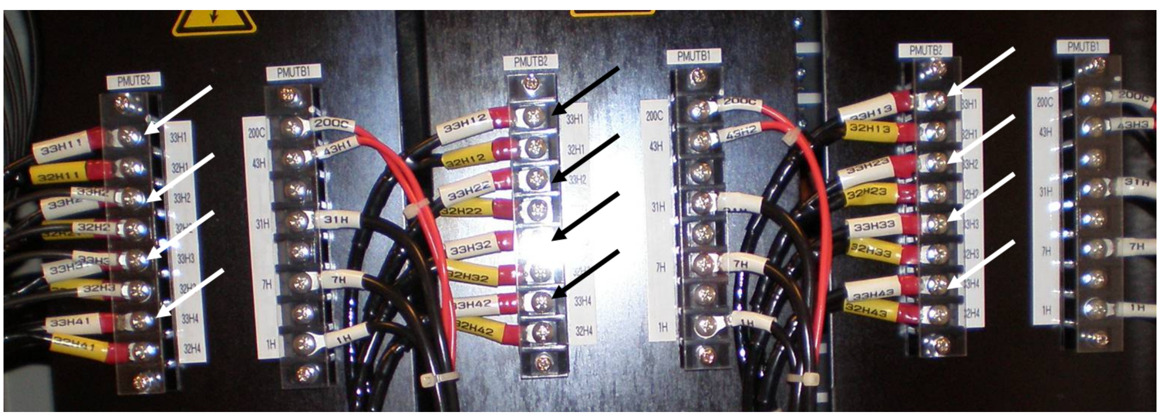

Figure A.4: Close-up of pulse generator, arrows denote leads going from pulse generator to brushes

sensor and connect it back to the terminal. This is shown for the case of the 33H13 wire in Figure A.5. Once the connection had been made, the exposed metal was wrapped in electrical tape, as seen in Figure A.6. This process was repeated for each of the eleven remaining leads, making sure that the current passes through the current sensor in the same direction for each lead, as shown in Figure A.7.

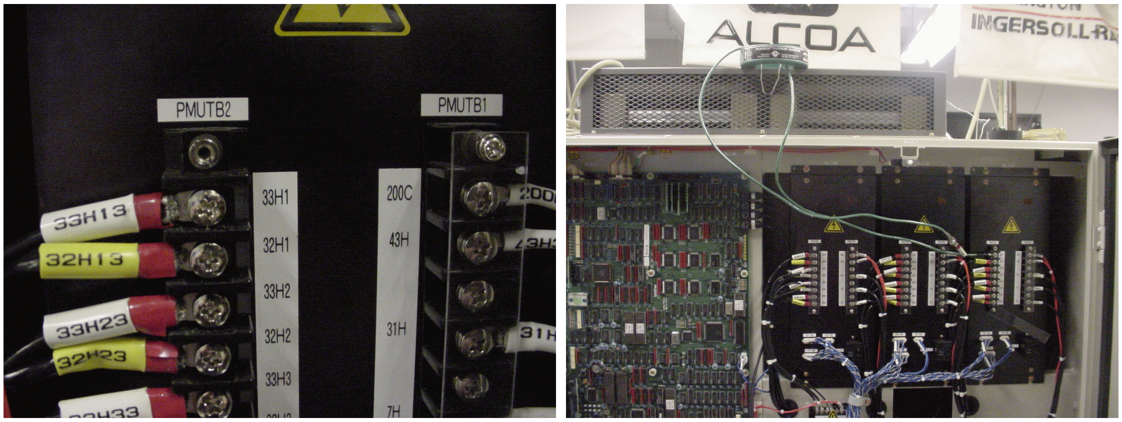

(a) 33H13 (b) New wire inserted

Figure A.5: A new wire is inserted so the current going through the 33H13 lead can be measured

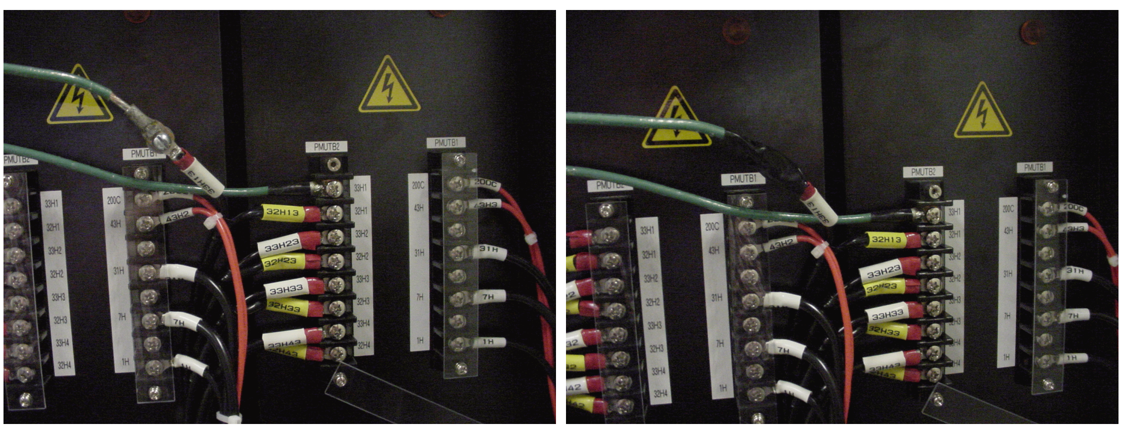

(a) Exposed connection (b) Insulated Connection

Figure A.6: Any exposed metal must be wrapped with electrical tape

Operation of the wire-EDM requires that the electrical cabinet doors remain open. Consequently, the safety switch shown in Figure A.8 must be disabled. It is imperative that the appropriate caution be taken due to the risk of electrical shock.

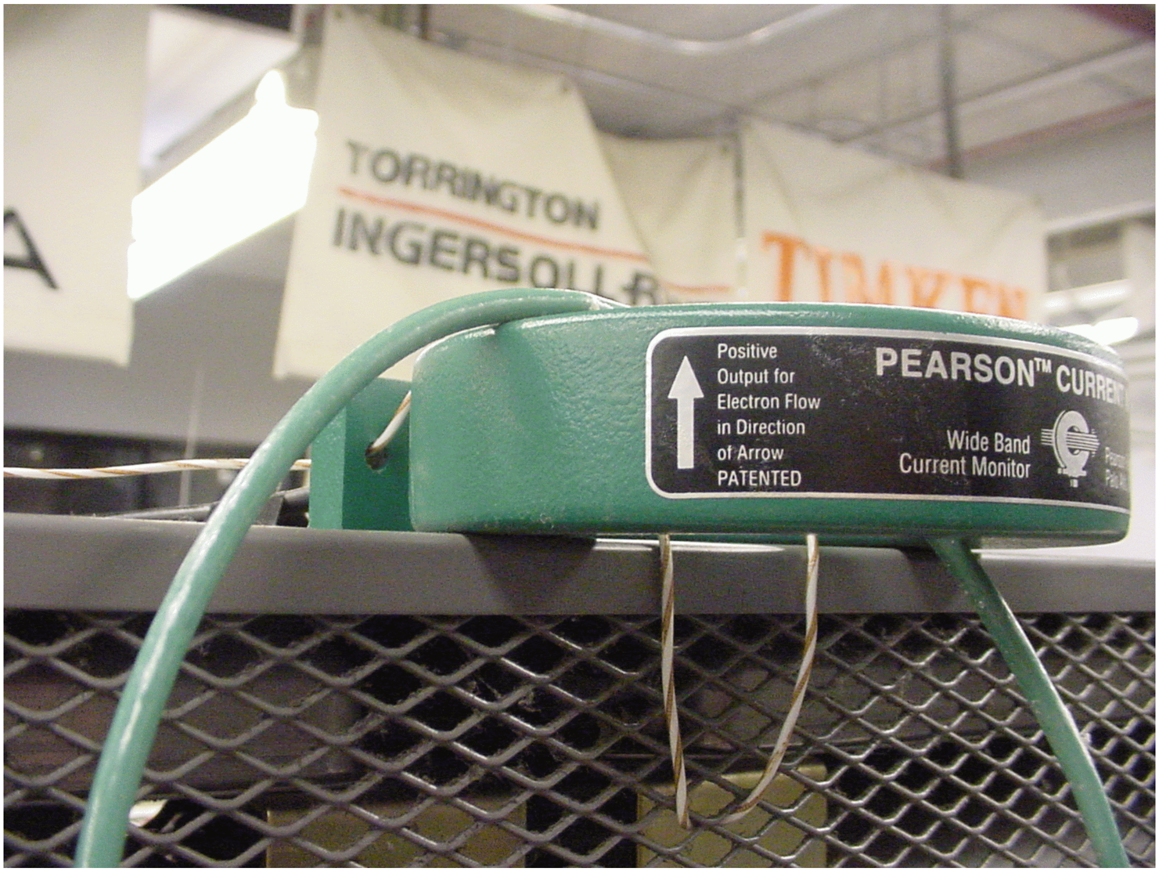

Figure A.7: All wires must be passed through the current sensor in the same direction

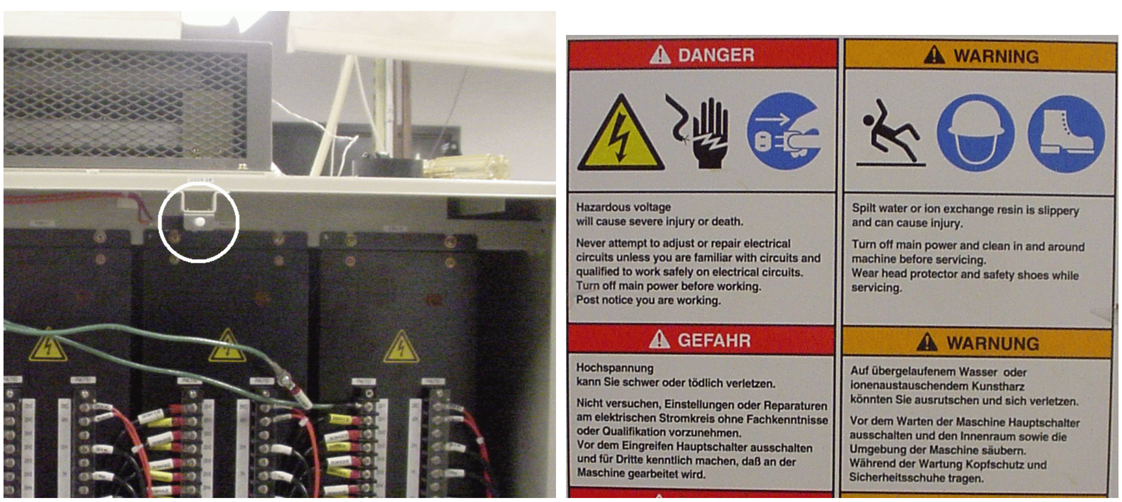

(a) Safety Switch

(b) Warning

Figure A.8: The safety switch must be disabled to operate the wire-EDM with the electrical cabinet open, so extreme caution must be taken

A.1.3 Oscilloscope

Due to the high bandwidth necessary to observe the current and voltage signals, the only system available to acquire the data was an oscilloscope. A Techtronix TDS420A 4-channel oscilloscope with a 200 MHz bandwidth was employed, and can be seen in Figure A.9. This particular model was able to store 30,000 data points at a time. By saving the data on a 3.5 inch floppy disk, these files could be transferred to a PC for analysis.

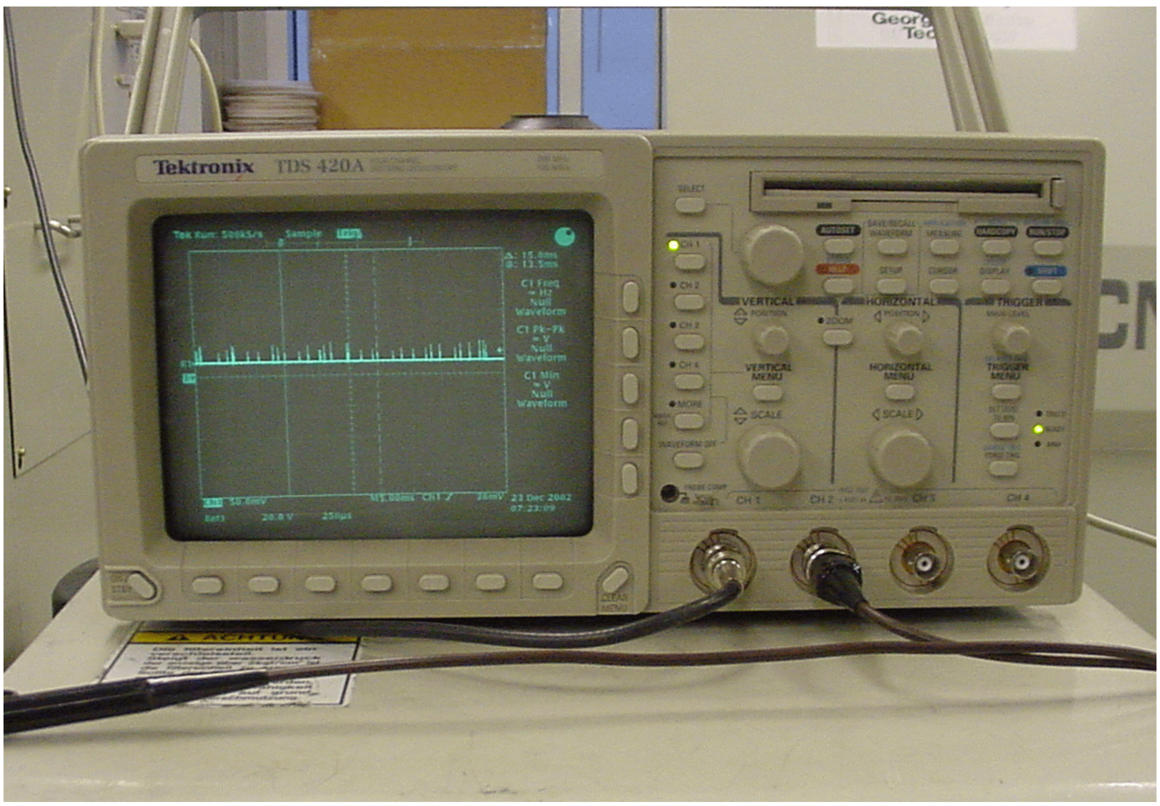

Figure A.9: Techtronix TDS420A 4-channel oscilloscope

A.2 Data Analysis

A Matlab script was written to analyze each dataset and output the average signal parameters, as well as generate plots of the current, voltage, energy and power. The code of the script is shown below.

```
%Thomas R. Newton
%06/18/2007

%This program will take time, discharge current and discharge voltage
%data from the Brother HS-3100 Wire-EDM and analyze it.

clc
clear all

tic

%Assume "Data" is a 3 column .csv file containing time, current and
% voltage.

%Set directory
FR = 875; %0.0775 ipm = 775
SC = 16; %16.0 us = 16
SE = '8';

directory = strcat( 'R:\Melkote\TNewton\Micro_Wire_EDM_Research...
\Waveforms\Experiments\04 wire\New_DOE\3\FR_0', num2str( FR ),...
 '_SC_', num2str( SC), '_SE_', num2str( SE ), '\' );

csvfile = strcat( 'FR-0', num2str( FR ), '-SC-', num2str( SC),...
 '-SE-', num2str( SE ) );
load_data = strcat( directory, csvfile,'.csv' );
```

```
data = importdata( load_data );

%set increment for plots and total number of data points to look at
increment = 2000;
total = 30000;

%find speed
file_char = double( csvfile );
feed_rate = char( file_char( 5 ) );
if feed_rate == '7'
    feed_rate = 0.0775; %in/min
elseif feed_rate == '8'
    feed_rate = 0.0875; %in/min
else
    fprintf( 'Unknown Feed Rate!\n' )
end


%Separate columns
time = data( :, 1);
if abs(mean( data( :, 3 ) )) > abs(mean( data( :, 2 ) ) )
    voltage = -data( :, 3 );
    current = data( :, 2 );
else
    voltage = -data( :, 2 );
    current = data( :, 3 );
end


%Scale columns
time = (time - time(1))*1e6; %in microseconds
voltage = voltage*10;
```

```
current = current*10;

%eliminate noise from current
cutoff = 6;
%current = current.*(abs(current)>(cutoff));


%Analyze Current
no_pulses = 0;
pulses = 0;
end_of_pulse = 0;
for index = 1:length( current )
    if end_of_pulse == 0
        if current( index ) > cutoff
            peak_current = 0;
            for index2 = index:index + 20
                if index2 == total
                    break
                end
                if current( index2 ) > peak_current
                    peak_current = current( index2 );
                    peak_current_index = index2;
                elseif peak_current_index < 8
                    break
                end
                if current( index2 ) < cutoff && current(...
                 index2 + 1 ) < cutoff
                    start_of_pulse_index = index;
                    end_of_pulse_index = index2-1;
                    duration_of_pulse = time( index2-1 )- time(...
                     index );
                    if duration_of_pulse ≤ 0.4
```

```
                        break
                    end
                    no_pulses = no_pulses + 1;
                    pulses( no_pulses, 1 ) = peak_current_index;
                    pulses( no_pulses, 2 ) = time(...
                     peak_current_index);
                    pulses( no_pulses, 3 ) = start_of_pulse_index;
                    pulses( no_pulses, 4 ) = duration_of_pulse;
                    pulses( no_pulses, 5 ) = end_of_pulse_index;
                    pulses( no_pulses, 6 ) = peak_current;
                    end_of_pulse = 1;
                    break
                end
                if index2 ≥ total
                    break
                end
            end
        else
            current( index ) = 0;
        end
    elseif index > index2+1
        end_of_pulse = 0;
    end
end
frequency_of_pulses = no_pulses./time( length(time) )*1e3; %kilohertz

%Analyze Voltage
voltage_pulses = 0;
for pulse_check = 1:no_pulses
    for find_on_time = pulses( pulse_check, 3 ):-1:10
        if pulse_check > 1 && find_on_time ≤ pulses(...
         pulse_check-1, 3 )
```

```
            break
        end
        if ( voltage( find_on_time ) < 40 && voltage( find_on_time...
         - 1 ) < 40 && voltage( find_on_time - 2 ) < 40 && voltage(...
          find_on_time - 3 ) < 40 && voltage( find_on_time - 4 )...
           < 40 && voltage( find_on_time - 10 ) < 40 ) |...
            find_on_time == 10
                if find_on_time ≤ 10
                    on_time_start_index = 5;
                else
                    on_time_start_index = find_on_time + 1;
                end
                on_time = time( pulses( pulse_check, 3 ) ) - time(...
                 on_time_start_index );
                if on_time<0
                    on_time_start_index = find_on_time;
                    on_time = 0;
                end
                if pulse_check == 1
                    off_time_start_index = 1;
                else
                    off_time_start_index = pulses( pulse_check-1, 5 );
                end
                off_time = time( on_time_start_index ) - time(...
                 off_time_start_index );
                avg_on_time_voltage = mean( voltage(...
                 on_time_start_index:pulses( pulse_check, 3 ) ) );
                avg_off_time_voltage = mean( voltage(...
                 off_time_start_index:on_time_start_index ) );
                avg_discharge_voltage = mean( voltage( pulses(...
                 pulse_check, 3 ):pulses( pulse_check, 5 ) ) );
                voltage_pulses( pulse_check, 1 ) =...
```

```
                     on_time_start_index;
                    voltage_pulses( pulse_check, 2 ) =...
                     time( on_time_start_index );
                    voltage_pulses( pulse_check, 3 ) =...
                     on_time;
                    voltage_pulses( pulse_check, 4 ) =...
                     off_time;
                    voltage_pulses( pulse_check, 5 ) =...
                     avg_on_time_voltage;
                    voltage_pulses( pulse_check, 6 ) =...
                     avg_off_time_voltage;
                    voltage_pulses( pulse_check, 7 ) =...
                     avg_discharge_voltage;
                    break
            end
        end
end


%find absolute power
power = abs(current.*voltage);

%find energy
inst_energy = power*( time( end )/ length(time) )/1e6;
tot_energy = inst_energy(1);
for energy_index = 2:length( inst_energy )
    tot_energy( energy_index ) = tot_energy( energy_index -1 ) +...
     inst_energy( energy_index );
end
%find energy per spark
spark_energy = 0;
for sparks = 1:no_pulses
```

```
    spark_energy( sparks ) = max( tot_energy( pulses( sparks, 3 )...
    -3:pulses( sparks, 5 )+3 ) ) - min(  tot_energy( pulses(...
     sparks, 3 )-3:pulses( sparks, 5 )+3 ) );
end
avg_spark_energy = tot_energy(end)/no_pulses;


%plot signal
scrnsz = get(0,'ScreenSize');
figure('Name', [ sprintf( 'Current, Voltage, Power & Energy...
 Profiles for'), csvfile ], 'NumberTitle','off', 'Position',...
  [ 0.05*scrnsz(3), 0.05*scrnsz(4), 0.9*scrnsz(3), 0.85*scrnsz(4) ] )

subplot(4,1,1)
plot( time, current )
xlabel( 'Time (microseconds)' )
ylabel( 'Current (amps)' )

subplot(4,1,2)
plot( time, voltage )
xlabel( 'Time (microseconds)' )
ylabel( 'Voltage (volts)' )

subplot(4,1,3)
plot( time, power/1000 )
xlabel( 'Time (microseconds)' )
ylabel( 'Power (kilowatts)' )

subplot(4,1,4)
plot( time, tot_energy )
xlabel( 'Time (microseconds)' )
ylabel( 'Energy (joules)' )
```

```
filename = sprintf( 'Current,_Voltage,_Power,_&_Energy' );
saveas( gcf, strcat( directory, filename ), 'fig' );
pause(2)
saveas( gcf, strcat( directory, filename ), 'emf' );
pause(2)
close


%plot current and voltage in 100 us increments
total_adj = total-increment+1;

plot_num = 0;
plot_total = floor( total/increment );

for dx=1:increment:total_adj
    plot_num = plot_num + 1;
    scrnsz = get(0,'ScreenSize');
    figure('Name', [ 'Current & Voltage Profiles ' csvfile sprintf(...
     ', Part %1.0f/%1.0f', plot_num, plot_total ) ], 'NumberTitle',...
     'off', 'Position', [ 0.05*scrnsz(3), 0.05*scrnsz(4),...
      0.9*scrnsz(3), 0.85*scrnsz(4) ]  )
    subplot(2,1,1)
    plot( time(dx:dx+increment-1), current(dx:dx+increment-1) )
    axis( [dx/10, (dx+increment)/10, -50, 250 ] )
    xlabel( 'Time (microseconds)' )
    ylabel( 'Current (amps)' )
    title( [ 'Current Profile for ' csvfile sprintf( ', Part...
     %1.0f/%1.0f', plot_num, plot_total ) ] )

    %pulse number
    for check_pulse = 1: no_pulses
```

```
        if pulses( check_pulse, 1 ).*( pulses( check_pulse, 1 )>dx...
         & pulses( check_pulse, 1 )<dx+increment-1)
            text( pulses( check_pulse,2), pulses( check_pulse,6)...
            +10, sprintf( '%1.f', check_pulse ) )
        end
    end

    subplot(2,1,2)
    plot( time(dx:dx+increment-1), voltage(dx:dx+increment-1) )
    axis( [dx/10, (dx+increment)/10, -150, 150 ] )
    xlabel( 'Time (microseconds)' )
    ylabel( 'Voltage (volts)' )
    title( [ 'Voltage Profile for ' csvfile sprintf( ', Part...
     %1.0f/%1.0f', plot_num, plot_total ) ] )

    %show on time
    for check_pulse = 1: no_pulses
        avg_on_time_index = round( 0.5.*( pulses( check_pulse, 3 )...
         + voltage_pulses( check_pulse, 1 ) ) );
        if (pulses( check_pulse, 3 ) > dx & pulses( check_pulse, 3...
        ) <dx+increment-1) | (voltage_pulses( check_pulse, 1 ) > dx...
& voltage_pulses( check_pulse, 1 )<dx+increment-1)
            if voltage_pulses( pulse_check, 1 ) > dx
                patch( [ pulses( check_pulse, 3 ), pulses(...
                 check_pulse, 3 ), voltage_pulses( check_pulse, 1 )...
                 , voltage_pulses( check_pulse, 1 ) ]/10, [ 0,...
                  voltage_pulses( check_pulse,5), voltage_pulses(...
                   check_pulse,5),0 ], 'y', 'FaceAlpha', 0.15,...
                    'EdgeAlpha', 0.15 )
            else
                patch( [ pulses( check_pulse, 3 ), pulses(...
                 check_pulse, 3 ), 0, 0 ]/10, [ 0, voltage_pulses(...
```

```
                  check_pulse,5), voltage_pulses( check_pulse,5)...
                  ,0 ], 'y', 'FaceAlpha', 0.15, 'EdgeAlpha', 0.15 )
            end


            if voltage_pulses( check_pulse, 3 ) > 8
                if time( avg_on_time_index ) - 0.25.*voltage_pulses...
                ( check_pulse, 3 ) < time( dx )
                    text( time( dx )+ 2, voltage_pulses( ...
                    check_pulse,5)/2, sprintf( '%1.f us', ...
                    voltage_pulses( check_pulse, 3 ) ) )
                elseif time( avg_on_time_index) - 0.25.*...
                voltage_pulses( check_pulse, 3 ) > time( dx +...
                 increment-1 )
                    text( time( dx + increment )- 8, voltage_pulses...
                    ( check_pulse,5)/2, sprintf( '%1.f us', ...
                    voltage_pulses( check_pulse, 3 ) ) )
                else
                    text( time( avg_on_time_index)-0.25.*...
                    voltage_pulses( check_pulse, 3 ), ...
                    voltage_pulses( check_pulse,5)/2, sprintf( ...
                    '%1.f us', voltage_pulses( check_pulse, 3 ) ) )
                end
            else
                text( time( avg_on_time_index), 100, sprintf...
                ( '%1.f us', voltage_pulses( check_pulse, 3 ) ) )
            end
        end

        %show discharge time
        if (pulses( check_pulse, 1 ) > dx & pulses( check_pulse,...
         1 )<dx+increment-1)
```

```
            patch( [ pulses( check_pulse, 3 ), pulses( check_pulse,...
             3 ), pulses( check_pulse, 5 ), pulses( check_pulse,...
              5 ) ]/10, [ 0, voltage_pulses( check_pulse,7), ...
              voltage_pulses( check_pulse,7),0 ], 'r', 'FaceAlpha',...
               0.5, 'EdgeAlpha', 0.5 )
        end
    end
    filename = sprintf( 'Current_and_Voltage_%02.0f_of_%02.0f',...
     plot_num, plot_total );
    saveas( gcf, strcat( directory, filename ), 'fig' );
    pause(2)
    saveas( gcf, strcat( directory, filename ), 'jpg' );
    pause(2)
    close



    %plot power and energy
    scrnsz = get(0,'ScreenSize');
    figure('Name', [ 'Power & Energy Profiles ' csvfile sprintf(...
     ', Part %1.0f/%1.0f', plot_num, plot_total ) ], 'NumberTitle',...
     'off', 'Position', [ 0.05*scrnsz(3), 0.05*scrnsz(4),...
      0.9*scrnsz(3), 0.85*scrnsz(4) ] )
    subplot(2,1,1)
    plot( time(dx:dx+increment-1), power(dx:dx+increment-1)/1000 )
    axis( [dx/10, (dx+increment)/10, 0, max(power)/1000+3 ] )
    xlabel( 'Time (microseconds)' )
    ylabel( 'Power (kilowatts)' )
    title( [ 'Power Profile for ' csvfile sprintf( ', Part...
     %1.0f/%1.0f', plot_num, plot_total ) ] )

    %pulse number
```

```
for check_pulse = 1: no_pulses
    if pulses( check_pulse, 1 ).*( pulses( check_pulse, 1 )>dx...
     & pulses( check_pulse, 1 )<dx+increment-1)
        if pulses( check_pulse,1) > 20 && pulses(...
         check_pulse,1) < (length( time )- 20)
            text( pulses( check_pulse,2), max( power( pulses(...
             check_pulse,1)-20:pulses( check_pulse,1)+20 ))...
             /1000+2, sprintf( '%1.f', check_pulse ) )
        elseif pulses( check_pulse,1) ≤ 20
           text( pulses( check_pulse,2), max( power( 1:pulses(...
            check_pulse,1)+20 ))/1000+2, sprintf( '%1.f',...
             check_pulse ) )
        elseif pulses( check_pulse,1) ≥ (length( time )- 20)
            text( pulses( check_pulse,2), max( power( pulses(...
             check_pulse,1)-20:length(time) ))/1000+2,...
              sprintf( '%1.f', check_pulse ) )
        else
        end
    end
end


subplot(2,1,2)
plot( time(dx:dx+increment-1), tot_energy(dx:dx+increment-1) )
xlim( [dx/10, (dx+increment)/10] )
xlabel( 'Time (microseconds)' )
ylabel( 'Energy (Joules)' )
title( [ 'Energy Profile for ' csvfile sprintf( ', Part ...
%1.0f/%1.0f', plot_num, plot_total ) ] )

%spark energy
for check_spark = 1: no_pulses
```

```
            if pulses( check_spark, 1 ).*( pulses( check_spark, 1 )...
            >dx & pulses( check_spark, 1 )<dx+increment−1)
                text( pulses( check_spark,2)+ 1, tot_energy( pulses(...
                 check_spark,1 ) )−.002, sprintf( '%2.1f mJ',...
                  1000*spark_energy( check_spark) ) )
            end
        end

        filename = sprintf( 'Power_and_Energy_%02.0f_of_%02.0f',...
         plot_num, plot_total );
        saveas( gcf, strcat( directory, filename ), 'fig' );
        pause(2)
        saveas( gcf, strcat( directory, filename ), 'emf' );
        pause(2)
        close


    energy_per_inch = avg_spark_energy*frequency_of_pulses*60...
    /feed_rate; %kJ/in.
    %
    %
    end



    try
        delete( strcat( directory, 'Summary.txt' ) );
    catch
    end


    diary( strcat( directory, 'Summary.txt' ) )
```

```
fprintf( ['\nREPORT FOR' ' ' strcat( csvfile, '\n' ) ])
fprintf( '\nAverage peak discharge current is %3.0f Amps\n',...
 mean( pulses( :, 6 ) ) )
fprintf( 'Average discharge current pulse width is %1.2f...
 microseconds\n', mean( pulses( :, 4) ) )
fprintf( 'Average discharge current pulse frequency is %2.2f...
 kHz\n', frequency_of_pulses )
fprintf( 'Average voltage on-time is %2.2f microseconds\n',...
 mean( voltage_pulses( :, 3 ) ) )
fprintf( 'Average voltage off-time is %2.2f microseconds\n',...
 mean( voltage_pulses( :, 4 ) ) )
fprintf( 'On-time average voltage is %2.2f volts\n',...
 mean( voltage_pulses( :, 5 ) ) )
fprintf( 'Off-time average voltage is %2.2f volts\n',...
 mean( voltage_pulses( :, 6 ) ) )
fprintf( 'Discharge average voltage is %2.2f volts\n',...
 mean( voltage_pulses( :, 7 ) ) )
fprintf( 'Average spark energy is %2.2f millijoules\n',...
 avg_spark_energy*1000 )
fprintf( 'Average energy per inch is %2.2f kJ/inch\n',...
 energy_per_inch )

fprintf( '\nPulse No.\tTime\t\tDuration\tPeak Current\tOn-Time...
\t\tOff-Time\tOn-Time Voltage\tOff-Time Voltage\tDischarge Voltage...
\tSpark Energy\n' )
for print_index = 1:no_pulses
    fprintf( '%3.0f\t\t\t%3.2f\t\t%2.2f\t\t%3.2f\t\t\t%2.2f\t\t...
    %2.2f\t\t%2.2f\t\t\t%2.2f\t\t\t\t%2.2f\t\t\t\t%2.2f\n',...
     print_index, pulses( print_index, 2 ),...
        pulses( print_index, 4 ), pulses( print_index, 6 ),...
         voltage_pulses( print_index, 3 ), voltage_pulses...
         ( print_index, 4 ), voltage_pulses( print_index, 5 )...
```

```
        , voltage_pulses( print_index, 6 ), voltage_pulses...
        ( print_index, 7 ), spark_energy( print_index )*1000 )
end

diary off

toc
```

APPENDIX B

RECAST LAYER THICKNESS MEASUREMENTS

Table B.1: Recast layer thickness measurements

Wire [μm]	Feed Rate [mm/min]	SC [μs]	SE	Recast Layer Thicknesses [μm]	Avg. [μm]	SD [μm]	CoV
100	1.969	16	4	10.82, 6.73, 9.48, 6.62, 7.95, 6.79, 7.94	8.07	1.74	0.216
100	1.969	16	6	5.16, 4.74, 5.40	5.10	0.34	0.066
100	1.969	16	8	6.84, 6.34, 6.53	6.57	0.25	0.039
100	1.969	28	4	7.58, 7.73, 6.19	7.17	0.85	0.119
100	1.969	28	6	5.07, 6.20, 5.11	5.46	0.65	0.118
100	1.969	28	8	8.02, 6.84, 8.05	7.63	0.69	0.090
100	2.223	16	4	5.35, 6.27, 6.03	5.88	0.48	0.081
100	2.223	16	6	6.20, 6.85, 6.15	6.40	0.39	0.061
100	2.223	16	8	7.15, 6.20, 7.22	6.86	0.57	0.083
100	2.223	28	4	6.01, 5.96, 6.76	6.24	0.45	0.072
100	2.223	28	6	5.81, 6.65, 6.00	6.15	0.44	0.072
100	2.223	28	8	7.04, 6.65, 8.86, 7.45	7.50	0.96	0.129
250	1.969	16	6	7.16, 8.42, 8.70	8.09	0.82	0.101
250	1.969	16	12	10.19, 7.45, 7.61, 5.67, 6.98, 12.45	8.39	2.47	0.295
250	1.969	16	18	7.77, 8.82, 6.43, 8.17	7.80	1.01	0.129
250	1.969	28	6	7.88, 6.73, 5.85	6.82	1.02	0.149
250	1.969	28	12	8.48, 8.75, 8.32	8.51	0.22	0.026
250	1.969	28	18	6.39, 7.64, 11.07, 7.22, 7.41, 7.34	7.84	1.63	0.209
250	2.223	16	6	5.78, 5.23, 6.12	5.71	0.45	0.079
250	2.223	16	12	7.15, 9.20, 7.64	8.00	1.07	0.134
250	2.223	16	18	7.18, 5.55, 7.27	6.67	0.97	0.145
250	2.223	28	6	7.11, 4.84, 5.57, 5.59, 6.38, 6.15	5.94	0.79	0.132
250	2.223	28	12	8.23, 5.16, 7.79, 7.41, 7.57, 7.12	7.21	1.07	0.149
250	2.223	28	18	7.45, 10.04, 6.34, 8.59, 8.14, 6.79	7.89	1.34	0.170

Table B.2: Recast layer thickness measurements after vibratory tumbling experiments

Region	Wire Diameter [μm]	Feed Rate [mm/min]	Spark Cycle [μs]	Spark Energy	Recast Layer Thicknesses [μm]	Avg. [μm]	SD [μm]	CoV
Flat Surface	250	1.969	28	12	5.17, 4.37, 3.82	4.46	0.68	0.153
Flat Surface (tumbled with liquid cleaner)	100	1.969	16	4	10.77, 6.07, 5.36	7.40	2.94	0.394
Flat Surface (tumbled dry)	100	1.969	16	4	3.47, 5.08, 4.12	4.22	0.81	0.192
Gear Tooth Root (tumbled dry)	100	1.969	16	4	5.16, 4.50, 3.51	4.39	0.83	0.189

APPENDIX C

SURFACE ROUGHNESS MEASUREMENTS

Table C.1: Surface roughness data for Sample 1 (wire diameter: 100 μm, table feed rate: 2.223 mm/min, spark cycle: 16 μs, spark energy: 4)

Replicate	RMS [μm]	Ra [μm]
1	2.625	2.024
2	2.713	2.12
3	2.57	2.012
Average	2.636	2.052
Std. Dev.	0.072	0.059

Table C.2: Surface roughness data for Sample 2 (wire diameter: 100 μm, table feed rate: 1.969 mm/min, spark cycle: 28 μs, spark energy: 8)

Replicate	RMS [μm]	Ra [μm]
1	2.899	2.258
2	3.011	2.323
3	2.926	2.27
Average	2.945	2.284
Std. Dev.	0.058	0.035

Table C.3: Surface roughness data for Sample 3 (wire diameter: 250 μm, table feed rate: 2.223 mm/min, spark cycle: 28 μs, spark energy: 6)

Replicate	RMS [μm]	Ra [μm]
1	2.824	2.18
2	2.854	2.218
3	2.889	2.207
Average	2.856	2.202
Std. Dev.	0.033	0.020

Table C.4: Surface roughness data for Sample 4 (wire diameter: 250 μm, table feed rate: 1.969 mm/min, spark cycle: 28 μs, spark energy: 18)

Replicate	RMS [μm]	Ra [μm]
1	3.761	2.937
2	4.506	3.561
3	4.103	3.15
Average	4.123	3.216
Std. Dev.	0.373	0.317

Table C.5: Surface roughness data for vibratory tumbled sample prior to tumbling (wire diameter: 250 μm, table feed rate: 1.969 mm/min, spark cycle: 28 μs, spark energy: 12)

Replicate	RMS [μm]	Ra [μm]
1	3.427	2.731
2	3.518	2.762
3	3.328	2.601
Average	3.424	2.698
Std. Dev.	0.095	0.085

Table C.6: Surface roughness data for vibratory tumbled sample (wire diameter: 250 μm, table feed rate: 1.969 mm/min, spark cycle: 28 μs, spark energy: 12)

Replicate	RMS [μm]	Ra [μm]
1	1.323	0.997
2	1.374	1.091
3	1.316	1.009
Average	1.338	1.032
Std. Dev.	0.032	0.051

APPENDIX D

DATA FROM X-RAY DIFFRACTION TESTS

D.1 Results of Scan Tables for Determination of d_0

Table D.1: Results of scan table for the (331) plane of the virgin surface of Sample 1 to find d_0

ψ [°]	$\sin^2\psi$ [°]	Φ [°]	Peak Position [°]	d-spacing Å	FWHM [°]	Integ. breadth [°]	Ratio
-55.25	0.675	0	138.1919	0.82457	2.071	2.528	0.819
-55.25	0.675	0	138.1842	0.824592	2.327	2.84	0.819
-45.44	0.508	0	137.9783	0.825159	1.929	2.354	0.819
-45.44	0.508	0	138.0168	0.825053	2.173	2.651	0.819
-35.65	0.34	0	137.8222	0.825592	1.888	2.304	0.819
-35.65	0.34	0	137.8539	0.825504	2.121	2.588	0.819
-24.43	0.171	0	137.7386	0.825825	1.682	2.053	0.819
-24.43	0.171	0	137.7148	0.825891	1.908	2.329	0.819
-0.25	0	0	137.5235	0.826426	2.37	2.893	0.819
-0.25	0	0	137.5671	0.826303	1.888	2.304	0.819
23.93	0.165	0	137.7518	0.825788	1.899	2.318	0.819
23.93	0.165	0	137.7284	0.825853	2.058	2.512	0.819
35.15	0.331	0	137.8735	0.825449	2.049	2.5	0.819
35.15	0.331	0	137.8384	0.825547	2.102	2.565	0.819
44.94	0.499	0	137.9264	0.825303	2.25	2.745	0.819
44.94	0.499	0	137.9733	0.825173	2.536	3.094	0.819
54.75	0.667	0	138.07	0.824906	3.068	3.744	0.819
-55.25	0.675	90	137.8607	0.825485	1.996	2.436	0.819
-55.25	0.675	90	137.8233	0.825589	2.133	2.602	0.819
-45.44	0.508	90	137.81	0.825626	2.357	2.876	0.819
-45.44	0.508	90	137.6788	0.825991	2.044	2.494	0.819
-35.65	0.34	90	137.7066	0.825914	1.941	2.369	0.819
-35.65	0.34	90	137.5983	0.826216	2.077	2.534	0.819
-24.43	0.171	90	137.6461	0.826083	2.401	2.93	0.819
-24.43	0.171	90	137.6784	0.825992	1.93	2.355	0.819
-0.25	0	90	137.6034	0.826202	2.01	2.453	0.819
-0.25	0	90	137.5569	0.826332	2.273	2.774	0.819
23.93	0.165	90	137.6342	0.826116	2.173	2.652	0.819
23.93	0.165	90	137.6375	0.826106	1.684	2.056	0.819
35.15	0.331	90	137.6376	0.826106	2.389	2.915	0.819
35.15	0.331	90	137.7466	0.825802	2.178	2.658	0.819
44.94	0.499	90	137.7877	0.825688	2.288	2.792	0.819
44.94	0.499	90	137.7718	0.825732	2.529	3.086	0.819
54.75	0.667	90	137.8101	0.825626	2.645	3.227	0.819
54.75	0.667	90	137.7528	0.825785	2.367	2.889	0.819

Table D.2: Results of scan table for the (420) plane of the virgin surface of Sample 1 to find d_0

ψ [°]	$\sin^2\psi$ [°]	Φ [°]	Peak Position [°]	d-spacing Å	FWHM [°]	Integ. breadth [°]	Ratio
-55.05	0.672	0	146.6949	0.804017	2.348	2.866	0.819
-55.05	0.672	0	146.8917	0.803605	2.658	3.244	0.819
-45.24	0.504	0	146.5167	0.804392	2.981	3.637	0.819
-35.45	0.336	0	146.3998	0.804639	2.362	2.883	0.819
-35.45	0.336	0	146.3885	0.804663	2.713	3.31	0.819
-24.23	0.168	0	146.0507	0.805384	2.959	3.61	0.819
-24.23	0.168	0	146.1662	0.805137	3.134	3.825	0.819
-0.05	0	0	145.8822	0.805746	2.854	3.482	0.819
-0.05	0	0	146.0344	0.805419	2.623	3.2	0.819
24.13	0.167	0	146.1036	0.80527	2.46	3.002	0.819
35.35	0.335	0	146.4092	0.804619	2.446	2.984	0.819
35.35	0.335	0	146.3961	0.804647	2.953	3.604	0.819
45.14	0.502	0	146.6423	0.804127	3.11	3.795	0.819
45.14	0.502	0	146.3641	0.804715	3.243	3.957	0.819
54.95	0.67	0	146.6352	0.804142	3.19	3.893	0.819
54.95	0.67	0	146.5897	0.804238	3.869	4.722	0.819
-55.05	0.672	90	146.3026	0.804846	2.527	3.084	0.819
-55.05	0.672	90	146.1808	0.805105	3.148	3.842	0.819
-45.24	0.504	90	146.1809	0.805105	3.144	3.837	0.819
-45.24	0.504	90	146.2354	0.804989	2.915	3.557	0.819
-35.45	0.336	90	146.0011	0.80549	3.281	4.004	0.819
-35.45	0.336	90	145.9955	0.805502	3.182	3.883	0.819
-24.23	0.168	90	146.0191	0.805452	2.798	3.415	0.819
-24.23	0.168	90	145.9194	0.805666	2.692	3.285	0.819
-0.05	0	90	145.9143	0.805677	2.494	3.043	0.819
-0.05	0	90	145.8457	0.805825	2.33	2.844	0.819
24.13	0.167	90	145.9763	0.805544	2.753	3.36	0.819
35.35	0.335	90	145.9587	0.805581	2.944	3.593	0.819
35.35	0.335	90	145.9149	0.805676	3.435	4.192	0.819
45.14	0.502	90	146.0823	0.805316	3.614	4.41	0.819
45.14	0.502	90	146.1302	0.805213	2.368	2.89	0.819
54.95	0.67	90	146.119	0.805237	4.027	4.915	0.819
54.95	0.67	90	146.1058	0.805266	2.371	2.894	0.819

D.2 Results of Scan Tables for Residual Stress Measurements

Table D.3: Results of scan table for the (331) plane of the wire-EDM cut surface of Sample 1

ψ [°]	$\sin^2\psi$ [°]	Φ [°]	Peak Position [°]	d-spacing Å	FWHM [°]	Integ. breadth [°]	Ratio
-55.25	0.675	0	137.0255	0.827831	1.048	1.278	0.819
-45.44	0.508	0	137.1974	0.827344	1.14	1.392	0.819
-35.65	0.34	0	137.3922	0.826794	0.992	1.211	0.819
-24.43	0.171	0	137.552	0.826346	1.214	1.465	0.829
-0.25	0	0	137.5495	0.826353	1.264	1.474	0.858
23.93	0.165	0	137.455	0.826618	1.373	1.723	0.797
35.15	0.331	0	137.416	0.826727	1.266	1.387	0.913
44.94	0.499	0	137.2691	0.827141	0.986	1.204	0.819
54.75	0.667	0	137.0178	0.827854	1.143	1.395	0.819
-55.25	0.675	90	137.157	0.827458	1.146	1.398	0.819
-45.44	0.508	90	137.2747	0.827126	1.17	1.428	0.819
-35.65	0.34	90	137.3943	0.826788	0.979	1.194	0.819
-24.43	0.171	90	137.4815	0.826543	0.974	1.189	0.819
-0.25	0	90	137.4722	0.826569	0.811	0.99	0.819
23.93	0.165	90	137.4696	0.826577	0.772	0.942	0.819
35.15	0.331	90	137.394	0.826789	0.896	1.093	0.819
44.94	0.499	90	137.2667	0.827148	1.171	1.428	0.819
54.75	0.667	90	137.1254	0.827548	1.343	1.639	0.819

Table D.4: Results of scan table for the (420) plane of the wire-EDM cut surface of Sample 1

ψ [°]	$\sin^2\psi$ [°]	Φ [°]	Peak Position [°]	d-spacing Å	FWHM [°]	Integ. breadth [°]	Ratio
-55.4	0.678	0	145.4324	0.806724	1.601	1.954	0.819
-45.59	0.51	0	145.5124	0.806549	1.792	2.187	0.819
-35.8	0.342	0	145.8731	0.805766	1.471	1.796	0.819
-24.58	0.173	0	145.9333	0.805636	1.048	1.279	0.819
-0.4	0	0	146.1444	0.805183	1.309	1.597	0.819
23.78	0.163	0	146.008	0.805476	1.5	1.83	0.819
35	0.329	0	145.7999	0.805924	1.105	1.348	0.819
44.79	0.496	0	145.6611	0.806225	0.906	1.106	0.819
54.6	0.664	0	145.3764	0.806847	1.543	1.883	0.819
-55.4	0.678	90	145.4965	0.806584	1.75	2.136	0.819
-45.59	0.51	90	145.6619	0.806223	2.102	2.566	0.819
-35.8	0.342	90	145.9239	0.805657	1.43	1.745	0.819
-24.58	0.173	90	146.0208	0.805448	1.39	1.696	0.819
-0.4	0	90	146.2492	0.80496	1.389	1.695	0.819
23.78	0.163	90	145.9755	0.805545	1.312	1.601	0.819
35	0.329	90	145.8727	0.805767	1.552	1.893	0.819
44.79	0.496	90	145.7081	0.806123	1.739	2.122	0.819
54.6	0.664	90	145.6504	0.806248	1.732	2.113	0.819

Table D.5: Results of scan table for the (331) plane of the wire-EDM cut surface of Sample 2

ψ [°]	$\sin^2\psi$ [°]	Φ [°]	Peak Position [°]	d-spacing Å	FWHM [°]	Integ. breadth [°]	Ratio
-55.25	0.675	0	136.9968	0.827913	1.054	1.286	0.819
-45.44	0.508	0	137.1537	0.827468	1.147	1.4	0.819
-35.65	0.34	0	137.3197	0.826998	0.85	1.037	0.819
-24.43	0.171	0	137.3632	0.826876	1.343	1.423	0.943
-0.25	0	0	137.3599	0.826885	0.642	1.315	0.488
23.93	0.165	0	137.3985	0.826777	1.302	1.652	0.788
35.15	0.331	0	137.3899	0.826801	1.313	1.545	0.85
44.94	0.499	0	137.2626	0.82716	1.053	1.285	0.819
54.75	0.667	0	137.1461	0.827489	1.213	1.48	0.819
-55.25	0.675	90	137.0652	0.827719	1.115	1.361	0.819
-45.44	0.508	90	137.1812	0.82739	1.095	1.336	0.819
-35.65	0.34	90	137.232	0.827246	1.012	1.236	0.819
-24.43	0.171	90	137.2888	0.827086	1.118	1.365	0.819
-0.25	0	90	137.3015	0.82705	0.971	1.185	0.819
23.93	0.165	90	137.3264	0.82698	1.04	1.269	0.819
35.15	0.331	90	137.2675	0.827146	1.005	1.226	0.819
44.94	0.499	90	137.1815	0.827389	1.114	1.36	0.819
54.75	0.667	90	137.0718	0.8277	1.143	1.394	0.819

Table D.6: Results of scan table for the (420) plane of the wire-EDM cut surface of Sample 2

ψ [°]	$\sin^2\psi$ [°]	Φ [°]	Peak Position [°]	d-spacing Å	FWHM [°]	Integ. breadth [°]	Ratio
-54.9	0.669	0	145.351	0.806903	1.72	2.099	0.819
-45.09	0.502	0	145.5636	0.806438	1.331	1.624	0.819
-35.3	0.334	0	145.6332	0.806286	1.439	1.756	0.819
-24.08	0.166	0	145.7665	0.805996	1.376	1.679	0.819
0.1	0	0	145.9148	0.805676	1.13	1.379	0.819
24.28	0.169	0	145.8693	0.805774	1.344	1.64	0.819
35.5	0.337	0	145.7256	0.806085	1.691	2.063	0.819
45.29	0.505	0	145.5024	0.806571	1.328	1.621	0.819
55.1	0.673	0	144.9644	0.807757	2.865	3.496	0.819
-54.9	0.669	90	145.3914	0.806814	1.676	2.046	0.819
-45.09	0.502	90	145.627	0.806299	1.743	2.127	0.819
-35.3	0.334	90	145.7135	0.806111	1.52	1.854	0.819
-24.08	0.166	90	145.8056	0.805912	1.292	1.577	0.819
0.1	0	90	145.8446	0.805828	1.281	1.563	0.819
24.28	0.169	90	145.7483	0.806036	1.578	1.926	0.819
35.5	0.337	90	145.6805	0.806183	1.399	1.708	0.819
45.29	0.505	90	145.5658	0.806433	1.463	1.786	0.819
55.1	0.673	90	145.4329	0.806723	1.701	2.076	0.819

Table D.7: Results of scan table for the (331) plane of the wire-EDM cut surface of Sample 2 (repeated)

ψ [°]	$\sin^2\psi$ [°]	Φ [°]	Peak Position [°]	d-spacing Å	FWHM [°]	Integ. breadth [°]	Ratio
-55.25	0.675	0	137.152	0.827472	1.172	1.43	0.819
-45.44	0.508	0	137.1094	0.827593	1.036	1.265	0.819
-35.65	0.34	0	137.192	0.827359	1.363	1.663	0.819
-24.43	0.171	0	137.3322	0.826963	1.406	1.412	0.995
-0.25	0	0	137.3408	0.826939	0.56	1.189	0.471
23.93	0.165	0	137.3098	0.827026	1.312	1.599	0.821
35.15	0.331	0	137.4212	0.826713	1.504	1.722	0.873
44.94	0.499	0	137.2092	0.827311	1.134	1.384	0.819
54.75	0.667	0	136.9769	0.82797	1.187	1.449	0.819
-55.25	0.675	90	137.0712	0.827702	1.146	1.398	0.819
-45.44	0.508	90	137.1783	0.827398	1.131	1.38	0.819
-35.65	0.34	90	137.2238	0.827269	1.095	1.336	0.819
-24.43	0.171	90	137.2766	0.82712	1.013	1.237	0.819
-0.25	0	90	137.321	0.826995	0.885	1.08	0.819
23.93	0.165	90	137.3121	0.82702	0.964	1.176	0.819
35.15	0.331	90	137.2158	0.827292	1.119	1.365	0.819
44.94	0.499	90	137.2075	0.827315	1.141	1.392	0.819
54.75	0.667	90	137.1	0.82762	1.243	1.517	0.819

Table D.8: Results of scan table for the (420) plane of the wire-EDM cut surface of Sample 2 (repeated

ψ [°]	$\sin^2\psi$ [°]	Φ [°]	Peak Position [°]	d-spacing Å	FWHM [°]	Integ. breadth [°]	Ratio
-54.9	0.669	0	145.2776	0.807064	1.449	1.768	0.819
-45.09	0.502	0	145.4144	0.806764	1.754	2.141	0.819
-35.3	0.334	0	145.6765	0.806192	1.428	1.743	0.819
-24.08	0.166	0	145.7531	0.806026	1.297	1.583	0.819
0.1	0	0	145.9174	0.80567	1.361	1.661	0.819
24.28	0.169	0	145.816	0.805889	1.194	1.457	0.819
35.5	0.337	0	145.7814	0.805964	1.432	1.748	0.819
45.29	0.505	0	145.4663	0.80665	1.077	1.315	0.819
55.1	0.673	0	145.2738	0.807073	1.91	2.331	0.819
-54.9	0.669	90	145.39	0.806817	1.665	2.032	0.819
-45.09	0.502	90	145.6348	0.806282	1.729	2.11	0.819
-35.3	0.334	90	145.6414	0.806268	1.26	1.537	0.819
-24.08	0.166	90	145.7625	0.806005	1.458	1.779	0.819
0.1	0	90	145.8526	0.80581	1.263	1.542	0.819
24.28	0.169	90	145.7631	0.806004	1.457	1.778	0.819
35.5	0.337	90	145.7005	0.80614	1.458	1.78	0.819
45.29	0.505	90	145.5456	0.806477	1.479	1.805	0.819
55.1	0.673	90	145.4487	0.806689	1.729	2.11	0.819

Table D.9: Results of scan table for the (331) plane of the wire-EDM cut surface of Sample 2 (repeated)

ψ [°]	$\sin^2\psi$ [°]	Φ [°]	Peak Position [°]	d-spacing Å	FWHM [°]	Integ. breadth [°]	Ratio
-55.25	0.675	0	137.0445	0.827777	1.114	1.359	0.819
-45.44	0.508	0	137.1246	0.82755	1.005	1.226	0.819
-35.65	0.34						
-24.43	0.171	0	137.2499	0.827195	1.291	1.576	0.819
-0.25	0	0	137.3106	0.827024	0.952	1.162	0.819
23.93	0.165	0	137.3104	0.827025	0.917	1.119	0.819
35.15	0.331	0	137.3272	0.826977	1.044	1.274	0.819
44.94	0.499	0	137.2337	0.827241	0.869	1.061	0.819
54.75	0.667	0	137.0889	0.827651	1.156	1.41	0.819
-55.25	0.675	90	137.0671	0.827713	1.207	1.473	0.819
-45.44	0.508	90	137.1804	0.827392	1.448	1.767	0.819
-35.65	0.34	90	137.242	0.827218	1.028	1.254	0.819
-24.43	0.171	90	137.2652	0.827152	0.841	1.026	0.819
-0.25	0	90					
23.93	0.165	90	137.2882	0.827087	1.142	1.393	0.819
35.15	0.331	90					
44.94	0.499	90	137.1331	0.827526	1.35	1.648	0.819
54.75	0.667	90	137.0772	0.827685	1.305	1.592	0.819

Table D.10: Results of scan table for the (420) plane of the wire-EDM cut surface of Sample 2 (repeated)

ψ [°]	$\sin^2\psi$ [°]	Φ [°]	Peak Position [°]	d-spacing Å	FWHM [°]	Integ. breadth [°]	Ratio
-54.9	0.669	0	145.3313	0.806946	1.677	2.047	0.819
-45.09	0.502	0	145.5369	0.806496	1.589	1.939	0.819
-35.3	0.334	0	145.6323	0.806288	1.535	1.873	0.819
-24.08	0.166	0	145.7736	0.805981	1.267	1.546	0.819
0.1	0	0	145.818	0.805885	1.436	1.752	0.819
24.28	0.169	0	145.887	0.805736	1.428	1.743	0.819
35.5	0.337	0	145.8044	0.805914	1.348	1.645	0.819
45.29	0.505	0	145.4982	0.80658	1.216	1.484	0.819
55.1	0.673	0	145.3717	0.806857	1.879	2.293	0.819
-54.9	0.669	90	145.5224	0.806527	2.209	2.695	0.819
-45.09	0.502	90	145.6047	0.806348	1.678	2.048	0.819
-35.3	0.334	90	145.6543	0.80624	1.632	1.992	0.819
-24.08	0.166	90	145.7806	0.805966	1.541	1.881	0.819
0.1	0	90	145.9034	0.805701	1.778	2.169	0.819
24.28	0.169	90	145.5658	0.806433	1.929	2.354	0.819
35.5	0.337	90	145.6455	0.806259	1.411	1.722	0.819
45.29	0.505	90	145.55	0.806467	1.758	2.145	0.819
55.1	0.673	90	145.3315	0.806946	1.636	1.997	0.819

Table D.11: Results of scan table for the (331) plane of the wire-EDM cut surface of Sample 3

ψ [°]	$\sin^2\psi$ [°]	Φ [°]	Peak Position [°]	d-spacing Å	FWHM [°]	Integ. breadth [°]	Ratio
-55.25	0.675	0	137.2135	0.827298	1.186	1.447	0.819
-45.44	0.508	0	137.3201	0.826997	1.175	1.434	0.819
-35.65	0.34	0	137.3936	0.82679	1.146	1.398	0.819
-24.43	0.171	0	137.4833	0.826538	1.3	1.508	0.862
-0.25	0	0	137.5506	0.82635	0.968	1.208	0.801
23.93	0.165	0	137.247	0.827204	1.17	1.397	0.838
35.15	0.331	0	137.6345	0.826115	1.387	1.589	0.873
44.94	0.499	0	137.3035	0.827044	1.384	1.812	0.764
54.75	0.667	0	137.1874	0.827372	1.128	1.376	0.819
-55.25	0.675	90	137.1657	0.827434	1.326	1.619	0.819
-45.44	0.508	90	137.3339	0.826958	1.173	1.432	0.819
-35.65	0.34	90	137.3968	0.826781	1.076	1.313	0.819
-24.43	0.171	90	137.514	0.826452	1.001	1.221	0.819
-0.25	0	90	137.5436	0.826369	0.92	1.123	0.819
23.93	0.165	90	137.4867	0.826529	0.918	1.12	0.819
35.15	0.331	90	137.4238	0.826705	0.916	1.118	0.819
44.94	0.499	90	137.3702	0.826856	1.055	1.287	0.819
54.75	0.667	90	137.2641	0.827155	1.344	1.64	0.819

Table D.12: Results of scan table for the (420) plane of the wire-EDM cut surface of Sample 3

ψ [°]	$\sin^2\psi$ [°]	Φ [°]	Peak Position [°]	d-spacing Å	FWHM [°]	Integ. breadth [°]	Ratio
-54.9	0.669	0	145.4551	0.806675	1.63	1.989	0.819
-45.09	0.502	0	145.5776	0.806407	1.449	1.768	0.819
-35.3	0.334	0	145.8835	0.805744	1.678	2.047	0.819
-24.08	0.166	0	146.158	0.805154	1.213	1.48	0.819
0.1	0	0	146.1972	0.80507	1.008	1.231	0.819
24.28	0.169	0	145.9737	0.805549	1.058	1.291	0.819
35.5	0.337	0	145.8668	0.80578	1.509	1.842	0.819
45.29	0.505	0	145.8108	0.805901	1.301	1.587	0.819
55.1	0.673	0	145.4741	0.806633	1.531	1.868	0.819
-54.9	0.669	90	145.5476	0.806472	1.703	2.078	0.819
-45.09	0.502	90	145.7882	0.80595	1.672	2.04	0.819
-35.3	0.334	90	145.9353	0.805632	1.523	1.858	0.819
-24.08	0.166	90	146.0691	0.805344	1.598	1.95	0.819
0.1	0	90	146.1957	0.805074	1.184	1.445	0.819
24.28	0.169	90	146.1484	0.805175	1.337	1.632	0.819
35.5	0.337	90	145.9388	0.805624	1.913	2.334	0.819
45.29	0.505	90	145.8495	0.805817	1.343	1.638	0.819
55.1	0.673	90	145.6283	0.806297	1.902	2.321	0.819

Table D.13: Results of scan table for the (331) plane of the wire-EDM cut surface of Sample 4

ψ [°]	$\sin^2\psi$ [°]	Φ [°]	Peak Position [°]	d-spacing Å	FWHM [°]	Integ. breadth [°]	Ratio
-55.25	0.675	0	137.0492	0.827763	1.242	1.515	0.819
-45.44	0.508	0	137.1265	0.827543	1.087	1.327	0.819
-35.65	0.34	0	137.1297	0.827534	1.009	1.231	0.819
-24.43	0.171	0	137.2986	0.827056	1.264	1.286	0.983
-0.25	0	0	137.3417	0.826935	0.571	1.164	0.491
23.93	0.165	0	137.1976	0.827342	0.535	1.248	0.428
35.15	0.331	0	137.2524	0.827187	1.468	1.622	0.905
44.94	0.499	0	137.0453	0.827774	1.76	2.118	0.831
54.75	0.667	0	137.1264	0.827543	1.26	1.537	0.819
-55.25	0.675	90	136.9266	0.828112	1.127	1.375	0.819
-45.44	0.508	90	137.0987	0.827622	1.175	1.434	0.819
-35.65	0.34	90	137.1713	0.827416	1.128	1.376	0.819
-24.43	0.171	90	137.2465	0.827203	1.022	1.248	0.819
-0.25	0	90	137.2254	0.827263	0.916	1.118	0.819
23.93	0.165	90	137.2329	0.827242	1.191	1.454	0.819
35.15	0.331	90	137.1838	0.827381	1.052	1.284	0.819
44.94	0.499	90	137.069	0.827706	1.131	1.38	0.819
54.75	0.667	90	137.0404	0.827787	1.247	1.522	0.819

Table D.14: Results of scan table for the (420) plane of the wire-EDM cut surface of Sample 4

ψ [°]	$\sin^2\psi$ [°]	Φ [°]	Peak Position [°]	d-spacing Å	FWHM [°]	Integ. breadth [°]	Ratio
-54.9	0.669	0	145.3335	0.80694	1.599	1.952	0.819
-45.09	0.502	0	145.4989	0.806577	1.515	1.849	0.819
-35.3	0.334	0	145.6549	0.806237	1.481	1.807	0.819
-24.08	0.166	0	145.7562	0.806017	1.28	1.562	0.819
0.1	0	0	145.6428	0.806263	1.781	2.173	0.819
24.28	0.169	0	145.621	0.806311	1.266	1.545	0.819
35.5	0.337	0	145.5673	0.806428	1.4	1.709	0.819
45.29	0.505	0	145.5563	0.806452	1.318	1.608	0.819
55.1	0.673	0	145.5322	0.806505	1.402	1.711	0.819
-54.9	0.669	90	145.3446	0.806915	1.768	2.157	0.819
-45.09	0.502	90	145.4698	0.806641	1.702	2.077	0.819
-35.3	0.334	90	145.6306	0.80629	1.59	1.94	0.819
-24.08	0.166	90	145.6925	0.806155	1.547	1.888	0.819
0.1	0	90	145.6952	0.806149	1.585	1.934	0.819
24.28	0.169	90	145.7427	0.806046	1.361	1.661	0.819
35.5	0.337	90	145.5807	0.806399	1.407	1.717	0.819
45.29	0.505	90	145.5148	0.806542	1.569	1.914	0.819
55.1	0.673	90	145.2698	0.80708	1.686	2.057	0.819

Table D.15: Results of scan table for the (331) plane of the wire-EDM cut surface of Sample 4 with 9 μm removed

ψ [°]	$\sin^2\psi$ [°]	Φ [°]	Peak Position [°]	d-spacing Å	FWHM [°]	Integ. breadth [°]	Ratio
-55.25	0.675	0	137.0493	0.827764	1.242	1.516	0.819
-45.44	0.508	0	137.1266	0.827544	1.087	1.327	0.819
-35.65	0.34	0	137.1298	0.827535	1.009	1.232	0.819
-24.43	0.171	0	137.4634	0.826594	0.986	1.203	0.819
-0.25	0	0	137.6616	0.826039	1.117	1.363	0.819
23.93	0.165	0	137.5418	0.826374	1.118	1.364	0.819
35.15	0.331	0	137.4178	0.826722	1.214	1.482	0.819
44.94	0.499	0	137.3733	0.826847	1.492	1.82	0.819
54.75	0.667	0	137.1403	0.827506	1.296	1.581	0.819
-55.25	0.675	90	136.9267	0.828113	1.127	1.375	0.819
-45.44	0.508	90	137.0988	0.827623	1.175	1.434	0.819
-35.65	0.34	90	137.1713	0.827418	1.128	1.376	0.819
-24.43	0.171	90	137.2466	0.827205	1.023	1.248	0.819
-0.25	0	90	137.2254	0.827265	0.917	1.119	0.819
23.93	0.165	90	137.233	0.827243	1.192	1.454	0.819
35.15	0.331	90	137.1897	0.827366	1.099	1.341	0.819
44.94	0.499	90	137.0736	0.827695	1.165	1.422	0.819
54.75	0.667	90	137.0405	0.827789	1.248	1.522	0.819

Table D.16: Results of scan table for the (420) plane of the wire-EDM cut surface of Sample 2 with 9 μm removed

ψ [°]	$\sin^2\psi$ [°]	Φ [°]	Peak Position [°]	d-spacing Å	FWHM [°]	Integ. breadth [°]	Ratio
-54.9	0.669	0	145.3493	0.806906	1.709	2.086	0.819
-45.09	0.502	0	145.525	0.806522	1.439	1.756	0.819
-35.3	0.334	0	145.501	0.806574	1.428	1.743	0.819
-24.08	0.166	0	145.6914	0.806159	1.217	1.485	0.819
0.1	0	0	145.6909	0.80616	1.351	1.649	0.819
24.28	0.169	0	145.64	0.806271	1.402	1.711	0.819
35.5	0.337	0	145.6397	0.806272	1.467	1.791	0.819
45.29	0.505	0	145.4668	0.806649	1.669	2.037	0.819
55.1	0.673	0	145.3968	0.806802	1.048	1.279	0.819
-54.9	0.669	90	145.4521	0.806681	1.676	2.045	0.819
-45.09	0.502	90	145.5468	0.806474	1.482	1.809	0.819
-35.3	0.334	90	145.5865	0.806388	1.458	1.779	0.819
-24.08	0.166	90	145.6902	0.806162	1.547	1.888	0.819
0.1	0	90	145.7506	0.806031	1.417	1.73	0.819
24.28	0.169	90	145.6693	0.806207	1.491	1.82	0.819
35.5	0.337	90	145.5625	0.80644	1.615	1.971	0.819
45.29	0.505	90	145.5626	0.80644	1.501	1.831	0.819
55.1	0.673	90	145.4001	0.806795	1.503	1.834	0.819

Table D.17: Results of scan table for the (331) plane of the wire-EDM cut surface of Sample 2 with 26 μm removed

ψ [°]	$\sin^2\psi$ [°]	Φ [°]	Peak Position [°]	d-spacing Å	FWHM [°]	Integ. breadth [°]	Ratio
-55.25	0.675	0	137.3833	0.826819	1.74	2.124	0.819
-45.44	0.508	0	137.3625	0.826878	1.017	1.242	0.819
-35.65	0.34	0	137.232	0.827246	0.928	1.133	0.819
-24.43	0.171	0	137.3213	0.826994	1.132	1.381	0.819
-0.25	0	0	137.2285	0.827256	0.967	1.179	0.819
23.93	0.165	0	137.2404	0.827222	1.087	1.327	0.819
35.15	0.331	0	137.3352	0.826955	1.055	1.288	0.819
44.94	0.499	0	137.3853	0.826814	0.714	0.871	0.819
54.75	0.667	0	137.5037	0.826481	0.955	1.166	0.819
-55.25	0.675	90	137.5711	0.826292	1.187	1.449	0.819
-45.44	0.508	90	137.4065	0.826754	1.064	1.298	0.819
-35.65	0.34	90	137.3331	0.826961	1.029	1.255	0.819
-24.43	0.171	90	137.2764	0.827121	1.01	1.232	0.819
-0.25	0	90	137.1745	0.827409	1.035	1.263	0.819
23.93	0.165	90	137.3074	0.827033	0.875	1.068	0.819
35.15	0.331	90	137.3435	0.826931	0.947	1.155	0.819
44.94	0.499	90	137.4054	0.826757	1.075	1.311	0.819
54.75	0.667	90	137.4821	0.826542	1.054	1.286	0.819

Table D.18: Results of scan table for the (420) plane of the wire-EDM cut surface of Sample 2 with 26 μm removed

ψ [°]	$\sin^2\psi$ [°]	Φ [°]	Peak Position [°]	d-spacing Å	FWHM [°]	Integ. breadth [°]	Ratio
-54.9	0.669	0	145.7889	0.805948	1.494	1.823	0.819
-45.09	0.502	0	145.7816	0.805964	1.414	1.726	0.819
-35.3	0.334	0	145.5917	0.806376	1.413	1.724	0.819
-24.08	0.166	0	145.6615	0.806224	1.499	1.83	0.819
0.1	0	0	145.4118	0.806769	1.303	1.59	0.819
24.28	0.169	0	145.8811	0.805749	1.203	1.468	0.819
35.5	0.337	0	145.7527	0.806026	0.984	1.201	0.819
45.29	0.505	0	145.7306	0.806074	1.739	2.122	0.819
55.1	0.673	0	145.7626	0.806005	1.064	1.298	0.819
-54.9	0.669	90	145.9549	0.80559	1.601	1.954	0.819
-45.09	0.502	90	145.8588	0.805797	1.606	1.96	0.819
-35.3	0.334	90	145.6893	0.806164	1.458	1.779	0.819
-24.08	0.166	90	145.6605	0.806227	1.469	1.793	0.819
0.1	0	90	145.6128	0.80633	1.649	2.013	0.819
24.28	0.169	90	145.6143	0.806327	1.408	1.719	0.819
35.5	0.337	90	145.7931	0.805939	1.42	1.732	0.819
45.29	0.505	90	145.7009	0.806139	1.977	2.413	0.819
55.1	0.673	90	145.8986	0.805711	1.865	2.276	0.819

Table D.19: Results of scan table for the (331) plane of the wire-EDM cut surface of Sample 2 with 26 μm removed (repeated)

ψ [°]	$\sin^2\psi$ [°]	Φ [°]	Peak Position [°]	d-spacing Å	FWHM [°]	Integ. breadth [°]	Ratio
-55.25	0.675	0	137.4237	0.826706	1.012	1.235	0.819
-45.44	0.508	0	137.3707	0.826855	0.927	1.131	0.819
-35.65	0.34	0	137.3117	0.827021	0.823	1.004	0.819
-24.43	0.171	0	137.3424	0.826934	1.145	1.397	0.819
-0.25	0	0	137.2353	0.827237	0.846	1.033	0.819
23.93	0.165	0	137.2538	0.827184	0.81	0.988	0.819
35.15	0.331	0	137.3472	0.826921	0.881	1.075	0.819
44.94	0.499	0	137.3715	0.826852	1.131	1.381	0.819
54.75	0.667	0	137.3721	0.826851	1.103	1.346	0.819
-55.25	0.675	90	137.5459	0.826363	1.189	1.451	0.819
-45.44	0.508	90	137.425	0.826702	0.943	1.151	0.819
-35.65	0.34	90	137.3172	0.827006	1.003	1.224	0.819
-24.43	0.171	90	137.3007	0.827052	0.961	1.173	0.819
-0.25	0	90	137.2065	0.827318	1.043	1.273	0.819
23.93	0.165	90	137.2782	0.827116	0.975	1.19	0.819
35.15	0.331	90	137.3282	0.826974	0.841	1.027	0.819
44.94	0.499	90	137.4158	0.826728	1.046	1.276	0.819
54.75	0.667	90	137.4786	0.826551	1.094	1.335	0.819

Table D.20: Results of scan table for the (420) plane of the wire-EDM cut surface of Sample 2 with 26 μm removed (repeated)

ψ [°]	$\sin^2\psi$ [°]	Φ [°]	Peak Position [°]	d-spacing Å	FWHM [°]	Integ. breadth [°]	Ratio
-54.9	0.669	0	145.8159	0.80589	1.162	1.418	0.819
-45.09	0.502	0	145.8114	0.805899	1.491	1.819	0.819
-35.3	0.334	0	145.6858	0.806171	1.045	1.276	0.819
-24.08	0.166	0	145.6987	0.806143	1.404	1.714	0.819
0.1	0	0	145.3524	0.8069	1.305	1.593	0.819
24.28	0.169	0	145.7837	0.805959	1.264	1.543	0.819
35.5	0.337	0	145.727	0.806082	1.325	1.617	0.819
45.29	0.505	0	145.8399	0.805838	1.112	1.357	0.819
55.1	0.673	0	145.8179	0.805885	1.443	1.761	0.819
-54.9	0.669	90	145.9259	0.805652	1.52	1.855	0.819
-45.09	0.502	90	145.8701	0.805772	1.505	1.837	0.819
-35.3	0.334	90	145.7154	0.806107	1.337	1.632	0.819
-24.08	0.166	90	145.6414	0.806268	1.334	1.628	0.819
0.1	0	90	145.6457	0.806259	1.686	2.057	0.819
24.28	0.169	90	145.6044	0.806349	1.235	1.508	0.819
35.5	0.337	90	145.7426	0.806048	1.212	1.479	0.819
45.29	0.505	90	145.7294	0.806077	1.428	1.742	0.819
55.1	0.673	90	145.8783	0.805755	1.877	2.29	0.819

APPENDIX E

DATA FROM NANO-INDENTATION HARNDNESS TESTS

Table E.1: Nano-indentation hardness data for generating depth profile in Sample 1

h_c [nm]	P_{max} [μN]	S [μN/nm]	A [nm^2]	h_{max} [nm]	h_{eff} [nm]	A	h_f [nm]	m	X [mm]	Y [mm]	Drift Correction [nm/s]	Distance from Edge [μm]	E_r [GPa]	H [GPa]
148.7	2484.9	67.11	608,304	177.1	176.5	11.135	125.5	1.376	-49.9760	93.5133	0.134	5	76.234	4.085
137.6	2485.9	70.04	531,976	165.2	164.2	14.182	116.7	1.338	-49.9791	93.5084	0.149	5	85.077	4.673
134.9	2486.5	64.70	514,169	164.8	163.7	21.430	116.3	1.232	-49.9754	93.5053	0.144	5	79.944	4.836
133.9	2486.5	63.11	507,752	164.2	163.4	18.432	113.9	1.257	-49.9742	93.5008	0.138	5	78.474	4.897
140.7	2485.4	61.75	552,874	171.6	170.9	19.640	121.1	1.238	-49.9693	93.4969	0.112	5	73.582	4.495
140.9	2484.6	60.46	554,206	172.2	171.7	21.137	121.7	1.218	-49.9689	93.4933	0.083	5	71.957	4.483
141.0	2483.6	59.29	554,580	172.9	172.4	22.648	122.1	1.199	-49.9691	93.4873	0.051	5	70.535	4.478
143.9	2483.9	60.44	574,756	175.2	174.7	17.996	123.3	1.251	-49.9715	93.4824	0.043	5	70.630	4.322
143.1	2484.1	55.09	569,200	177.7	176.9	18.290	121.7	1.224	-49.9654	93.4735	0.035	5	64.699	4.364
139.7	2484.3	58.01	546,359	172.5	171.9	18.470	119.0	1.235	-49.9716	93.4694	0.034	5	69.534	4.547
103.6	2489.6	63.49	481,110	133.6	133.0	27.161	86.8	1.179	-50.0572	93.3881	-0.016	5	81.102	5.175
106.3	2488.8	63.77	499,759	136.2	135.6	28.645	90.0	1.169	-50.0609	93.3670	0.007	5	79.924	4.980
104.3	2490.7	89.94	486,324	126.0	125.1	35.920	91.7	1.208	-50.1027	90.3356	0.113	5	114.266	5.121
109.5	2489.0	64.94	521,838	139.0	138.2	26.164	92.6	1.192	-50.0594	93.3701	0.002	6	79.654	4.770
104.0	2488.5	63.62	484,018	134.1	133.3	23.772	86.1	1.207	-50.0636	93.3642	-0.016	6	81.020	5.141
105.6	2489.7	91.12	494,633	127.1	126.1	23.957	90.5	1.301	-50.1023	90.3270	0.047	6	114.797	5.033
104.7	2489.5	90.11	488,947	126.5	125.5	31.702	91.3	1.236	-50.1025	90.3222	0.043	6	114.172	5.091
103.0	2490.4	89.50	477,068	124.9	123.8	38.709	90.7	1.190	-50.1014	90.3169	0.023	7	114.813	5.220
113.0	2488.1	68.77	546,595	141.3	140.1	26.406	96.6	1.204	-50.0992	90.5250	0.042	7	82.409	4.552
110.3	2489.0	67.23	527,272	139.3	138.0	23.121	92.6	1.226	-50.0994	90.5211	0.033	7	82.029	4.721
108.2	2489.3	66.19	512,663	137.2	136.4	24.489	90.9	1.210	-50.0591	93.3800	0.020	8	81.899	4.856
107.2	2489.0	67.10	505,952	136.1	135.0	21.665	89.1	1.239	-50.0598	93.3846	0.016	9	83.586	4.919
106.8	2487.7	68.52	503,218	135.0	134.1	26.937	90.5	1.199	-50.0622	93.3879	-0.051	9	85.583	4.944
104.0	2488.6	66.72	483,678	132.7	131.9	25.209	86.9	1.206	-50.0643	93.3681	-0.009	9	84.999	5.145
103.4	2489.2	65.84	480,119	132.8	131.8	19.994	84.5	1.251	-50.0668	93.3645	0.001	9	84.189	5.184
105.0	2489.7	87.24	490,618	127.3	126.4	42.739	93.2	1.161	-50.1007	90.3133	0.017	9	110.347	5.075
105.0	2489.4	85.15	490,896	127.6	126.9	29.537	90.8	1.236	-50.0934	90.9430	-0.050	9	107.678	5.071
97.1	2490.8	94.26	438,745	118.1	116.9	34.242	84.4	1.231	-50.0930	90.9253	-0.002	9	126.081	5.677
128.9	2486.8	78.36	475,758	152.9	152.7	41.106	116.4	1.143	-49.9756	92.1479	-0.007	10	100.657	5.227
126.8	2487.0	83.48	462,511	149.9	149.1	28.133	112.1	1.241	-49.9756	92.1379	-0.014	10	108.750	5.377
133.1	2485.7	81.89	502,678	156.7	155.9	29.508	118.7	1.226	-49.9756	92.1279	-0.029	10	102.338	4.945
132.8	2486.2	81.17	500,786	157.2	155.8	21.683	116.3	1.290	-49.9756	92.1179	-0.021	10	101.630	4.965
137.5	2486.2	78.23	531,571	162.3	161.4	24.788	121.6	1.251	-49.9756	92.1079	-0.017	10	95.065	4.677

Continued on next page...

Table E.1: Nano-indentation hardness data for generating depth profile in Sample 1 (continued)

h_c [nm]	P_{max} [μN]	S [μN/nm]	A [nm^2]	h_{max} [nm]	h_{eff} [nm]	A	h_f [nm]	m	X [mm]	Y [mm]	Drift Correction [nm/s]	Distance from Edge [μm]	E_r [GPa]	H [GPa]
105.2	2488.4	64.95	492,063	134.7	133.9	24.263	87.7	1.208	-50.0589	93.3768	-0.001	10	82.033	5.057
104.9	2488.4	64.70	489,803	134.4	133.7	30.037	89.0	1.162	-50.0592	93.3730	0.004	10	81.905	5.080
105.6	2489.5	85.56	494,763	128.2	127.4	32.235	92.0	1.218	-50.0934	90.9400	-0.022	10	107.769	5.032
111.3	2488.9	87.68	534,228	133.5	132.5	27.249	96.7	1.262	-50.0934	90.9368	-0.010	10	106.289	4.659
112.8	2488.8	87.68	545,319	134.8	134.1	32.591	99.4	1.222	-50.0936	90.9327	-0.016	10	105.202	4.564
107.4	2490.0	88.97	507,292	129.0	128.4	27.457	93.0	1.264	-50.0935	90.9290	-0.014	10	110.670	4.908
103.5	2489.6	67.38	480,666	132.1	131.2	26.037	86.8	1.202	-50.0632	93.3718	-0.013	11	86.103	5.180
103.3	2490.1	91.16	479,360	124.5	123.8	33.636	90.3	1.226	-50.1087	90.3299	-0.002	11	116.661	5.195
99.9	2490.0	83.37	456,768	123.5	122.3	24.912	84.5	1.267	-50.0933	90.9214	0.000	11	109.293	5.451
104.4	2489.6	67.58	486,748	133.1	132.0	27.306	88.1	1.193	-50.0632	93.3842	-0.017	12	85.820	5.115
104.4	2489.0	69.07	486,400	132.3	131.4	22.554	86.8	1.238	-50.0627	93.3801	-0.012	12	87.748	5.117
103.3	2488.5	69.78	479,101	130.8	130.0	27.849	87.3	1.197	-50.0657	93.3880	-0.047	12	89.322	5.194
104.6	2490.0	96.17	488,110	125.3	124.0	24.415	90.1	1.312	-50.1087	90.3259	-0.003	12	121.954	5.101
100.7	2490.8	91.56	462,058	122.2	121.1	36.781	88.3	1.207	-50.1086	90.3223	-0.005	12	119.346	5.391
102.2	2489.5	90.48	471,641	123.6	122.8	37.367	89.8	1.201	-50.1078	90.3187	-0.013	12	116.727	5.278
105.2	2488.6	62.05	492,142	135.9	135.3	20.882	86.1	1.227	-50.0937	90.5379	0.056	12	78.361	5.057
106.8	2489.3	63.87	503,025	136.7	136.0	21.066	88.0	1.233	-50.0962	90.5341	0.063	12	79.794	4.949
113.7	2488.5	72.99	551,747	140.3	139.3	27.328	97.9	1.212	-50.1042	90.5223	0.010	12	87.064	4.510
100.2	2489.6	90.72	458,391	122.2	120.7	33.515	87.1	1.225	-50.1083	90.3352	-0.003	13	118.720	5.431
110.3	2489.1	69.56	527,721	138.1	137.2	22.806	92.9	1.238	-50.0986	90.5297	0.047	13	84.836	4.717
102.3	2488.7	67.98	472,867	131.1	129.8	25.209	85.5	1.211	-50.0630	93.3764	-0.024	14	87.591	5.263
133.8	2485.5	74.26	506,999	159.5	158.9	24.891	117.5	1.237	-49.9897	93.5086	-0.007	15	92.404	4.902
133.6	2484.8	70.46	506,005	161.4	160.1	23.589	116.5	1.234	-49.9871	93.5035	-0.013	15	87.760	4.911
135.1	2485.6	70.12	515,638	162.1	161.7	23.629	118.0	1.233	-49.9838	93.4994	-0.007	15	86.521	4.820
136.6	2484.8	67.16	525,188	164.8	164.3	26.539	120.0	1.197	-49.9809	93.4949	-0.013	15	82.105	4.731
139.3	2484.5	65.69	543,058	168.2	167.6	23.350	121.5	1.218	-49.9771	93.4918	-0.010	15	78.984	4.575
137.9	2484.1	65.89	534,181	166.9	166.2	19.611	118.9	1.255	-49.9785	93.4869	-0.008	15	79.876	4.650
137.1	2485.3	67.65	528,865	165.4	164.7	25.157	120.2	1.210	-49.9830	93.4831	-0.026	15	82.418	4.699
133.3	2484.5	67.75	503,856	161.7	160.8	24.156	116.1	1.219	-49.9842	93.4771	-0.033	15	84.567	4.931
139.4	2483.4	64.41	544,297	169.1	168.4	26.623	122.6	1.186	-49.9824	93.4726	-0.001	15	77.353	4.563
133.8	2485.4	65.85	507,437	162.6	162.2	20.784	115.2	1.243	-49.9834	93.4684	-0.020	15	81.901	4.898
135.2	2485.3	61.77	516,450	166.5	165.4	20.337	115.9	1.231	-49.9793	93.4665	-0.009	15	76.156	4.812
128.7	2487.2	85.77	474,704	151.5	150.5	30.053	114.7	1.234	-49.9806	92.1479	0.003	15	110.292	5.239

Continued on next page...

Table E.1: Nano-indentation hardness data for generating depth profile in Sample 1 (continued)

h_c [nm]	P_{max} [μN]	S [μN/nm]	A [nm^2]	h_{max} [nm]	h_{eff} [nm]	A	h_f [nm]	m	X [mm]	Y [mm]	Drift Correction [nm/s]	Distance from Edge [μm]	E_r [GPa]	H [GPa]
128.4	2486.9	85.15	472,826	151.8	150.3	23.870	112.9	1.282	-49.9806	92.1379	-0.015	15	109.713	5.260
130.4	2486.6	78.77	485,304	155.5	154.1	36.252	117.1	1.171	-49.9806	92.1279	-0.015	15	100.187	5.124
130.8	2486.6	86.59	488,171	153.6	152.4	17.115	113.4	1.359	-49.9806	92.1179	-0.020	15	109.801	5.094
135.5	2485.8	81.10	518,196	159.3	158.5	21.510	118.9	1.291	-49.9806	92.1079	-0.019	15	99.813	4.797
99.0	2490.4	92.88	451,054	120.0	119.1	28.525	85.1	1.268	-50.1074	90.3138	-0.014	15	122.530	5.521
96.6	2490.2	97.47	435,114	116.9	115.7	28.446	83.0	1.282	-50.1125	90.3302	-0.014	15	130.924	5.723
97.9	2490.3	98.28	443,445	117.9	116.9	25.891	83.8	1.305	-50.1125	90.3254	-0.001	15	130.766	5.616
106.4	2489.4	74.16	500,089	132.4	131.5	27.972	90.9	1.211	-50.1074	90.5206	0.000	15	92.913	4.978
100.6	2489.6	70.70	461,180	128.1	127.0	22.334	83.1	1.246	-50.0671	93.3838	-0.029	16	92.240	5.398
102.1	2488.8	70.94	471,341	129.7	128.4	28.695	86.5	1.195	-50.0693	93.3875	-0.038	16	91.553	5.280
97.3	2490.7	98.71	439,749	116.9	116.2	24.167	82.9	1.322	-50.1125	90.3217	-0.025	16	131.880	5.664
107.6	2488.5	70.65	508,789	134.9	134.0	30.729	92.5	1.179	-50.1033	90.5283	0.002	16	87.756	4.891
102.9	2489.9	69.75	476,370	130.4	129.6	27.400	86.8	1.200	-50.0674	93.3795	-0.011	17	89.533	5.227
99.4	2490.6	98.49	453,761	119.5	118.4	28.656	86.0	1.283	-50.1109	90.3158	-0.009	17	129.547	5.489
105.2	2489.0	64.37	492,377	134.9	134.2	28.672	89.0	1.171	-50.0973	90.5413	-0.030	17	81.277	5.055
109.6	2488.9	72.07	522,776	136.8	135.5	21.990	92.2	1.255	-50.1017	90.5344	0.003	17	88.313	4.761
106.3	2489.3	91.76	499,865	127.8	126.7	32.441	93.2	1.236	-50.1014	90.9431	-0.040	17	114.989	4.980
102.4	2490.5	89.96	473,336	124.0	123.2	32.962	89.2	1.227	-50.1017	90.9393	-0.010	17	115.845	5.262
101.1	2489.6	70.56	464,563	128.8	127.6	23.569	84.0	1.235	-50.0677	93.3761	-0.016	18	91.718	5.359
102.2	2489.3	68.75	472,056	130.5	129.4	28.240	86.3	1.190	-50.0678	93.3719	-0.012	18	88.663	5.273
108.2	2489.0	70.92	512,919	135.8	134.5	28.257	92.5	1.198	-50.0998	90.5386	0.014	18	87.735	4.853
102.3	2490.6	92.51	472,410	123.4	122.5	24.721	87.5	1.298	-50.1019	90.9358	-0.016	18	119.251	5.272
100.7	2490.3	93.19	461,747	121.6	120.7	25.980	86.3	1.289	-50.1019	90.9322	-0.009	18	121.503	5.393
101.5	2490.3	93.74	467,202	122.5	121.4	25.970	87.1	1.291	-50.1018	90.9285	-0.010	18	121.510	5.330
99.7	2490.9	90.69	455,496	121.4	120.3	28.386	85.6	1.262	-50.1018	90.9251	-0.007	18	119.052	5.469
103.5	2489.5	91.80	480,616	124.5	123.8	30.001	89.9	1.253	-50.1018	90.9214	-0.014	18	117.319	5.180
98.7	2489.7	69.82	448,886	126.4	125.4	26.146	82.3	1.210	-50.0698	93.3820	-0.016	19	92.327	5.546
96.9	2490.8	95.43	437,517	117.6	116.5	31.733	83.8	1.251	-50.1125	90.3347	-0.001	19	127.826	5.693
130.2	2487.0	89.38	483,779	152.5	151.0	24.175	115.0	1.293	-49.9856	92.1479	0.012	20	113.854	5.141
127.1	2487.5	85.32	464,654	149.7	149.0	33.862	113.8	1.207	-49.9856	92.1379	-0.014	20	110.894	5.353
131.0	2486.1	84.93	488,930	154.2	152.9	24.249	115.5	1.278	-49.9856	92.1279	-0.021	20	107.609	5.085
132.3	2486.4	87.36	497,351	154.6	153.6	19.373	115.6	1.335	-49.9856	92.1179	-0.018	20	109.757	4.999
135.3	2485.6	86.53	516,626	157.9	156.8	18.035	118.1	1.347	-49.9856	92.1079	0.001	20	106.662	4.811

Continued on next page...

Table E.1: Nano-indentation hardness data for generating depth profile in Sample 1 (continued)

h_c [nm]	P_{max} [μN]	S [μN/nm]	A [nm^2]	h_{max} [nm]	h_{eff} [nm]	A	h_f [nm]	m	X [mm]	Y [mm]	Drift Correction [nm/s]	Distance from Edge [μm]	E_r [GPa]	H [GPa]
112.6	2488.6	78.45	543,938	137.8	136.4	23.325	96.3	1.265	-50.1072	90.5338	-0.011	20	94.242	4.575
108.4	2489.1	74.29	514,319	134.7	133.6	32.826	94.1	1.178	-50.1075	90.5277	-0.002	20	91.777	4.840
131.6	2487.0	78.88	492,781	156.1	155.2	24.318	115.6	1.258	-49.9928	93.5122	0.067	25	99.564	5.047
127.2	2487.1	78.17	465,172	151.9	151.0	34.814	113.6	1.178	-49.9958	93.5090	0.042	25	101.547	5.347
129.4	2487.3	77.44	479,118	155.1	153.5	26.635	113.9	1.233	-49.9940	93.5028	0.027	25	99.121	5.191
132.3	2485.9	75.56	497,784	157.5	157.0	29.581	117.4	1.204	-49.9921	93.4975	0.015	25	94.884	4.994
129.3	2487.1	73.09	478,689	155.5	154.9	34.535	115.3	1.163	-49.9899	93.4931	0.018	25	93.592	5.196
130.4	2486.0	73.25	485,451	156.6	155.9	27.480	114.7	1.212	-49.9879	93.4880	0.024	25	93.144	5.121
130.2	2487.0	72.45	484,327	156.8	156.0	29.137	114.9	1.197	-49.9891	93.4829	0.010	25	92.236	5.135
130.5	2486.0	73.23	486,200	157.5	156.0	27.528	114.9	1.212	-49.9891	93.4775	0.011	25	93.050	5.113
131.3	2485.9	71.89	491,242	158.0	157.3	30.508	116.3	1.185	-49.9911	93.4714	0.012	25	90.881	5.060
131.6	2485.6	69.17	492,888	159.7	158.5	29.271	116.0	1.184	-49.9883	93.4678	0.006	25	87.296	5.043
133.8	2485.2	68.87	506,914	161.5	160.8	23.825	116.6	1.226	-49.9852	93.4649	-0.009	25	85.704	4.903
128.8	2487.3	90.00	475,379	150.3	149.5	27.363	114.5	1.268	-49.9906	92.1479	0.019	25	115.654	5.232
127.7	2486.4	88.83	468,551	149.5	148.7	29.153	113.7	1.251	-49.9906	92.1379	-0.021	25	114.984	5.307
130.1	2486.1	88.61	483,196	152.4	151.1	21.033	114.0	1.321	-49.9906	92.1279	-0.016	25	112.944	5.145
133.6	2485.8	87.89	505,604	155.8	154.8	17.755	116.4	1.355	-49.9906	92.1179	-0.023	25	109.518	4.917
136.2	2486.1	84.03	522,620	160.2	158.4	29.699	121.9	1.231	-49.9906	92.1079	-0.002	25	102.989	4.757
99.9	2489.7	72.44	456,685	126.7	125.7	34.585	85.8	1.160	-50.1042	90.5429	-0.027	25	94.979	5.452
105.1	2489.2	71.10	491,694	132.4	131.4	34.914	91.0	1.154	-50.1064	90.5392	-0.016	26	89.832	5.063
131.4	2487.1	90.69	491,490	152.9	151.9	25.408	116.7	1.286	-49.9956	92.1479	0.014	30	114.610	5.060
130.5	2486.7	89.08	486,007	152.6	151.4	24.052	115.3	1.293	-49.9956	92.1379	-0.019	30	113.215	5.117
132.2	2486.5	87.01	496,744	154.5	153.6	27.928	117.8	1.254	-49.9956	92.1279	-0.025	30	109.374	5.006
133.3	2486.3	83.57	503,811	156.3	155.6	31.626	119.4	1.216	-49.9956	92.1179	-0.032	30	104.314	4.935
134.7	2486.2	85.75	512,664	157.3	156.4	23.555	119.1	1.287	-49.9956	92.1079	-0.036	30	106.113	4.850
131.9	2486.4	88.72	495,169	153.7	153.0	28.861	117.9	1.252	-50.0006	92.1479	0.053	35	111.704	5.021
130.2	2485.9	80.10	483,836	153.3	153.4	48.686	119.0	1.111	-50.0006	92.1379	-0.016	35	102.027	5.138
130.5	2485.4	86.84	486,143	152.6	152.0	30.437	116.6	1.235	-50.0006	92.1279	-0.032	35	110.351	5.113
129.8	2486.3	81.24	481,608	153.3	152.8	45.398	118.2	1.130	-50.0056	92.1479	0.029	35	103.717	5.162
129.8	2486.3	81.24	481,608	153.3	152.8	45.398	118.2	1.130	-50.0056	92.1479	0.029	40	103.717	5.162
133.3	2485.8	91.13	503,905	154.8	153.8	26.201	118.8	1.281	-50.0056	92.1379	-0.020	40	113.736	4.933
135.8	2486.1	88.15	520,216	158.0	157.0	28.626	121.6	1.252	-50.0056	92.1179	0.012	40	108.290	4.779
137.0	2485.5	85.89	528,261	159.7	158.7	29.237	122.8	1.241	-50.0056	92.1079	-0.016	40	104.701	4.705

Continued on next page…

Table E.1: Nano-indentation hardness data for generating depth profile in Sample 1 (continued)

h_c [nm]	P_{max} [μN]	S [μN/nm]	A [nm^2]	h_{max} [nm]	h_{eff} [nm]	A	h_f [nm]	m	X [mm]	Y [mm]	Drift Correction [nm/s]	Distance from Edge [μm]	E_r [GPa]	H [GPa]
130.1	2487.1	86.23	483,287	152.4	151.7	30.736	116.2	1.231	-50.0166	93.5141	0.018	45	109.903	5.146
129.8	2485.5	83.60	481,664	152.9	152.1	26.157	114.7	1.258	-50.0187	93.5108	-0.021	45	106.726	5.160
130.7	2487.3	84.70	487,257	154.0	152.7	27.409	116.0	1.251	-50.0195	93.5043	0.007	45	107.510	5.105
130.7	2486.7	84.02	487,148	153.8	152.9	25.111	115.4	1.268	-50.0162	93.4982	-0.003	45	106.662	5.105
130.0	2486.6	81.42	482,932	153.7	152.9	29.865	115.6	1.222	-50.0140	93.4937	-0.017	45	103.810	5.149
131.0	2486.5	81.89	488,960	154.7	153.7	30.194	116.7	1.221	-50.0119	93.4892	0.001	45	103.756	5.085
133.7	2486.5	83.61	506,423	156.9	156.0	27.995	119.0	1.243	-50.0140	93.4831	0.040	45	104.101	4.910
132.1	2486.4	81.82	496,233	156.4	154.9	23.680	116.2	1.273	-50.0128	93.4786	-0.015	45	102.910	5.011
132.4	2486.5	82.24	498,432	156.8	155.1	26.825	117.4	1.248	-50.0105	93.4745	0.029	45	103.213	4.989
133.4	2486.3	80.43	504,331	157.8	156.6	24.356	117.5	1.262	-50.0083	93.4692	0.024	45	100.347	4.930
131.3	2486.5	74.66	491,203	157.4	156.3	35.860	117.7	1.160	-50.0026	93.4651	0.017	45	94.377	5.062

Table E.2: Nano-indentation hardness data for generating depth profile in Sample 2

h_c [nm]	P_{max} [μN]	S [μN/nm]	A [nm^2]	h_{max} [nm]	h_{eff} [nm]	A	h_f [nm]	m	X [mm]	Y [mm]	Drift Correction [nm/s]	Distance from Edge [μm]	E_r [GPa]	H [GPa]
132.0	2495.9	53.52	495,841	167.2	167.0	8.636	103.39	1.364	-65.0327	45.4954	1.722803	5	67.340	5.034
139.9	2494.1	54.77	547,683	174.6	174.1	8.135	111.15	1.382	-65.0331	45.4901	1.631729	5	65.568	4.554
129.1	2494.4	52.42	477,278	165.3	164.8	7.651	99.03	1.382	-65.0339	45.4807	1.407188	5	67.226	5.226
143.0	2491.3	53.79	568,803	178.4	177.8	6.888	112.49	1.410	-65.0376	45.4729	1.192981	5	63.188	4.380
138.7	2490.1	53.00	539,190	174.6	173.9	5.428	105.72	1.451	-65.0388	45.4650	0.968337	5	63.949	4.618
136.0	2489.3	51.50	521,609	172.8	172.3	4.671	101.12	1.472	-65.0379	45.4589	0.706576	5	63.184	4.772
126.8	2487.1	67.35	462,759	155.0	154.5	11.098	103.62	1.377	-65.0720	44.9892	0.202590	5	87.721	5.375
123.4	2487.5	69.50	441,838	151.0	150.2	22.601	105.85	1.240	-65.0712	44.9823	0.150007	5	92.633	5.630
123.2	2488.1	67.78	440,961	151.2	150.8	16.413	103.07	1.299	-65.0755	44.9778	0.152353	5	90.431	5.643
121.7	2487.4	71.19	431,799	148.6	147.9	20.880	103.80	1.262	-65.0714	44.9686	0.078091	5	95.984	5.761
124.5	2487.6	66.76	448,481	153.0	152.4	13.635	102.74	1.333	-65.0759	44.9574	0.092597	5	88.321	5.547
130.7	2486.3	65.39	487,281	159.9	159.2	17.866	110.84	1.272	-65.0790	44.9507	0.096137	5	82.994	5.102
123.2	2487.2	66.74	440,872	151.4	151.2	15.893	102.65	1.302	-65.0753	44.9439	0.010429	5	89.061	5.642
132.3	2486.9	56.77	497,456	165.5	165.2	6.063	101.66	1.449	-65.1043	44.8903	0.124444	5	71.313	4.999
125.5	2486.8	52.01	454,780	161.9	161.4	13.855	100.87	1.265	-65.1071	44.8863	0.119285	5	68.328	5.468
130.3	2485.4	49.64	484,433	168.3	167.8	14.610	105.55	1.243	-65.1062	44.8826	0.106592	5	63.188	5.131
130.2	2486.2	53.71	483,986	165.5	164.9	10.879	103.77	1.321	-65.1087	44.8789	0.084172	5	68.406	5.137
130.0	2485.5	54.68	482,657	164.8	164.1	9.934	103.02	1.343	-65.1063	44.8769	0.070821	5	69.739	5.150
120.8	2486.6	66.21	426,268	150.0	148.9	23.732	103.24	1.217	-65.1433	44.4250	-0.053434	10	89.845	5.833
124.6	2486.6	67.67	449,212	152.7	152.1	21.515	106.47	1.243	-65.1424	44.4228	0.004368	10	89.452	5.535
121.3	2487.0	68.21	429,425	150.0	148.7	16.849	101.42	1.296	-65.1421	44.4197	-0.005430	10	92.227	5.791
125.0	2487.0	65.76	451,449	154.2	153.3	22.684	107.00	1.225	-65.1429	44.4167	0.000858	10	86.710	5.509
124.6	2486.4	63.93	449,345	154.4	153.8	16.277	103.78	1.286	-65.1444	44.4142	0.004494	10	84.495	5.533
123.5	2486.5	63.14	442,788	154.0	153.1	20.587	104.46	1.234	-65.1459	44.4111	0.006815	10	84.072	5.616
130.5	2485.6	62.43	485,836	160.9	160.3	17.057	109.78	1.270	-65.1450	44.4085	-0.003445	10	79.362	5.116
129.0	2486.7	68.37	476,648	157.3	156.3	10.625	105.73	1.391	-65.1436	44.4053	-0.013257	10	87.743	5.217
123.5	2487.1	67.75	442,579	151.8	151.0	15.909	103.10	1.306	-65.1427	44.4017	-0.034175	10	90.229	5.620
141.9	2483.8	57.91	561,277	174.6	174.1	15.553	119.68	1.269	-65.0990	44.8970	-0.022826	12	68.489	4.425
134.0	2485.2	59.99	508,536	165.7	165.1	12.610	110.39	1.320	-65.0991	44.8942	0.021425	12	74.536	4.887
141.4	2484.5	56.05	557,897	175.6	174.7	9.715	114.67	1.354	-65.0993	44.8891	0.009741	12	66.482	4.453
139.2	2484.1	56.35	542,932	172.9	172.3	11.458	113.97	1.323	-65.0994	44.8843	0.016999	12	67.755	4.575
127.9	2486.2	58.84	469,767	160.3	159.6	18.950	107.49	1.233	-65.0997	44.8801	0.001980	12	76.059	5.292
126.6	2485.8	59.22	461,319	158.6	158.0	18.461	105.98	1.240	-65.0996	44.8762	0.016086	12	77.254	5.389

Continued on next page...

Table E.2: Nano-indentation hardness data for generating depth profile in Sample 2 (continued)

h_c [nm]	P_{max} [μN]	S [μN/nm]	A [nm^2]	h_{max} [nm]	h_{eff} [nm]	A	h_f [nm]	m	X [mm]	Y [mm]	Drift Correction [nm/s]	Distance from Edge [μm]	E_r [GPa]	H [GPa]
138.4	2487.7	56.30	537,592	172.0	171.6	6.139	107.74	1.445	-65.0243	45.4950	0.561743	15	68.034	4.627
134.5	2499.1	54.83	511,497	169.3	168.7	6.931	104.23	1.413	-65.0251	45.4883	0.473688	15	67.928	4.886
120.8	2487.3	72.06	426,560	147.8	146.7	19.332	102.47	1.282	-65.1359	44.4255	-0.035657	17	97.749	5.831
122.3	2487.2	68.28	435,076	150.3	149.6	28.033	106.22	1.190	-65.1346	44.4230	-0.031962	17	91.722	5.717
126.7	2486.8	68.95	462,079	154.5	153.7	25.940	110.14	1.209	-65.1340	44.4201	-0.029089	17	89.875	5.382
119.1	2486.3	65.70	416,232	148.4	147.5	24.071	101.59	1.212	-65.1351	44.4161	-0.021013	17	90.223	5.973
119.0	2487.7	64.54	415,899	149.0	147.9	25.069	101.70	1.199	-65.1368	44.4138	-0.003383	17	88.662	5.982
119.2	2487.3	62.65	417,138	149.5	149.0	21.529	100.45	1.223	-65.1384	44.4106	-0.012338	17	85.942	5.963
120.8	2486.0	60.66	426,171	151.8	151.5	28.571	104.07	1.157	-65.1373	44.4079	-0.036017	17	82.333	5.833
125.1	2485.9	65.73	452,274	154.2	153.5	20.985	106.53	1.241	-65.1370	44.4049	-0.002668	17	86.590	5.496
127.7	2486.4	64.49	468,401	157.2	156.6	21.803	109.28	1.228	-65.1353	44.4015	-0.008993	17	83.481	5.308
129.8	2485.7	61.41	481,303	160.6	160.1	17.271	108.99	1.263	-65.0927	44.8969	-0.046987	19	78.429	5.164
124.5	2485.8	59.99	448,477	156.1	155.5	19.108	104.30	1.237	-65.0927	44.8932	-0.021871	19	79.365	5.543
129.0	2486.1	62.30	476,408	159.6	158.9	17.641	108.53	1.262	-65.0929	44.8885	-0.011032	19	79.973	5.218
127.3	2486.3	63.06	465,907	157.7	156.9	20.154	108.05	1.238	-65.0930	44.8838	-0.000124	19	81.856	5.336
130.1	2485.4	60.90	483,766	161.5	160.8	15.460	108.38	1.283	-65.0927	44.8799	-0.013996	19	77.579	5.138
123.8	2485.7	58.98	444,531	156.4	155.4	19.209	103.53	1.231	-65.0937	44.8762	0.016205	19	78.383	5.592
121.8	2487.6	66.55	432,097	150.5	149.8	15.714	101.07	1.303	-65.0865	44.9001	0.106524	26	89.703	5.757
116.6	2488.2	66.65	401,599	145.4	144.6	16.717	96.37	1.291	-65.0858	44.8946	0.084030	26	93.177	6.196
119.2	2487.4	65.83	416,796	148.4	147.5	16.071	98.55	1.296	-65.0886	44.8906	0.070784	26	90.339	5.968
118.9	2487.5	65.27	414,924	148.5	147.4	19.942	99.83	1.249	-65.0877	44.8870	0.058682	26	89.770	5.995
122.2	2487.5	63.70	434,545	152.3	151.5	18.778	102.43	1.255	-65.0902	44.8832	0.057375	26	85.618	5.724
117.6	2487.9	63.42	407,331	147.7	147.0	16.521	96.75	1.280	-65.0878	44.8813	0.024247	26	88.042	6.108
116.5	2487.5	66.71	401,433	145.1	144.5	31.523	101.26	1.160	-65.1298	44.4236	-0.010579	27	93.293	6.196
118.0	2488.4	71.23	410,146	145.4	144.2	21.284	100.27	1.259	-65.1278	44.4199	0.052723	27	98.545	6.067
118.9	2488.1	72.45	415,398	145.4	144.7	18.729	100.40	1.290	-65.1286	44.4157	0.087608	27	99.597	5.990
117.0	2489.4	72.39	403,868	143.6	142.7	18.188	98.20	1.296	-65.1306	44.4118	0.088214	27	100.930	6.164
118.1	2487.4	72.06	410,518	145.2	144.0	28.322	102.52	1.201	-65.1302	44.4065	0.096602	27	99.644	6.059
120.9	2488.0	71.75	427,155	147.9	146.9	23.447	103.93	1.240	-65.1277	44.4032	0.038379	27	97.262	5.825
116.6	2488.8	73.44	401,546	143.3	142.0	18.881	98.20	1.292	-65.1232	44.4235	0.013388	32	102.688	6.198
117.9	2488.2	71.79	409,400	145.0	143.9	25.839	101.63	1.220	-65.1221	44.4189	0.031787	32	99.407	6.078
116.9	2487.9	73.61	403,370	143.4	142.2	20.821	99.24	1.272	-65.1238	44.4149	0.032196	32	102.693	6.168
118.8	2488.0	71.60	414,682	145.5	144.9	23.662	101.87	1.238	-65.1257	44.4113	0.031224	32	98.506	6.000

Continued on next page...

Table E.2: Nano-indentation hardness data for generating depth profile in Sample 2 (continued)

h_c [nm]	P_{max} [μN]	S [μN/nm]	A [nm^2]	h_{max} [nm]	h_{eff} [nm]	A	h_f [nm]	m	X [mm]	Y [mm]	Drift Correction [nm/s]	Distance from Edge [μm]	E_r [GPa]	H [GPa]
121.3	2487.7	71.65	429,389	147.9	147.3	22.807	104.10	1.246	-65.1241	44.4065	0.004874	32	96.878	5.794
121.3	2487.5	72.21	429,450	147.7	147.1	22.178	103.97	1.254	-65.1221	44.4030	-0.020011	32	97.634	5.792
123.1	2486.5	62.58	440,160	153.7	152.9	19.758	103.61	1.240	-65.0805	44.9014	-0.016341	33	83.571	5.649
122.2	2486.8	64.36	434,704	151.8	151.2	17.505	102.00	1.272	-65.0806	44.8985	0.002909	33	86.486	5.721
118.3	2487.6	65.66	411,921	147.6	146.8	16.480	97.89	1.290	-65.0808	44.8934	-0.001638	33	90.643	6.039
110.5	2488.6	66.06	367,326	139.7	138.8	19.271	91.30	1.259	-65.0809	44.8886	0.002827	33	96.566	6.775
118.2	2487.3	68.28	411,312	146.4	145.6	20.742	99.92	1.253	-65.0812	44.8844	0.007603	33	94.328	6.047
117.8	2487.0	66.62	408,951	146.5	145.8	22.703	100.00	1.228	-65.0811	44.8805	-0.028992	33	92.302	6.081
114.2	2487.5	73.85	388,168	140.1	139.5	23.780	97.55	1.245	-65.1150	44.4190	0.005282	39	105.016	6.408
117.0	2487.6	70.71	403,932	144.1	143.4	27.471	101.03	1.203	-65.1166	44.4145	-0.010499	39	98.572	6.158
119.0	2487.9	71.44	415,676	145.9	145.1	23.460	101.96	1.239	-65.1184	44.4114	-0.000351	39	98.171	5.985
116.8	2487.9	73.13	402,711	142.8	142.3	23.328	99.88	1.246	-65.1170	44.4064	-0.015421	39	102.107	6.178
120.4	2487.1	74.78	423,939	146.3	145.3	25.278	104.25	1.235	-65.1151	44.4029	-0.007466	39	101.763	5.867
118.5	2487.0	67.89	412,700	147.0	145.9	16.205	98.24	1.302	-65.0741	44.9013	-0.035753	40	93.637	6.026
119.9	2486.8	66.24	420,902	148.7	148.0	18.926	100.58	1.264	-65.0741	44.8976	-0.024572	40	90.457	5.908
120.1	2487.4	68.80	422,056	147.9	147.2	14.152	98.96	1.334	-65.0743	44.8928	-0.019393	40	93.823	5.894
119.6	2486.8	66.51	419,080	148.5	147.6	19.319	100.47	1.261	-65.0744	44.8881	-0.024766	40	91.033	5.934
122.1	2486.1	66.80	434,047	150.7	150.0	21.246	103.76	1.242	-65.0741	44.8842	-0.025881	40	89.828	5.728
119.3	2486.9	67.09	417,770	147.6	147.1	26.691	102.81	1.196	-65.0752	44.8805	-0.017120	40	91.966	5.953
111.8	2488.8	66.77	374,798	140.3	139.8	15.756	91.21	1.304	-65.0675	44.9001	0.054574	47	96.637	6.640
112.6	2488.0	65.84	378,969	141.2	140.9	25.819	95.65	1.198	-65.0668	44.8946	0.045508	47	94.764	6.565
115.9	2488.1	66.25	397,770	144.6	144.1	19.174	96.70	1.261	-65.0696	44.8906	0.053815	47	93.063	6.255
118.1	2487.5	66.46	410,547	146.9	146.2	18.352	98.60	1.271	-65.0687	44.8870	0.045082	47	91.897	6.059
118.2	2486.7	62.96	411,150	148.3	147.8	21.739	99.55	1.222	-65.0712	44.8832	0.034973	47	86.997	6.048
120.7	2487.0	64.23	425,787	150.3	149.7	17.972	100.70	1.266	-65.0688	44.8813	0.017226	47	87.207	5.841
116.7	2488.3	74.79	402,451	142.7	141.7	15.206	97.02	1.342	-65.1112	44.4246	0.017637	47	104.458	6.183
117.2	2488.2	73.60	405,337	143.5	142.6	23.361	100.39	1.248	-65.1085	44.4220	0.012275	47	102.432	6.139
111.8	2489.0	74.46	374,497	138.0	136.9	25.180	95.58	1.235	-65.1072	44.4168	0.036636	47	107.809	6.646
116.5	2488.6	74.64	400,969	142.3	141.5	22.281	99.41	1.261	-65.1090	44.4126	0.046381	47	104.429	6.206
116.6	2488.5	77.16	401,603	141.5	140.8	15.844	97.47	1.342	-65.1111	44.4078	0.041153	47	107.884	6.196
119.1	2488.8	79.05	416,520	143.5	142.7	20.238	101.90	1.297	-65.1093	44.4032	0.013492	47	108.525	5.975
117.3	2486.5	72.50	406,124	144.0	143.1	24.092	100.64	1.237	-65.1045	44.4260	-0.068978	52	100.799	6.122
115.3	2488.4	77.33	394,478	141.1	139.5	23.256	98.86	1.262	-65.1019	44.4158	0.003707	52	109.092	6.308

Continued on next page. . .

Table E.2: Nano-indentation hardness data for generating depth profile in Sample 2 (continued)

h_c [nm]	P_{max} [μN]	S [μN/nm]	A [nm^2]	h_{max} [nm]	h_{eff} [nm]	A	h_f [nm]	m	X [mm]	Y [mm]	Drift Correction [nm/s]	Distance from Edge [μm]	E_r [GPa]	H [GPa]
115.5	2489.2	75.38	395,736	141.1	140.3	25.013	99.39	1.239	-65.1034	44.4117	0.011771	52	106.167	6.290
114.0	2488.6	74.14	387,129	139.9	139.2	21.583	96.71	1.266	-65.1047	44.4077	0.014512	52	105.574	6.428
117.5	2487.8	75.95	406,943	142.9	142.1	25.190	101.44	1.240	-65.1023	44.4031	0.004372	52	105.492	6.113
115.6	2486.9	69.80	396,314	143.1	142.4	20.561	97.46	1.260	-65.0615	44.9014	-0.014616	54	98.236	6.275
120.1	2487.4	69.98	422,460	147.6	146.8	23.821	103.06	1.230	-65.0616	44.8985	0.009407	54	95.387	5.888
116.1	2487.6	68.21	398,938	144.1	143.5	20.210	97.58	1.258	-65.0618	44.8934	0.003768	54	95.676	6.236
119.0	2487.4	67.94	415,873	147.1	146.5	18.162	99.65	1.279	-65.0619	44.8886	0.011603	54	93.349	5.981
119.2	2486.5	68.31	416,684	147.2	146.5	17.445	99.54	1.289	-65.0622	44.8844	0.005474	54	93.762	5.967
117.7	2488.3	79.01	407,885	142.0	141.3	24.217	101.63	1.259	-65.0934	44.4253	-0.067175	59	109.609	6.101
113.6	2488.7	77.69	384,771	137.9	137.6	19.708	96.06	1.298	-65.0929	44.4163	-0.001781	59	110.972	6.468
110.0	2489.2	78.42	364,430	134.5	133.8	20.956	92.91	1.288	-65.0964	44.4122	0.001290	59	115.101	6.830
117.2	2487.7	77.32	405,479	142.0	141.4	23.385	100.81	1.260	-65.0972	44.4075	0.001100	59	107.589	6.135
115.7	2487.6	70.85	396,724	142.5	142.1	42.797	103.10	1.109	-65.0950	44.4032	-0.026880	59	99.660	6.270
122.3	2486.5	72.46	435,367	148.8	148.0	19.451	104.05	1.282	-65.0551	44.9013	-0.005954	61	97.299	5.711
118.5	2487.3	69.19	413,127	146.2	145.5	21.275	100.54	1.251	-65.0551	44.8976	-0.005035	61	95.375	6.021
117.1	2488.0	69.21	404,759	144.5	144.1	20.287	98.74	1.261	-65.0553	44.8928	-0.001148	61	96.379	6.147
118.1	2487.2	67.48	410,682	146.5	145.8	20.808	99.73	1.249	-65.0554	44.8881	-0.016143	61	93.291	6.056
120.6	2487.1	69.65	424,952	148.3	147.3	17.524	101.17	1.293	-65.0551	44.8842	-0.004689	61	94.670	5.853
122.4	2486.8	68.19	435,971	150.4	149.8	18.328	103.14	1.278	-65.0562	44.8805	0.002734	61	91.495	5.704
113.3	2488.6	81.03	382,899	137.1	136.3	9.798	91.58	1.457	-65.0916	44.4247	0.031156	67	116.026	6.499
112.2	2489.4	80.02	377,045	136.4	135.6	21.554	95.54	1.287	-65.0910	44.4183	0.060347	67	115.469	6.602
115.6	2487.6	76.15	395,849	140.7	140.1	25.032	99.50	1.242	-65.0904	44.4127	0.033639	67	107.239	6.284
117.1	2488.0	77.52	404,701	141.8	141.2	23.119	100.62	1.264	-65.0901	44.4096	0.040585	67	107.970	6.148
113.8	2489.1	81.57	386,046	137.6	136.7	22.038	97.44	1.288	-65.0897	44.4056	0.035842	67	116.322	6.448
115.0	2488.8	79.96	392,821	139.1	138.4	26.237	99.63	1.245	-65.0897	44.4020	0.008491	67	113.030	6.336
114.6	2487.6	78.53	390,345	139.0	138.4	24.547	98.63	1.254	-65.0861	44.4217	0.021146	72	111.370	6.373
114.7	2488.1	78.63	391,044	139.2	138.5	22.373	98.13	1.274	-65.0860	44.4188	0.004023	72	111.406	6.363
116.0	2488.6	79.76	398,063	140.0	139.4	23.649	99.84	1.266	-65.0856	44.4141	0.009040	72	112.006	6.252
112.8	2488.3	79.16	380,147	137.0	136.4	21.158	95.88	1.288	-65.0856	44.4097	-0.007350	72	113.748	6.546
113.2	2488.1	76.26	382,558	138.4	137.7	28.487	98.06	1.215	-65.0854	44.4056	0.002704	72	109.241	6.504
114.5	2488.8	80.46	389,780	138.4	137.7	28.232	99.63	1.231	-65.0854	44.4020	0.004448	72	114.187	6.385
114.5	2487.9	78.95	389,654	138.6	138.1	26.032	98.94	1.243	-65.0799	44.4233	-0.031061	77	112.059	6.385
115.2	2487.9	81.21	393,893	139.2	138.2	20.140	98.20	1.306	-65.0799	44.4190	-0.000286	77	114.647	6.316

Continued on next page...

Table E.2: Nano-indentation hardness data for generating depth profile in Sample 2 (continued)

h_c [nm]	P_{max} [μN]	S [μN/nm]	A [nm^2]	h_{max} [nm]	h_{eff} [nm]	A	h_f [nm]	m	X [mm]	Y [mm]	Drift Correction [nm/s]	Distance from Edge [μm]	E_r [GPa]	H [GPa]
113.2	2488.2	79.02	382,233	137.4	136.8	24.235	97.15	1.259	-65.0798	44.4125	-0.012784	77	113.249	6.510
114.3	2488.8	77.82	388,810	138.9	138.3	29.087	99.44	1.216	-65.0797	44.4095	0.003106	77	110.581	6.401
112.7	2489.3	82.09	379,845	136.0	135.5	23.638	96.84	1.274	-65.0796	44.4055	-0.014877	77	118.013	6.553
117.0	2488.5	83.52	403,920	140.2	139.3	19.125	99.85	1.325	-65.0790	44.4021	-0.000962	77	116.427	6.161
115.1	2488.4	76.68	393,289	139.7	139.5	29.822	100.31	1.206	-65.0751	44.4248	-0.024195	82	108.329	6.327
112.9	2488.1	79.41	380,538	137.1	136.4	22.360	96.35	1.277	-65.0747	44.4201	-0.015945	82	114.058	6.538
114.8	2488.0	79.87	391,259	138.6	138.1	21.290	97.96	1.289	-65.0746	44.4162	-0.006287	82	113.132	6.359
117.4	2487.4	79.61	406,401	141.5	140.8	23.205	101.15	1.270	-65.0746	44.4130	-0.003654	82	110.639	6.120
115.7	2488.4	77.27	396,889	140.6	139.9	27.382	100.40	1.227	-65.0745	44.4097	-0.024216	82	108.677	6.270
113.6	2488.2	80.54	384,402	137.1	136.7	29.462	98.98	1.222	-65.0741	44.4050	-0.010048	82	115.097	6.473

Table E.3: Nano-indentation hardness data for generating depth profile in Sample 3

h_c [nm]	P_{max} [μN]	S [μN/nm]	A [nm^2]	h_{max} [nm]	h_{eff} [nm]	A	h_f [nm]	m	X [mm]	Y [mm]	Drift Correction [nm/s]	Distance from Edge [μm]	E_r [GPa]	H [GPa]
94.0	2491.4	120.41	418,744	110.8	109.5	22.312	80.5	1.401	-64.4341	-5.8949	0.020	5	164.856	5.950
93.5	2491.0	119.93	415,999	110.3	109.1	32.152	81.8	1.315	-64.4347	-5.8988	0.010	5	164.752	5.988
97.2	2491.1	120.91	438,993	113.3	112.6	29.496	85.1	1.338	-64.4352	-5.9017	0.005	5	161.690	5.675
102.0	2490.8	118.57	470,764	119.1	117.8	23.096	88.6	1.388	-64.4366	-5.9412	0.058	5	153.115	5.291
97.8	2491.8	109.06	443,434	115.8	115.0	27.048	84.7	1.326	-64.4367	-5.2873	0.133	5	145.112	5.619
96.3	2491.1	123.02	433,646	112.6	111.5	30.189	84.4	1.338	-64.4306	-5.3017	-0.071	5	165.511	5.745
101.4	2490.9	126.42	466,360	117.5	116.1	27.067	89.1	1.372	-64.4323	-5.2574	0.037	5	164.021	5.341
99.0	2491.0	121.84	451,088	115.5	114.4	32.847	87.5	1.315	-64.4317	-5.2755	0.010	5	160.733	5.522
95.7	2492.0	123.78	429,999	111.8	110.8	19.983	82.0	1.435	-64.4300	-5.8784	0.061	6	167.248	5.795
94.9	2491.3	131.37	424,851	110.0	109.2	30.513	83.4	1.356	-64.4308	-5.8812	0.080	6	178.570	5.864
95.7	2492.1	116.60	429,667	112.7	111.7	31.324	83.7	1.313	-64.4315	-5.8846	0.046	6	157.603	5.800
97.9	2491.1	114.98	443,503	114.9	114.1	39.144	86.9	1.257	-64.4333	-5.8875	0.042	6	152.966	5.617
97.3	2491.6	118.89	440,043	113.6	113.0	27.999	84.9	1.344	-64.4327	-5.8909	0.020	6	158.787	5.662
95.3	2491.0	115.49	427,059	112.6	111.5	36.497	84.0	1.274	-64.4358	-5.9329	0.105	6	156.577	5.833
99.0	2490.8	119.15	450,942	115.7	114.7	22.337	85.5	1.397	-64.4366	-5.9376	0.085	6	157.203	5.524
92.3	2490.5	113.21	408,177	110.0	108.8	31.934	80.2	1.299	-64.4304	-5.9209	-0.033	6	156.999	6.101
96.6	2491.2	127.56	435,619	112.2	111.3	26.717	84.4	1.378	-64.4294	-5.2989	-0.084	6	171.236	5.719
102.6	2490.9	123.44	474,764	118.8	117.8	30.245	90.8	1.338	-64.4327	-5.2540	0.037	6	158.722	5.247
101.6	2490.4	124.73	467,629	117.3	116.5	29.784	89.7	1.345	-64.4318	-5.2620	0.033	6	161.604	5.326
99.1	2491.1	123.34	451,653	115.3	114.3	41.604	88.8	1.263	-64.4315	-5.2667	0.018	6	162.604	5.515
99.6	2491.6	121.09	454,792	116.7	115.0	30.276	87.6	1.332	-64.4315	-5.2722	0.021	6	159.084	5.478
97.8	2490.9	117.58	443,353	114.6	113.7	29.613	85.6	1.328	-64.4310	-5.5882	-0.006	7	156.457	5.618
94.3	2490.8	116.11	420,996	111.8	110.4	32.179	82.4	1.305	-64.4304	-5.5912	-0.010	7	158.543	5.916
95.7	2490.8	120.96	429,859	112.4	111.2	20.835	82.0	1.418	-64.4303	-5.5941	0.015	7	163.465	5.794
96.4	2491.2	127.07	434,219	112.3	111.1	16.580	82.0	1.486	-64.4305	-5.5975	0.020	7	170.850	5.737
97.3	2491.7	116.45	439,924	114.1	113.4	33.156	85.6	1.299	-64.4307	-5.6013	0.009	7	155.552	5.664
100.5	2490.9	114.76	460,836	117.0	116.8	36.508	89.2	1.273	-64.4316	-5.6089	0.016	7	149.783	5.405
97.4	2491.1	118.54	440,355	114.4	113.1	32.016	85.5	1.313	-64.4309	-5.9243	0.010	7	158.269	5.657
93.8	2490.9	121.72	417,438	110.3	109.1	26.251	81.1	1.367	-64.4314	-5.9271	-0.005	7	166.914	5.967
94.1	2492.2	123.10	419,806	110.4	109.3	20.449	80.4	1.428	-64.4326	-5.2934	-0.073	7	168.338	5.936
97.1	2490.5	114.13	438,652	114.2	113.5	32.350	85.1	1.299	-64.4307	-5.6053	-0.004	8	152.675	5.678
99.3	2490.0	116.31	452,913	116.3	115.4	32.304	87.4	1.305	-64.4339	-5.2904	-0.048	8	153.122	5.498
93.7	2491.3	120.04	417,247	110.9	109.3	29.555	81.6	1.335	-64.4318	-5.9307	-0.011	9	164.648	5.971

Continued on next page...

Table E.3: Nano-indentation hardness data for generating depth profile in Sample 3 (continued)

h_c [nm]	P_{max} [μN]	S [μN/nm]	A [nm^2]	h_{max} [nm]	h_{eff} [nm]	A	h_f [nm]	m	X [mm]	Y [mm]	Drift Correction [nm/s]	Distance from Edge [μm]	E_r [GPa]	H [GPa]
97.6	2490.9	121.76	441,701	114.3	112.9	26.822	85.1	1.362	-64.4328	-5.9418	-0.025	9	162.319	5.639
95.5	2490.9	124.50	428,333	111.6	110.5	22.852	82.4	1.406	-64.4266	-5.9220	-0.047	9	168.547	5.815
98.9	2491.1	128.44	450,389	114.7	113.5	16.397	84.5	1.493	-64.4283	-5.2763	-0.006	9	169.566	5.531
95.3	2491.9	125.81	427,283	111.6	110.2	36.186	84.4	1.302	-64.4298	-5.8962	-0.005	10	170.521	5.832
100.1	2490.9	129.13	457,737	115.5	114.5	35.576	89.2	1.314	-64.4306	-5.9001	0.001	10	169.101	5.442
97.6	2491.0	122.47	441,702	113.9	112.8	28.634	85.4	1.349	-64.4321	-5.9337	-0.003	10	163.271	5.640
99.7	2491.2	124.72	455,742	116.3	114.7	26.850	87.4	1.369	-64.4331	-5.2785	-0.037	10	163.685	5.466
103.8	2490.2	127.43	482,884	119.2	118.5	26.237	91.5	1.381	-64.4343	-5.2831	-0.019	10	162.476	5.157
96.5	2491.4	127.78	434,954	111.8	111.2	29.397	84.7	1.356	-64.4261	-5.2995	-0.052	10	171.656	5.728
99.9	2490.3	122.52	457,012	116.1	115.2	34.511	88.7	1.305	-64.4265	-5.2609	0.002	10	160.570	5.449
99.7	2490.2	125.75	455,549	115.5	114.6	28.738	87.7	1.356	-64.4260	-5.2650	-0.014	10	165.078	5.466
96.8	2491.1	120.37	436,662	113.0	112.3	38.025	85.9	1.277	-64.4277	-5.8910	-0.019	11	161.389	5.705
97.0	2490.4	123.85	438,006	112.9	112.1	22.732	83.8	1.405	-64.4323	-5.9366	-0.015	11	165.797	5.686
98.1	2490.8	122.33	445,250	115.0	113.4	17.184	83.6	1.465	-64.4322	-5.9395	-0.015	11	162.431	5.594
91.8	2491.7	115.20	405,310	109.5	108.0	29.780	79.5	1.321	-64.4271	-5.9249	-0.011	11	160.317	6.148
93.9	2490.6	119.56	418,075	110.9	109.5	23.504	80.6	1.386	-64.4273	-5.9271	-0.034	11	163.831	5.957
94.3	2491.2	116.86	421,139	111.8	110.3	34.290	82.8	1.292	-64.4274	-5.9300	-0.023	11	159.553	5.915
101.7	2490.7	125.96	468,809	117.8	116.6	30.878	90.1	1.340	-64.4259	-5.2578	-0.006	11	162.989	5.313
97.6	2490.6	126.54	442,072	113.5	112.4	22.933	84.6	1.410	-64.4258	-5.2713	-0.008	11	168.624	5.634
94.6	2491.2	120.82	422,532	110.9	110.0	25.998	81.9	1.367	-64.4248	-5.8848	-0.019	12	164.686	5.896
97.6	2491.0	122.99	441,955	113.8	112.8	28.809	85.5	1.348	-64.4261	-5.8879	-0.022	12	163.919	5.636
99.0	2490.8	125.75	451,187	114.7	113.9	30.524	87.3	1.342	-64.4279	-5.9019	-0.007	12	165.863	5.521
92.1	2491.4	119.33	407,477	108.7	107.8	31.237	80.2	1.320	-64.4259	-5.5884	-0.043	12	165.624	6.114
93.5	2491.4	120.96	415,997	110.4	109.0	20.707	79.7	1.419	-64.4253	-5.5913	-0.021	12	166.161	5.989
95.1	2491.0	114.46	425,595	112.0	111.4	42.580	84.5	1.236	-64.4252	-5.5941	-0.012	12	155.445	5.853
96.4	2491.0	120.74	433,915	112.5	111.8	22.723	83.0	1.397	-64.4252	-5.5979	-0.004	12	162.404	5.741
97.9	2491.1	125.21	443,786	113.6	112.8	15.913	83.2	1.491	-64.4254	-5.6016	-0.010	12	166.526	5.613
97.1	2490.0	123.02	438,309	113.6	112.2	32.219	85.5	1.323	-64.4327	-5.2865	-0.065	12	164.639	5.681
101.2	2490.9	126.10	465,120	116.9	116.0	27.435	89.0	1.368	-64.4264	-5.2547	-0.011	12	163.818	5.355
95.3	2491.1	115.96	427,099	112.1	111.4	45.081	85.1	1.226	-64.4242	-5.8814	-0.021	13	157.216	5.832
96.3	2491.7	110.02	433,366	114.0	113.3	64.640	87.7	1.127	-64.4260	-5.8946	-0.019	13	148.074	5.750
99.2	2491.4	126.65	452,012	115.0	113.9	17.639	85.0	1.471	-64.4252	-5.6055	-0.003	13	166.905	5.512
97.5	2490.4	118.57	441,133	114.1	113.2	23.869	84.3	1.380	-64.4264	-5.6101	-0.004	13	158.166	5.645

Continued on next page...

Table E.3: Nano-indentation hardness data for generating depth profile in Sample 3 (continued)

h_c [nm]	P_{max} [μN]	S [μN/nm]	A [nm^2]	h_{max} [nm]	h_{eff} [nm]	A	h_f [nm]	m	X [mm]	Y [mm]	Drift Correction [nm/s]	Distance from Edge [μm]	E_r [GPa]	H [GPa]
97.4	2490.2	119.18	440,728	114.7	113.1	26.807	84.8	1.355	-64.4222	-5.9224	-0.052	13	159.053	5.650
93.5	2491.9	116.42	415,649	110.5	109.5	27.780	80.8	1.340	-64.4233	-5.8786	-0.066	14	159.991	5.995
98.1	2490.3	120.80	445,148	114.7	113.6	33.399	86.6	1.309	-64.4275	-5.9337	-0.020	14	160.411	5.594
97.3	2489.7	124.76	439,905	113.1	112.3	24.704	84.6	1.389	-64.4283	-5.9368	-0.011	14	166.659	5.660
98.4	2490.8	121.24	446,856	114.9	113.8	28.177	86.1	1.349	-64.4288	-5.9424	-0.020	14	160.690	5.574
96.2	2491.3	124.11	432,671	111.9	111.2	33.951	84.9	1.313	-64.4276	-5.2900	-0.074	14	167.172	5.758
99.1	2489.3	123.37	451,222	115.2	114.2	26.126	86.5	1.372	-64.4266	-5.2934	-0.079	14	162.726	5.517
99.6	2490.4	125.01	454,732	115.3	114.5	27.011	87.3	1.369	-64.4244	-5.2787	-0.089	14	164.246	5.477
94.5	2490.8	128.80	422,040	110.2	109.0	23.683	81.7	1.409	-64.4285	-5.9390	-0.017	15	175.667	5.902
97.8	2491.0	120.05	443,413	114.1	113.4	37.179	86.8	1.282	-64.4289	-5.2803	-0.092	15	159.734	5.618
98.4	2491.0	126.12	446,851	114.0	113.2	28.015	86.3	1.363	-64.4295	-5.2830	-0.080	15	167.164	5.575
99.1	2490.9	124.81	451,381	114.7	114.0	28.785	87.0	1.353	-64.4288	-5.2857	-0.065	15	164.596	5.518
100.2	2490.0	133.11	458,923	115.0	114.3	18.933	86.7	1.472	-64.4219	-5.2979	-0.062	15	174.091	5.426
100.2	2491.6	129.92	458,639	115.3	114.6	24.663	87.7	1.402	-64.4208	-5.3022	-0.073	15	169.970	5.432
95.3	2491.9	122.76	426,854	111.5	110.5	25.519	82.5	1.376	-64.4204	-5.2652	-0.019	15	166.476	5.838
100.5	2491.0	130.08	460,866	116.3	114.9	19.195	86.9	1.461	-64.4218	-5.2766	-0.006	15	169.770	5.405
96.8	2489.9	123.25	436,475	113.0	111.9	34.200	85.5	1.309	-64.4230	-5.8921	-0.019	16	165.288	5.704
94.9	2491.2	117.90	424,945	112.1	110.8	32.556	83.2	1.307	-64.4229	-5.9290	-0.019	16	160.247	5.862
101.7	2490.2	121.92	468,584	117.9	117.0	23.587	88.6	1.392	-64.4206	-5.2690	-0.012	16	157.804	5.314
98.0	2491.1	125.59	444,636	113.9	112.9	24.465	85.3	1.393	-64.4206	-5.2722	-0.018	16	166.867	5.603
97.2	2490.8	121.36	439,077	113.7	112.6	37.295	86.2	1.284	-64.4200	-5.8846	-0.030	17	162.273	5.673
99.2	2490.8	120.30	452,348	115.3	114.8	37.916	88.3	1.278	-64.4211	-5.8887	-0.026	17	158.473	5.506
99.3	2490.4	122.84	452,879	115.6	114.5	29.414	87.3	1.343	-64.4206	-5.2547	-0.028	17	161.732	5.499
98.8	2492.0	125.30	449,542	115.0	113.7	25.120	86.1	1.386	-64.4200	-5.2576	-0.036	17	165.574	5.543
96.4	2491.2	125.28	434,097	112.7	111.3	25.143	83.7	1.386	-64.4201	-5.2598	-0.023	17	168.473	5.739
94.2	2491.1	121.99	420,527	110.3	109.6	24.546	81.3	1.383	-64.4187	-5.8793	-0.036	18	166.671	5.924
95.7	2491.0	123.47	429,709	111.6	110.8	26.639	83.2	1.368	-64.4196	-5.5885	-0.042	18	166.875	5.797
96.7	2490.5	127.52	435,934	112.1	111.3	23.103	83.8	1.411	-64.4194	-5.5921	-0.018	18	171.123	5.713
96.0	2491.1	125.46	431,459	111.8	110.9	22.748	82.9	1.409	-64.4195	-5.5957	-0.016	18	169.225	5.774
96.0	2491.3	127.86	431,389	111.8	110.6	25.449	83.5	1.390	-64.4195	-5.6008	-0.003	18	172.475	5.775
98.1	2490.9	119.86	445,326	114.9	113.7	32.352	86.4	1.314	-64.4231	-5.9327	-0.017	18	159.139	5.593
96.4	2490.9	130.27	434,083	111.7	110.7	22.577	83.5	1.424	-64.4237	-5.2881	-0.051	18	175.188	5.738
98.7	2490.5	127.80	448,992	114.3	113.3	25.215	86.2	1.392	-64.4224	-5.2926	-0.073	18	168.987	5.547

Continued on next page…

Table E.3: Nano-indentation hardness data for generating depth profile in Sample 3 (continued)

h_c [nm]	P_{max} [μN]	S [μN/nm]	A [nm^2]	h_{max} [nm]	h_{eff} [nm]	A	h_f [nm]	m	X [mm]	Y [mm]	Drift Correction [nm/s]	Distance from Edge [μm]	E_r [GPa]	H [GPa]
96.4	2490.5	127.70	434,145	111.9	111.0	22.894	83.5	1.414	-64.4192	-5.6050	-0.010	19	171.714	5.737
98.5	2490.8	122.38	447,922	114.5	113.8	27.353	86.2	1.359	-64.4193	-5.6088	-0.014	19	162.012	5.561
100.1	2490.9	125.10	458,106	115.7	115.0	22.290	86.9	1.413	-64.4196	-5.6116	0.000	19	163.762	5.437
99.6	2490.2	130.32	454,919	115.2	114.0	17.822	85.7	1.478	-64.4232	-5.9366	-0.011	19	171.185	5.474
97.6	2491.7	127.52	441,775	113.5	112.2	19.597	83.9	1.449	-64.4227	-5.9402	-0.005	20	169.988	5.640
97.4	2490.4	125.53	440,827	113.6	112.3	27.120	85.2	1.369	-64.4215	-5.9435	-0.001	20	167.519	5.649
98.1	2491.0	123.68	444,782	114.1	113.2	33.355	86.7	1.316	-64.4242	-5.2823	-0.074	20	164.314	5.601
100.4	2491.0	125.07	460,038	116.1	115.3	34.388	89.2	1.312	-64.4238	-5.2854	-0.054	20	163.371	5.415
95.3	2492.0	121.04	426,933	111.5	110.7	26.131	82.6	1.366	-64.4207	-5.2651	0.093	22	164.124	5.837
96.0	2491.8	117.02	431,656	113.2	112.0	34.039	84.4	1.294	-64.4208	-5.2685	0.081	22	157.808	5.773
96.8	2491.5	119.91	436,456	113.4	112.3	28.487	84.4	1.343	-64.4206	-5.2723	0.059	22	160.806	5.708
97.5	2492.4	121.50	441,212	114.2	112.9	34.640	86.2	1.302	-64.4199	-5.2575	0.117	23	162.069	5.649
99.2	2491.7	129.01	452,451	115.0	113.7	23.366	86.4	1.412	-64.4198	-5.2619	0.106	23	169.928	5.507
96.3	2491.6	119.60	433,556	113.0	111.9	38.602	85.4	1.272	-64.4194	-5.2541	0.137	24	160.932	5.747
97.3	2491.4	123.92	439,655	113.6	112.3	28.826	85.2	1.351	-64.4146	-5.2539	0.022	27	165.578	5.667
100.5	2490.8	129.28	460,587	115.7	114.9	22.692	87.6	1.420	-64.4151	-5.2576	0.054	27	168.782	5.408
99.4	2491.2	132.36	453,693	114.7	113.5	23.814	86.9	1.416	-64.4150	-5.2620	0.031	27	174.106	5.491
96.9	2491.9	123.39	437,143	112.9	112.0	24.177	83.9	1.390	-64.4156	-5.2664	0.026	27	165.347	5.701
97.1	2492.3	117.02	438,328	113.9	113.0	43.811	86.7	1.236	-64.4158	-5.2707	0.008	27	156.597	5.686
96.2	2491.5	118.96	433,111	113.5	111.9	35.827	85.0	1.288	-64.4157	-5.2733	0.016	27	160.151	5.753
98.7	2490.9	128.16	448,736	114.1	113.2	21.759	85.5	1.427	-64.4120	-5.2757	-0.013	30	169.503	5.551
98.2	2491.0	125.12	445,533	114.0	113.1	28.994	86.2	1.352	-64.4109	-5.2641	-0.008	31	166.079	5.591
98.1	2491.0	119.87	444,887	115.2	113.7	35.019	86.7	1.295	-64.4113	-5.2683	0.003	31	159.225	5.599
99.8	2491.0	124.19	456,261	116.1	114.9	24.732	87.1	1.387	-64.4116	-5.2709	-0.005	31	162.903	5.460
96.8	2490.7	125.80	436,908	112.7	111.7	32.810	85.4	1.325	-64.4104	-5.2598	0.006	32	168.621	5.701
95.2	2490.8	127.35	426,376	111.0	109.8	25.212	82.6	1.391	-64.4088	-5.2542	-0.022	33	172.798	5.842
94.6	2491.4	120.15	422,962	111.1	110.2	25.395	81.8	1.370	-64.4075	-5.2729	-0.015	35	163.686	5.890
101.2	2490.8	126.69	465,080	117.1	115.9	18.372	87.2	1.462	-64.4076	-5.2766	-0.010	35	164.595	5.356
99.5	2491.0	125.89	454,031	115.7	114.3	27.248	87.2	1.369	-64.4056	-5.2635	-0.002	36	165.537	5.486
96.9	2490.8	128.87	437,064	112.2	111.4	24.576	84.3	1.400	-64.4064	-5.2673	-0.008	36	172.706	5.699
98.8	2491.0	130.11	449,679	114.4	113.2	20.630	85.5	1.444	-64.4052	-5.2591	-0.008	37	171.911	5.540
98.1	2491.4	124.17	445,192	114.6	113.2	29.511	86.2	1.346	-64.4038	-5.2545	-0.035	38	164.877	5.596
94.8	2491.4	127.49	423,959	110.7	109.4	24.796	82.2	1.395	-64.4035	-5.2712	-0.011	38	173.486	5.877

Continued on next page...

Table E.3: Nano-indentation hardness data for generating depth profile in Sample 3 (continued)

h_c [nm]	P_{max} [μN]	S [μN/nm]	A [nm^2]	h_{max} [nm]	h_{eff} [nm]	A	h_f [nm]	m	X [mm]	Y [mm]	Drift Correction [nm/s]	Distance from Edge [μm]	E_r [GPa]	H [GPa]
97.7	2490.1	119.60	442,335	114.3	113.3	28.942	85.4	1.339	-64.4041	-5.2759	-0.016	38	159.328	5.629
98.6	2491.3	125.72	448,117	114.8	113.4	30.354	86.8	1.343	-64.4026	-5.2672	0.000	39	166.391	5.559
97.2	2490.5	127.42	439,106	112.9	111.8	25.541	84.7	1.388	-64.4016	-5.2614	-0.016	40	170.370	5.672
99.7	2491.5	125.92	455,510	115.8	114.6	26.957	87.4	1.371	-64.4003	-5.2566	-0.016	41	165.302	5.470
97.3	2490.5	124.47	439,918	113.2	112.3	28.075	85.1	1.358	-64.4022	-5.2676	0.052	45	166.273	5.661
93.9	2491.8	129.35	418,140	110.0	108.3	16.110	79.4	1.499	-64.4023	-5.2710	0.050	45	177.229	5.959
90.6	2492.2	121.86	397,711	107.0	105.9	28.854	78.4	1.345	-64.4021	-5.2748	0.032	45	171.207	6.266
95.4	2492.0	120.40	427,713	111.4	110.9	28.648	83.1	1.343	-64.4009	-5.2566	0.088	46	163.117	5.826
97.0	2491.8	125.00	438,246	113.5	112.0	23.844	84.1	1.397	-64.4014	-5.2600	0.066	46	167.299	5.686
93.4	2491.4	121.96	415,427	109.5	108.8	26.670	80.9	1.364	-64.4013	-5.2644	0.062	46	167.654	5.997
92.6	2492.1	119.73	410,079	109.2	108.2	31.632	80.7	1.318	-64.3966	-5.2601	0.016	50	165.656	6.077
95.0	2490.8	125.44	425,540	110.9	109.9	23.249	82.0	1.404	-64.3965	-5.2645	0.007	50	170.370	5.853
96.3	2491.4	125.71	433,714	112.2	111.2	26.663	84.0	1.373	-64.3971	-5.2689	0.011	50	169.122	5.744
93.5	2491.9	127.11	415,889	109.3	108.2	25.509	81.0	1.387	-64.3973	-5.2732	0.011	50	174.636	5.992
93.0	2491.2	132.66	412,940	108.3	107.1	17.272	79.1	1.492	-64.3972	-5.2758	0.015	50	182.914	6.033
94.4	2491.6	118.29	421,297	111.1	110.2	35.196	83.0	1.290	-64.3961	-5.2564	0.020	51	161.471	5.914
96.0	2490.8	124.92	431,818	112.6	111.0	24.521	83.3	1.391	-64.3928	-5.2708	0.000	53	168.426	5.768
92.5	2491.6	122.71	409,476	108.6	107.7	25.472	79.8	1.376	-64.3931	-5.2734	0.001	53	169.899	6.085
92.4	2491.9	129.17	408,861	107.9	106.8	21.935	79.3	1.427	-64.3935	-5.2782	0.001	53	178.978	6.095
97.3	2491.9	133.07	440,092	112.4	111.4	25.257	85.1	1.404	-64.3924	-5.2666	-0.002	54	177.718	5.662
97.2	2491.9	124.12	439,506	113.2	112.3	32.443	85.7	1.324	-64.3919	-5.2623	-0.003	55	165.884	5.670
94.5	2491.4	121.88	421,969	110.5	109.8	28.364	82.2	1.349	-64.3903	-5.2567	-0.022	56	166.243	5.904
95.1	2490.8	122.59	425,837	111.1	110.3	29.697	83.1	1.340	-64.3890	-5.2754	-0.016	58	166.447	5.849
94.1	2491.4	115.56	419,846	111.0	110.3	46.598	84.1	1.218	-64.3891	-5.2791	0.002	58	158.015	5.934
100.7	2491.5	136.74	462,212	115.1	114.4	15.635	86.6	1.525	-64.3871	-5.2660	-0.006	59	178.196	5.390
98.1	2491.1	134.96	445,310	112.9	112.0	17.944	84.5	1.489	-64.3879	-5.2698	0.002	59	179.192	5.594
95.7	2491.3	125.46	429,758	111.7	110.6	19.960	82.0	1.440	-64.3867	-5.2616	-0.009	60	169.555	5.797
95.2	2491.4	117.58	426,609	111.9	111.1	43.809	84.9	1.237	-64.3853	-5.2570	-0.010	61	159.504	5.840
96.1	2491.3	121.16	432,226	112.4	111.5	27.270	83.6	1.356	-64.3856	-5.2784	-0.013	61	163.286	5.764
95.9	2491.3	126.42	431,155	111.7	110.7	26.987	83.7	1.372	-64.3841	-5.2697	-0.015	62	170.587	5.778
92.8	2492.3	127.46	411,550	108.1	107.5	30.354	81.1	1.347	-64.3850	-5.2737	0.004	62	176.033	6.056
96.3	2490.7	123.55	433,237	112.3	111.4	25.009	83.5	1.383	-64.3831	-5.2639	-0.018	63	166.307	5.749
96.2	2491.7	125.36	433,011	112.0	111.1	25.035	83.6	1.387	-64.3818	-5.2591	-0.017	64	168.784	5.754

Continued on next page...

Table E.3: Nano-indentation hardness data for generating depth profile in Sample 3 (continued)

h_c [nm]	P_{max} [μN]	S [μN/nm]	A [nm^2]	h_{max} [nm]	h_{eff} [nm]	A	h_f [nm]	m	X [mm]	Y [mm]	Drift Correction [nm/s]	Distance from Edge [μm]	E_r [GPa]	H [GPa]
93.1	2491.6	122.41	413,364	109.2	108.4	29.741	81.1	1.340	-64.3842	-5.2676	0.064	67	168.690	6.028
95.7	2491.1	121.82	429,570	111.8	111.0	38.082	84.8	1.280	-64.3843	-5.2710	0.044	67	164.677	5.799
93.7	2490.7	124.55	416,884	109.6	108.7	28.404	81.6	1.356	-64.3841	-5.2748	0.031	67	170.913	5.974
95.6	2491.8	120.29	428,993	112.4	111.1	35.767	84.4	1.291	-64.3834	-5.2600	0.064	68	162.723	5.808
98.5	2491.8	127.25	447,894	114.3	113.2	18.868	84.7	1.457	-64.3833	-5.2644	0.071	68	168.460	5.563
95.5	2491.8	123.23	428,578	111.7	110.7	21.986	82.1	1.411	-64.3829	-5.2566	0.060	69	166.782	5.814
93.3	2492.3	121.92	414,333	109.4	108.6	32.502	81.6	1.318	-64.3786	-5.2601	0.009	72	167.816	6.015
97.7	2491.2	124.86	442,151	113.6	112.6	34.565	86.5	1.311	-64.3785	-5.2645	0.013	72	166.373	5.634
94.2	2491.8	129.27	420,408	109.8	108.7	31.009	82.7	1.347	-64.3791	-5.2689	0.025	72	176.648	5.927
91.5	2491.4	120.60	403,343	107.6	107.0	33.232	79.9	1.309	-64.3793	-5.2732	0.016	72	168.245	6.177
96.3	2491.3	123.79	433,622	112.0	111.4	27.544	84.0	1.361	-64.3792	-5.2758	-0.007	72	166.562	5.745
95.2	2491.0	127.63	426,487	110.9	109.8	23.964	82.4	1.403	-64.3781	-5.2564	0.013	73	173.149	5.841
94.9	2491.5	129.67	424,372	110.1	109.3	18.783	81.1	1.465	-64.3751	-5.2734	-0.003	75	176.362	5.871
94.2	2491.5	117.28	420,104	111.0	110.1	23.823	80.9	1.377	-64.3755	-5.2782	-0.003	75	160.319	5.931
91.9	2491.3	128.49	406,153	107.7	106.5	19.316	78.3	1.455	-64.3744	-5.2666	-0.013	76	178.626	6.134
94.9	2491.0	126.83	424,533	110.5	109.6	21.346	81.6	1.428	-64.3748	-5.2708	-0.013	76	172.464	5.868
95.6	2491.5	129.12	428,800	111.1	110.0	19.256	81.9	1.457	-64.3739	-5.2623	0.007	77	174.702	5.810
99.0	2490.8	127.55	450,938	114.3	113.7	22.306	85.9	1.419	-64.3723	-5.2567	-0.012	78	168.289	5.524
92.5	2491.8	121.70	409,786	108.8	107.9	24.700	79.6	1.381	-64.3710	-5.2754	0.005	80	168.441	6.081
94.5	2492.0	120.56	422,322	110.6	110.0	25.360	81.7	1.372	-64.3711	-5.2791	0.004	80	164.363	5.901
91.9	2491.1	121.69	406,155	108.2	107.3	23.329	78.8	1.394	-64.3691	-5.2660	-0.027	81	169.180	6.133
90.6	2491.8	123.59	397,922	106.4	105.7	27.230	78.2	1.363	-64.3699	-5.2698	-0.010	81	173.586	6.262
92.1	2491.8	122.69	406,991	108.3	107.3	18.908	78.0	1.445	-64.3687	-5.2616	-0.023	82	170.398	6.123
93.3	2492.2	125.54	414,424	109.4	108.2	27.224	81.0	1.368	-64.3673	-5.2570	-0.025	83	172.775	6.014
92.5	2491.7	118.50	409,712	109.0	108.3	34.441	81.0	1.296	-64.3670	-5.2737	0.002	83	164.032	6.082
93.5	2491.1	123.68	416,164	109.5	108.7	26.854	81.1	1.367	-64.3676	-5.2784	0.005	83	169.866	5.986
91.2	2490.8	124.44	401,770	107.1	106.2	26.964	78.9	1.368	-64.3661	-5.2697	-0.008	84	173.941	6.200
94.0	2491.5	122.99	418,952	110.2	109.2	23.936	81.0	1.391	-64.3651	-5.2639	-0.018	85	168.356	5.947
91.2	2491.7	126.68	401,494	106.6	105.9	29.043	79.3	1.356	-64.3638	-5.2591	-0.031	86	177.129	6.206

Table E.4: Nano-indentation hardness data for generating depth profile in Sample 4

h_c [nm]	P_{max} [μN]	S [μN/nm]	A [nm^2]	h_{max} [nm]	h_{eff} [nm]	A	h_f [nm]	m	X [mm]	Y [mm]	Drift Correction [nm/s]	Distance from Edge [μm]	E_r [GPa]	H [GPa]
91.6	2491.6	113.25	403,931	109.1	108.1	26.763	78.6	1.340	-111.0918	50.7549	0.069	5	157.877	6.168
98.0	2490.8	125.69	444,689	113.5	112.9	35.792	87.1	1.304	-111.1537	48.6369	0.040	5	166.999	5.601
96.0	2491.4	113.63	431,404	113.3	112.4	33.228	84.1	1.291	-111.0910	50.7607	0.084	6	153.283	5.775
99.0	2491.3	135.68	451,049	113.7	112.8	17.882	85.4	1.491	-111.1552	48.6406	0.052	6	178.989	5.523
95.2	2490.3	128.31	426,513	110.8	109.8	26.175	82.9	1.384	-111.1394	48.8642	-0.079	6	174.067	5.839
94.3	2491.3	123.34	420,685	110.1	109.4	25.718	81.6	1.376	-111.1421	48.8609	0.008	6	168.486	5.922
95.5	2490.2	125.38	428,614	111.3	110.4	24.795	82.8	1.389	-111.1437	48.8575	0.010	6	169.673	5.810
97.5	2490.1	131.53	441,419	112.6	111.7	20.540	84.3	1.449	-111.1461	48.8546	0.014	6	175.398	5.641
99.1	2491.1	125.93	451,573	114.7	113.9	22.574	86.0	1.412	-111.1479	48.8516	0.004	6	166.036	5.516
95.9	2491.8	129.28	430,948	111.3	110.4	25.945	83.6	1.389	-111.1490	48.8481	0.005	6	174.488	5.782
96.3	2491.7	118.16	433,552	113.1	112.1	26.581	83.6	1.355	-111.0884	50.7676	0.068	7	159.001	5.747
95.5	2491.4	114.38	428,376	112.7	111.8	26.703	82.6	1.343	-111.0903	50.7637	0.096	7	154.838	5.816
90.7	2491.9	125.85	398,614	106.5	105.6	25.389	78.1	1.385	-111.1578	48.6546	0.107	7	176.615	6.251
92.9	2492.9	128.98	411,925	108.4	107.4	20.984	79.6	1.437	-111.1577	48.6513	0.101	7	178.049	6.052
90.3	2492.3	119.53	396,003	106.6	105.9	17.042	75.5	1.460	-111.1574	48.6484	0.075	7	168.289	6.294
96.4	2491.8	131.78	434,231	111.6	110.6	23.194	83.7	1.421	-111.1563	48.6440	0.063	7	177.184	5.738
98.5	2491.6	123.12	447,838	114.3	113.7	50.947	89.1	1.215	-111.1506	48.8445	0.004	8	163.009	5.564
99.4	2491.0	131.15	453,540	115.2	113.7	17.569	85.5	1.484	-111.1533	48.8413	0.025	8	172.541	5.492
92.5	2491.3	113.94	409,696	109.7	108.9	29.144	80.0	1.322	-111.0881	50.7573	0.037	9	157.716	6.081
125.5	2487.4	122.69	455,065	141.8	140.7	19.826	111.7	1.434	-111.1156	49.5082	0.043	9	161.146	5.466
122.8	2488.0	103.24	438,662	142.7	140.9	31.029	110.1	1.279	-111.1158	49.5041	0.056	9	138.101	5.672
121.7	2487.8	121.52	431,687	138.3	137.0	39.083	111.0	1.274	-111.1197	49.4951	0.050	9	163.875	5.763
120.3	2487.9	122.51	423,502	136.2	135.5	27.016	107.9	1.362	-111.1201	49.4903	0.034	9	166.790	5.875
120.2	2488.4	124.31	422,986	136.0	135.2	33.612	108.9	1.316	-111.1166	49.4869	0.007	9	169.340	5.883
99.5	2490.0	137.85	453,979	113.8	113.0	25.595	87.5	1.413	-111.1372	48.8620	-0.060	10	181.268	5.485
92.6	2491.4	122.48	410,501	108.8	107.9	32.328	81.0	1.320	-111.1430	48.8504	-0.008	10	169.369	6.069
95.6	2491.3	114.31	429,008	112.8	111.9	38.126	84.4	1.261	-111.0849	50.7675	0.004	11	154.625	5.807
93.1	2491.7	112.14	413,643	110.6	109.8	29.233	80.5	1.317	-111.0863	50.7632	0.032	11	154.482	6.024
96.1	2490.7	130.95	432,237	111.1	110.4	18.075	82.3	1.477	-111.1390	48.8581	-0.028	11	176.473	5.762
95.3	2491.2	127.68	427,177	110.8	109.9	28.175	83.3	1.365	-111.1414	48.8536	-0.013	11	173.083	5.832
95.0	2491.3	128.47	425,446	110.5	109.6	30.080	83.4	1.352	-111.1448	48.8472	-0.013	11	174.502	5.856
92.7	2491.6	127.20	410,758	108.5	107.4	32.780	81.3	1.329	-111.1523	48.6493	0.003	12	175.848	6.066
95.2	2490.8	128.08	426,625	110.6	109.8	29.208	83.4	1.358	-111.1502	48.6413	0.000	12	173.737	5.838

Continued on next page...

Table E.4: Nano-indentation hardness data for generating depth profile in Sample 4 (continued)

h_c [nm]	P_{max} [μN]	S [μN/nm]	A [nm^2]	h_{max} [nm]	h_{eff} [nm]	A	h_f [nm]	m	X [mm]	Y [mm]	Drift Correction [nm/s]	Distance from Edge [μm]	E_r [GPa]	H [GPa]
99.4	2490.9	127.85	453,607	115.0	114.0	36.355	88.6	1.306	-111.1484	48.6375	-0.001	12	168.193	5.491
95.6	2491.0	124.59	428,953	111.3	110.6	37.342	84.7	1.292	-111.1464	48.8435	-0.026	12	168.538	5.807
94.1	2491.3	123.11	419,343	110.3	109.2	34.917	82.8	1.304	-111.1515	48.6456	-0.005	13	168.440	5.941
93.8	2491.5	117.32	417,487	110.5	109.7	37.590	82.7	1.272	-111.1488	48.8407	0.010	13	160.868	5.968
96.0	2491.0	118.91	431,510	112.4	111.7	44.137	85.7	1.239	-111.1512	48.6532	-0.021	14	160.380	5.773
124.8	2487.9	122.38	450,471	140.9	140.0	33.445	113.4	1.312	-111.1109	49.5034	-0.051	14	161.550	5.523
123.3	2487.7	107.99	441,300	141.3	140.6	25.788	109.8	1.334	-111.1119	49.4983	-0.001	14	144.026	5.637
125.6	2487.7	124.61	455,457	141.4	140.6	33.599	114.3	1.317	-111.1136	49.4947	0.012	14	163.591	5.462
125.1	2487.9	133.38	452,310	140.3	139.1	20.902	112.0	1.450	-111.1140	49.4906	0.009	14	175.709	5.500
125.0	2488.1	126.97	451,449	140.6	139.7	31.942	113.5	1.334	-111.1098	49.4870	-0.012	14	167.433	5.511
95.3	2490.4	143.66	427,428	109.5	108.3	3.888	76.1	1.860	-111.1337	48.8597	-0.071	15	194.685	5.826
97.4	2491.5	125.40	440,251	113.4	112.3	23.508	84.4	1.402	-111.1355	48.8563	-0.026	15	167.453	5.659
95.9	2491.1	128.35	430,854	111.4	110.4	45.223	86.1	1.255	-111.1375	48.8522	-0.020	15	173.249	5.782
93.8	2490.9	131.23	417,575	108.7	108.0	30.562	82.3	1.355	-111.1391	48.8482	-0.006	15	179.924	5.965
98.8	2490.8	126.05	449,605	114.5	113.6	43.039	88.7	1.262	-111.1446	48.6384	-0.012	16	166.563	5.540
99.4	2491.0	135.06	453,687	114.1	113.3	26.482	87.5	1.398	-111.1478	48.6459	-0.003	17	177.652	5.490
95.9	2491.3	136.68	431,001	110.6	109.6	32.213	84.9	1.356	-111.1453	48.6425	-0.007	17	184.466	5.780
98.1	2491.1	135.55	444,954	112.9	111.9	24.908	85.9	1.414	-111.1406	48.8451	-0.001	17	180.044	5.598
96.8	2491.3	129.13	436,416	111.9	111.2	24.874	84.3	1.398	-111.1426	48.8416	-0.002	18	173.183	5.709
101.4	2490.4	140.13	466,386	115.7	114.7	8.977	85.2	1.662	-111.1460	48.6527	-0.047	19	181.806	5.340
93.4	2490.5	127.86	415,550	109.0	108.1	40.922	83.2	1.278	-111.1342	48.8485	-0.068	20	175.731	5.993
93.7	2491.5	127.40	417,301	109.5	108.4	40.761	83.4	1.278	-111.1375	48.8440	0.003	20	174.741	5.970
118.5	2488.8	132.06	412,894	133.7	132.6	14.357	103.8	1.533	-111.1013	49.5081	0.039	24	182.090	6.028
121.5	2488.3	125.72	430,839	137.1	136.4	29.953	109.7	1.346	-111.1009	49.5043	0.048	24	169.695	5.776
122.9	2487.8	124.63	439,265	138.6	137.9	36.754	112.1	1.296	-111.1024	49.4987	0.049	24	166.606	5.664
121.9	2488.4	125.30	432,729	137.8	136.8	33.754	110.6	1.317	-111.1062	49.4957	0.047	24	168.758	5.750
123.1	2488.2	134.91	440,264	138.2	136.9	19.882	109.9	1.465	-111.1058	49.4909	0.028	24	180.148	5.652
122.9	2488.6	126.65	439,119	138.6	137.7	31.385	111.4	1.338	-111.1011	49.4870	0.011	24	169.331	5.667
118.2	2488.9	124.69	411,044	133.8	133.2	40.534	107.8	1.273	-111.0951	49.5082	-0.028	29	172.311	6.055
118.4	2488.0	124.32	412,542	134.7	133.5	40.516	108.0	1.272	-111.0953	49.5041	0.000	29	171.488	6.031
119.5	2488.0	126.61	418,895	135.2	134.3	36.583	108.7	1.302	-111.0961	49.4986	0.022	29	173.327	5.939
120.6	2488.4	124.05	424,985	136.6	135.6	35.048	109.4	1.305	-111.0992	49.4951	0.016	29	168.596	5.855
118.9	2489.0	110.39	415,074	136.4	135.8	51.831	109.2	1.180	-111.0996	49.4903	0.008	29	151.814	5.996

Continued on next page...

Table E.4: Nano-indentation hardness data for generating depth profile in Sample 4 (continued)

h_c [nm]	P_{max} [μN]	S [μN/nm]	A [nm^2]	h_{max} [nm]	h_{eff} [nm]	A	h_f [nm]	m	X [mm]	Y [mm]	Drift Correction [nm/s]	Distance from Edge [μm]	E_r [GPa]	H [GPa]
118.0	2488.3	124.90	409,966	133.9	133.0	44.492	108.0	1.251	-111.0961	49.4869	-0.005	29	172.828	6.070
118.6	2487.1	130.51	413,555	133.6	132.9	31.048	107.2	1.350	-111.0904	49.5034	-0.050	34	179.806	6.014
120.5	2488.3	135.53	424,565	135.4	134.3	19.953	107.4	1.466	-111.0914	49.4983	0.000	34	184.291	5.861
120.3	2488.4	131.98	423,445	135.5	134.4	30.947	108.9	1.354	-111.0931	49.4947	0.006	34	179.696	5.877
118.9	2488.6	129.05	415,413	134.6	133.4	30.554	107.4	1.350	-111.0935	49.4906	0.009	34	177.406	5.991
119.7	2489.4	124.82	419,880	135.7	134.7	52.797	110.5	1.210	-111.0893	49.4870	-0.004	34	170.676	5.929
117.3	2488.9	126.67	405,711	132.9	132.0	19.949	103.7	1.443	-111.0817	49.5094	0.037	44	176.194	6.135
119.5	2488.6	124.66	418,734	135.6	134.5	26.899	107.2	1.369	-111.0818	49.5052	0.050	44	170.690	5.943
119.4	2488.2	120.13	417,828	135.6	134.9	37.466	108.4	1.280	-111.0818	49.5008	0.029	44	164.661	5.955
118.2	2488.0	113.57	411,141	135.2	134.6	53.455	108.8	1.181	-111.0823	49.4962	0.035	44	156.934	6.052
119.7	2487.9	121.04	420,146	136.1	135.2	31.166	107.9	1.325	-111.0849	49.4902	0.035	44	165.452	5.922
116.8	2488.5	126.02	403,224	132.8	131.7	36.088	105.9	1.303	-111.0831	49.4846	0.050	44	175.831	6.171
120.8	2487.6	127.88	426,141	136.4	135.3	25.823	108.4	1.386	-111.0753	49.5094	-0.026	50	173.562	5.837
119.1	2487.9	125.38	416,496	134.6	134.0	29.073	107.2	1.352	-111.0754	49.5048	0.004	50	172.129	5.973
117.7	2488.0	124.51	407,983	133.8	132.7	33.086	106.3	1.320	-111.0728	49.5000	0.007	50	172.706	6.098
121.0	2487.8	123.27	427,325	137.1	136.1	48.601	111.3	1.226	-111.0744	49.4953	0.020	50	167.075	5.822
120.6	2488.4	130.09	425,303	135.7	135.0	25.000	108.2	1.400	-111.0786	49.4890	0.020	50	176.744	5.851
118.9	2488.0	124.06	415,434	134.8	134.0	46.149	109.1	1.241	-111.0770	49.4847	0.022	50	170.529	5.989
117.8	2487.5	119.80	408,554	133.9	133.3	39.840	107.1	1.265	-111.0658	49.5089	-0.055	57	166.059	6.089
119.4	2487.6	117.63	417,985	135.9	135.2	40.373	108.7	1.256	-111.0659	49.5041	-0.009	57	161.204	5.952
121.6	2487.7	128.36	431,392	136.9	136.2	29.986	110.0	1.353	-111.0655	49.4990	0.000	57	173.156	5.767
120.7	2488.3	128.69	425,611	136.0	135.2	32.133	109.3	1.337	-111.0682	49.4946	0.004	57	174.776	5.846
122.0	2488.1	114.62	433,403	139.7	138.3	71.764	114.1	1.113	-111.0704	49.4904	0.015	57	154.255	5.741
120.1	2487.8	131.13	422,533	135.3	134.4	29.002	108.4	1.367	-111.0678	49.4856	-0.006	57	178.730	5.888
115.2	2488.5	125.18	393,764	131.3	130.1	27.860	103.0	1.362	-111.0615	49.5091	0.051	64	176.742	6.320
117.6	2489.0	129.31	407,800	133.3	132.1	27.706	105.6	1.374	-111.0605	49.5040	0.093	64	179.414	6.103
119.5	2489.1	125.86	418,787	135.5	134.3	33.456	108.2	1.321	-111.0635	49.4986	0.104	64	172.317	5.944
119.6	2488.9	125.62	419,538	135.1	134.5	28.903	107.7	1.354	-111.0640	49.4933	0.100	64	171.831	5.933
119.0	2489.1	125.42	415,661	134.8	133.9	34.757	107.9	1.311	-111.0639	49.4879	0.098	64	172.365	5.988
120.9	2488.2	129.77	427,014	136.2	135.3	30.638	109.4	1.351	-111.0615	49.4854	0.067	64	175.948	5.827
116.5	2488.3	124.56	401,379	132.7	131.5	31.411	104.9	1.332	-111.0539	49.5088	0.004	70	174.199	6.199
120.0	2488.0	128.51	421,851	136.0	134.6	23.875	107.3	1.406	-111.0543	49.5040	0.032	70	175.307	5.898
119.3	2488.2	131.42	417,733	135.2	133.5	16.128	105.1	1.504	-111.0561	49.4986	0.046	70	180.153	5.956

Continued on next page. . .

Table E.4: Nano-indentation hardness data for generating depth profile in Sample 4 (continued)

h_c [nm]	P_{max} [μN]	S [μN/nm]	A [nm^2]	h_{max} [nm]	h_{eff} [nm]	A	h_f [nm]	m	X [mm]	Y [mm]	Drift Correction [nm/s]	Distance from Edge [μm]	E_r [GPa]	H [GPa]
122.2	2487.9	129.41	434,957	137.6	136.7	29.332	110.5	1.360	-111.0581	49.4933	0.051	70	173.849	5.720
119.9	2488.7	127.29	420,958	135.2	134.5	29.225	108.0	1.356	-111.0573	49.4885	0.039	70	173.818	5.912
121.7	2487.6	128.82	431,928	137.2	136.2	20.643	108.4	1.441	-111.0547	49.4848	0.018	70	173.668	5.759
119.2	2488.2	124.63	416,800	135.5	134.1	49.795	109.7	1.224	-111.0479	49.5091	-0.003	76	171.037	5.970
119.7	2489.0	122.42	420,091	135.7	135.0	39.662	109.1	1.272	-111.0479	49.5028	0.012	76	167.346	5.925
112.9	2489.8	124.81	380,679	128.7	127.9	37.418	102.1	1.292	-111.0505	49.4972	0.018	76	179.225	6.540
120.3	2488.3	122.19	423,720	136.9	135.6	43.129	110.1	1.252	-111.0532	49.4919	0.014	76	166.312	5.873
116.0	2488.8	118.99	398,135	132.2	131.7	51.500	106.5	1.202	-111.0491	49.4882	0.003	76	167.077	6.251
116.8	2489.1	129.51	402,988	132.2	131.2	31.588	105.4	1.343	-111.0461	49.4851	-0.002	76	180.759	6.177
115.1	2492.3	130.69	393,453	130.3	129.4	20.787	101.9	1.444	-111.0405	49.5065	0.450	84	184.599	6.335
119.6	2491.9	125.23	419,153	135.5	134.5	30.817	107.9	1.338	-111.0435	49.5011	0.391	84	171.378	5.945
114.4	2490.9	128.96	389,015	129.6	128.9	33.555	103.2	1.328	-111.0440	49.4958	0.310	84	183.199	6.403
116.8	2488.4	122.95	403,133	132.6	132.0	39.539	106.2	1.274	-111.0439	49.4904	-0.026	84	171.574	6.173
117.1	2488.7	118.74	404,415	133.5	132.8	55.479	108.0	1.184	-111.0415	49.4879	-0.020	84	165.429	6.154
117.5	2488.0	121.64	407,130	134.0	132.9	48.414	107.8	1.223	-111.0339	49.5113	-0.069	90	168.903	6.111
116.4	2488.2	111.61	400,370	134.0	133.1	60.329	107.5	1.147	-111.0343	49.5065	-0.033	90	156.285	6.215
117.6	2489.4	130.41	407,418	132.9	131.9	36.423	106.8	1.312	-111.0361	49.5011	-0.022	90	181.016	6.110
119.7	2488.6	122.66	420,027	135.7	134.9	29.077	107.6	1.346	-111.0381	49.4958	-0.013	90	167.688	5.925
116.2	2488.4	122.09	399,342	132.5	131.5	45.546	106.2	1.239	-111.0373	49.4910	-0.019	90	171.173	6.231
117.8	2488.9	122.39	408,694	133.9	133.0	51.207	108.4	1.212	-111.0347	49.4873	-0.021	90	169.625	6.090
116.9	2488.0	120.55	403,355	133.0	132.3	38.385	106.0	1.276	-111.0279	49.5116	-0.080	96	168.172	6.168
119.6	2489.2	130.41	419,040	135.1	133.9	26.210	107.4	1.389	-111.0279	49.5053	-0.018	96	178.494	5.940
119.2	2488.2	116.18	416,672	135.5	135.2	39.367	108.3	1.259	-111.0305	49.4997	-0.017	96	159.469	5.972
116.3	2489.1	115.38	400,338	133.1	132.5	52.330	106.9	1.190	-111.0332	49.4944	-0.004	96	161.561	6.218
117.5	2489.3	126.05	407,084	133.9	132.3	28.874	105.6	1.356	-111.0291	49.4907	-0.018	96	175.045	6.115
117.7	2489.0	122.50	408,358	134.0	133.0	38.979	107.0	1.277	-111.0261	49.4876	-0.025	96	169.841	6.095

Table E.5: Nano-indentation hardness data for Sample 1 bulk

h_c [nm]	P_{max} [μN]	S [μN/nm]	A [nm^2]	h_{max} [nm]	h_{eff} [nm]	A	h_f [nm]	m	X [mm]	Y [mm]	Drift Correction [nm/s]	E_r [GPa]	H [GPa]
111.8	2488.7	143.57	374,833	127.0	124.8	12.463	97.2	1.595	-55.8945	92.1980	-0.011	207.763	6.639
112.2	2488.9	137.67	376,853	126.5	125.8	22.842	99.7	1.439	-55.8895	92.1980	-0.020	198.702	6.605
110.6	2489.8	135.75	367,746	125.3	124.3	21.899	97.8	1.444	-55.8845	92.1980	-0.042	198.330	6.771
110.3	2488.7	111.99	366,410	127.2	127.0	89.791	103.6	1.054	-55.8795	92.1980	-0.055	163.915	6.792
115.0	2488.0	133.62	392,488	129.9	128.9	26.620	103.0	1.394	-55.8745	92.1980	-0.081	188.964	6.339
111.8	2489.4	134.24	374,546	126.7	125.7	30.914	100.5	1.360	-55.8945	92.2030	-0.057	194.348	6.646
111.6	2488.9	132.49	373,354	126.7	125.7	31.107	100.2	1.354	-55.8895	92.2030	-0.054	192.116	6.666
112.9	2489.0	134.20	380,882	128.0	126.8	30.058	101.5	1.366	-55.8845	92.2030	-0.039	192.654	6.535
113.1	2488.7	121.79	381,926	129.0	128.4	41.354	102.7	1.261	-55.8795	92.2030	-0.046	174.600	6.516
115.2	2488.8	143.99	393,658	129.3	128.1	27.701	103.8	1.409	-55.8740	92.2030	-0.043	203.338	6.322
111.5	2489.6	135.73	372,769	126.3	125.2	22.365	98.8	1.440	-55.8945	92.2075	-0.041	196.970	6.679
113.1	2489.3	133.92	381,577	127.7	127.0	29.382	101.5	1.371	-55.8895	92.2075	-0.049	192.077	6.524
116.4	2488.5	148.25	400,454	130.2	129.0	12.141	101.9	1.614	-55.8845	92.2080	-0.043	207.568	6.214
115.1	2488.5	141.09	393,432	129.5	128.4	16.187	101.4	1.528	-55.8795	92.2080	-0.056	199.300	6.325
115.9	2488.3	129.80	397,883	131.5	130.3	27.823	104.0	1.374	-55.8745	92.2080	-0.068	182.319	6.254

Table E.6: Nano-indentation hardness data for Sample 2 bulk

h_c [nm]	P_{max} [μN]	S [μN/nm]	A [nm^2]	h_{max} [nm]	h_{eff} [nm]	A	h_f [nm]	m	X [mm]	Y [mm]	Drift Correction [nm/s]	E_r [GPa]	H [GPa]
109.4	2488.9	138.86	361,165	123.6	122.8	20.445	96.5	1.468	-58.9900	43.6135	-0.094	204.715	6.891
107.4	2489.1	132.69	350,438	122.5	121.5	23.127	94.8	1.424	-58.9850	43.6135	-0.092	198.588	7.103
109.9	2488.3	136.29	363,950	124.4	123.6	27.635	98.2	1.391	-58.9800	43.6135	-0.080	200.161	6.837
109.5	2489.1	142.83	361,717	123.7	122.5	13.722	95.2	1.571	-58.9745	43.6135	-0.082	210.415	6.881
112.2	2488.3	143.29	376,675	126.1	125.2	15.369	98.4	1.546	-58.9945	43.6180	-0.067	206.851	6.606
112.4	2488.9	134.55	378,060	127.1	126.3	20.208	99.3	1.460	-58.9900	43.6180	-0.057	193.884	6.583
110.8	2489.0	140.70	368,864	125.1	124.0	13.360	96.2	1.572	-58.9855	43.6180	-0.053	205.263	6.748
111.2	2489.3	143.55	371,413	125.2	124.2	20.861	98.7	1.475	-58.9800	43.6180	-0.027	208.696	6.702
111.2	2489.2	140.60	370,992	125.6	124.4	20.505	98.4	1.472	-58.9750	43.6180	-0.018	204.514	6.710
109.7	2489.2	133.43	363,036	124.3	123.7	23.728	97.2	1.420	-58.9950	43.6235	-0.034	196.203	6.857
108.8	2489.4	137.45	357,908	123.0	122.4	25.415	96.8	1.414	-58.9900	43.6235	-0.032	203.566	6.955
112.4	2488.4	139.40	377,923	127.0	125.8	26.549	100.7	1.408	-58.9850	43.6235	-0.034	200.913	6.584
110.3	2489.2	138.68	366,520	124.9	123.8	23.606	98.1	1.434	-58.9795	43.6235	-0.034	202.952	6.792
111.9	2489.1	141.72	375,187	126.1	125.1	18.820	98.8	1.495	-58.9750	43.6235	-0.041	204.997	6.634

Table E.7: Nano-indentation hardness data for Sample 3 bulk

h_c [nm]	P_{max} [μN]	S [μN/nm]	A [nm^2]	h_{max} [nm]	h_{eff} [nm]	A	h_f [nm]	m	X [mm]	Y [mm]	Drift Correction [nm/s]	E_r [GPa]	H [GPa]
111.8	2487.6	110.73	374,592	129.0	128.7	63.944	103.2	1.132	-58.1950	-4.3460	-0.200	160.296	6.641
115.1	2487.9	128.03	393,110	130.7	129.7	34.483	104.0	1.319	-58.1900	-4.3455	-0.149	180.918	6.329
114.0	2487.2	120.94	387,196	130.9	129.5	39.819	103.4	1.268	-58.1850	-4.3455	-0.140	172.197	6.424
114.5	2488.8	127.47	389,626	130.3	129.1	38.794	103.9	1.290	-58.1800	-4.3455	-0.104	180.932	6.388
112.9	2488.3	137.28	380,991	127.2	126.5	15.501	98.8	1.529	-58.1755	-4.3455	-0.112	197.060	6.531
112.3	2488.6	136.13	377,112	127.1	126.0	27.166	100.5	1.395	-58.1950	-4.3400	-0.093	196.405	6.599
110.2	2489.7	135.52	365,912	125.0	124.0	22.245	97.6	1.440	-58.1900	-4.3405	-0.063	198.490	6.804
112.7	2487.8	135.67	379,589	127.8	126.5	30.185	101.3	1.369	-58.1850	-4.3405	-0.062	195.106	6.554
117.8	2488.5	145.75	409,043	131.6	130.7	9.139	102.1	1.673	-58.1750	-4.3405	-0.050	201.904	6.084
112.1	2489.5	133.88	376,498	126.9	126.1	26.060	100.1	1.399	-58.1945	-4.3355	-0.041	193.311	6.612
109.5	2489.3	131.87	361,895	124.7	123.7	18.985	96.0	1.468	-58.1900	-4.3355	-0.043	194.224	6.878
108.3	2490.1	139.70	355,094	122.8	121.6	72.828	100.9	1.165	-58.1850	-4.3355	-0.025	207.706	7.012
110.6	2489.4	140.15	367,924	124.7	123.9	17.832	97.2	1.503	-58.1800	-4.3355	-0.024	204.708	6.766
111.8	2489.5	133.15	374,689	126.8	125.8	32.019	100.6	1.349	-58.1755	-4.3355	-0.032	192.731	6.644

Table E.8: Nano-indentation hardness data for Sample 4 bulk

h_c [nm]	P_{max} [μN]	S [μN/nm]	A [nm^2]	h_{max} [nm]	h_{eff} [nm]	A	h_f [nm]	m	X [mm]	Y [mm]	Drift Correction [nm/s]	E_r [GPa]	H [GPa]
111.1	2489.1	136.95	370,570	125.5	124.7	32.493	100.1	1.354	-106.0775	49.4300	-0.053	199.320	6.717
114.3	2488.8	129.37	388,661	129.0	128.7	31.122	102.8	1.346	-106.0720	49.4300	-0.024	183.852	6.403
112.1	2488.6	136.46	376,337	126.4	125.8	37.322	101.7	1.320	-106.0675	49.4300	-0.015	197.091	6.613
110.4	2488.6	136.89	366,824	124.8	124.0	27.753	98.7	1.392	-106.0620	49.4300	-0.014	200.256	6.784
109.5	2489.7	138.98	361,717	123.6	122.9	36.454	99.1	1.332	-106.0825	49.4350	-0.004	204.742	6.883
110.7	2489.2	126.00	368,378	125.8	125.5	52.105	101.5	1.216	-106.0775	49.4350	-0.018	183.926	6.757
113.1	2489.0	137.78	381,936	127.4	126.7	28.637	101.6	1.386	-106.0720	49.4350	-0.005	197.524	6.517
114.0	2489.5	137.65	387,116	128.5	127.6	24.505	101.9	1.423	-106.0675	49.4350	-0.009	196.021	6.431
112.2	2489.1	128.94	376,558	127.4	126.6	46.288	102.5	1.251	-106.0620	49.4350	-0.014	186.165	6.610
114.0	2488.9	136.25	386,812	129.6	127.7	25.606	101.9	1.409	-106.0825	49.4400	-0.001	194.091	6.434
114.0	2488.5	140.79	387,094	128.6	127.3	21.902	101.5	1.457	-106.0775	49.4400	-0.005	200.487	6.429
114.3	2489.2	137.18	388,878	128.9	128.0	24.883	102.2	1.418	-106.0720	49.4400	0.008	194.897	6.401
112.6	2490.3	134.32	378,853	127.3	126.5	25.222	100.4	1.408	-106.0675	49.4400	-0.008	193.342	6.573
109.2	2490.2	133.79	360,401	124.2	123.2	27.535	97.4	1.386	-106.0620	49.4400	0.005	197.449	6.910

APPENDIX F

VIBRATORY TUMBLING DATA

F.1 250 μm Wire Samples

The ten specimens cut with the 250 μm diameter wire and vibratory tumbled were periodically measured along all three dimensions, as shown in Figure F.1. Height and width were measured twice for each sample, while thickness was measured only once. The recast layer removal was evident in the height and width measurements.

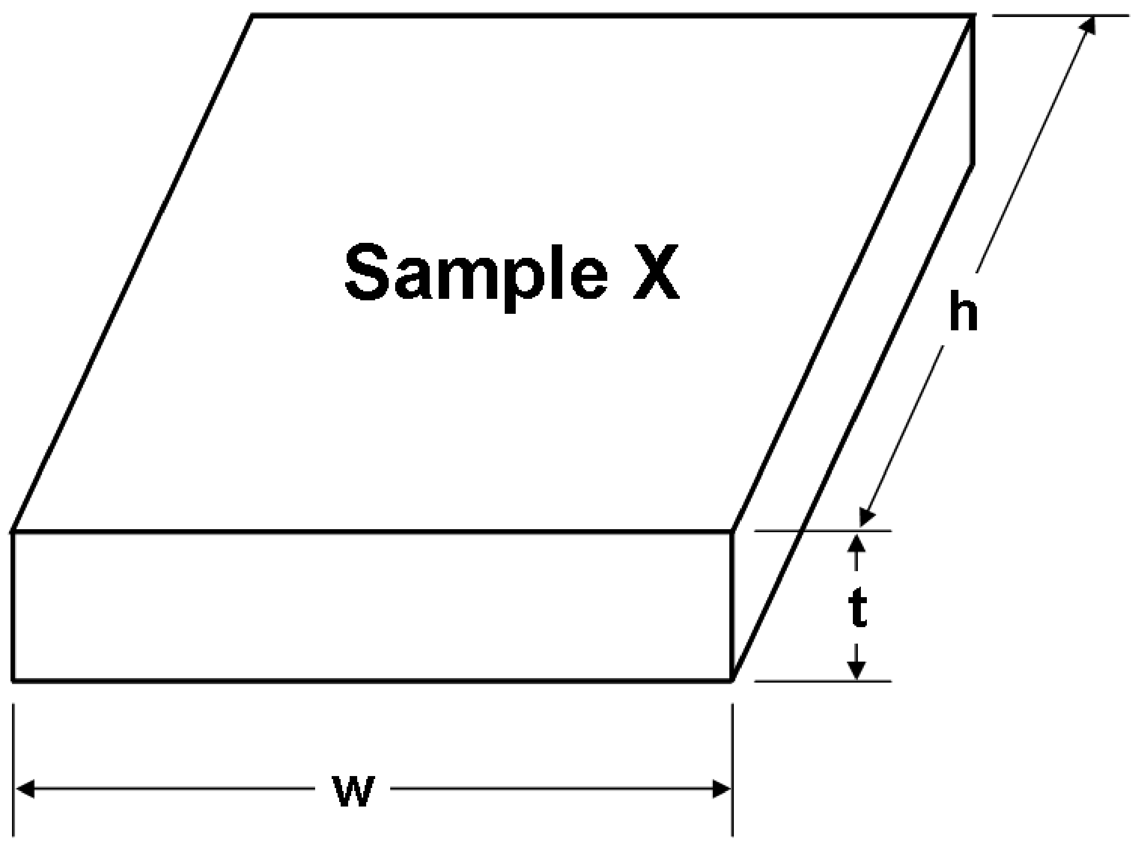

Figure F.1: Measurements of specimens during vibratory tumbling

Table F.1: Measurements of vibratory tumbled specimens (in mm) over time

0 min	Dim.	1	2	3	4	5	6	7	8	9	10
	h	25.032	25.034	25.029	25.027	25.027	25.032	25.029	25.029	25.016	25.029
	w	25.037	25.037	25.034	25.027	25.027	25.027	25.029	25.029	25.024	25.027
	h	25.029	25.032	25.029	25.032	25.027	25.029	25.029	25.029	25.011	25.027
	w	25.032	25.034	25.032	25.027	25.024	25.027	25.027	25.027	25.024	25.027
	t	4.082	4.084	4.084	4.082	4.084	4.082	4.084	4.082	4.079	4.077
20 min	Dim.	1	2	3	4	5	6	7	8	9	10
	h	25.024	25.024	25.024	25.024	25.014	25.019	25.019	25.014	25.004	25.019
	w	25.024	25.024	25.027	25.016	25.014	25.014	25.019	25.014	25.009	25.011
	h	25.016	25.019	25.019	25.016	25.011	25.016	25.014	25.016	25.006	25.016
	w	25.022	25.022	25.024	25.011	25.011	25.011	25.014	25.011	25.006	25.011
	t	4.084	4.087	4.082	4.084	4.079	4.082	4.084	4.084	4.079	4.077
40 min	Dim.	1	2	3	4	5	6	7	8	9	10
	h	25.014	25.016	25.014	25.011	25.009	25.014	25.011	25.014	25.001	25.011
	w	25.019	25.016	25.022	25.009	25.009	25.009	25.011	25.009	25.006	25.009
	h	25.014	25.014	25.011	25.014	25.011	25.014	25.011	25.011	24.999	25.014
	w	25.016	25.016	25.019	25.009	25.009	25.009	25.011	25.011	25.006	25.009
	t	4.079	4.084	4.082	4.082	4.079	4.077	4.082	4.082	4.077	4.079
60 min	Dim.	1	2	3	4	5	6	7	8	9	10
	h	25.011	25.014	25.011	25.009	25.009	25.011	25.011	25.011	24.999	25.011
	w	25.016	25.014	25.016	25.009	25.009	25.009	25.009	25.009	25.004	25.009
	h	25.014	25.011	25.011	25.009	25.009	25.011	25.011	25.011	24.999	25.011
	w	25.014	25.014	25.016	25.009	25.006	25.009	25.009	25.009	25.004	25.006
	t	4.079	4.084	4.084	4.084	4.082	4.082	4.084	4.082	4.079	4.077

Table F.2: Measurements of vibratory tumbled specimens (in mm) over time - continued

130 min	Dim.	1	2	3	4	5	6	7	8	9	10
	h	25.011	25.009	25.009	25.006	25.006	25.009	25.006	25.009	24.991	25.006
	w	25.011	25.011	25.014	25.006	25.004	25.004	25.004	25.006	25.001	25.004
	h	25.009	25.006	25.006	25.006	25.004	25.009	25.006	25.006	24.994	25.006
	w	25.011	25.009	25.011	25.004	25.004	25.004	25.004	25.004	25.001	25.004
	t	4.079	4.082	4.077	4.082	4.079	4.079	4.082	4.082	4.077	4.079
250 min	Dim.	1	2	3	4	5	6	7	8	9	10
	h	25.009	25.006	25.006	25.004	25.004	25.006	25.004	25.006	24.989	25.006
	w	25.011	25.009	25.011	25.004	25.001	25.001	25.004	25.004	24.999	25.004
	h	25.006	25.006	25.006	25.006	25.004	25.006	25.004	25.004	24.989	25.006
	w	25.009	25.006	25.009	25.001	25.001	25.001	25.004	25.004	24.999	25.004
	t	4.079	4.084	4.079	4.079	4.079	4.079	4.082	4.082	4.074	4.077
490 min	Dim.	1	2	3	4	5	6	7	8	9	10
	h	25.006	25.006	25.006	25.004	25.004	25.006	25.004	25.004	24.989	25.004
	w	25.009	25.006	25.009	25.001	25.001	25.001	25.004	25.004	24.999	25.001
	h	25.006	25.006	25.006	25.004	25.001	25.006	25.004	25.004	24.989	25.004
	w	25.009	25.006	25.009	25.001	25.001	25.001	25.001	25.004	24.999	25.001
	t	4.079	4.082	4.079	4.079	4.079	4.079	4.082	4.079	4.074	4.074
970 min	Dim.	1	2	3	4	5	6	7	8	9	10
	h	25.006	25.006	25.004	25.004	25.001	25.004	25.001	25.001	24.986	25.004
	w	25.009	25.006	25.006	25.001	25.001	25.001	25.001	25.001	24.996	24.999
	h	25.004	25.004	25.004	25.004	25.001	25.001	25.001	25.004	24.989	25.004
	w	25.006	25.006	25.006	24.999	24.999	25.006	25.001	25.004	24.996	25.001
	t	4.074	4.079	4.077	4.074	4.074	4.074	4.077	4.074	4.072	4.072

REFERENCES

[1] Certificate of test. Provided by Rolled Alloys, Inc., February 2006.

[2] G. Spur and J. Schönbeck. Anode erosion in wire-EDM - a theoretical model. *Annals of the CIRP*, 42(1):253–256, 1993.

[3] B. Lazarenko and N. Lazarenko. Machining by erosion. *American Machinist*, 91 (25):120–121, December 1947.

[4] K. Inoue. Spark discharge contouring machine using wire electrode. Patent: 2794216, March 1961.

[5] L. Gillespie. *Deburring and edge finishing handbook*. Society of Manufacturing Engineers (SME), 1999.

[6] ASM Handbook Committee. *Metals Handbook: Volume 10, Materials Characterization*. American Society for Metals, ninth edition, 1986.

[7] I. Noyan and J. Cohen. *Residual stresses: Measurement by diffraction and interpretation*. Springer-Verlag, first edition, 1986.

[8] W. Oliver and G. Pharr. An improved technique for determining hardness and elastic modulus using load and displacement sensing indentation experiments. *Journal of Materials Research*, 7:1564–1583, 1992.

[9] Hysitron Nanoindentation. http://hysitron.com, 2007.

[10] D. DiBitonto, P. Eubank, M. Patel, and M. Barrufet. Theoretical models of the electrical discharge machining process. I. A simple cathode erosion model. *Journal of Applied Physics*, 66(9):4095–4103, November 1989.

[11] F. Han, M. Kunieda, T. Sendai, and Y. Imai. High precision simulation of WEDM using parametric programming. *Annals of the CIRP*, 51(1):165–168, 2002.

[12] André Anders. Tracking down the origin of arc plasma science I. Early pulsed and oscillating discharges. *IEEE Transactions on Plasma Science*, 31(4):1052–1059, August 2003.

[13] Robert Magidoff. Soviets claim “electroerosion” revolutionizes metal cutting. *American Machinist*, 90(10):162, May 1947.

[14] H. Rawdon. The nature of martensite: Discussion. *Transactions of the American Institute of Mining and Metallurgical Engineers*, 70:37, 1924.

[15] M. Barash. Electric spark machining. *International Journal of Machine Tool Design and Research*, 2:281–295, 1962.

[16] J. Huang, Y. Liao, and W. Hsue. Determination of finish-cutting operation number and machining-parameters setting in wire-electrical discharge machining. *Journal of Materials Processing Technology*, 87:69–81, 1999.

[17] B. Yan, H. Tsai, F. Huang, and L. Lee. Examination of wire electrical discharge machining of AL2O3/6061Al composites. *International Journal of Machine Tools & Manufacture*, 45:251–259, 2005.

[18] T. Spedding and Z. Wang. Study on modeling of wire EDM process. *Journal of Materials Processing Technology*, 69:18–28, 1997.

[19] S. Sarkar, S. Mitra, and B. Bhattacharyya. Parametric analysis and optimization of wire electrical discharge machining of γ-titanium aluminide alloy,. *Journal of Materials Processing Technology*, 159:286–294, 2005.

[20] Y. Liao, J. Huang, and H. Su. A study on the machining-parameters optimization of wire electrical discharge machining. *Journal of Materials Processing Technology*, 71:487–493, 1997.

[21] A. Hasçalýk and U. Çaydaş. Experimental study of wire electrical discharge machining of AISI D5 tool steel. *Journal of Materials Processing Technology*, 148:362–367, 2004.

[22] Y. Liao, J. Huang, and Y. Chen. A study to achieve a fine surface finish in wire-EDM. *Journal of Materials Processing Technology*, 149:165–171, 2004.

[23] R. Ramakrishnan and L. Karunamoorthy. Modeling and multi response optimization of Inconel 718 on machining of CNC WEDM process. *Journal of Materials Processing Technology*, 2007. In Press: Accepted Manuscript.

[24] H. Lee and J. Yur. Characteristic analysis of EDMed surfaces using the Taguchi approach. *Materials and Manufacturing Processing*, 15(6):781–806, 2000.

[25] S. Kuriakose and M. Shunmugam. Characteristics of wire-electro discharge machined Ti6Al4V surface. *Materials Letters*, 58:2231–2237, 2004.

[26] M. Hewidy, T. El-Taweel, and M. El-Safty. Modelling the machining parameters of wire electrical discharge machining of Inconel 601 using RSM. *Journal of Materials Processing Technology*, 169:328–336, 2005.

[27] R. Williams and K. Rajurkar. Study of wire electrical discharge machined surface characteristics. *Journal of Materials Processing Technology*, 28:127–138, 1991.

[28] F.Han, J. Jiang, and D. Yu. Influence of discharge current on machined surface by thermo-analysis in finish cut of WEDM. *International Journal of Machine Tools & Manufacture*, 47:1187–1196, June 2007.

[29] M. Kunieda and C. Furudate. High precision finish cutting by dry WEDM. *Annals of the CIRP*, 50:121–124, 2001.

[30] M. Jennes, R. Snoeys, and W. Dekeyser. Comparison of various approaches to model the thermal load on the EDM-wire electrode. *Annals of the CIRP*, 33: 93–98, 1984.

[31] K. Masui and T. Sone. The electrolytic corrosion on wire-EDM's surface. *Journal of the Japan Society for Precision Engineering*, 54:160–165, 1988.

[32] T. Magara, H. Yamada, S. Sato, T. Yatomi, and K. Kobayashi. Improvement of surface quality by non-electrolysis wire-EDM. *Journal of the Japan Society for Precision Engineering*, 59:1157–1162, 1993.

[33] C. Wilkins. EDM wire covers all the angles. *Cutting Tool Engineering*, pages 40–45, April 1996.

[34] A. Schoth, R. Förster, and W. Menz. Micro wire EDM for high aspect ratio 3D microstructuring of ceramics and metals. *Microsystem Technologies*, 11:250–253, 2005.

[35] G. Benavides, L. Bieg, M. Saavadra, and E. Bryce. High aspect ratio meso-scale parts enabled by wire micro-EDM. *Microsystem Technologies*, 8:395–401, 2002.

[36] F. Klocke, D. Lung, D. Thomaidis, and G. Antonoglou. Micro wire-EDM investigations using thin wires. *Proceedings of the First International Conference for Manufacturing Engineering (ICMEN)*, pages 737–744, 2002.

[37] J. Fordham, R. Pilkington, and C. Tang. The effect of different profiling techniques on the fatigue performance of metallic membranes of AISI 301 and Inconel 718. *International Journal of Fatigue*, 19:487–501, 1997.

[38] C. Huang, C. Shih, K. Li, and Y. Chang. The surface alloying behavior of martensitic stainless steel cut with wire electrical discharge machine. *Applied Surface Science*, 252:2915–2926, 2006.

[39] C. Huang, F. Hsu, and S. Yao. Microstructure analysis of the martensitic stainless steel surface fine-cut by the wire electrode discharge machining (WEDM). *Materials Science and Engineering A*, 371:119–126, 2004.

[40] C. Huang, C. Hsu, and H. Kuo. The surface characteristics of P/M high-speed steel (ASP 23) multi-cut with wire electrical discharge machining (WEDM). *Journal of Materials Processing Technology*, 140:298–302, 2003.

[41] H. Obara, Y. Iwata, and T. Oshumi. An attempt to detect wire temperature distribution during wire EDM. *Proceedings of the 11th International Symposium on Electromachining (ISEM)*, pages 67–73, 1995.

[42] W. Wang and K. Rajurkar. Adaptive control of WEDM by on-line identifying workpiece height. *Transactions of the North American Manufacturing Research Institution/Society of Manufacturing Engineers (NAMRI/SME)*, XXII: 73–78, 1994.

[43] J. Prohaszka, A. Mamalis, and N. Vaxevanidis. The effect of electrode material on machinability in wire electro-discharge machining. *Journal of Materials Processing Technology*, 69:233–237, 1997.

[44] H. Groos. Schnellschneidende electrode zur schneiderosionsbearbeitung [german]. German Patent: DE3415055A1, 1984.

[45] M. Yan and H. Chien. Monitoring and control of the micro wire-EDM process. *International Journal of Machine Tools & Manufacture*, 48(1):148–157, 2007.

[46] Y. Liao, S. Chen, and C. Lin. Development of a high precision tabletop versatile cnc wire-EDM for making intricate micro parts. *Journal of Micromechanics & Microengineering*, 15:245–253, 2005.

[47] E. Uhlmann, S. Piltz, and U. Doll. Machining of micro/miniature dies and moulds by electrical discharge machining-recent developments. *Journal of Materials Processing Technology*, 167:488–493, 2005.

[48] M. Yan, C. Huang, C. Cheng, and C. Chang. Development of a prototype micro-wire-EDM. *Journal of Materials Processing Technology*, 149:99–105, 2004.

[49] F. Klocke, D. Lung, D. Thomaidis, and G. Antonoglou. Using ultra thin electrodes to produce micro-parts with wire-EDM. *Journal of Materials Processing Technology*, 149:579–584, 2004.

[50] D. Pham, S. Dimov, S. Bigot, A. Ivanov, and K. Popov. Micro-EDM-recent developments and research. *Journal of Materials Processing Technology*, 149: 50–57, 2004.

[51] S. Jeelani and M. Collins. Effect of electric discharge machining on the fatigue life of Inconel 718. *International Journal of Fatigue*, 10(2):121–125, 1988.

[52] J.R. Davis and ASM International Handbook Committee. *ASM Specialty Handbook: Nickel, Cobalt and Their Alloys*. ASM International, first edition, 2000.

[53] Inconel 718. Alloy Digest: Ni-65, April 1961.

[54] R. Kennedy, W. Cao, T. Bayha, and R. Jeneski. Allvac 718Plus: A Ni-Cr-Fr-Co alloy with 1300°F (704°C) capability. *Cobalt News*, pages 5–7, April 2005.

[55] Technical data blue sheet: Allegheny Ludlum Altem 718 alloy nickel-base superalloy (UNS designation N07718). Provided by Allegheny Ludlum Corporation., February 1998.

[56] ASM International Handbook Committee. *ASM Handbook: Volume 4, Heat Treating*. ASM International, tenth edition, 1991.

[57] L. Rhoades. Removing EDM recast layer. *Socitey of Manufacturing Engineers (SME) Technical Paper*, MR87-643, 1987.

[58] T. Loveless, R. Williams, and K. Rajurkar. A study on the effects of abrasive-flow finishing on various machined surfaces. *Journal of Materials Processing Technology*, 47:133–151, 1994.

[59] A. Wang and S. Weng. Developing the polymer abrasive gels in AFM process. *Journal of Materials Processing Technology*, 192-193:486–490, 2007.

[60] J. Qun, A. Shih, R. Scattergood, and J. Luo. Abrasive micro-blasting to improve surface integrity of electrical discharge machined WC-Co composites. *Journal of Materials Processing Technology*, 166:440–448, 2005.

[61] H. Ramasawmy and L. Blunt. 3D surface characterization of electropolished EDMed surface and quantitative assessment of process variables using Taguchi Methodology. *International Journal of Machine Tools & Manufacture*, 42:1129–1133, 2002.

[62] C. Zhou, E. Taylor, J. Sun, L. Gebhart, E. Stortz, and R. Renz. Electrochemical machining of hard passive alloys with pulse reverse current. *Transactions of the North American Manufacturing Research Institution/Society of Manufacturing Engineers (NAMRI/SME)*, XXV:147–152, 1997.

[63] B. Lilly, J. Brevick, and C. Chen. The effect of pulsed electrochemical machining on the fatigue life of H-13 steel. *Transactions of the North American Manufacturing Research Institution/Society of Manufacturing Engineers (NAMRI/SME)*, XXV:153–158, 1997.

[64] G. Macdonald. A procedure for high integrity edm surfaces. *American Society of Tool and Manufacturing Engineers (ASTME) Technical Paper*, MR69-291, 1969.

[65] K. Rajurkar, D. Zhu, J. McGeough, J. Kozak, and A. De Silva. New developments in electro-chemical machining. *Annals of the CIRP*, 48:567–579, 1999.

[66] D. Zhu, K. Wang, and N. Qu. Micro wire electrochemical cutting by using in situ fabricated wire electrode. *Annals of the CIRP*, 56:241–244, 2007.

[67] H. Tönshoff, R. Egger, and F. Klocke. Environmental and safety aspects of electrophysical and electrochemical processes. *Annals of the CIRP*, 45:553–568, 1996.

[68] Improve fatigue strength with abrasive tumbling. *Iron Age*, pages 129–131, February 1959.

[69] K. Elmblad and A. Kuutila. Mass finishing techniques. *Society of Manufacturing Engineers (SME) Technical Paper*, FC99-195, 1999.

[70] M. Kutz. *Mechanical engineers' handbook*. Wiley, 1986.

[71] W. Renshi, Z. Xuecong, S. Deyu, and Y. Yuanfa. Shot peening of superalloys and its fatigue properties at elevated temperature. *Proceedings of the First International Conference on Shot Peening*, pages 395–404, 1981.

[72] B. Yan, G. Chang, J. Chang, and R. Hsu. Improving electrical discharge machined surfaces using magnetic abrasive finishing. *Machining Science and Technology*, 8:103–118, 2004.

[73] G. Yan, Y. Lin, and F. Huang. Surface modification of Al-Zn-Mg alloy by combined electrical discharge machining with ball burnishing. *International Journal of Machine Tools & Manufacture*, 42:925–934, 2002.

[74] C. Kao and A. Shih. Sub-nanosecond monitoring of micro-hole electrical discharge machining pulses and modeling of discharge ringing. *International Journal of Machine Tools & Manufacture*, 46:1996–2008, 2006.

[75] Y. Liao and Y. Yu. The energy aspect of material property in WEDM and its application. *Journal of Materials Processing Technology*, 149:77–82, 2004.

[76] George Blann of Buehler Ltd. Personal Communication, August 2006.

[77] George F. Vander Voort. *Buehler SUM-MET: The Science Behind Materials Preparation*, page 77. Buehler Ltd., first edition, 2004.

[78] J. Radavich. Metallography of alloy 718. *Journal of Metals*, pages 42–43, July 1988.

[79] ASM Handbook Committee. *Metals Handbook*, volume 8, pages 100–104. American Society for Metals, eighth edition, 1973.

[80] Electroless nickel. Alloy Digest: Ni-332, April 1986.

[81] V. Hauk, R. Oudelhoven, and G. Vaessen. The state of residual stress in the near surface region of homogeneous and heterogeneous materials after grinding. *Metallurgical and Materials Transactions A*, 13:1239–1244, July 1982.

[82] I. Ogata and Y. Mukoyama. Residual stress on surface machined by wire electric discharge. *International Journal of the Japan Society for Precision Engineering*, 25(4):273–278, 1991.

[83] J. Kruth and P. Bleys. Measuring residual stress caused by Wire EDM of tool steel. *International Journal of Electrical Machining*, 5:23–28, 2000.

[84] C. Suryanarayana and M. Norton. *X-Ray Diffraction: A Practical Approach*. Plenum Press, first edition, 1998.

[85] W. Oliver and G. Pharr. Measurement of hardness and elastic modulus by instrumented indentation: advances in understanding and refinements to methodology. *Journal of Materials Research*, 19:3–20, 2004.

[86] Hysitron Inc. Triboscope users manual, February 2003.

[87] G. Sines and R. Carlson. Hardness measurement for determination of residual stress. *Bulletin of the American Society of Testing Materials*, 180:35–37, 1952.

[88] A. Warren, Y. Guo, and M. Weaver. The influence of machining induced residual stress and phase transformation on the measurement of subsurface mechanical behavior using nanoindentation. *Surface Coatings & Technology*, 200:3459–3467, 2006.

[89] S. Thompson. Selection of vibratory finishing equipment. *Society of Manufacturing Engineers (SME) Technical Paper*, MR81-381, 1981.